Cell-Surface Auxin Signaling: Linking molecular pathways to plant development

by

Aline Monzer

February, 2025

A thesis submitted to the
Graduate School
of the
Institute of Science and Technology Austria
in partial fulfillment of the requirements
for the degree of
Doctor of Philosophy

Committee in charge:
Mario de Bono, Chair
Jiří Friml
Eva Benková
Michael Wrzaczek

The thesis of Aline Monzer, titled *Cell-Surface Auxin Signaling: Linking molecular pathways to plant development*, is approved by:

Supervisor: Jiří Friml, ISTA, Klosterneuburg, Austria

Signature: _____

Committee Member: Eva Benková, ISTA, Klosterneuburg, Austria

Signature: _____

Committee Member: Michael Wrzaczek, University of South Bohemia, České Budějovice, Czech Republic

Signature: _____

Defense Chair: Mario de Bono, ISTA, Klosterneuburg, Austria

Signature: _____

Signed page is on file

ISTA Thesis, ISSN: 2663-337X

ISBN: 978-3-99078-054-1

I hereby declare that this thesis is my own work and that it does not contain other people's work without this being so stated; this thesis does not contain my previous work without this being stated, and the bibliography contains all the literature that I used in writing the dissertation.

I accept full responsibility for the content and factual accuracy of this work, including the data and their analysis and presentation, and the text and citation of other work.

I declare that this is a true copy of my thesis, including any final revisions, as approved by my thesis committee, and that this thesis has not been submitted for a higher degree to any other university or institution.

I certify that any republication of materials presented in this thesis has been approved by the relevant publishers and co-authors.

Signature: _____

Aline Monzer

March, 2025

Signed page is on file

Abstract

Plant growth and development rely significantly on phytohormones, with auxin serving as a master regulator, orchestrating processes from embryogenesis to organogenesis, vascular patterning, and environmental adaptation. Since its conceptual proposition by Charles Darwin in 1880 as an endogenous chemical signal influencing phototropism in grass, auxin has captivated scientists seeking to understand how such a small molecule exerts a profound influence on plant development.

One particularly fascinating aspect of auxin function is its ability to self-organize its transport. Through a feedback mechanism between auxin perception and directional transport—primarily mediated by PIN auxin transporters—auxin establishes narrow transport channels. This phenomenon, known as auxin canalization, is fundamental to vascular formation, regeneration, and other key developmental processes. Despite advances in our understanding, driven by experimental studies and computational models, auxin canalization remains an enigma, with many unanswered questions.

Like other hormones, auxin functions through intricate signaling pathways. It operates through at least two distinct signaling mechanisms: the well-characterized canonical pathway and the less understood non-canonical pathway. While significant progress has been made in elucidating the canonical pathway, the non-canonical mechanisms remain less defined and require further investigation.

In this study, we revisit the non-canonical auxin signaling pathway mediated by the cell-surface complex Auxin Binding Protein 1-Transmembrane Kinase 1 (ABP1-TMK1), with a particular focus on its downstream phosphorylation events. We reveal that this auxin-mediated phosphorylation is conserved across the green lineage, underscoring its fundamental role in plant development. We explore key phosphorylation targets, particularly PIN2, which is essential for root gravitropism. To further understand TMK1's role in diverse developmental processes, we identified and investigated its interactors as potential co-receptors or regulatory components within its signaling network.

Given the previously established role of ABP1-TMK1 in auxin canalization, we sought to further investigate this process and identified several TMK1 interactors also involved in this intricate mechanism.

These findings provide new insights into the complex regulation of auxin canalization, highlighting a broader and more interconnected signaling framework than previously understood.

Dedication

To my father, whose belief in me continues to inspire my every step, even though he is no longer with us. I know he would have been proud of this achievement.

Acknowledgments

I would like to express my gratitude to my supervisor, Jiří Friml, for his guidance, support, and insightful feedback throughout both my internship and PhD journey. His expertise and encouragement were essential to the success of this work.

I would like to acknowledge the facilities at ISTA, particularly LSF, IOF, and, of course, the plant facility, for providing the necessary resources for my research.

I am also grateful to all the lab members, both former and current, for creating such a friendly and supportive environment. Thank you, Moni and Karolina, for your help in ordering supplies and dealing with all the chaos in the lab. A special thanks to the members of our English club—Dorota, Huihuang, Minxia, Han, and Linlin—for all the lunches, deep conversations, and memorable trips we shared together. I would also like to thank Lukas F. for his care, support, and kind heart, not to mention the kiwis we shared.

I would like to extend my thanks to Inge, Michelle, and Jakub for their support in the lab, as well as the mental and emotional encouragement they provided throughout my journey here.

My heartfelt thanks also go to the friends I made along the way. Nathalie G., I can't thank you enough for simply being you, for the constant support, and for sharing all my frustrtations with me. Silvie, I will always cherish our perfume hunts and French classes. Jakob, thank you for founding with me our ice cream club, and for enjoying ice cream even in the coldest, winter temperatures. Nath, thank you for the wonderful dinners and for offering the comforting cuddles with your cats. Natalia, thank you for all the brunches, coffees, and for making the best tiramisu I've ever had. Galien and Arka, thank you for the time spent together and for the amazing trips showing us around in Belgium and India. I've also loved our Spartan training sessions and seeing the dedication, well for some more than others. Michael R., thank you for all the deep and philosophical conversations, the books, the poems, and, of course, the chocolate you shared.

I would also like to thank my dear friends, Elsa and Mhamad. Visiting each other was incredibly important to me, and it brought the Lebanese warmth I deeply miss, making me feel closer to home.

I want to express my deepest gratitude to my Can, for his love, patience, and support. Being silly together has meant the world to me, especially during the toughest moments of this journey. Thank you for always being there, making me laugh, and bringing so much joy into my life.

I want to thank my sister for all the amazing food you cooked for me and for being a constant source of strength and an inspiring example for me.
Last but not least, I want to thank my mum for her endless love, strength, and patience. Even from a distance, you always find a way to make things feel easier.

About the Author

Aline Monzer earned a Bachelor's degree in Agricultural Sciences, specializing in Plant Science and Technology, from the Lebanese University in Beirut. She then pursued a Master's degree in Agricultural Sciences, focusing on Plant Production, where her research examined the impact of water quality and irrigation management on *Paulownia tomentosa* growth in Central Bekaa. Continuing her academic journey, Aline obtained a second Master's degree in Horticultural Genetics and Biotechnology from the CIHEAM-Mediterranean Agronomic Institute of Chania (MAICh) in Greece. Her thesis investigated the role of tomato *prolyl 4 hydroxylase 3* in abscission. Afterwards, Aline worked as an intern in the Friml group at IST Austria and stayed for her PhD studies. Her research focuses on auxin signaling, particularly exploring the TRANSMEMBRANE KINASE 1 (TMK1) pathway.

List of publications appearing in the thesis

1. **Monzer A**, Friml J. Historical and mechanistic perspective on ABP1/TMK1-mediated cell surface auxin signaling. *npj Sci. Plants.* 2024- under revision

2. Friml J, Gallei M, Gelová Z, Johnson A, Mazur E, **Monzer A**, et al. ABP1–TMK auxin perception for global phosphorylation and auxin canalization. *Nature*. 2022;609(7927):575-581. doi:10.1038/s41586-022-05187-x

3. Kuhn A, Roosjen M, Mutte S, Dubey SM, Carrasco PC, **Monzer A**, et al. RAF-like protein kinases mediate a deeply conserved, rapid auxin response. *Cell*. 2024;187(1):130-148.e17. doi:10.1016/j.cell.2023.11.021

4. Rodriguez L, Fiedler L, Zou M, Giannini C, Yu Y, **Monzer A,** et al. ABP1/ABL3-TMK1 cell-surface auxin signaling directly targets PIN2-mediated auxin fluxes for root gravitropism. Published online November 30, 2022. doi:10.1101/2022.11.30.518503

5. **Monzer A**, Mazur E, Rodriguez L, Gallei M, et al. TMK interacting network of receptor like kinases for auxin canalization and beyond. Published online March 02, 2025. doi:10.1101/2025.02.28.640727

Table of Contents

List of Figures

List of Abbreviations

2,4-D	2,4-Dichlorophenoxy-acetic acid
ABA	Abscisic acid
ABL	ABP1-LIKE
ABP1	AUXIN-BINDING PROTEIN 1
AFB	AUXIN SIGNALING F-BOX
ARF	AUXIN RESPONSE FACTOR
AUX/IAA	AUXIN/ INDOLE-3-ACETIC ACID
BA	Benzoic acid
BiFC	Bimolecular fluorescence complementation
CAMEL	CANALIZATION-RELATED AUXIN-REGULATED MALECTIN-TYPE RLK
CANAR	CANALIZATION-RELATED RECEPTOR-LIKE KINASE
CD	Circular Dichroism
CETSA	Cellular thermal shift assay
CRAP	CpGFP ROP Activity Probe
DAA	Days after application
DARTS	Drug Affinity Responsive Target Stability
DAW	Days after wounding
ECD	Extracellular domain
ER	Endoplasmic reticulum
FA	Formic acid
FRET-FLIM	Fluorescence Lifetime Imaging Microscopy
GCI	Grating-Coupled Interferometry
GLP	Germin-like protein
GO	Gene ontology
HL	Hydrophilic loop
IAA	Indole-3-acetic acid
IP	Immunoprecipitation
KD	Kinase domain
LRR-RLK	Leucine-rich repeat receptor-like kinase
MAPK	MITOGEN-ACTIVATED PROTEIN KINASE

MP	Membrane potential
MST	Microscale Thermophoresis
NAA	Naphthylacetic acid
NAP	Nuclear auxin pathway
PB1	Phox-Bem1
PC	Pavemenmt cell
PIN	PIN-FORMED
PM	Plasma membrane
RAF	RAPIDLY ACCELERATED FIBROSARCOMA
RIC	ROP-INTERACTIVE CRIB MOTIF-CONTAINING PROTEIN
ROP	RHO OF PLANT GTPASES
RT	Room temperature
TBO	Toluidine blue O
TEM	Transmission electron microscopy
TINT	TMK1 INTERACTOR
TIR1	TRANSPORT INHIBITOR RESPONSE 1
TMK1	TRANSMEMBRANE KINASE
UBQ	Ubiquitin
WT	Wild-type

1 Introduction

1.1 The discovery and role of auxin in plant development

Auxin is the first plant hormone to be discovered, and for a while, the term phytohormone was used interchangeably with auxin, before other plant hormones were identified. The discovery of auxin can be traced back to 1880[1], when Charles Darwin first observed its role as a growth-promoting substance that influences the bending of grass seedlings in response to light. However, it wasn't until 1926 that Frits Went demonstrated that this substance, responsible for the bending, was released from the tip of the plant[2]. Went named this substance auxin, derived from the Greek word *auxein*, meaning "to grow" or "to increase." It was only later, in the 1930s, that the first natural form of auxin, indole-3-acetic acid (IAA), was isolated and chemically identified[3].

Auxin research is one of the earliest branches of experimental plant biology, with its underlying mechanisms having inspired, and continuing to inspire, scientists, particularly as it became evident that auxin orchestrates a wide range of processes crucial to plant growth and development. Starting at the cellular level, auxin regulates cell division[4] by contributing to the formation of new organs and promotes cell elongation[5] by modifying cell wall plasticity. Beyond cellular growth, auxin plays a crucial role in major developmental processes such as embryogenesis by establishing bilateral symmetry in the embryo[6], organogenesis[7], root growth[8], apical dominance[9], and vascular tissue formation[10]. It is also involved in key events like fruit development and leaf abscission[11], ensuring proper growth and organ separation. Additionally, auxin is essential for plant adaptation to environmental changes, mediating responses to light[1,2] and gravity[12], as well as enhancing defense mechanisms against pathogens[13] and abiotic stresses[14] such as drought and temperature fluctuations.

1.2 Auxin signaling pathway

1.2.1 Canonical auxin signaling pathway

After the discovery of auxin and its various functions, understanding how this hormone operates at the molecular level became increasingly important. One key aspect is auxin signaling, the mechanism by which auxin is perceived and sensed by cells to translate the signal into specific responses.

The canonical auxin signaling pathway involves several key components: the Transport Inhibitor Response1/ Auxin-Signaling F-Box **(**TIR1/AFB) receptors, Auxin/ Indole-3-Acetic Acid **(**Aux/IAA) transcriptional co-repressors, and Auxin Response Factor (ARF) transcription factors[15]. When auxin levels are low, Aux/IAA proteins bind to ARFs, inhibiting their transcriptional activity and preventing the expression of auxin-responsive genes. However, when auxin concentrations are high, auxin binds to the TIR1/AFB receptors, which also function as F-box ubiquitin ligases. This binding triggers the ubiquitination and degradation of the Aux/IAA proteins. As a result, the inhibition of ARFs is lifted, allowing them to activate the transcription of genes involved in various plant growth and developmental processes[15].

1.2.2 Cell surface auxin signaling pathway

Adapted and modified from:

Monzer A, Friml J. Historical and mechanistic perspective on ABP1/TMK1-mediated cell surface auxin signaling. *npj Sci. Plants.* 2024- under revision

Auxin is a central hormone in plant development, governing processes ranging from cell elongation to pattern formation and stress responses[1,2]. Understanding how auxin is perceived and translated into cellular responses has been a cornerstone of plant biology research. Within this context, Auxin-Binding Protein 1 (ABP1) has played a pivotal role in shaping our understanding of auxin signaling in plants.

Discovered over 50 years ago as the first potential hormone receptor in plants, ABP1 was initially celebrated as an auxin receptor responsible for orchestrating auxin-mediated growth and development[3]. After detailed biochemical characterization, its critical role in development was supported by genetic evidence, including the embryo-lethal phenotype of the *abp1* null mutants in the model *Arabidopsis thaliana*[4].

Subsequent insights into ABP1's signaling mechanisms and roles were limited and overshadowed by the successful characterization of the canonical Transport Inhibitor Response 1/ Auxin Signaling F-box (TIR1/AFB)-dependent pathway[5]. Nonetheless, studies using conditional *abp1* knock-down lines[6] have linked ABP1 function to the regulation of endocytosis and trafficking, particularly of PIN auxin transporters. This suggested a role for ABP1 in feedback regulation of auxin transport[7].

In 2015, the identification of new *abp1* CRISPR-based null mutants indistinguishable from wild-type plants[8], along with the failure of the *ABP1* gene to rescue the previously reported embryo-lethal phenotype[9], raised serious doubts about the physiological and developmental relevance of ABP1.

Recent reevaluation of ABP1's role as an auxin receptor[10] has rekindled interest in its involvement as part of the cell-surface auxin-sensing complex. Specifically, ABP1, in cooperation with Transmembrane Kinase 1 (TMK1), has been shown to mediate ultrafast phosphorylation response to auxin, complementing the traditional transcriptional pathway[11].

This breakthrough not only redefined ABP1's role in extracellular auxin perception but also highlighted its crucial involvement in auxin transport-mediated canalization.

This review aims to trace the historical journey of ABP1, exploring its function, molecular interactions, and role in auxin perception and downstream signaling. Special attention is given to its partnership with TMKs. By revisiting the long and exciting history of ABP1 and integrating recent findings, we aim to provide a cohesive narrative of how ABP1, in conjunction with TMK1 and other molecular components, functions as a linchpin in auxin signaling and plant development.

1.2.2.1 The historical journey of ABP1: from discovery to resurrection

ABP1 has a rich, 50-year history, rising to prominence as a key auxin-binding protein, initially thought essential for plants' survival[4], only to see its role devalued[8,9] and, finally, regained within the complex landscape of cell surface auxin signaling[10]. This epic journey is well worth exploring in detail.

After the discovery of auxin and the multitude of its effects on plant growth and development, scientists became keen to identify its receptor for a deeper understanding of the action of this prominent hormone. To achieve this, a radiolabeled azido-assay to identify auxin binders from corn coleoptiles (*Zea mays*) was conducted, resulting in the identification of ABP1 in 1972[3]. In the following 17 years, ABP1's primary sequence was finally revealed along with its predominant localization in the endoplasmic reticulum (ER)[12]. This was a key step, opening doors for biochemists and geneticists to test the role of ABP1 as an auxin receptor. After

decades of detailed biochemical and structural analyses[13], the embryo-lethal phenotype of the *abp1* null mutant strengthened the hypothesis on ABP1's importance for plant's survival[4]. Further studies using conditional knockdowns[6] confirmed its involvement in post-embryonic plant growth and development. In particular, ABP1 was proposed to regulate plasma membrane (PM) processes, including endocytosis, endocytic trafficking, and thus PM-incidence of PIN auxin efflux carriers[14], thereby feedback regulating polar auxin transport[15,16].

Much of the ABP1 history revolved around the identification of the so-called "docking protein" that would transmit the signal from the cell surface, where ABP1 was proposed to act, to the cell interior. This proposal was spectacularly fulfilled by the identification of ABP1's interaction partners[17], the Transmembrane Kinase (TMK) family, which belongs among the Leucine-rich repeat receptor-like kinases (LRR-RLKs).

ABP1 was long considered a "red herring" in plant hormone research[18]. A persistent debate centered on its predominant presence in the endoplasmic reticulum (ER), where the pH is not favorable for auxin binding[19]. Furthermore, two major setbacks to ABP1's reputation occured simultaneously in 2015: (i) the identification of two new *abp1* null alleles similar to wild-type plants[8]; and (ii) the failure of the *ABP1* genomic fragment or coding sequence to rescue the embryo-lethal phenotype[9]. These findings led part of the community to doubt ABP1's significance in auxin signaling and plant development, despite the studies of the gain-of-function mutants continuing to suggest its role in the regulation of auxin transport and development[7,9,20].

It took a full seven years before ABP1 regained its position on the map of auxin signaling. This renaissance came when *Arabidopsis* ABP1 was characterized, its auxin-binding ability and dual localization in the ER and extracellular space were reconfirmed, and its crucial importance in auxin canalization and vasculature regeneration was identified genetically[10]. This work demonstrated that both ABP1 and TMK1 are essential for auxin-induced global, ultrafast phosphorylation as well as for several other cellular processes, including PM-ATPase activation and PIN regulation[21,22]. Subsequent research found that ABP1-like (ABL) proteins share ABP1's functional role, interacting with TMK1 to form a similar complex that senses extracellular auxin[22,23]. These exciting discoveries put ABP1-TMK cell surface auxin signaling back into a research focus.

1.2.2.2 ABP1-TMK1 cell surface auxin perception for global, ultrafast phosphorylation

ABP1 is a single-copy gene in most species, including *Arabidopsis*, and is distantly related to the cupin superfamily[24], specifically to the Germin-like protein (GLP) family, which is found in all plants. The GLP family shares with ABP1 a conserved tertiary structure—a stable, barrel-like fold—despite the limited similarity in the overall primary sequence[25]. In ABP1, this conserved β-barrel structure, known as the cupin fold, forms a binding pocket for auxin. Within this cupin domain, ABP1 contains a conserved germin box motif, composed of about 20 amino acid residues, which play a key role in coordinating a metal ion, typically zinc[24].

While ABP1 resides predominantly in the ER, a portion is secreted to the cell surface, where transmission electron microscopy (TEM) revealed that it forms aggregates in the apoplast[10]. Maize ABP1 was identified based on its strong binding to 1-naphthylacetic acid (1-NAA) in radiolabeled binding assays[3]. This binding was later confirmed also for tobacco ABP through purification and biochemical assays, while the crystallization was achieved with maize ABP1[24]. Notably, the auxin binding assays repeatedly demonstrated preferential auxin binding at a low pH of 5 and 5.5[24], which corresponds to the pH of the apoplast. New binding assays were conducted with the natural auxin indole-3-acetic acid (IAA) to demonstrate that also *Arabidopsis* ABP1 binds to IAA preferentially at the apoplastic pH[10].

ABP1 and/or TMK1 have been mentioned in numerous studies associated with various signaling and developmental processes. However, it was the discovery of the global, ultrafast auxin phosphorylation response[10] that provided a clearer mechanistic understanding of how ABP1 with TMKs activates the downstream responses.

A phosphoproteomic approach in *Arabidopsis* roots revealed that, within just two minutes, auxin triggers the phosphorylation of close to a thousand proteins, independently of the canonical TIR1/AFB pathway[10]. Subsequent findings showed that auxin-induced phosphorylation can occur within as little as 30 seconds and is deeply conserved across the plant kingdom[26]. Notably, the phosphorylation response was found to be highly specific to the natural auxin IAA, as no similar response was observed with the synthetic auxins, benzoic acid, or formic acid[26]. Of particular interest, this phosphorylation response in *Arabidopsis* requires ABP1 and TMK1, with an overlap of many phospho-sites[10].

One of the interesting targets of ABP1-TMK1-triggered phosphorylation is the motor protein Myosin XI and Myosin binding (adaptor) protein (MadB2). Together, Myosin XI and MadB2 regulate the trafficking and dynamic distribution of PIN proteins, playing a crucial role in the feedback loop between auxin signaling and auxin transport across various developmental stages[27]. PIN proteins themselves are prominent phosphorylation targets; this regulation will be discussed in detail later. Another key target of the ABP1-TMK1 complex is the *Arabidopsis* H^+-ATPase (AHA), which regulates proton pumping across membranes, contributing to cellular pH changes and influencing processes such as cell expansion[28,29]. The role and mechanism of AHAs in the context of auxin will be elaborated upon in the TMK1 section. An important, conserved downstream target of the auxin phosphorylation response is the Rapidly Accelerated Fibrosarcoma (RAF)-like kinases[26]. These B4 RAF-like kinases in *Arabidopsis* and *Marchantia* are essential for the auxin phosphoresponse and play a pivotal role in growth and development. As both ABP1 and TMK1 are required for the auxin-induced phosphorylation of RAF-like kinases, they provide a link between the ABP1-TMK1 cell surface auxin signaling and the global, ultrafast auxin phosphoresponse[26].

1.2.2.3 TMKs and their downstream signaling in plant growth and development

In *Arabidopsis thaliana*, the TMK family includes four members[30]. They are composed of: (i) an extracellular domain (ECD) consisting of leucine-rich repeats and adopting a horseshoe shape where ligands bind; (ii) a transmembrane domain that anchors the protein in the PM and connects the ECD to the cytosolic domain; and (iii) an intracellular domain, consisting of a kinase domain, responsible for all downstream signaling pathways[31].

TMK1 protein was structurally and biochemically characterized in *Arabidopsis thaliana* for the first time in 1992, highlighting that it encodes a receptor-like kinase and proposing its potential role in transmembrane signaling in plants[32]. Later, in 2000, TMK1 homologue in *Nicotiana tabacum* was isolated showing high homology with the one of *Arabidopsis* as well as with rice[33]. The initial role of TMK1, along with its three subfamily members (TMK2, TMK3, and TMK4), in plant growth was only demonstrated in 2013, especially in regulating cell expansion and cell proliferation[30]. Since then, research on the role of the TMK subfamily in signaling, specifically in the context of auxin, has proliferated. The TMK receptor kinases are involved in multiple developmental processes at different stages and in various organs during plant growth; most of which are linked to auxin action.

Starting with the emergence of the seedling from the soil, TMK1 modulates the formation and the maintenance of the apical hook of the young seedling in order to protect the cotyledons and the shoot apical meristem from any injury[34–36]. Auxin concentrations at the concave (inner) side of the apical hook are higher than at the convex (outer) side. This accumulation of auxin leads to the cleavage of TMK1 kinase domain by the peptidases family DA1, followed by its

translocation to the nucleus where it phosphorylates two non-canonical transcriptional repressors, called Auxin/ Indole-3-Acetic Acid (Aux/IAA). Consequently, the ubiquitination of these IAA32 and IAA34 by the E3 ubiquitin ligases Cytokinin Induced Root Waving 1 (CKRW1)/ Wavy Growth 3 (WAV3) is prevented, resulting in their stabilization and the subsequent repression of the transcription factors; Auxin Response Factor (ARF), thereby inhibiting the cell elongation at the inner side of the apical hook.

In the hypocotyl, TMK1 regulates the elongation process through the acid growth theory mechanism[37]. In response to auxin, TMK1 interacts with and phosphorylates AHA H^+-ATPases at the PM[28]. This phosphorylation activates AHAs, promoting H^+ export, which leads to the acidification of the apoplast. The resulting acidic environment activates cell wall-modifying enzymes, causing the cell wall to loosen and soften, ultimately facilitating cell expansion[38].

On the other hand, in the root, the auxin-dependent phosphorylation of AHAs by TMK1 also occurs; however, it is antagonized and dominated by the increase in H^+ influx, which is regulated by the intracellular canonical TIR1/AFB, leading to the alkalization of the apoplast and thus inhibiting the root growth[29]. These two antagonistic processes presumably play a crucial role in fine-tuning root navigation through the soil[39].

TMK1 and TMK4 are also involved in the development of lateral roots by controlling the cell division pattern through activating Mitogen-Activated Protein Kinase (MAPK) signaling[40]. TMK1 and TMK4 phosphorylate MKK4 and MKK5 in an auxin-dependent manner and thus activate MPK4 and MPK6 signaling. Therefore, the development of the lateral root requires also coordination between the two auxin signaling pathways: the TIR1/AFB-dependent nuclear transcriptional pathway and the presumed posttranscriptional regulation by TMK1 and TMK4.

TMK1, acting together with ABP1/ABL3 auxin co-receptors, is also a major contributor to the root bending response to gravistimulation[22,41]. Gravistimulation triggers the sedimentation of dense, starch-filled organelles called statoliths in the root tip cells, leading to the relocalization of PIN auxin transporters in these cells. This relocalization correlates with auxin redistribution towards the lower root side, resulting in its accumulation in the epidermal cells at the lower side of the root. With increased auxin accumulation, the Membrane-Associated Kinase Regulator2 (MAKR2), which normally inhibits TMK1, translocates from the PM into the cytosol[41]. Consequently, TMK1 is activated, interacts with, and phosphorylates the hydrophilic loop of the PIN2 auxin transporter. This phosphorylation stabilizes PIN2, enhancing auxin asymmetry and promoting differential cell elongation[22]. This process ultimately causes the root to bend downward in response to gravity. It is an example of a feedback regulation between cell-surface auxin signaling and auxin transport, which also acts between TMK1 and PIN1 during organogenesis and vascular tissue development[21].

In *Arabidopsis* leaves, TMK1 is crucial for the interdigitation of epidermal pavement cells (PCs), mediated by auxin via ABP1/ABL1/2, as it activates Rho of plant GTPases (ROP) signaling pathways[23,42,43]. The jigsaw-puzzle appearance of PCs results from their spatially coordinated insertion between neighboring cells. At the lobe site, the activated ROP2, through its effector ROP-interactive CRIB motif-containing protein 4 (RIC4), promotes the formation of cortical F-actin microfilaments. Whereas in the opposing indenting site, ROP6, through activating its effector ROP-interactive CRIB motif-containing protein 1 (RIC1), promotes the microtubules and suppresses ROP2 activation. These two antagonistic mechanisms lead to the formation of lobes and indentations. To gain further insight, the relationship between local cell coordination and global tissue-wide coordination was examined in detail[44]. This investigation highlighted an additional layer of interaction between cell-surface auxin signaling and the canonical, nuclear auxin pathway. In this process, TIR1/AFB activates the expression of auxin biosynthesis genes, leading to the formation of a global auxin gradient with the maxima at the

leaf tips. Auxin then, across the entire tissue, locally activates the TMK mechanism, which subsequently triggers downstream ROP signaling pathways leading to the interdigitated growth of individual leaf epidermal cells.

So far, all the aforementioned functions stress the role of TMK in auxin signaling and the downstream developmental processes. However, it is important to emphasize the specific involvement of TMK4 in the inhibition of auxin biosynthesis[45]. This regulation is post-transcriptional, where TMK4, activated by auxin, phosphorylates Tryptophan Aminotransferase of Arabidopsis 1 (TAA1)—a key enzyme in auxin biosynthesis—at threonine 101 (T101), which is essential for TAA1 enzymatic activity. When phosphorylated, this site renders TAA1 inactive, thereby reducing auxin levels. Another role of TMK4 in auxin biosynthesis regulation involves its auxin-dependent phosphorylation of the FKBP12-Interacting Protein 37 (FIP37). This modification enhances FIP37 interaction with RNA, increasing the N6-methyladenosine (m6A) modification and thus the mRNA decay of the Nitrilase 1 (*NIT1*) gene which is involved in auxin biosynthesis[46].

Another interesting regulation is the involvement of TMK1 in the crosstalk between auxin and another phytohormone, abscisic acid (ABA)[47]. When auxin levels are high, TMK1 targets and phosphorylates ABA Insensitive 2 (ABI2), inhibiting its phosphatase activity. This inhibition releases SNF1-related protein kinases 2 (SnRK2s), which activate ABA responses. In contrast, low auxin concentrations do not trigger ABA signaling.

Another hypothesized role of TMK1 and TMK4 is mediating the crosstalk between auxin and brassinosteroids during hypocotyl elongation[48]. Auxin promotes the elongation by activating MPK3 and MPK6, which phosphorylate general regulatory factor 4 (GRF4) leading to the accumulation of brassinazole-resistant 1 (BZR1), a key transcription factor in brassinosteroid signaling. Although TMK1 and TMK4 have already been shown to activate MAPK signaling in lateral root development, their involvement in hypocotyl elongation requires further investigation.

Above-mentioned examples likely represent only snippets of the more general and broader roles of the members of the TMK family in various cellular and developmental processes. It remains to be seen whether all these TMK functions will be matched by similar functions of ABP1 and ABLs, or whether TMKs or ABP1/ABLs also have independent functions.

1.2.2.4 **The role of ABP1-TMK1 auxin signaling in auxin canalization**

Among all the different developmental roles that have been so far associated with ABP1 and TMKs, the best characterized is their role in auxin canalization. We cannot truly discuss the concept of auxin canalization without acknowledging the foundational contributions of Tsvi Sachs, whose pioneering work has shaped our understanding of this critical process in plant development. Through this process, plants optimize their development by flexibly connecting new organs with preexisting vasculature network, establishing, and regenerating their vasculature. Auxin canalization is a self-organizing process in which auxin establishes narrow transport channels, known as auxin 'canals' [49], by a feedback mechanism between auxin signaling—where the auxin source is sensed—and the directional auxin transport, primarily mediated by PIN auxin transporters. The subcellular positioning (polarity) of these PINs is adjusted in such a way that auxin is transported away from the source towards a sink, thereby forming the transport channels[1]. To achieve this, individual cells within the tissue synchronize their polarizations, allowing them to work together to establish a unified pattern of auxin flow. This coordinated behavior enables the tissue to form a well-organized structure, ensuring the efficient formation of auxin transport routes that will provide a positional signal for the formation of new vasculature. The role of auxin channels in adjusting development can be illustrated through several examples. For instance, the prearranged positioning of PIN channels

plays a crucial role in leaf venation, guiding the formation of veins[50]. Similarly, during vascular regeneration following wounding, PIN-expressing channels guide the new connection to circumvent the wound[51]. Another notable example is the integration of new organs formed at the shoot apical meristem[52] or lateral buds emerging from dormancy[53], where PIN-expressing channels play an essential role in establishing connections with the existing vascular network.
Besides experimental studies, the computational models have also been developed to help explain the mechanisms behind the coordination of PIN polarity during canalization. These models typically focus on two mechanisms: (i) the impact of auxin on cellular growth and the transmission of mechanical stresses through the cell wall, which influences microtubule orientation and governs PIN polarity; and (ii) the role of both intracellular and extracellular auxin perception in regulating PIN expression and PIN endocytic trafficking[54]. In the second mechanism, the nuclear auxin signaling affects *PIN* transcription, while the extracellular perception regulates PIN endocytosis, affecting its incidence at the PM[55].
Recent studies have enriched the auxin canalization model, shedding light on the molecular players and cellular processes involved[54]. These discoveries have advanced our understanding of cell surface auxin signaling, highlighting its role in auxin canalization and its influence on directional auxin transport. Among the prominent molecular components, a PM-localized complex formed by two LRR-RLKs, the Canalization-related Auxin-regulated Malectin-type RLK (CAMEL) and the Canalization-related Receptor-like Kinase (CANAR), has been described[56]. CAMEL contains a malectin domain in its extracellular region, while CANAR acts as a pseudokinase and serves as a negative regulator of CAMEL. CAMEL phosphorylates PIN1, influencing its polarization. This complex is required for vascular tissue regeneration after wounding and leaf venation, with knockout mutants of these receptors exhibiting defects in both. While PIN1 phosphorylation is also regulated by the AGCIII-type kinases like PINOID and D6PK[57], CAMEL uniquely phosphorylates new sites in the hydrophilic loop of PIN1, distinct from those dependent on other kinases. This complex operates downstream of the transcription factor WRKY23[58], a key node in transcriptional auxin signaling mediated by TIR1/AFB. By linking this auxin signaling to PIN1 polarization, the CAMEL-CANAR complex serves as a mediator of auxin-driven developmental processes.
As introduced earlier, the ABP1-TMK1 auxin perception complex at the cell surface plays a key role in auxin canalization, which underscores the concept of diverse auxin perception mechanisms, converging on the regulation of the directional auxin transport. Both *abp1* and *tmk1* loss-of-function mutants exhibit defects in *de novo* vasculature formation and its regeneration in the inflorescence stems[10] . As noted earlier, Myosin and its binding partner MadB2 serve as downstream targets of rapid phosphorylation by the ABP1-TMK1 complex in response to auxin. This phosphorylation event plays a critical role in coordinating PIN subcellular localization during canalization. Furthermore, as mentioned, TMK1 can directly target and phosphorylate PIN hydrophilic loops, linking TMK1 activity to the modulation of PIN polarity and auxin distribution, also during canalization[21,22]. These elements represent a few of the possible intermediaries, through which the ABP1-TMK1 complex exerts its role in auxin canalization, although further research is needed to fully elucidate their precise contributions.

1.2.2.5 **Conclusion and open questions**

Auxin is a versatile hormone that orchestrates a wide range of processes in plants, operating at varying time scales[1,2]. This complexity arises from auxin's reliance on at least two distinct perception mechanisms and their branched downstream signaling cascades tailored to mediate specific responses[5,59,60]. The TIR1/AFB-mediated canonical pathway operates in the nucleus by modulating transcription, while the non-transcriptional branch of this pathway operates in

the cytoplasm[61,62]. The ABP1-TMK-dependent pathway acts at the cell surface mediating both transcriptional and non-transcriptional responses[34]. These pathways likely act in coordination, to harmonize diverse physiological responses across the plant. Such connections are exemplified in the apical hook maintenance, where the TMK1 kinase domain is cleaved and translocated from the PM to the nucleus, regulating IAA32/34 and altering the expression of auxin-responsive genes[34–36]. Similarly, during lateral root development, the regulation of lateral root initiation by TIR1/AFB must coordinate with the post-transcriptional regulation by TMKs[40]. Another partly characterized example of auxin's dual regulatory modes is observed in root growth inhibition, where the rapid phosphorylation and activation of the PM H^+-ATPases at the cell surface[10], promoting cell wall acidification[28], is antagonized by TIR1/AFB-mediated alkalinization[29]. This dual auxin action ensures precise spatial and temporal balance of root growth.

Unlike other plant hormones, auxin is unique in its ability to be transported directionally[14]. This directional transport is crucial for the formation of the asymmetric auxin distribution (local maxima and gradients), which dictate many aspects of plant development[63]. The PIN-dependent auxin network can integrate many endogenous and environmental signals, and the resulting auxin flow redirections and modifications enable plants to adapt and optimize their growth patterns in response to environmental and developmental cues[14]. Among the most important endogenous signals converging on PIN polarity is auxin itself. This tight feedback regulation between auxin signaling and transport is the key prerequisite for auxin canalization and the resulting vasculature formation[49].

A key player in the feedback regulation is the ABP1-TMK1 auxin sensing complex, which, following auxin binding, mediates downstream phosphorylation events[10] essential, among others, for regulating auxin transport. By triggering downstream phosphorylation of myosin[27], PIN1[21] and PIN2[22], ABP1-TMK1 modulate trafficking, polarization, and stability of auxin transporters, influencing distinct developmental processes. Despite significant progress in understanding the roles of ABP1 and TMK1, a major question remains: what are the other downstream players involved in this signaling cascade? For example, the involvement of the CAMEL-CANAR complex, which also regulates auxin transport through the phosphorylation of PIN1[56], adds another layer of complexity to this regulation. Exploring their potential connection to the ABP1-TMK1 pathway would provide valuable insights into how auxin signaling is integrated across different PM sub-compartments and developmental processes. Recent studies have also identified ABL proteins, which, like ABP1, form surface complexes with TMK1 to sense auxin[22,23]. This finding expands our understanding of cell surface auxin perception and underscores the need to investigate how these proteins contribute to the regulation of other developmental processes beyond canalization.

Despite over 50 years of ABP1 research, its role within the ER where the majority of ABP1 and ABLs are found, remains enigmatic. This is just one example of the many mysteries of the ABP1/ABL-TMK pathway waiting to be exposed.

1.2.2.6 **Acknowledgements**

We gratefully acknowledge the funding by the Austrian Science Fund (FWF; I 6123-B and P 37051-B) and the European Research Council (ERC; 101142681 CYNIPS).We would like to thank Lukas Fiedler for his significant input and thoughtful revision of this manuscript.

1.2.2.7 **Figure**

Figure 1- Cell-Surface Auxin Signaling Mediated by the ABP1/ABLs-TMK1 Complex

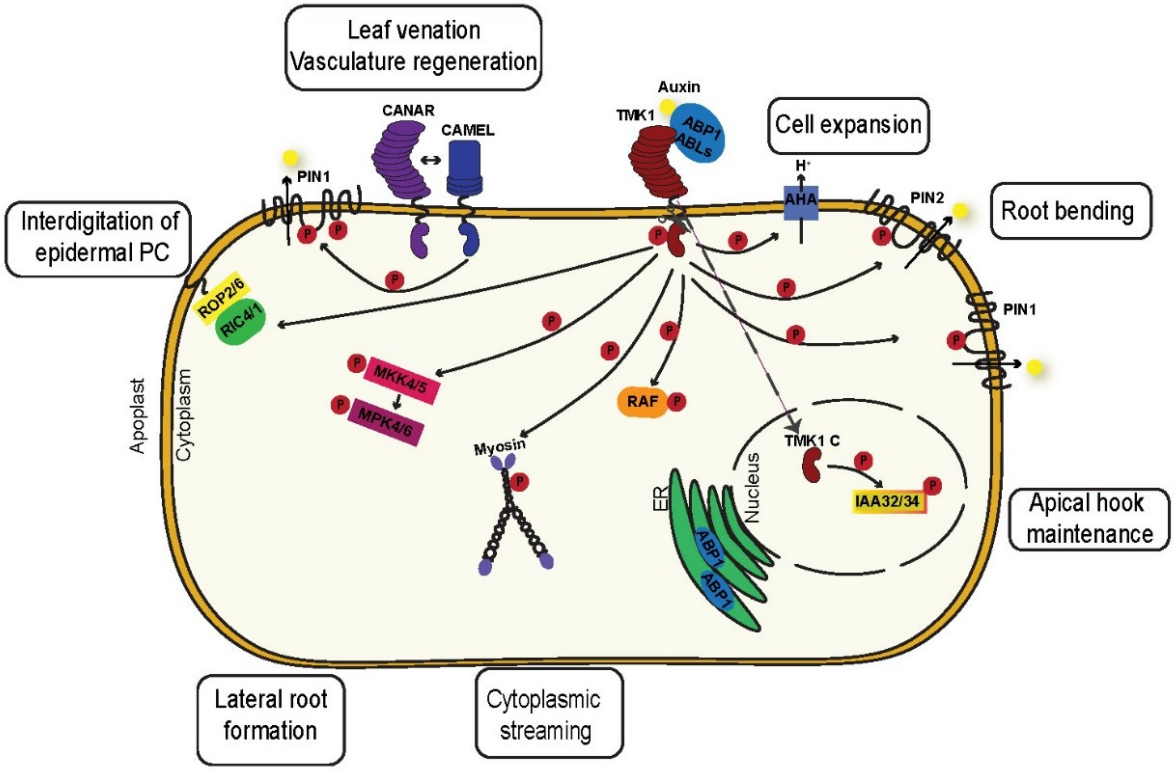

Figure 1.2-1 Cell-Surface Auxin Signaling Mediated by the ABP1/ABLs-TMK1 Complex

The figure depicts the physical interaction between ABP1 (Auxin-Binding Protein 1)/ABLs (ABP1-like proteins) and TMK1 (Transmembrane Kinase 1), mediated by the presence of auxin. Upon auxin binding, the complex becomes activated, initiating a downstream phosphorylation cascade. This cascade regulates various auxin-dependent developmental processes. The specific roles of the ABP1/ABLs-TMK1 complex in auxin signaling are outlined in labeled boxes placed outside the cell representation. Arrows represent the direction of signaling flow, and phosphorylation events are indicated with a "P" inside a red circle. Additionally, the CAMEL-CANAR complex is illustrated, demonstrating its role in phosphorylating PIN1, a key regulator of auxin transport.

1.2.2.8 References

1. Friml, J. Fourteen Stations of Auxin. *Cold Spring Harbor Perspectives in Biology* **14**, (2022).
2. Caumon, H. & Vernoux, T. A matter of time: auxin signaling dynamics and the regulation of auxin responses during plant development. *Journal of Experimental Botany* **74**, 3887–3902 (2023).
3. Hertel, R., Thomson, K.-S. & Russo, V. E. A. In-vitro auxin binding to particulate cell fractions from corn coleoptiles. *Planta* **107**, 325–340 (1972).
4. Chen, J. G., Ullah, H., Young, J. C., Sussman, M. R. & Jones, A. M. ABP1 is required for organized cell elongation and division in Arabidopsis embryogenesis. *Genes and Development* **15**, 902–911 (2001).
5. Salehin, M., Bagchi, R. & Estelle, M. SCFTIR1/AFB-based auxin perception: mechanism and role in plant growth and development. *The Plant cell* **27**, 9–19 (2015).
6. Braun, N. *et al.* Conditional Repression of AUXIN BINDING PROTEIN1 Reveals That It Coordinates Cell Division and Cell Expansion during Postembryonic Shoot Development in *Arabidopsis* and Tobacco. *Plant Cell* **20**, 2746–2762 (2008).
7. Robert, S. *et al.* ABP1 Mediates Auxin Inhibition of Clathrin-Dependent Endocytosis in Arabidopsis. *Cell* **143**, 111–121 (2010).
8. Gao, Y. *et al.* Auxin binding protein 1 (ABP1) is not required for either auxin signaling or Arabidopsis development. *Proc. Natl. Acad. Sci. U.S.A.* **112**, 2275–2280 (2015).
9. Grones, P. *et al.* Auxin-binding pocket of ABP1 is crucial for its gain-of-function cellular and developmental roles. *J. Exp. Bot.* **66**, 5055–5065 (2015).
10. Friml, J. *et al.* ABP1–TMK auxin perception for global phosphorylation and auxin canalization. *Nature* **609**, 575–581 (2022).
11. Abel, S. & Theologis, A. Early Genes and Auxin Action. *Plant Physiol.* **111**, 9–17 (1996).
12. Inohara, N., Shimomura, S., Fukui, T. & Futai, M. Auxin-binding protein located in the endoplasmic reticulum of maize shoots: molecular cloning and complete primary structure. *Proceedings of the National Academy of Sciences of the United States of America* **86**, 3564–8 (1989).
13. Woo, E. *et al.* Crystal structure of auxin-binding protein 1 in complex with auxin. *EMBO J.* **21**, 2877–2885 (2002).
14. Luschnig, C. & Friml, J. Over 25 years of decrypting PIN-mediated plant development. *Nat. Commun.* **15**, 9904 (2024).
15. Robert, S. *et al.* ABP1 mediates auxin inhibition of clathrin-dependent endocytosis in arabidopsis. *Cell* **143**, 111–121 (2010).
16. Čovanová, M. *et al.* Overexpression of the Auxin Binding PROTEIN1 Modulates PIN-Dependent Auxin Transport in Tobacco Cells. *PLoS ONE* **8**, (2013).
17. Xu, T. *et al.* Cell Surface ABP1-TMK Auxin-Sensing Complex Activates ROP GTPase Signaling. *Science* **343**, 1025–1028 (2014).
18. Venis, M. A. Auxin binding protein 1 is a red herring? Oh no it isn't! *Journal of Experimental Botany* **46**, 463–465 (1995).
19. Tian, H., Klämbt, D. & Jones, A. M. Auxin-binding protein 1 does not bind auxin within the endoplasmic reticulum despite this being the predominant subcellular location for this hormone receptor. *J. Biol. Chem.* **270**, 26962–26969 (1995).
20. Gelová, Z. *et al.* Developmental roles of Auxin Binding Protein 1 in Arabidopsis thaliana. *Plant Sci.* **303**, 110750 (2021).
21. Wang, J. *et al.* Self-regulation of PIN1-driven auxin transport by cell surface-based auxin signaling in Arabidopsis. Preprint at https://doi.org/10.1101/2022.11.30.518523 (2022).

22. Rodriguez, L. *et al.* Cell surface auxin signalling directly targets PIN-mediated auxin fluxes for adaptive plant development. Preprint at https://doi.org/10.1101/2022.11.30.518503 (2022).
23. Yu, Y. *et al.* ABLs and TMKs are co-receptors for extracellular auxin. *Cell* **186**, 5457-5471.e17 (2023).
24. Napier, R. The Story of Auxin-Binding Protein 1 (ABP1). *Cold Spring Harbor Perspectives in Biology* **13**, (2021).
25. Dunwell, J. M., Gibbings, J. G., Mahmood, T. & Naqvi, S. M. S. Germin and germin-like proteins: Evolution, structure, and function. *Crit. Rev. Plant Sci.* **27**, 342–375 (2008).
26. Kuhn, A. *et al.* RAF-like protein kinases mediate a deeply conserved, rapid auxin response. *Cell* **187**, 130–148 (2024).
27. Han, H. *et al.* Rapid auxin-mediated phosphorylation of Myosin regulates trafficking and polarity in Arabidopsis. Preprint at https://doi.org/10.1101/2021.04.13.439603 (2021).
28. Lin, W. *et al.* TMK-based cell-surface auxin signalling activates cell-wall acidification. *Nature* **599**, 278–282 (2021).
29. Li, L. *et al.* Cell surface and intracellular auxin signalling for H+ fluxes in root growth. *Nature* **599**, 273–277 (2021).
30. Dai, N., Wang, W., Patterson, S. E. & Bleecker, A. B. The TMK Subfamily of Receptor-Like Kinases in Arabidopsis Display an Essential Role in Growth and a Reduced Sensitivity to Auxin. *PLoS ONE* **8**, 1–12 (2013).
31. Liu, J., Li, W., Wu, G. & Ali, K. An update on evolutionary, structural, and functional studies of receptor-like kinases in plants. *Front. Plant Sci.* **15**, (2024).
32. Chang, C. *et al.* The TMK1 gene from Arabidopsis codes for a protein with structural and biochemical characteristics of a receptor protein kinase. *Plant Cell* **4**, 1263–1271 (1992).
33. Cho, H. S. & Pai, H.-S. Cloning and Characterization of NtTMK1 Gene Encoding a TMK1-homologous Receptor-like Kinase in Tobacco. *Mol. Cells* **10**, 317–324 (2000).
34. Cao, M. *et al.* TMK1-mediated auxin signalling regulates differential growth of the apical hook. *Nature* **568**, 240–243 (2019).
35. Gu, B. *et al.* Modulation of receptor-like transmembrane kinase 1 nuclear localization by DA1 peptidases in Arabidopsis. *Proc. Natl. Acad. Sci. U.S.A.* **119**, (2022).
36. Wang, J. L. *et al.* WAV E3 ubiquitin ligases mediate degradation of IAA32/34 in the TMK1-mediated auxin signaling pathway during apical hook development. *Proc. Natl. Acad. Sci. U.S.A.* **121**, (2024).
37. Dünser, K. & Kleine-Vehn, J. Differential growth regulation in plants—the acid growth balloon theory. *Curr. Opin. Plant. Biol.* **28**, 55–59 (2015).
38. Du, M., Spalding, E. P. & Gray, W. M. Rapid Auxin-Mediated Cell Expansion. *Annu. Rev. Plant Biol.* **71**, 379–402 (2020).
39. Li, L., Gallei, M. & Friml, J. Bending to auxin: fast acid growth for tropisms. *Trends Plant Sci.* **27**, 440–449 (2022).
40. Huang, R. *et al.* Noncanonical auxin signaling regulates cell division pattern during lateral root development. *Proceedings of the National Academy of Sciences of the United States of America* **116**, 21285–21290 (2019).
41. Marquès-Bueno, M. M. *et al.* Auxin-Regulated Reversible Inhibition of TMK1 Signaling by MAKR2 Modulates the Dynamics of Root Gravitropism. *Current Biology* **31**, 228-237.e10 (2021).
42. Xu, T. *et al.* Cell surface- and Rho GTPase-based auxin signaling controls cellular interdigitation in Arabidopsis. *Cell* **143**, 99–110 (2010).
43. Suzuki, R. *et al.* Molecular editing of cellular responses by the high-affinity receptor for IgE. *Science* **343**, 1021–1025 (2014).

44. Pérez-Henríquez, P. *et al.* Hierarchical global and local auxin signals coordinate cellular interdigitation in *Arabidopsis*. Preprint at https://doi.org/10.1101/2024.06.17.599171 (2024).
45. Wang, Q. *et al.* A phosphorylation-based switch controls TAA1-mediated auxin biosynthesis in plants. *Nature Communications* **11**, 679 (2020).
46. Li, B. *et al.* TMK4-mediated FIP37 phosphorylation regulates auxin-triggered N-methyladenosine modification of auxin biosynthetic genes in Arabidopsis. *Cell Reports* **43**, 114597 (2024).
47. Yang, J. *et al.* TMK1-based auxin signaling regulates abscisic acid responses via phosphorylating ABI1/2 in Arabidopsis. *Proceedings of the National Academy of Sciences of the United States of America* **118**, (2021).
48. Yu, Z. *et al.* Auxin promotes hypocotyl elongation by enhancing BZR1 nuclear accumulation in *Arabidopsis*. *Sci. Adv.* **9**, eade2493 (2023).
49. Sachs, T. The Control of the Patterned Differentiation of Vascular Tissues. in *Advances in Botanical Research* vol. 9 151–262 (Elsevier, 1981).
50. Scarpella, E., Marcos, D., Friml, J. & Berleth, T. Control of leaf vascular patterning by polar auxin transport. *Genes Dev.* **20**, 1015–1027 (2006).
51. Mazur, E., Benková, E. & Friml, J. Vascular cambium regeneration and vessel formation in wounded inflorescence stems of Arabidopsis. *Scientific Reports* **6**, (2016).
52. Benková, E. *et al.* Local, Efflux-Dependent Auxin Gradients as a Common Module for Plant Organ Formation. *Cell* **115**, 591–602 (2003).
53. Balla, J., Kalousek, P., Reinöhl, V., Friml, J. & Procházka, S. Competitive canalization of PIN-dependent auxin flow from axillary buds controls pea bud outgrowth. *The Plant Journal* **65**, 571–577 (2011).
54. Hajný, J., Tan, S. & Friml, J. Auxin canalization: From speculative models toward molecular players. *Current Opinion in Plant Biology* **65**, (2022).
55. Wabnik, K. *et al.* Emergence of tissue polarization from synergy of intracellular and extracellular auxin signaling. *Molecular Systems Biology* **6**, (2010).
56. Hajný, J. *et al.* Receptor kinase module targets PIN-dependent auxin transport during canalization. *Science* **370**, 550–557 (2020).
57. Bassukas, A. E. L., Xiao, Y. & Schwechheimer, C. Phosphorylation control of PIN auxin transporters. *Curr. Opin. Plant. Biol.* **65**, 102146 (2022).
58. Prát, T. *et al.* WRKY23 is a component of the transcriptional network mediating auxin feedback on PIN polarity. *PLoS Genet.* **14**, e1007177 (2018).
59. Gallei, M., Luschnig, C. & Friml, J. Auxin signalling in growth: Schrödinger's cat out of the bag. *Curr. Opin. Plant. Biol.* **53**, 43–49 (2020).
60. Fiedler, L. & Friml, J. Rapid auxin signaling: Unknowns old and new. *Curr. Opin. Plant. Biol.* **75**, 102443 (2023).
61. Dubey, S. M. *et al.* The AFB1 auxin receptor controls the cytoplasmic auxin response pathway in Arabidopsis thaliana. *Mol. Plant* **16**, 1120–1130 (2023).
62. Chen, H., Li, L., Zou, M., Qi, L. & Friml, J. Distinct functions of TIR1 and AFB1 receptors in auxin signaling. *Mol. Plant* **16**, 1117–1119 (2023).
63. Vanneste, S. & Friml, J. Auxin: A Trigger for Change in Plant Development. *Cell* **136**, 1005–1016 (2009).

2 Results and discussion

The results section presents key research articles on auxin signaling, with a particular focus on the non-canonical pathway. The chapters delve into cell surface auxin signaling mediated by the TMK1-ABP1 complex and the resulting ultrafast downstream phosphorylation events that influence developmental processes. Special emphasis is placed on auxin canalization and further exploration of this intricate signaling network.
Each research article is accompanied by a brief introduction to the central topic of the study, followed by a summary of the most relevant findings.
Contributions of Aline Monzer to each research article are detailed in the respective contributions section of each subchapter.

2.1 Chapter one: ABP1-TMK auxin perception for global phosphorylation and auxin canalization

Adapted and modified from:

Friml J, Gallei M, Gelová Z, Johnson A, Mazur E, **Monzer A**, et al. ABP1–TMK auxin perception for global phosphorylation and auxin canalization. *Nature*. 2022;609(7927):575-581. doi:10.1038/s41586-022-05187-x

While auxin's transcriptional signaling is well understood, its rapid non-transcriptional pathway remains unclear. To address this, we investigated the role of ABP1 as an auxin receptor in cell-surface signaling and plant development. Using biochemical, genetic, and physiological approaches, we demonstrate that ABP1 binds auxin at the acidic pH of the apoplast and cooperates with TMK1 to mediate a rapid, global auxin phospho-response. Our findings show that the ABP1-TMK1 signaling complex regulates key auxin-induced cellular processes, including H^+-ATPase activation and cytoplasmic streaming, and plays a crucial role in auxin canalization and vascular development. By establishing ABP1 as an auxin receptor in cell-surface signaling, we provide new insights into auxin's rapid signaling beyond transcriptional regulation.

2.1.1 Introduction

The plant hormone auxin is a key regulator of growth and development[1]. The best-characterized auxin signalling mechanism operates in the nucleus and relies on canonical TIR1/AFB receptors, Aux/IAA repressors and ARF transcriptional regulators, which mediate global transcriptional changes leading to developmental reprogramming[2,3]. Some classical auxin activities including regulation of root growth also depend on TIR1/AFBs[5,6] but are too fast to involve transcription, suggesting existence of an unknown non-transcriptional branch of TIR1/AFB signalling[7,8]. Other transcriptional mechanisms involve direct binding of auxin to transcription factors[9] or auxin-triggered cleavage and nuclear translocation of plasma membrane-localized TMK1[10].
Very rapid cellular auxin effects have been known for decades; e.g. plasma membrane (PM) hyperpolarization, PM H^+-fluxes, cytosolic Ca^{2+}-transients or protoplast swelling[11]. Another rapid, TIR1/AFB-independent auxin effect is the regulation of endocytic trafficking of PIN

auxin transporters[12–14]. This auxin feedback on its own transport is the main prerequisite of so called auxin canalization, a mechanism underlying self-organizing development, such as flexible vasculature formation[15]. Furthermore, we recently found that auxin induces very rapidly the phosphorylation of about a thousand of proteins involved in diverse cellular functions in TIR1/AFB-independent manner[16]. Those include PM H^+-ATPases, which mediate growth regulation[17,18] or Myosin XI and associated proteins involved in the above-mentioned trafficking and polarization of PIN transporters[16]. All these observations support the existence of fast, non-transcriptional responses relying on so far unknown auxin perception and signalling mechanisms[7,8]. Cell surface-localized TMK receptor-like kinases are candidates to contribute to this uncharacterized auxin signalling since they mediate auxin effects on growth, lateral root formation and auxin biosynthesis[19]. Nonetheless, this remains ambiguous, mainly due to the lack of an established auxin perception mechanism for this pathway.

Auxin Binding Protein 1 (ABP1), already identified in early 1970s[20] as potentially binding auxin, is a candidate for mediating auxin input into the TMK pathway; not the least on account of its association with TMK1[21]. Nonetheless, auxin binding has not been confirmed for *Arabidopsis thaliana* ABP1, for which all genetic studies have been conducted and, more importantly, those studies were called in question after the original *abp1* loss-of-function mutants were found erroneous[22–24]. Thus ABP1 and its eventual physiological roles remain controversial[4] and the mechanism of auxin perception for TMK signalling and for rapid auxin responses in general, remains obscure.

Here, we critically evaluated potential of the ABP1-TMK auxin perception module to act in fast auxin responses as well as in developmental regulations. Analysis of loss-of-function alleles and their complementation by different ABP1 variants identified strong similarities between *abp1* and *tmk* mutant phenotypes and revealed that auxin binding to ABP1 is crucial for its function. This establishes ABP1 as the auxin receptor for TMK1-mediated signalling upstream of a subset of rapid cellular effects and auxin canalization-mediated development.

2.1.2 Results

2.1.2.1 *Arabidopsis* ABP1 binds IAA at apoplastic pH

Members of the leucine-rich repeat receptor-like kinase (LRR-RLK) family, to which TMKs belong, are known to act as receptors for various ligands via their extracellular domain[25]. Nonetheless, we did not find any supporting evidence for direct auxin association to TMKs (exemplified by TMK1) *in planta* or to the TMK1 extracellular domain *in vitro* (Extended Data Fig. 1a-c). Therefore, we focused on *Arabidopsis* ABP1, which has been associated with TMK-based signalling[21] and its homologue from maize (*Zea mays*) has been shown to bind the synthetic auxin, 1-napthalene acetic acid (NAA)[26].

First, we verified a possible binding of natural auxin (indole-3-acetic acid, IAA) to *Arabidopsis* ABP1 using Drug Affinity Responsive Target Stability (DARTS). Both, *in planta* studies using a *35S::ABP1-GFP* transgenic line and *in vitro* experiments using heterologously expressed ABP1, suggested IAA association with ABP1 (Fig. 1a and Extended Data Fig. 1d,e). Next, we used Grating-Coupled Interferometry (GCI)-assisted analysis with purified ABP1, which detected binding of IAA to ABP1 in the micromolar range. This binding occurred at pH 5.5 but with a far smaller affinity at pH 7.6 (Fig. 1b) and was specific since no interaction was found with benzoic acid (BA) (Extended Data Fig. 1f). We also used Microscale Thermophoresis (MST). Again, the IAA binding to ABP1 occurred at pH 5.5 but not 7 or 7.5 (Extended Data Fig. 1g-i), and no interaction was found with BA or L-Trp (Fig. 1c).

The detected *in vitro* binding affinities are weaker than those reported for IAA binding to the TIR1-Aux/IAA pair[2,3]. Nevertheless, ABP1 affinity for auxin *in planta* is likely to be much

stronger, given that ABP1 (unlike TIR1) was repeatedly identified by auxin affinity approaches in different species[4]. This suggests that we might be missing additional factors in our *in vitro* assays. Nevertheless, these and previous observations[4] collectively show that ABP1 from *Arabidopsis* and other species specifically binds IAA and other auxins, preferentially at the acidic pH 5.5.

2.1.2.2 **ABP1 is partly secreted to cell surface**

IAA binding to ABP1 at the apoplast-like pH 5.5 reopened the question about extracellular localization of ABP1, which has remained a matter of debate since decades. Previously, maize ABP1 was shown to localize mainly to the endoplasmic reticulum (ER), consistent with the ER-retention signal in the ABP1 sequence, but to a minor extent also to the extracellular space[27]. This was also suggested for *Arabidopsis* ABP1 based on staining with heterologous antibodies[21].

To address this question, we utilized immunostaining and Transmission Electron Microscopy (TEM). We optimized pre-embedding labelling on intact samples, which preserved the PM and thus ensured the unequivocal localization of the immunogold signals to the intra- or extra-cellular areas. We used anti-GFP antibodies in *RPS5A::ABP1-GFP* roots with chemical fixation and in combinations with high-pressure freezing techniques. Both approaches revealed consistent signals that were absent in the non-transgenic controls. Intracellular ABP1 was detected in ER-like structures and absent from other organelles, for example the mitochondria or Golgi apparatus (Fig. 1e and Extended Data Fig. 2a,c). Besides intracellular signals, we detected ABP1 in the apoplast, which was slightly increased after IAA treatment. Notably, we observed regularly that the apoplastic signal formed clusters (ranging between 3-20 particles) with apparent increase in cluster appearance upon IAA treatment (Fig. 1e and Extended Data Fig. 2a-c).

Similar TEM analysis was conducted using the shoot apical meristem of the complementing *ABP1::GFP-ABP1* (= *comp-c1*; see Extended Data Fig. 4c) line expressing functional GFP-ABP1 under the endogenous promotor[28]. Samples were fixed using high-pressure freezing and subjected to post-embedding labelling. Taking into account the 19 nm resolution limitation of this method, we found a similar pattern of ABP1 localization at the outer PM side as in roots, which significantly increased upon IAA treatment (Fig. 1d and Extended Data Fig. 2d). The IAA-induced GFP-ABP1 signal increase was observed mainly in the PM vicinity; consistent with auxin-induced ABP1-TMK1 interaction[21]. The small increase of background signal in WT after IAA treatment (Fig. 1d) was never significant and may be related to a change of cell wall properties after IAA treatment.

In summary, different immunostaining TEM methods on two different GFP-tagged lines confirmed that *Arabidopsis* ABP1, besides residing predominantly in the ER, is also secreted to the apoplast. Despite the proportion of secreted ABP1 being low, especially in the non-overexpressing lines, our careful and blind analysis can reliably detect it, which is also supported by previous observations from Arabidopsis[21] and other species[4]. Collectively, these data are in line with IAA binding to ABP1 at acidic pH and with ABP1 association to PM-localized TMKs[21].

2.1.2.3 **ABP1-TMK1 mediate ultrafast auxin phospho-response**

Recently we showed that auxin, within 2 minutes, induces phosphorylation of about a thousand proteins in *Arabidopsis* roots by a mechanism largely independent of the TIR1/AFB auxin receptors[16]. We therefore tested whether TMK1 as a kinase and the associated ABP1 may be required for this rapid, global auxin-triggered phospho-response.

We compared this phospho-response in WT to *tmk1* and *abp1* mutants across 4 biological replicates for each genotype for both 100 nM IAA and solvent control treatments. In WT, over 1000 individual phospho-sites (P-sites) were hyper-phosphorylated after IAA treatment. Conversely, in the *tmk1-1* and *abp1-TD1* mutants, this hyper-phosphorylation response was almost completely abolished with the majority of P-sites being moderately hypo-phosphorylated, when compared to the distribution of hyper-phosphorylation in WT (Fig. 2a). This opposite tendency to hypo-phosphorylation in the mutants may be in part due to large differences in steady-state phosphorylation in the mutants (Extended Data Fig. 3a), as well as due to potential feedback regulations.

When comparing phospho-proteomes of untreated WT, *tmk1* and *abp1* roots, we found 2104 hypo-phosphorylated P-sites in the *tmk1-1* mutant, constituting potential substrates of the TMK1 kinase. Similar hypo-phosphorylation was found in the *abp1-TD1* mutant with 2589 hypo-phosphorylated P-sites as compared to WT (Extended Data Fig. 3a). The identified P-sites showed a significant overlap (Fisher's Exact Test: Odds Ratio=9.53, 95% Confidence Interval=8.28 – 11.00, $p < 2.2e-16$) between the *tmk1-1* and *abp1-TD1* mutants (Fig. 2c; Extended Data Fig. 3b, c) suggesting that TMK1 and ABP1 act together in mediating this rapid phospho-response. This is further substantiated by a high co-linearity between *tmk1-1* and *abp1-TD1* effects on the phosphorylation levels of individual sites. Notably, whereas most of the P-sites were co-regulated in *abp1* and *tmk1* mutants, about 5% showed an opposite regulation (Fig. 2b).

These observations suggest that ABP1 and TMK1 together mediate the rapid auxin effect on global protein phosphorylation.

2.1.2.4 **ABP1-TMK1 mediate subset of rapid responses**

Prominent among the hypo-phosphorylated P-sites in the *abp1* mutant were TMK1, TMK3, and TMK4 (TMK2 was not detected at all, presumably due to its low expression in roots) (Fig. 2d), suggesting that ABP1 is required for the auxin-induced phosphorylation and thus activation of TMKs. This is also supported by a common requirement of both these regulators for auxin-induced phosphorylation of many targets, prominent among them PM H^+-ATPases, the established direct targets of TMK1[17,18].

PM H^+-ATPases generate H^+ gradient across the PM, which acidifies apoplast and contributes to membrane potential (MP); both classical rapid cellular auxin responses[11]. Indeed, consistent with lower phosphorylation of PM H^+-ATPases (Fig. 2e), roots of *abp1-c1* and *abp1-TD1* have lower PM ATPase activity than WT (Fig. 2f), similar to *tmk1* roots[17]. This diminished auxin-induced PM ATPase activity correlates well with a previously shown inability of *abp1* mutant shoot-derived protoplasts to undergo auxin-induced swelling[29]. On the other hand, electrophysiological[30] and growth measurements[17] detected normal auxin-triggered MP depolarization in the *abp1* roots[31] (Extended Data Fig. 3e) along with normal auxin sensitivity of their growth (Extended Data Fig. 3f,g). These observations are consistent with a dominant role of TIR1/AFB signalling in the subset of rapid cellular responses related to auxin-induced root growth inhibition[5,32].

Other prominent targets of ABP1-TMK1 auxin phospho-response are cytoskeletal motor protein Myosin XI and MadB Myosin-binding proteins[16] (Fig. 2g and Extended Data Fig. 3d). A known cellular process dependent on Myosin XI function is cytoplasmic streaming[33]. We monitored this essential cellular process in the root elongation zone by quantifying movement of small intracellular organelles. These experiments revealed that IAA treatment promotes cytoplasmic streaming as inferred from particle velocity in a concentration-dependent manner (Extended Data Fig. 3h). This phenomenon can be observed in WT and *abp1* complemented lines (*comp-c1* and *comp-TD1*) but not in *abp1-c1*, *abp1-TD1* mutants (Fig. 2h; Extended Data

Fig. 3i). Notably, also *tmk1-1* or *tmk4-1* roots are defective in this process (Extended Data Fig. 3j). This shows that both ABP1 and TMK1 are involved auxin-triggered acceleration of cytoplasmic streaming consistent with a drop of auxin-triggered Myosin XI phosphorylation in those mutants (Fig. 2g).
These results suggest that ABP1 is required in auxin-triggered activation of TMK1 signalling and that both components are required for a subset of rapid cellular auxin responses such as PM H^+-ATPase activation and cytoplasmic streaming acceleration, providing examples of cellular targets for the ultrafast auxin phospho-response mediated by the ABP1-TMK1 module.

2.1.2.5 **ABP1-TMKs mediate vasculature regeneration**

Notably, Myosin XI also plays a role in the auxin feedback on its own transport and formation of auxin channels[16], which is part of the auxin canalization processes underlying self-organizing aspects of plant development[15]. A classic example of these canalization-mediated processes is vasculature regeneration after wounding when new vasculature is generated to circumvent the wound[34–37] (Fig. 3a).

We first evaluated ABP1 expression during vasculature regeneration. Previous studies suggested ABP1 expression in most tissues including inflorescence stems[4]. Closer analysis of the *ABP1::GUS* line revealed upregulation of expression 1–7 days after wounding (daw) induced by a horizontal cut. Early after wounding (before 2 daw), the GUS staining was visible strongly and specifically above and below the wound and gradually weakened over time (Fig. 3b). Similar expression pattern was observed also in the *ABP1::GFP-ABP1* stems (Extended Data Fig. 4b) confirming upregulation of ABP1 expression during vasculature regeneration.

Next, we assessed the ABP1 requirement for the vasculature regeneration after wounding. As visualized by toluidine blue (TBO) staining in WT or in *abp1* complemented lines (*comp-c1*, *comp-TD1*), the vasculature fully developed, and both newly regenerated vessel cells and lignified parenchyma cells stained in blue were visibly circumventing the wound. In contrast, in *abp1-c1* and *abp1-TD1* mutant stems, regeneration was defective, with cells failing to form a continuous strand of regenerated tissue (Fig. 3c, e and Extended Data Fig. 4c). Notably, the gain-of-function *35S::ABP1-GFP* line showed increased regeneration with more prominent regenerated vasculature strands (Fig. 3c, e).

We also analysed a role of TMKs in vasculature regeneration. *TMK::GUS* transgenic lines revealed the strongest expression of *TMK4* above and below the wound (2 daw) with a gradual formation of a channel-like pattern around the wound (4–6 daw), similar but weaker expression of *TMK3* and even weaker expression of *TMK1* (Extended Data Fig. 4a). Analysis of the corresponding loss-of-function mutants (*tmk1-1*, *tmk2-1*, *tmk3-1* and *tmk4-1*) revealed the strongest regeneration defects in *tmk4-1*, followed by *tmk3-1* and *tmk1-1*, whereas *tmk2-1* showed normal regeneration capacity consistent with the lack of TMK2 expression during regeneration (Fig. 3d, e and Extended Data Fig. 4e).

These results show that both ABP1 and various TMKs are expressed following wounding and their function is required for the stem's capacity to regenerate vasculature around the wound.

2.1.2.6 **ABP1-TMKs mediate auxin canalization**

A direct manifestation of the canalization processes, is the formation of auxin-transporting channels followed by vasculature differentiation originating from a local, exogenous auxin source[37] (Fig. 4a).

Application of an IAA droplet on the stem side led to the *de novo* formation of a distinct

vascular strand (visualized by TBO) connecting the external auxin source to the pre-existing vasculature (Extended Data Fig. 4d). Similar experiments in *PIN1::PIN1-GFP* auxin transporter and *DR5rev::GFP* auxin response marker lines confirmed formation of PIN1-expressing, DR5-positive auxin channels already 4 days after application (daa), preceding the differentiation of new vasculature (Fig. 4b, c). All these processes related to auxin channel and vasculature formation were defective in *abp1* and *tmk* loss-of-function mutants. *abp1-c1* and *abp1-TD1* mutant alleles failed to form channels, as seen by PIN1-GFP and DR5 markers as well as TBO staining, whereas their corresponding complemented lines (*comp-c1*, *comp-TD1*) formed channels normally. As observed for vasculature regeneration, *tmk4-1* showed the strongest defects in channel formation followed by *tmk3-1* and *tmk1-1* (Fig. 4b–d and Extended Data Fig. 4d-f).

Overall, these experiments revealed a crucial role for ABP1 and TMKs in the formation of auxin transporting channels for vasculature formation originating from a local auxin source.

2.1.2.7 **Auxin binding to ABP1 is crucial for its function**

Strong defects of *abp1* mutants in vasculature regeneration and auxin canalization allowed us to test the importance of auxin binding to ABP1 for its function. To this end, we engineered the ABP1^{M2X} version with a mutation in the predicted auxin-binding site[23]. Indeed, this ABP1^{M2X} protein variant did not associate with IAA in the DARTS assay and did not bind to IAA as confirmed by MST and GCI analysis (Fig. 5b; Extended Data Fig. 5c,d). The heterologously expressed and purified ABP1^{M2X} behaved similar to the ABP1^{WT} in terms of (*i*) stability as shown by Western blot; (*ii*) dimerization assessed by Mass photometry; and (*iii*) protein folding as inferred from thermal melts and Circular Dichroism (CD) spectra (Fig. 5a; Extended Data Fig. 5a,b). Therefore, although we cannot completely exclude that the M2X mutation affects ABP1 functionalities other than auxin binding, ABP1^{M2X} protein stability, folding and dimerization seem to be largely unaffected.

We introduced *ABP1::GFP-ABP1* or *ABP1::GFP-ABP1^{M2X}* into *abp1-c1* mutants and compared their ability to complement defects in the vasculature regeneration (visualized by TBO staining) and in the formation of auxin channels from external auxin source (visualized by TBO and *DR5rev::GFP* expression). *ABP1::GFP-ABP1* fully complemented the defects in both processes, whereas no complementation was observed in any of the four independent lines, which verifiably expressed stable GFP-ABP1^{M2X} protein (Fig. 5c,d; Extended Data Fig. 5b,e-h).

The failure of the ABP1^{M2X} variant to complement the *abp1* developmental phenotypes suggests that the ABP1 ability to bind auxin is crucial for its function, thus providing strong support for ABP1 acting as auxin receptor mediating auxin canalization.

2.1.3 Discussion and Conclusion

In this study we addressed a long-debated role of ABP1 in auxin perception and its relevance to plant development. We show that *Arabidopsis* ABP1 binds natural auxin IAA at a pH typical for the apoplast and that a fraction of ABP1 is secreted. This provides a possibility for extracellular ABP1 to mediate auxin input into the cell surface TMK receptor like kinase-dependent signalling; also supported by their auxin-induced interaction[21] and diminished auxin-triggered TMK phosphorylation in *abp1* mutants. What is the role of the majority ABP1 pool in the ER lumen and whether it involves auxin binding remains unclear.

The ABP1-TMK1 signalling module at the cell surface is required for the rapid, global auxin phospho-response[16] as evidenced by lack of this response and largely overlapping hypo-

phosphorylation detected in *abp1* and *tmk1* mutant roots. Among the common phospho-targets are previously established direct substrates of TMK1, PM H^+-ATPases[17,18] or Myosin XI and Myosin-binding proteins[16]. Accordingly, *abp1* and *tmk* mutants show defects in a related subset of auxin-triggered cellular responses, such as H^+-ATPase activation, shoot protoplasts swelling[29] or accelerated cytoplasmic streaming. Other rapid responses, such as PM depolarization[32], calcium transients[6] or root growth inhibition[5] do not seem to require ABP1 but are mediated by a so far elusive non-transcriptional branch of TIR1/AFB signalling[7,8].

The ultrafast, auxin-induced global protein phosphorylation is a novel rapid auxin response with yet largely unknown biological roles. The massive misregulation of protein phosphorylation seen in *abp1* and *tmk1* mutants establishes ABP1 and TMKs as key regulators of this process, but this is reflected by only mild developmental defects reported for *abp1* and *tmk1* mutants grown under standard growth conditions[28,38]. It remains an open question and topic for future investigations to ascertain what roles and under which conditions the ultrafast auxin phospho-response plays in growth and development.

Nonetheless, analysis of loss-of-function alleles and complemented lines revealed crucial roles of both ABP1 and TMKs in the auxin-triggered *de novo* formation and regeneration of shoot vasculature, a classic output of auxin canalization, a mechanism behind much self-organizing plant development[39]. These strong defects in auxin canalization-dependent processes suggest that ABP1-TMK cell surface signalling provides a long-sought mechanism for auxin input into the feedback regulation of auxin transport. This is the main pre-requisite of coordinated tissue polarization during canalization[15,40], which is also targeted by the CAMEL-CANAR receptor complex acting upstream of PIN auxin transporters[41]. It remains unclear whether and how ABP1-TMK and CAMEL-CANAR cooperate during canalization and how these processes, which take typically days to complete, are linked to the rapid auxin phospho-response.

abp1 mutants show stronger defects in the phospho-response or canalization as compared to the *tmk1* mutant. This is likely due to the redundant action of TMKs as suggested by overlapping expression and similar phenotypes of mutants in other members. On the other hand, multiple *tmk* mutants have much stronger developmental phenotypes than *abp1*[28,38]. This is either due to ABP1 having also functions independent of TMKs or possible functional redundancy of ABP1 with other members of the cupin superfamily[1,4], some of which were also shown to bind auxin[42].

The long-contested role of ABP1 as an auxin receptor is now strongly supported by *abp1* mutant defects in several auxin-triggered rapid cellular processes and in auxin canalization-related development. Further strong support comes from the observation that the $ABP1^{M2X}$ variant, which does not bind auxin, is non-functional in complementing the developmental phenotypes. The ABP1-TMK auxin perception complex at the cell surface thus mediates an ultrafast auxin phospho-response, providing now a means to interrogate biological roles of this global auxin regulation in canalization processes and beyond.

2.1.4 Material and methods

Genetic material and growth conditions

All *A. thaliana* lines are in the Columbia-0 (Col-0) background with the exception of *abp1-TD1*, which is in Col-4. The following lines were described previously: *abp1-c1* and *abp1-TD1* (ref. [22]), *tmk1-1* (SALK_016360), *tmk2-1* (SAIL_1242_H07), *tmk3-1* (SALK_129759) and *tmk4-1* (GABI_348E01)(ref. [10]), *DR5rev::GFP* (ref. [44]), *PIN1::PIN1-GFP* (ref. [45]), *ABP1::GUS* (ref. [46]) and *abp1* complemented lines (*comp-TD1 = ABP1::ABP1/abp1-TD1*; *comp-c1 = ABP1::GFP-ABP1/abp1-c1*) (ref. [29]). To generate *TMK1::GUS*, *TMK2::GUS*, *TMK3::GUS* and *TMK4::GUS* transgenic lines,

genomic fragments covering 2,000 bp upstream from the start codon of *TMK1*, *TMK2*, *TMK3* and *TMK4* were amplified from Col-0 genomic DNA. These promoter fragments were inserted into a *pDONR P4-P1r* vector by BP recombination reaction and subsequently cloned into a *pB7m24GW.3* vector together with *pEN-L1-GUS-L2* (Invitrogen) by a MultiSite Gateway LR recombination reaction.
The ABP1(M2X) variant was generated by substitutions of two histidine residues (H59V, H61V) by valine residues[23] into a *pABP1::GFP-ABP1* construct using the QuikChange Lightning Site-Directed Mutagenesis Kit (Agilent Technologies) and the following primers: M2X_Val-F (5′-AAAAACCTCTTCACAGGAGACCCTGACAATTGGTGTCTCTGAACCTGGAG-3′) and M2X_Val-R (5′-CTCCAGGTTCAGAGACACCAATTGTCAGGGTCTCCTGTGAAGAGGTTTTT-3′).
The *RPS5A::ABP1-GFP* plasmid was constructed with Gateway cloning technology (Invitrogen). The *ABP1-GFP* coding sequence14 and the *RPS5A* promoter region were recombined into the expression vector *pB7m24GW,3*. The resulting constructs were transformed into *Arabidopsis* plants by floral dipping in *Agrobacterium tumefaciens* cultures. Seeds were sterilized overnight by chlorine gas, sown on solid *Arabidopsis* medium (half-strength Murashige and Skoog basal salts, 1% sucrose and 0.8% phyto-agar, pH 5.7) and stratified at 4 °C for at least two days before transfer to a growth room with a 16-h light–8-h dark light cycle at 21 °C. Seedlings were grown vertically for four or six days, depending on the assay[17].

Heterologous expression and purification of recombinant proteins

To express the extracellular domain (ECD) of TMK1 the ECD residues determined as described[26] were cloned in the pECIA2 and pECIA14 plasmids[47]. To enhance expression and ease purification, the ER-retaining C-terminal KDEL sequence in the full-length coding sequence of ABP1 was replaced by KEQL. ABP1(M2X) mutations in the Zn^{2+}-associated predicted auxin-binding pocket were introduced as described[23]. Both ABP1(WT) and ABP1(M2X) were also introduced into pECIA2 and pECIA14. All sequences were N-terminally fused with the TEV pronase site, StrepII- and 9×His-tag. These purified plasmids were transformed into DH10EMBacY *E. coli*. Selected colonies contained the recombinant bacmids from which recombinant bacmid DNA could be stored. Three micrograms of this recombinant DNA was then transfected into Sf9 baculovirus cell cultures. Yellow fluorescent protein (YFP) indicated the efficiency of the transfection. Hi5 insect cells were infected with the three generated baculovirus stocks following the published protocol[48]. Owing to the initial plasmids used, protein purification could proceed from the medium of the expression cultures. For all three proteins, 2 l of cell culture was used. ABP1(WT) and ABP1(M2X) proteins were purified from Hi5 insect cells using a HisTrap Excel column (Cytiva) with gradual washes up to 50 mM imidazole in 50 mM HEPES/NaOH, 500 mM NaCl buffer at pH 7.5. Elution from the column was performed with 500 mM imidazole and the eluted fractions were pooled, concentrated (Vivaspin 20, 10-kDa molecular-weight cut-off (MWCO)) and loaded onto a Superdex 200 16/60 column. Size-exclusion chromatography (SEC) was performed in 50 mM citrate buffer pH 5.5 containing 250 mM NaCl and 0.05 mM $ZnCl_2$. Fractions were analysed on SDS–PAGE and on the basis of size and purity were selected and pooled for another concentration step. Aliquots were frozen and stored at −80 °C. TMK1 ECD protein was purified from Hi5 insect cells using a cOmplete His-tag purification column (Roche) with gradual washes up to 50 mM imidazole in 50 mM HEPES/NaOH, 500 mM NaCl buffer at pH 7.5. Elution from the column was performed with 500 mM imidazole and the eluted fractions were pooled and concentrated (Vivaspin 20, 10-kDa MWCO). To exchange the buffer, the

concentrated His-eluted fraction was loaded onto a HiPrep 16/10 desalting column, equilibrated with 10% 50 mM HEPES/NaOH, 1 M NaCl buffer at pH 7.5. To increase the purity of the target protein, sample was loaded onto a 5-ml ANX FF high sub ion exchange (IEX) column. Bound protein was eluted with 100% 50 mM HEPES/NaOH, 1 M NaCl buffer at pH 7.5. The flow-through from IEX was concentrated (Vivaspin, MWCO 10 kDa) and loaded onto a Superdex 200 16/60 column. SEC was performed in 50 mM NaH_2PO_4/Na_2HPO_4 buffer containing 200 mM NaCl and 5% glycerol at pH 7.5. Fractions were analysed on SDS–PAGE and on the basis of size and purity were selected and pooled for another concentration step. Aliquots were frozen and stored at −80 °C.

DARTS

The DARTS assay, for testing the binding of IAA to ABP1 or TMK1, was performed as previously reported[49]. Roots of seven-day-old *TMK1::TMK1-GFP* seedlings or full seven-day-old seedlings expressing *35S::ABP1-GFP* were used for total protein extraction. After harvesting, the samples were ground in liquid nitrogen, resuspended at a 1:2 (w/v) ratio in protein extraction buffer (25 mM Tris-HCl, pH 7.5; 150 mM NaCl; 0.1% IGEPAL CA-630, Roche cOmplete protease inhibitor cocktail, EDTA free) and spun down to discard the cell debris. After quantifying the protein concentration (Quick Start Bradford Reagent, Bio-Rad), the cell lysate was aliquoted and incubated with 0, 1, 10 or 50 µM IAA or benzoic acid. As both IAA and benzoic acid were dissolved in dimethyl sulfoxide (DMSO), the equivalent volume of DMSO was added in one mock aliquot. Cell lysate plus small molecule were incubated for 1 h at 4 °C while mixing at a low speed. Subsequently, the treated extracts were further aliquoted and mixed with different concentrations of pronase (Roche) in pronase buffer (25 mM Tris-HCl, pH 7.5; 150 mM NaCl). After incubation at 25 °C for 30 min, the proteolytic digestion was terminated by adding Roche cOmplete protease inhibitor cocktail and the samples were kept on ice for 10 min. The protein samples were then analysed by western blotting. Band intensity was quantified using the Plot lane function in ImageJ. GFP-fused proteins were detected by an anti-GFP antibody (JL8, Clontech, 1:2,000) or using anti-His–HRP for the in vitro experiments (Agrisera, AS15–2930, 1:5,000). Anti-actin (Sigma-Aldrich A0480, 1:5,000) was used as a loading control on the blots from the plant extracts. HRP activity was detected by the SuperSignal Western Detection Reagents (Thermo Fisher Scientific) and imaged with a GE Healthcare Amersham 600RGB system.

MST

IAA binding affinities were analysed by MST[50]. All recombinant proteins were fluorescently labelled using the Monolith Protein Labelling Kit RED-NHS 2nd Generation (MO-L011, NanoTemper Technologies) according to the manufactured manual, including the buffer-exchange step. ABP1(WT) and ABP1(M2X) were labelled in NHS labelling buffer (130 mM $NaHCO_3$, 50 mM NaCl, pH 8.2-8.3) followed by elution in either 50 mM citrate buffer pH 5.5 containing 250 mM NaCl, 0.05 mM $ZnCl_2$, 0.01% (w/v) TWEEN20 for measurements at pH 5.5 or in HEPES buffer pH 7.5 or pH 7 supplemented with 250 mM NaCl, 50 µM $ZnCl_2$, 0.01% (w/v) TWEEN20 to perform measurements at pH 7.5 or pH 7. TMK1 was labelled using the same kit, but elution was performed in 50 mM NaH_2PO_4/Na_2HPO_4 buffer containing 200 mM NaCl and 0.01% (w/v) TWEEN20 at pH 7.5.

All experiments were carried out on a Monolith NT.115 Blue/Green system (NanoTemper Technologies) and were performed in premium glass capillaries (MO-K025, NanoTemper Technologies). The target protein concertation was kept constant in the reaction as follows: 100 nM or 75 nM ABP1(WT) or ABP1(M2X), respectively, for binding study at pH 5.5, 100 nM ABP1 for binding study at pH 7.5 and pH 7 and 150 nM for the TMK1 ECD. IAA, benzoic acid and L-Trp as ligands were serially diluted 1:1 from 2 mM to 61 nM in the ABP1

experiments. IAA, NAA, benzoic acid and L-Trp as ligands were serially diluted from 200 µM to 3 nM and MST power 80% with excitation power 80% was used for binding measurements of ABP1 at pH 5.5, pH 7 and pH 7.5; MST power 80% with excitation power 40% was used for binding measurements of ABP1(M2X) at pH 5.5 and MST power 40% with excitation power 20% was used for binding measurements of the TMK1 ECD. All ABP1-related MST measurements were running in 3/3/3/25 s intervals. For the TMK1 ECD, 5/30/25 s intervals were used. During these intervals fluorescence is measured: 3/5 s before switching on the MST IR laser, the temperature gradient is established and thermophoretic movement is recorded during 3/30 seconds, afterwards diffusion is measured for 3/5 s and 25 s are allowed to recover (delay between samples). ten times in each experiment. ABP1 binding at pH 5.5 was performed in three independent replicates; all other experiments in two independent replicates. The evaluation of the binding of the TMK1 ECD to auxin was repeated four times. F_{norm} was calculated as the ratio of fluorescence after thermodiffusion to the initial fluorescence. ΔF_{norm} was obtained by subsequently subtracting the F_{norm} of the unbound state. MST traces were analysed in MO.Affinity Analysis software (NanoTemper Technologies) at the time point 1.5 s on time. Data were fitted to a K_d model assuming a 1:1 stoichiometry per binding partner and the confidence interval of the K_d was calculated from the variance of the fitted parameter using a standard fitting mode.

GCI

GCI measurements were done on the WAVEsystem (Creoptix). All experiments were performed on 4PCH WAVEchips (polycarboxylate hydrogel chips, Creoptix). Proteins were immobilized on the chip surface with standard amine-coupling (7-min activation (1:1 mix of 400 mM *N*-(3-dimethylaminopropyl)-*N*′-ethylcarbodiimide hydrochloride and 100 mM *N*-hydroxysuccinimide) (Xantec), followed by the injection of ABP1 on channel 2 (50 µg ml^{-1} in 10 mM sodium acetate pH 5); ABP1(M2X) on channel 3 (50 µg ml^{-1} in 10 mM sodium acetate pH 5) and TMK1 on channel 4 (120 µg ml^{-1} in 10 mM sodium acetate pH 4.5). High protein density was reached for each protein and mentioned in the Results table displayed in Extended Data Fig. 1f and 5d. Finally, the surface was deactivated with 1 M ethanolamine pH 8 for 7 min (Xantec). Channel 1 was also activated/deactivated and served as a reference channel. All kinetic analyses were performed at 25 °C with eight dilutions in a 1:3 dilution series from 200 µM of either IAA or benzoic acid, diluted in a 50 mM citrate buffer of pH 5.5 (250 mM NaCl, 50 µM $ZnCl_2$ and 1% DMSO) or HBS buffer of pH 7.6 (250 mM NaCl, 50 µM $ZnCl_2$ and 1% DMSO). Blank injections were used for double referencing and a DMSO calibration curve for bulk correction. Data analysis was performed using the Creoptix WAVE control software and a 1:1 Langmuir model was applied. The confidence interval of the K_d was calculated from the variance of the fitted parameter.

TEM

Wild-type and transgenic lines expressing *pABP1::ABP1-GFP* or *RPS5A::ABP1-GFP* were grown for four to five days on *Arabidopsis* medium (AM) plates, incubated in a mock or 1 µM IAA solution for 3 h and subjected to immuno-electron microscopy.

Pre-embedding immunometal electron microscopy: samples were fixed with 4% formaldehyde and 0.05% glutaraldehyde in phosphate buffer (0.1 M, pH 7.4) for 1 h at room temperature under vacuum. The samples were washed with phosphate buffer, incubated in increasing gradients of sucrose in phosphate buffer (10% and 20%) and then 20% sucrose plus 5% glycerol in phosphate buffer for 1 h each at room temperature. They were then rapidly frozen on liquid nitrogen and thawed in hand-warm phosphate buffer containing 20% sucrose to increase the penetration of reagents.This freeze-thawing cycle was repeated three times.

Samples were then washed with phosphate-buffered saline (PBS; 0.1 M, 0.9% NaCl, pH 7.4) and MilliQ water briefly, and incubated with 2% driselase in PBS for 30 min at 37 °C. They were then washed with Tris-buffered saline (TBS; 0.05 M, 0.9% NaCl, pH 7.4) and 50 mM glycine in TBS for 1 h at room temperature to quench free aldehyde groups, followed by incubation in 10% normal goat serum (NGS), 2% bovine serum albumin (BSA) and 0.2% fish-skin gelatin (FSG) in TBS for 90 min at room temperature to block nonspecific binding sites. An anti-GFP antibody raised in rabbit (Abcam, ab6556) was then applied in TBS containing 2% BSA at a concentration of 0.2 $\mu g\,ml^{-1}$ for 48 h at 15 °C with gentle agitation. After consecutive washes with TBS and TBS containing 2% BSA, 1.4 Nanogold-conjugated Fab' fragments (Nanoprobes; 1:100 in TBS containing 2% BSA) were applied for 16 h at 15 °C. The samples were washed with MilliQ water and post-fixed with 2% glutaraldehyde in 0.1 M phosphate buffer. Nanogold particles were then amplified with silver using the HQ SilverTM Enhancement kit (Nanoprobes) for 7–8 min at room temperature under light microscopy control, and amplification was stopped by washing with MilliQ water. Samples were fixed again with 2% glutaraldehyde in phosphate buffer for 20 min at room temperature, and incubated in phosphate buffer. For conventional resin embedding, samples were contrast-enhanced by applying 0.5% (w/v) tannic acid in 0.1 M phosphate buffer for 1 h at 4 °C, 1% (w/v) osmium tetroxide for 30 min at 4 °C and 1% (w/v) uranyl acetate in 50% ethanol (aqueous) for 30 min at 4 °C in the dark. Samples were dehydrated in graded ethanol (50%, 70%, 90%, 96% and 100%), incubated in propylene oxide twice for 10 min each, and embedded in epoxy resin (Durcupan ACM, Fluka). For polymerization, the samples were transferred to BEEM capsules (EMS; Hatfield) and the capsules filled with freshly prepared Durcupan and cured for 48 h at 60 °C. For samples subjected to high-pressure freezing fixation, root tips were rapidly frozen and freeze-substituted after the immunolabelling to minimize structural impairments during the dehydration and embedding steps. For this, root tips were dissected, immersed in 5% (w/v) sucrose in water and placed into aluminium carriers (2-mm inner diameter, indentation 200 µm; Wohlwend). The flat side of a carrier with a 300-µm indentation was used as a lid. The sandwiched samples were high-pressure-frozen using an HPM 010 (Leica Microsystems). Freeze-substitution was carried out in an EM AFS I device (Leica Microsystems). The following protocol was applied: 24-h substitution in 0.1% (w/v) tannic acid in anhydrous acetone at −85 °C, followed by 3× 20-min washes in acetone at −85 °C, 6-h substitution in 1% (w/v) osmium tetroxide plus 0.2% (w/v) uranyl acetate in acetone at −85 °C, raising of the temperature 15 °C per h to −60 °C, 6-h incubation at −60 °C, raising of the temperature 15 °C per h to −20 °C, 2-h incubation at −20 °C, raising of the temperature 15 °C per h to 4 °C, and 30-min incubation at 4 °C. Samples were washed in acetone for 3× 20 min each at 4 °C, removed from the carriers and embedded in epoxy resin (Durcupan ACM, Fluka) as described above. Ultrathin sections (70–80 nm) were cut from the blocks using an ultramicrotome UC7 (Leica Microsystems), collected onto Formvar-coated copper slot grids and stained with 1% uranyl acetate in water and 0.3% lead citrate. Sections were examined under a Tecnai 10 transmission electron microscope (Thermo Fisher Scientific) at 80 kV and imaged with a side-mounted camera Megaview G3 (EMSIS).

Post-embedding immunogold electron microscopy: samples were grown on AM plates as described above. After incubation in mock or IAA, samples were immersed in 15% (w/v) polyvinylpyrrolidone (Sigma) in growth medium, high-pressure-frozen in the HPM 010 (Leica Microsystems) and freeze-substituted in the EM AFS I (Leica Microsystems). The following protocol was applied to the samples: substitution in anhydrous acetone containing 0.2% (w/v) uranyl acetate, 2% (v/v) methanol, 0.15% (v/v) glutaraldehyde and 1% (w/v) paraformaldehyde for 32 h at −85 °C, raising of the temperature 15 °C per h to −60 °C, 6-h incubation at −60 °C, raising of the temperature 15 °C per h to −20 °C, 2-h incubation at −20 °C, and raising of the

temperature 15 °C per h to 4 °C. Samples were removed from the substitution chamber immediately, rinsed in dry ethanol for 3× 20 min each at 4 °C, and embedded in LR-White resin (Hard grade acrylic resin; London Resin Company). Then, the following procedure was applied to the samples: infiltration in 1:1 dry ethanol to LR White for 30 min at room temperature, 1:2 dry ethanol to LR White for 30 min at room temperature and pure LR White overnight at room temperature. Samples were transferred to gelatin capsules and the capsules were fully filled with fresh resin, tightly capped and polymerized for 24 h at 50 °C. Ultrathin sections (80 nm) were cut using the ultramicrotome UC7 (Leica Microsystems), collected onto Formvar-coated nickel slot grids and processed for immunogold labelling. Samples were first washed in drops of TBS containing 0.1% Triton X-100 (T-TBS) for 20 min at room temperature. Then they were incubated in 50 mM glycine in TBS to quench free aldehyde groups for 1 h at room temperature, and T-TBS containing 10% NGS plus 2% BSA and 1% FSG for 90 min at room temperature to block nonspecific binding sites. The rabbit anti-GFP antibody (Abcam) was applied at a concentration of 1 µg ml^{-1} in T-TBS containing 2% BSA overnight at 4 °C. After consecutive washes with TBS and T-TBS containing 2% BSA and 1% FSG, goat anti-rabbit immunoglobulins conjugated to 10-nm gold particles were applied (British BioCell International) at a dilution of 1:50 in TBS-T containing 2% BSA and 0.05% polyethylene glycol for 90 min at room temperature. Sections were then rinsed in TBS and air-dried. Sections were contrast-enhanced by applying 1% aqueous uranyl acetate for 20 min at room temperature and 0.3% lead citrate for 6 min at room temperature. Sections were examined under a Tecnai 10 transmission electron microscope (Thermo Fisher Scientific) at 80 kV and imaged with a side-mounted camera Megaview G3 (EMSIS).

Sampling and analysis of data: for root samples, 5–7 seedlings of each line were included per immunolabelling experiment, and three experimental runs were performed. For quantification of the immunoreaction product, sections were selected randomly per seedling and per experiment. For shoot apical meristem samples, at least two repetitions were performed, and the experimenter was blinded during acquisition and analysis. The density of the immunoparticles in the apoplast was calculated by counting the particles that were clearly visible in the apoplastic areas and dividing this by the area of the plasma membrane manually measured using ImageJ. For the post-embedded samples, for each particle, the distance to the plasma membrane was determined. If this distance was greater than 19 nm (the size of the immuno-complex), it was classified as such. Particles greater than this distance were classified as bona fide apoplastic signals.

Phosphoproteomics

For rapid auxin-induced phosphorylation analysis, *Arabidopsis* Col-0, *tmk1-1* or *abp1*-TD1 seeds were surfaced-sterilized, suspended in 0.1% agarose and stratified for 48 h. Seeds were sowed in two lines on half-strength Murashige and Skoog plates covered with sterile nylon mesh with a pore size of 100 µm. Plates were grown vertically in a growth chamber at 22 °C in long-day lighting (16-h–8-h light–dark). Five days after germination, root tips were locally treated for two minutes by applying liquid half-strength Murashige and Skoog medium (MS medium) with 100 nM IAA, or equivalent volume DMSO solvent control, directly to the root tips. After exactly two minutes, each row of root tips (around 10 mm) was cut with a surgical blade and frozen in liquid nitrogen. Plates were treated one by one to stay within a two-minute time frame. In total, 4 biological replicates per condition were collected on consecutive days, in total pooling 10–15 plates per biological replicate.

For protein extraction, frozen root tips were ground to a fine powder in liquid nitrogen using a mortar and pestle. Proteins were subsequently extracted in SDS lysis buffer (100mM Tris pH 8.0, 4% SDS and 10 mM DTT) and sonicated in a cooled CupHorn sonicator (QSonica) for

10 min at 90% amplitude with a 30-s on/30-s off cycle. The lysate was cleared by centrifugation at maximum speed (13,000*g*) in a table-top centrifuge for 30 min. Protein concentrations were determined using Bradford reagent (Bio-Rad).

For all samples, 500 µg protein was used for filter-aided sample preparation (FASP)51. For FASP, 30-kDa cut-off amicon filter units (Merck Millipore) were used. Filters were first tested by applying 1,000 µl UT buffer (8 M urea and 100 mM Tris, pH 8.5) and centrifuging for 20 min at 6,000 rpm at 20 °C. All further centrifugation steps were at this speed and temperature. The desired amount of protein sample was next mixed with UT buffer to a volume of 5,000 µl, applied to the filter and centrifuged for 20 min. Filters were washed with UT buffer and centrifuged for 20 min. Retained proteins were alkylated with 50 mM acrylamide (Sigma) in UT buffer for 30 min at 20 °C while gently shaking. The filter was centrifuged and afterwards washed three times with UT buffer for 20 min. Next, filters were washed three times with 50 mM ammonium bicarbonate buffer (ABC). After the last wash, proteins were cleaved overnight by adding trypsin (Roche) in a 1:100 trypsin: protein ratio. The filter was transferred to a new tube and peptides were eluted by 20 min centrifugation. Further elution was completed by twice adding (500 µl) 50 mM ABC buffer and centrifuging.

For peptide desalting and concentrating, C18 Stagetips were used. Pipette tips (1,000 µl) were fitted with two plugs of C18 octadecyl 47 mm Disks 2215 (Empore) material and 10 µg of LiChroprep RP-18 peptides (Merck). Tips were sequentially equilibrated with 100% methanol, 80% acetonitrile (ACN) in 0.1% formic acid and twice with 0.1% formic acid with intermittent centrifugation for 4 min at 1,500*g*. After equilibration, peptides were loaded and centrifuged for 20 min at 400*g*. Bound peptides were washed with 0.1% formic acid and eluted with 80% ACN in 0.1% formic acid by spinning for 4 min at 1,500*g*. Eluted peptides were subsequently concentrated using a vacuum concentrator for 30 min at 45 °C and resuspended in 50 µl Ti^{4+}-IMAC loading buffer (Resyn Biosciences).

Phospho-peptide enrichment was performed using Ti^{4+}-IMAC magnetic beads as per the manufacturer's instruction (Resyn Biosciences). After phospho-peptide enrichment, peptides were desalted and concentrated using C18 Stagetips. Eluted peptides were subsequently concentrated using a vacuum concentrator for 30 min at 45 °C and resuspended in 50 µl 0.1% formic acid. For liquid chromatography–tandem mass spectrometry (LC–MS/MS) analysis, a maximum of 5 µl prepared sample was injected into a 0.10 × 250 mm ReproSil-Pur 120 C18-AQ 1.9-µm beads analytical column (prepared in-house) at a constant pressure of 825 bar using a 1-h gradient from 9 to 34% ACN in water with 0.1% formic acid in 50 min by nano-LC–MS/MS (Thermo Fisher Scientific nLC 1000 coupled to a Q Exactive-HFX). MS and MS/MS AGC (Automatic Gain Control) target values were set to 3.106, 50,000, respectively, or maximum ion injection times of 50 ms (MS) and 25 ms (MS/MS) were used. HCD (Higher-energy C-trap dissociation)-fragmented (isolation width 1.2 *m*/*z*, 24% normalized collision energy) MS/MS scans of the 25 most abundant 2–5+ charged peaks in the MS scan were recorded in data-dependent mode (threshold 1.2×10^5, 15 s exclusion duration for the selected $m/z \pm 10$ ppm).

The MaxQuant quantitative proteomics software package was used to analyse LC–MS data with all MS/MS spectra. The following settings were used: FDR ≤ 0.01; the proteome of *A. thaliana* (UniProt ID UP000006548) was used as the protein database; maximum missed cleavage was set at 2; variable modifications Oxidation (M), Acetyl (protein N-term), Deamidation (NQ), pPhospho (STY); fixed modification AcrylAmide (C); match between runs was selected.

Perseus was used for filtering and further bioinformatics and statistical analysis of the MaxQuant ProteinGroups files[52]. The data were filtered on reverse and potential contaminant hits. P-site localization probability was filtered using a cut-off ≥ 0.75. Data were further filtered

on a minimum of 75% valid values in at least one condition. From the phospho-peptides passing this filtering, normality was checked using histograms. Data were normalized using median subtraction. Missing values were imputed from a normal distribution using standard settings in Perseus. FDR permutation-based *t*-tests were done in pairwise comparisons (that is, wild-type IAA versus mock or *tmk1-1* IAA versus mock, and so on). Phospho-peptides passing an FDR cut-off ≤ 0.05 were used for further analysis. Data were visualized using R and Adobe illustrator.

To quantify the overlap between phospho-sites that were significantly downregulated under mock conditions in *tmk1-1* and *abp1-TD1*, we used total filtered phospho-peptides as a reference set. The result reported in the main text can be obtained by running the following command in R: "fisher.test(rbind(c(1739, 850), c(365, 1702)))".

The mass spectrometry proteomics data, protein lists and intensity values of all samples have been deposited to the ProteomeXchange Consortium via the PRIDE[53] partner repository with the dataset identifier PXD031063.

ATPase activity

The excised roots from seven-day-old seedlings, which were pre-treated with 30 µM kynurenine for 24 h and then treated with 10 nM IAA for 60 min under dark conditions, were homogenized in homogenization buffer (50 mM MOPS-KOH (pH 7.0), 100 mM KNO_3, 2 mM sodium molybdate, 0.1 mM NaF, 2 mM EGTA, 1 mM PMSF and 20 µM leupeptin) and were centrifuged at 10,000*g* for 10 min. The supernatant was centrifuged at 45,000 rpm for 60 min. The resultant precipitate was resuspended in the homogenization buffer, and was addressed as a microsomal fraction. ATP hydrolytic activity in the microsomal fraction was measured in a vanadate-sensitive manner following a previously published method[54] with some modifications. In brief, the microsomal fraction (22.5 µl) was mixed with an equal volume of the reaction buffer (60 mM Mes-Tris (pH 6.5), 6 mM $MgSO_4$, 200 mM KNO_3, 1 mM ammonium molybdate, 10 µg ml^{-1} oligomycin, 2 mM NaN_3, 0.1% Triton X-100, 1 mM PMSF and 20 µM leupeptin) with or without 1 µl of 10 mM sodium orthovanadate. The sample solution was incubated with 5 µl of 20 mM ATP at 30 °C, and was added with 50 µl of the stop solution (2.6% (w/v) SDS, 0.5% (w/v) sodium molybdate and 0.6 N H_2SO_4) after 30 min. The inorganic phosphate released from ATP was measured.

Plasma-membrane potential

Arabidopsis seeds were surface-sterilized for 60 s with 96% (v/v) ethanol and commercial bleach (4–6% NaClO) in a 1:1 ratio and placed in Petri dishes with 15 ml of solid 1/2 MS medium (half-concentrated MS medium, 1% (w/v) sucrose, 100 mg l^{-1} myo-inositol and 1% (w/v) agar, pH 5.8). After cold stratification at 4 °C for three days in the dark, Petri dishes were transferred to light (35 ± 2 µmol m^{-2} s^{-1}; 16-h–8-h light–dark) and kept vertically in racks at 25 ± 2 °C. Petri dishes were not sealed with parafilm to prevent excessive ethylene accumulation. Four- to five-day-old seedlings were used for membrane-potential measurements. Seedlings were attached to glass slides in air together with agar growing medium taken from a Petri dish above the hypocotyl, whereas the root was free and was immersed into electrophysiological solution (basic salt medium (BSM): 0.1 mM $CaCl_2$, 0.2 mM KCl, pH 5.5 non-buffered). The root was immobilized in an experimental chamber by a silicon tube and the seedling was conditioned for 20 min before the onset of the measurements. The experimental chamber with the seedling was transferred onto the three-dimensional (3D) stage in a Faraday cage and the membrane-potential measurements were performed with the conventional glass microelectrodes inserted into the epidermal cells of mature root zone with a manually operated 3D micromanipulator, under a visual observation

with a horizontal Leitz stereomicroscope (×160 magnification) using a Leitz micromanipulator. The glass microelectrodes were pulled (a tip diameter of around 0.5 μm) from capillaries with an internal filament (GB150F, Science Products) on a vertical pipette puller (700C, David Kopf Instruments) and filled with 1 M KCl. The reference electrode was an Ag/AgCl wire in a small glass tube, also filled with 1 M KCl, contacting the BSM through a piece of porous ceramic, as previously described[55]. The microelectrode was connected to a custom-made high-input impedance (>1,015 Ω) amplifier BBA18 (OP Amplifier LMC 6081, National Instruments) through an Ag-AgCl half-cell, and recorded by data acquisition card (DAQ, LabJack U3-LV, National Instruments) and LabVIEW 7.1 program with a sampling rate of 12 ms. Once the root was impaled with the microelectrode, the membrane potential was recorded for several minutes to provide a stable level. The root was treated with auxin (100 nM IAA) that was added into the experimental chamber when the membrane potential reached a steady-state level and the membrane potential was recorded for at least 20–30 min after the start of treatment.

Auxin sensitivity of root growth

Measurements of root growth were done as described[29] with minor modifications. Four-day-old seedlings were transferred to AM+ agar plates supplemented with 3 nM or 5 nM IAA, or an equivalent amount of DMSO as a mock treatment. Plates were imaged using a vertically placed flatbed scanner (Epson Perfection V370 Photo) for 4 h with 20-min intervals with a resolution of 1,200 dpi in 24-bit colour mode as described with modifications). Time-lapse image series were registered using the plugin 'StackReg' in ImageJ. For each seedling, growth in μm for each time point was calculated with manual tracking of root tips. The average growth rate for each treatment and each genotype was calculated as the average of all scanning time points for all seedlings. To compare the auxin sensitivity of different genotypes, the growth rate on IAA was normalized to the growth rate on control treatment.

Cytoplasmic streaming

Cytoplasmic streaming was recorded using a widefield microscope (Nikon Ti2E) with a bright-field module via aPlan Apo λ 40×/0.95 air objective. Four-to-five-day-old seedlings were taken into the microscopy room 30 min in advance to allow seedlings to adapt to the environment. To further ensure equal experimental conditions, wild-type, mutant and complemented lines were placed in the same square of medium (1/2 MS containing 1% agar), with or without IAA (10 mM IAA stock in ethanol) and then moved to a coverglassed chamber for 30 min before imaging. Cytoplasmic streaming was recorded in the epidermal cells of the root elongation zone at a 1-s interval for 30 s. The maximal velocities of cytoplasm streaming were determined by tracing particles of 0.5–1.0 μm in diameter that were smoothly moving for at least 3 s by using Fiji manual tracking (three fastest particles per cell, three cells per seedling and seven seedlings per treatment).

Vasculature regeneration after wounding in inflorescence stems

The regeneration experiments were performed as described previously[36,38]. Plants with immature inflorescence stems (9–10-cm tall) were used. Stems were decapitated with a sharp razor blade, the apical floral parts (1 to 2 cm) were removed and the artificial weight, a 2.5 g lead ball connected with a plastic tube, was applied. Decapitated stems covered by the artificial weight were additionally supported by a wood stick to avoid their bending. With this method, secondary tissue architecture could be obtained six days after weight application in the basal parts of previously immature *Arabidopsis* stems (5-mm segments above the rosette).

For observation of regeneration, inflorescence stems were wounded precisely with a sharp razor blade at a distance of approximately 5 mm from the rosette in the transversal plane of the

basal sectors with vascular cambium and secondary tissues, to interrupt their longitudinal continuum. During all experimental steps, plants were still covered with the artificial weights. Axillary buds grown above the rosette leaves were not removed, thus remaining the source of endogenous auxin. After 0, 4 and 6 days after wounding, stem segments were cut with an automated vibratome (Leica VT1200 S, Leica Microsystems) and 70-µm-thick native sections were prepared. The native sections were stained with a 0.025% TBO aqueous solution and regeneration was analysed in stems with fully developed, closed cambial rings, and secondary tissues in their basal parts. The native sections were observed using a bright-field microscope (Zeiss Axioscope.A1) and pictures of vasculature were photographed with a camera (Axiocam 506) at 10× magnification.
For observation of GUS activity after wounding, the same technique of plant preparation was used as described previously for the regeneration analysis. After 0, 4 and 6 days after wounding, stem segments were incubated with X-Gluc solution at 37 °C overnight, and fixed with a 70% ethanol solution at room temperature. The samples with a positive GUS reaction were cut with an automated vibratome and 70-µm-thick native sections were prepared. The native sections were cleared in a solution containing 4% HCl and 20% methanol for 15 min at 65 °C, followed by a 15-min incubation in 7% NaOH and 70% ethanol at room temperature. In the next step, seedlings were rehydrated by successive incubations in 70%, 50%, 25% and 10% ethanol for 10 min at room temperature, followed by an incubation in a solution containing 25% glycerol and 5% ethanol for 10 min at room temperature. Finally, seedlings were mounted in 50% glycerol and observed using a bright-field microscope. Pictures of GUS activity were photographed with a camera at 10× magnification.

Auxin-induced canalization in inflorescence stems

The auxin canalization experiments were performed as before[38]. *Arabidopsis* plants with young, 10-cm-tall inflorescence stems were chosen for exogenous auxin application. Stems were wounded by a transversal incision 3–4 mm above the rosette to interrupt the vascular cambium and secondary tissues and hence also the polar, basipetal transport of endogenous auxin. We then applied 10 µM IAA (Sigma-Aldrich, 15148-2G) in a droplet of lanoline paste below the cut. This droplet was replaced every two days to ensure the constant presence of auxin. Samples were collected and the manual longitudinal stem sections were obtained using a NIKON SMZ1500 stereomicroscope. Sections were stained in 0.05% TBO and mounted in a 50% glycerol aqueous solution. Images of these sections were obtained using an Olympus BX43 microscope equipped with an Olympus SC30 Camera. The number of analysed stems was more than 10; typically 20.

Characterization of ABP1(WT) and ABP1(M2X) proteins

The behaviour of ABP1(WT) and ABP1(M2X) proteins was analysed by mass photometry56. Landing assays of single molecules in solution, data acquisition and image processing were performed with Refeyn TwoMP mass photometer and software. The instrument was calibrated by running standard proteins, such as BSA and immunoglobulin G (IgG) (from Sigma-Aldrich), diluted to a concentration of 10 nM. The resulting calibration parameters were used as a conversion between measured contrast and the mass of ABP1(WT) and ABP1(M2X) proteins. ABP1(WT) and ABP1(M2X) were measured at a concentration of 40 nM in ABP1 buffer (50 mM citrate pH 5.5, 250 mM NaCl and 0.05 mM $ZnCl_2$).
Circular dichroism (CD) spectral measurement and data analysis were done by the VBCF ProTech facility. ABP1(WT) and ABP1(M2X) were diluted in ABP1 buffer to 0.3 mg ml^{-1}. A Chirascan Plus CD Spectrophotometer by Applied Photophysics was used to generate CD spectra. The ellipticity (CD; mdeg) and the absorbance (optical density) of ABP1(WT),

ABP1(M2X) and ABP1 buffer are recorded with a spectral scan from 190 to 280 nm at 20 °C and only the significant region from 185 to 260 nm is shown. Three repeats of the spectrum were collected for each sample. To get the normalized CD spectra of ABP1(WT) and ABP1(M2X), spectral normalization was done as follows.
The three repeats of each measured CD spectrum were averaged. The averaged buffer spectrum was subtracted to calculate the correct spectrum (θ_{corr}). The 260–280-nm region is used to correct the shift in CD baseline. In general, those spectra should be closed to zero in the wavelength range between 260 and 280, so if drift exists, we subtract the average CD value from 260 to 280 nm.

$$\theta corr\,(\lambda) = \bar{\theta}sample(\lambda) - \bar{\theta}buffer(\lambda) \quad (1)$$

$$\theta dcorr(\lambda) = \theta corr(\lambda) - \bar{\theta}corr, 260nm - 280nm$$

To account for each unit that gives a CD signal, we can use equation (2) to calculate the mean residue ellipticity, θ_{mrw} (ref. [57]):

$$\theta mrw(\lambda) = \theta dcorr(\lambda) \,/\, 10dc \times (N - 1) \quad (2)$$

where d is the path length of the cuvette in cm, c is the concentration in mol l^{-1} and N is the number of amino acids of the protein. Instead of using equation (2), one can account for a total amount of protein (d·c) using the Lambert–Beer law $A = \varepsilon dc$. Therefore, for a known extinction coefficient (ε_{205}) and a measured absorbance at 205 nm (A_{205}), equation (2) can be rewritten to:

$$\theta mrw(\lambda) = \theta dcorr(\lambda) \times \varepsilon 205 \,/\, 10 \times A205 \times (N - 1) \quad (3)$$

ε_{205} depends on the number of peptide bones and the amino acid composition and can be calculated using the primary sequence[58]. To accurately determine the absorbance at 205 nm for each sample, the three repeats of each absorbance measurement were averaged and the averaged buffer absorbance was subtracted according to the equation:

$$A205 = \bar{A}sample - \bar{A}buffer$$

The resulting spectra were expressed as the molar differential extinction coefficient ($\Delta\varepsilon[M^{-1}cm^{-1}]$). $\Delta\varepsilon$ and θ_{mrw} are easily converted to each by equation (4) (ref. [57]):

$$\Delta\varepsilon(\lambda) = \theta mrw(\lambda) \,/\, 3{,}298 \quad (4)$$

2.1.5 Acknowledgments

We acknowledge K. Kubiasová for excellent technical assistance, J. Neuhold, A. Lehner and A. Sedivy for technical assistance with protein production and purification at Vienna Biocenter Core Facilities; Creoptix for performing GCI; and the Bioimaging, Electron Microscopy and Life Science Facilities at ISTA, the Plant Sciences Core Facility of CEITEC Masaryk University, the Core Facility CELLIM (MEYS CR, LM2018129 Czech-BioImaging) and J. Sprakel for their assistance. J.F. is grateful to R. Napier for many insightful suggestions and support. We thank all past and present members of the Friml group for their support and for other contributions to this effort to clarify the controversial role of ABP1 over the past seven years. The project received funding from the European Research Council (ERC) under the European Union's Horizon 2020 research and innovation program (grant agreement no. 742985 to J.F. and 833867 to D.W.); the Austrian Science Fund (FWF; P29988 to J.F.); the Netherlands Organization for Scientific Research (NWO; VICI grant 865.14.001 to D.W. and VENI grant VI.Veni.212.003 to A.K.); the Ministry of Education, Science and Technological

Development of the Republic of Serbia (contract no. 451-03-68/2022-14/200053 to B.D.Ž.); and the MEXT/JSPS KAKENHI to K.T. (20K06685) and T.K. (20H05687 and 20H05910).

2.1.6 Contributions

J.F. conceived and coordinated the experiments and wrote the paper with input from all authors. J.F., D.W. and T.K. interpreted the results. The following individuals conducted the experiments, analysed the data and contributed to their design and interpretation: A.J., P.G. and W.A.K. (TEM); A.K., D.W., L.F. and M. Roosjen (rapid phosphoproteomics); A.M. and L.R. (western blotting, cloning and analysis of kinase activity); A.T., J.F., M.G., M.H., M.N., M. Randuch and S.T. (phenotype analysis); B.D.Ž. (measurements of membrane potential); C.G. (mass photometry); H.R. (cloning, localization and phenotype analysis); E.M. and N.R. (regeneration and canalization analysis, GUS staining); I.V. (DARTS and MST); K.T. and T.K. (plasma-membrane ATPase activity); M.Z. (cytoplasmic streaming, circular dichroism analysis and GUS staining); and Z.G. (MST, western blotting, cloning and expression analysis).

2.1.7 Figures

Figure 1- Auxin binding to *Arabidopsis thaliana* ABP1 and its apoplastic localization.

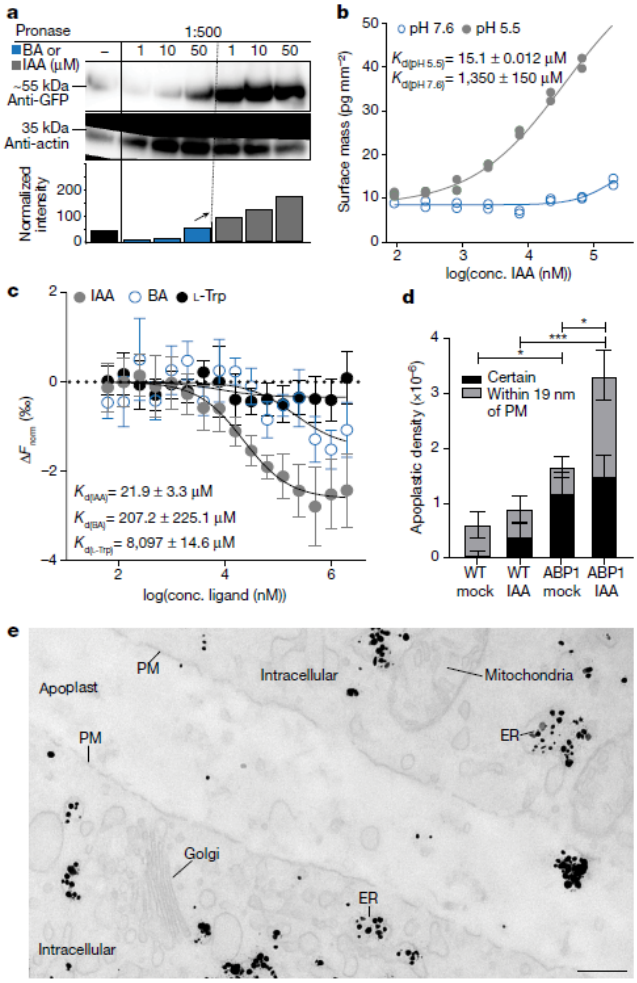

Figure 2.1-1 Auxin binding to Arabidopsis thaliana ABP1 and its apoplastic localization.

(a) DARTS assay on *35S::ABP1-GFP* plants. Protein extracts incubated with IAA (blue) or BA (grey) and with different pronase quantities. Blots and quantifications (normalized to actin) show less degradation in the presence of IAA suggesting that ABP1 binds IAA but not BA. Representative of 3 independent experiments with similar outcome. (b) GCI-assisted analysis using the Creoptix® WAVEsystem. Binding kinetics of immobilized ABP1 to different concentrations of IAA in running buffer revealed IAA binding at pH 5.5 as opposed to pH 7.6. 2 independent experiments plotted. (c) MST analysis of ABP1 binding properties at pH 5.5. The inferred Kd values show strong binding of IAA in contrast to BA and L-Trp. Plots are mean ± SD from 10 measurements; 3 or 4 independent experiments. (d) Quantification of apoplast-localized anti-GFP signal densities in shoot apical meristem of WT and *ABP1::GFP-ABP1* (Extended Data Fig. 2d) after mock or 1 μM IAA. The chart shows stacked bars; and the y-axis is therefore directly comparable with black bars only. Grey bars denote gold particles detected within 19 nm of the PM, black bars are spots localized outside this range. Plots are mean ± SEM. n: WT mock, 2 repetitions, 16 images; WT IAA, 3 repetitions, 16 images; ABP1 Mock, 4 repetitions, 16 images; ABP1 IAA, 2 repetitions, 18 images. Kruskal-Wallis analysis on total spots (χ^2=20.18, df=3, P=0.0002) followed by uncorrected unpaired two-sided Wilcoxon rank sum tests. WT mock versus IAA: P=0.5210, WT mock versus ABP1 mock: P=0.0270, WT IAA versus ABP1 IAA: P=0.0009, ABP1 mock versus IAA: P=0.0310. * P≤0.05, *** P≤0.001. (e) Example TEM image of a IAA-treated *RPS5A::ABP1-GFP* root cell labelled with anti-GFP immunogold particles (dark spots) using a high-pressure freezing/freeze-substitution. ABP1-GFP detected in the ER and as individual signals or clusters in the apoplast. PM, plasma membrane; Scale bar, 200 nm.

Figure 2- ABP1 and TMK1 in global auxin phospho-response and downstream cellular effects.

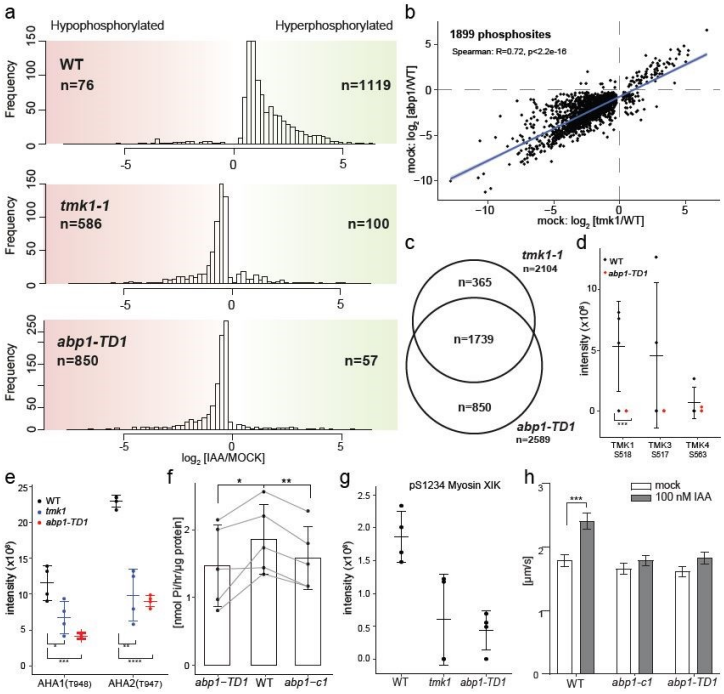

Figure 2.1-2 ABP1 and TMK1 in global auxin phospho-response and downstream cellular effects.

(a) Rapid phospho-proteomics in *Arabidopsis* roots. Distributions of $\log_2$ fold changes for significantly regulated P-sites (FDR<0.05) after IAA (100 nM; 2 min) compared to mock in WT, *tmk1-1*, and *abp1-TD1*. Auxin-triggered hyper-phosphorylation is absent in either mutant.

(b) P-sites significantly regulated (FDR<0.05) in both mock-treated *tmk1-1* and *abp1-TD1* (compared to WT) exhibit positive correlation in $\log_2$ fold change magnitudes. A least squares linear regression line is shown in blue with 95% confidence interval as grey shading. The figure shows a p-value from a two-sided Spearman's rank correlation coefficient test together with the computed coefficient.

(c) Large overlap between significantly downregulated (FDR<0.05) P-sites from mock-treated *tmk1-1* and *abp1-TD1* (compared to WT).

(d) Lower relative MS intensities of TMK1^{S518}, TMK3^{S517} and TMK4^{S563} P-sites in *abp1-TD1* mutants suggest that TMK phosphorylation is dependent on ABP1. 4 biological replicates, mean ± SD. TMK1^{S518} in WT versus *abp1-TD1*: P=0.00997. Statistics for TMK3^{S517} and TMK4^{S563} are not given due to low overall detection of these sites. *** P≤0.001. (e) Relative MS intensity for P-sites known to activate AHA PM H^+-ATPases after 100 nM IAA treatment, 4 biological replicates, mean ± SD. AHA1^{T948}: WT versus *tmk1*: P=0.0329, WT versus *abp1-TD1*: P=0.00013; AHA2^{T947}: WT versus *tmk1*: P=0.0038, WT versus *abp1-TD1*: P=0.000001. * P≤0.05, ** P≤0.01, *** P≤0.001, ****P ≤ 0.0001.

(f) ATP hydrolysis activity in WT and *abp1* mutant roots after 10 nM IAA treatment. Grey lines connect paired data from 5 independent experiments. Both *abp1* alleles show lower activity. Barplots depict mean ± SD. Repeated measures ANOVA ($F_{2,8}$=5.73, P=0.0290) followed by uncorrected two-sided paired t-tests. WT versus *abp1-TD1*: P=0.0404, WT versus *abp1-C1*: P=0.0018. * P≤0.05, ** P≤0.01

(g) Relative MS intensity for auxin-regulated Myosin XIK P-site after 100 nM IAA treatment, 4 independent biological replicates, mean ± SD. WT versus *tmk1*: P=0.0866, WT versus *abp1-TD1*: P=0.0537.

(h) Cytoplasmic streaming in WT and *abp1* root epidermal cells after 100 nM IAA treatment. IAA increases the velocity of fast-moving particles in WT but not in *abp1* alleles. Error bars represent mean ± SD (n=63 particles from 21 cells in 7 seedlings for each condition, except WT IAA where n=60 particles). Two-way ANOVA (interaction effect: $F_{2,369}$=3.75, P=0.0244) with Šidák's multiple comparison tests as indicated in the figure. **** P ≤ 0.0001

Figure 3- ABP1 and TMKs in vasculature regeneration after wounding.

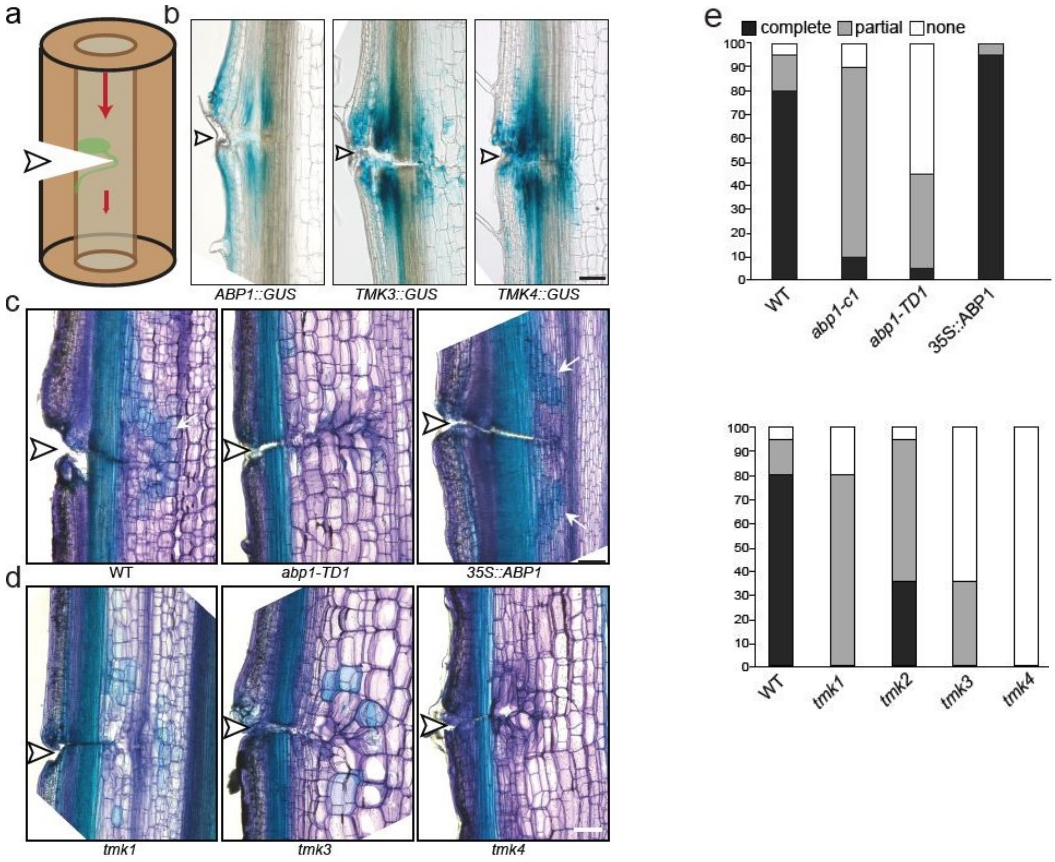

Figure 2.1-3 ABP1 and TMKs in vasculature regeneration after wounding.

(a) Schematics of vasculature regeneration in wounded *Arabidopsis* stems. The incision site is marked by an arrowhead. Red arrows indicate auxin flow. Green depicts auxin accumulation above the wound and regenerated vasculature circumventing it.

(b) GUS staining revealed specific upregulation of *ABP1::GUS*, *TMK3::GUS* and *TMK4::GUS* expression around the wound 2 days after wounding (daw). Representative micrographs from 3 experiments (n=8 for each). Scale bar, 100 µm.

(c) Vasculature regeneration 6 daw. All WT stems regenerated vascular tissue around the wound which was almost completed, as visualized by toluidine blue staining (TBO). In the *abp1-TD1* mutant, this regeneration did not occur, and in *35S::ABP1* more massive vasculature developed (indicated by white arrows). Scale bar, 100 µm.

(d) *tmk* mutants show defective vasculature regeneration. *tmk1* regenerates only partially with fragmented vasculature; *tmk3* shows stronger defects and in *tmk4* the vasculature regeneration is blocked. Scale bar, 100 µm.

(e) Quantification of vasculature regeneration in wounded *Arabidopsis* stems of WT, *abp1* and *tmk* mutants 6 daw. Total number of samples for each observation n=40.

Figure 4- ABP1 and TMKs in auxin channel formation.

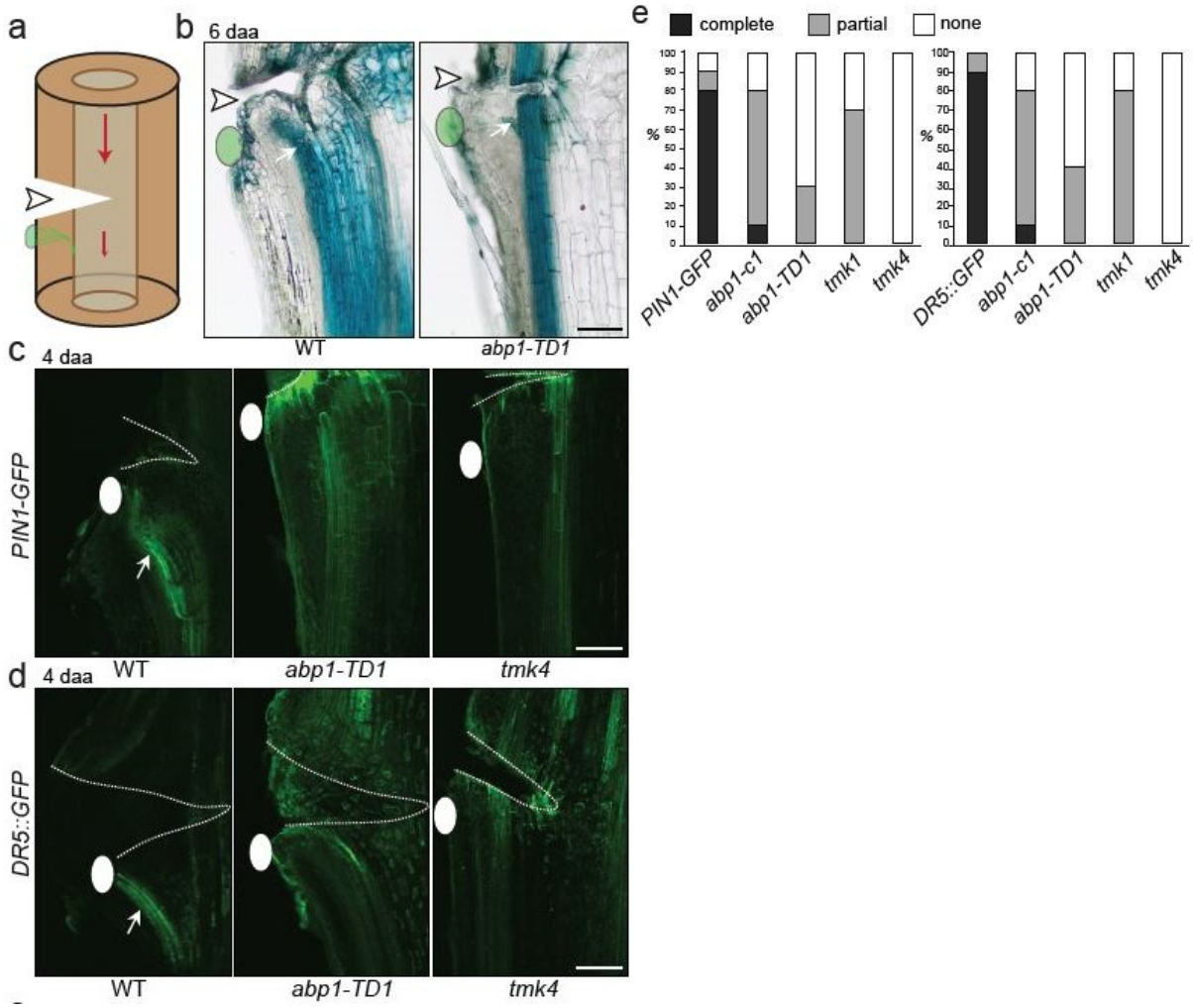

Figure 2.1-4 ABP1 and TMKs in auxin channel formation.

(a) Schematics of canalization and vasculature formation from local auxin application in wounded *Arabidopsis thaliana* stems. The incision site is marked by a white arrowhead. Red arrows indicate auxin flow. Green depicts local auxin application and *de novo* formed vasculature.

(b) Exogenous IAA application (white oval) on *PIN1::PIN1-GFP* stems triggered the formation of a PIN1-expressing channel (indicated by white arrow) from this source in WT but not in *abp1-TD1* or *tmk4* mutants. 4 daa. Scale bar, 100 µm.

(c) Exogenous IAA application (white oval) on *DR5rev::GFP* stems triggered the formation of a DR5-visualized high-auxin-response channel (indicated by white arrow) from the source in WT but not in *abp1-TD1* or *tmk4* mutants. 4 daa. Scale bar, 100 µm.

(d) Quantification of *de novo* vasculature formation from local auxin source in *PIN1::PIN1-GFP* (b) and *DR5rev::GFP* (c) lines. 4 daa. Total number of samples for each observation n=40.

Figure 5- Importance of auxin binding to ABP1 for its role in canalization.

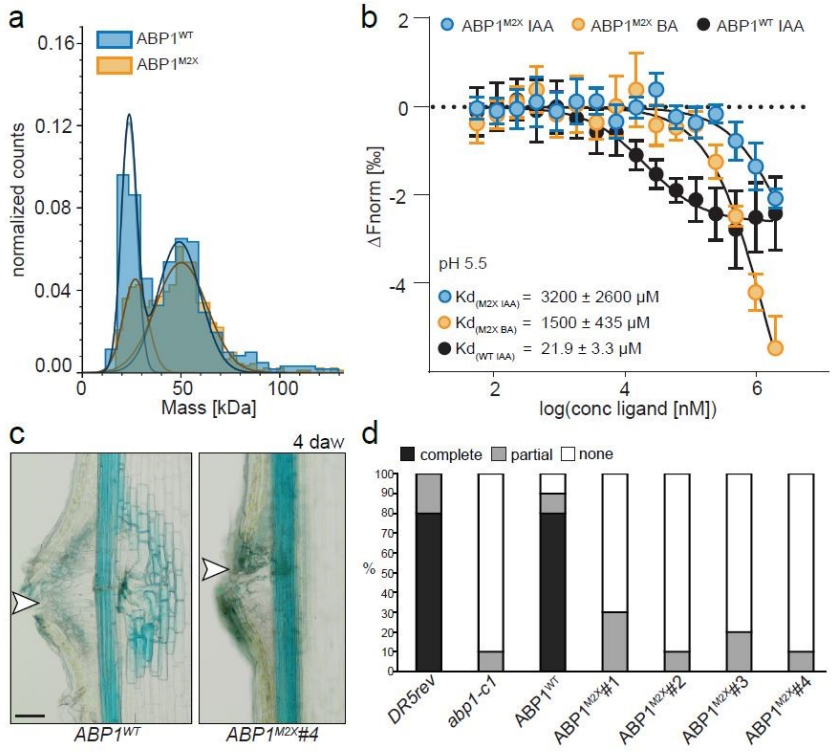

Figure 2.1-5 Importance of auxin binding to ABP1 for its role in canalization.

(a) Mass photometry analysis of ABP1^{WT} and ABP1^{M2X} proteins. Histograms of measured landing events and the respective fitted Gaussians show similar peaks for ABP1^{WT} (blue profile) and ABP1^{M2X} (orange profile) proteins, indicating that both are mainly found as homodimers (around 50 kDa), while approximately 30% exist in solution as monomers (around 25 kDa). 2 technical replicates: ABP1^{WT} peak at 24 kDa, σ 3.9, 124 counts, 35%; peak at 49 kDa, σ 10.8, 179 counts, 51%; ABP1^{M2X} peak at 27 kDa, σ 6.1, 186 counts, 30%; peak at 50 kDa, σ 13.0, 469 counts, 76%.

(b) MST analysis of ABP1 binding properties at pH 5.5. The inferred Kd values show strong binding of IAA to ABP1^{WT} compared to no binding to ABP1^{M2X}. Note that the data on IAA binding to ABP1^{WT} are duplicated here from Fig. 1c for comparison purposes. Plots are mean ± SD from 10 measurements; 2 (ABP1^{M2X} IAA, ABP1^{M2X} BA) or 4 (ABP1 IAA) independent experiments.

(c) Examples of vasculature regeneration 6 days after wounding as visualized by TBO staining. *abp1-c1* mutant transformed with *ABP1::GFP-ABP1^{WT}*, but not with *ABP1::GFP-ABP1^{M2X}*, regenerated vascular tissue around the wound. Scale bar, 100 µm.

(d) Quantification of vasculature regeneration from (c) shows inability of *ABP1::GFP-ABP1^{M2X}* to rescue *abp1-c1* regeneration in four characterized lines. Total number of samples for each observation n=40.

Figure S1- Analysis of auxin binding to Arabidopsis thaliana TMK1 and ABP1.

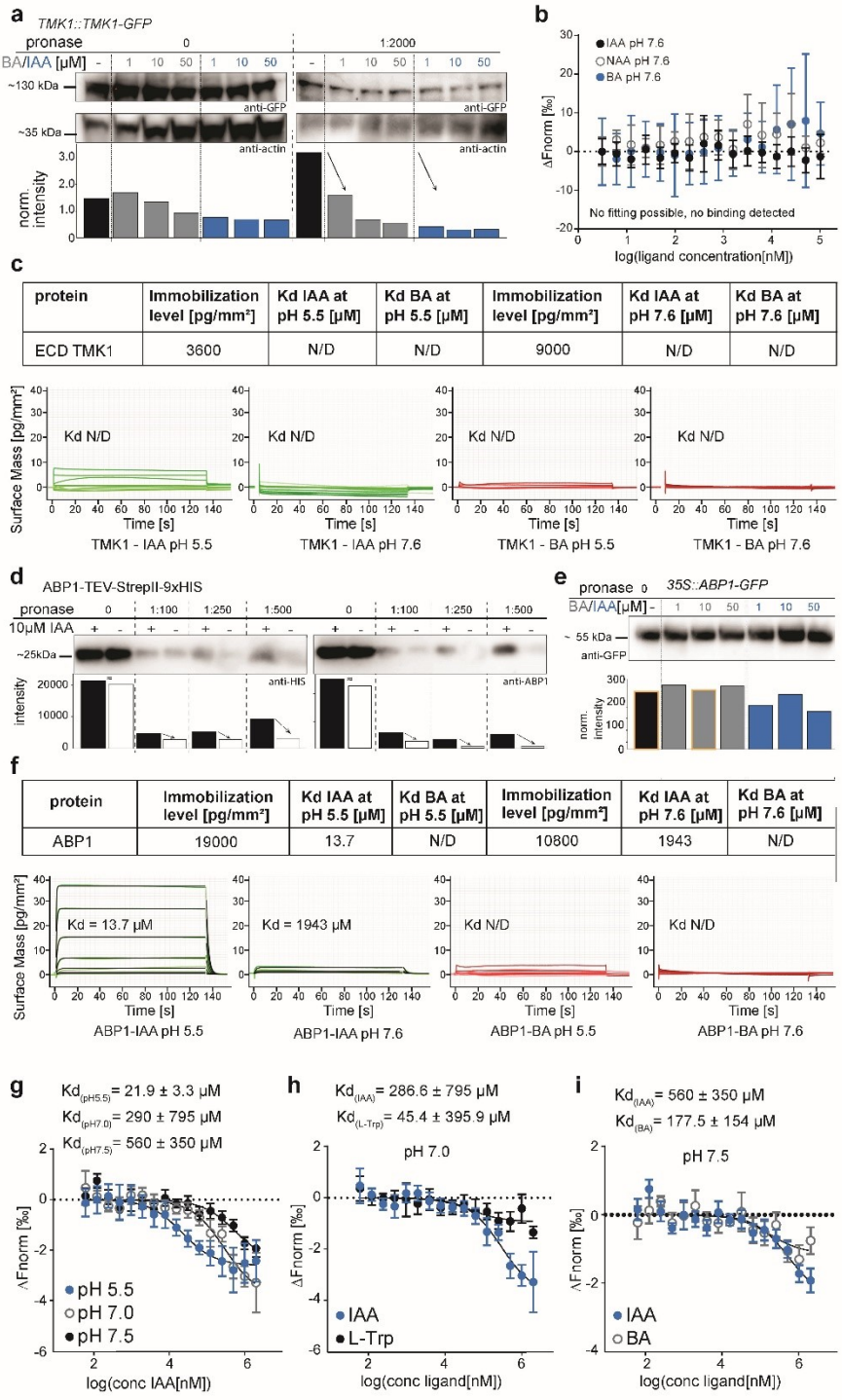

Figure 2.1-6 Analysis of auxin binding to Arabidopsis thaliana TMK1 and ABP1.

(a) DARTS assay on *TMK1::TMK1-GFP* plants. Protein extracts were incubated with IAA (in blue) or benzoic acid (in grey). Afterwards, different pronase quantities were added. Blots and quantifications (normalized to actin levels) show comparable pronase-induced degradation in the presence of both IAA and benzoic acid, suggesting no specific IAA binding to TMK1. Representative of 3 independent experiments with similar outcome. (b) MST analysis of auxin binding to TMK1. Normalized binding curves of IAA, NAA and benzoic acid in the presence of 150 nM TMK1 heterologously expressed and purified extracellular domain (ECD). Plots are mean ± SD from 10 measurements (3 or 4 independent experiments) but no curve fitting to determine binding kinetics was possible. (c) GCI-assisted analysis of binding properties of TMK1 ECD to IAA or benzoic acid as a control ligand, using the Creoptix® WAVEsystem. Heterologously expressed and purified TMK1 ECD was immobilized to the surface at the indicated levels, following which the response to different concentrations of IAA or benzoic acid in running buffer at different pH (resp. 5.5 and 7.6) was monitored for analysis of binding kinetics. No binding of IAA to TMK1 ECD was detected. (d) DARTS assay on heterologously expressed ABP1. Purified protein was mixed with different quantities of pronase enzyme mixture. Blots and quantifications show that pronase-induced proteolysis of tagged ABP1 occurred less in the presence of 10 µM IAA, which was consistent for multiple pronase dilutions, indicating IAA association with ABP1. This was verified both by the anti-HIS-HRP antibody to ensure specificity of the visualized band. The intensity profiles are plotted in the graph below the blots. Representative of 3 independent experiments with similar outcome shown. (e) Control no-pronase samples for DARTS results represented in Fig. 1a. Protein extracts from *35S::ABP1-GFP* expressing plants were incubated with benzoic acid (in grey) or IAA (in blue). Blot intensities were quantified and normalized to the average actin intensity for the no-pronase samples. In these no-pronase control samples, we verified that the presence of the respective potential ligand at their concentration did not affect target protein stability as such. Representative of 3 independent experiments with similar outcome. (f) Overview table and graphs of all GCI-based binding analyses for ABP1. The potential ligands IAA and benzoic acid were evaluated in serial dilution ranging from 91.5 nM to 200 µM. IAA binding kinetics was detectable, giving a Kd estimate of 13.7 µM at pH 5.5 and 1943 µM at pH 7.6. (g) MST analysis of IAA binding to ABP1 at varying pH. Normalized binding curve of IAA in presence of 75 nM ABP1 at pH 5.5 (blue), 100 nM ABP1 at pH 7.0 (grey) or 100 nM ABP1 pH 7.5 (black). The IAA concentration varied from 61 nM to 2 mM. Plots are mean ± SD from 10 measurements; 2 (pH 7.5) or 4 (pH 5.5, pH 7.0) independent experiments. The estimated Kd values confirm efficient IAA binding at the apoplastic pH of 5.5, whereas the estimated Kd values with large SD indicate no binding at the pH 7.0 and pH 7.5. (h) MST analysis of ligand binding to ABP1 at pH 7.0. Normalized binding curve of IAA (blue; identical to grey in S1g) and L-Trp (black) to 100 nM ABP1. The ligand concentration varied from 61 nM to 2 mM. Plots are mean ± SD from 10 measurements; 4 independent experiments. The estimated Kd values with large SD indicate no binding of these ligands at pH 7.0. (i) MST analysis of ligand binding to ABP1 at pH 7.5. Normalized binding curve of IAA (blue, same as black in Extended Data Fig. 1g) and control ligand benzoic acid (grey) to 75 nM ABP1. The ligand concentration varied from 61 nM to 2 mM. Plots are mean ± SD from 10 measurements; 2 independent experiments. The estimated Kd values and SDs are much higher than those obtained for pH 5.5 and indicate no binding of these ligands at pH 7.5.

Figure S2- TEM analysis of apoplastic ABP1 localization.

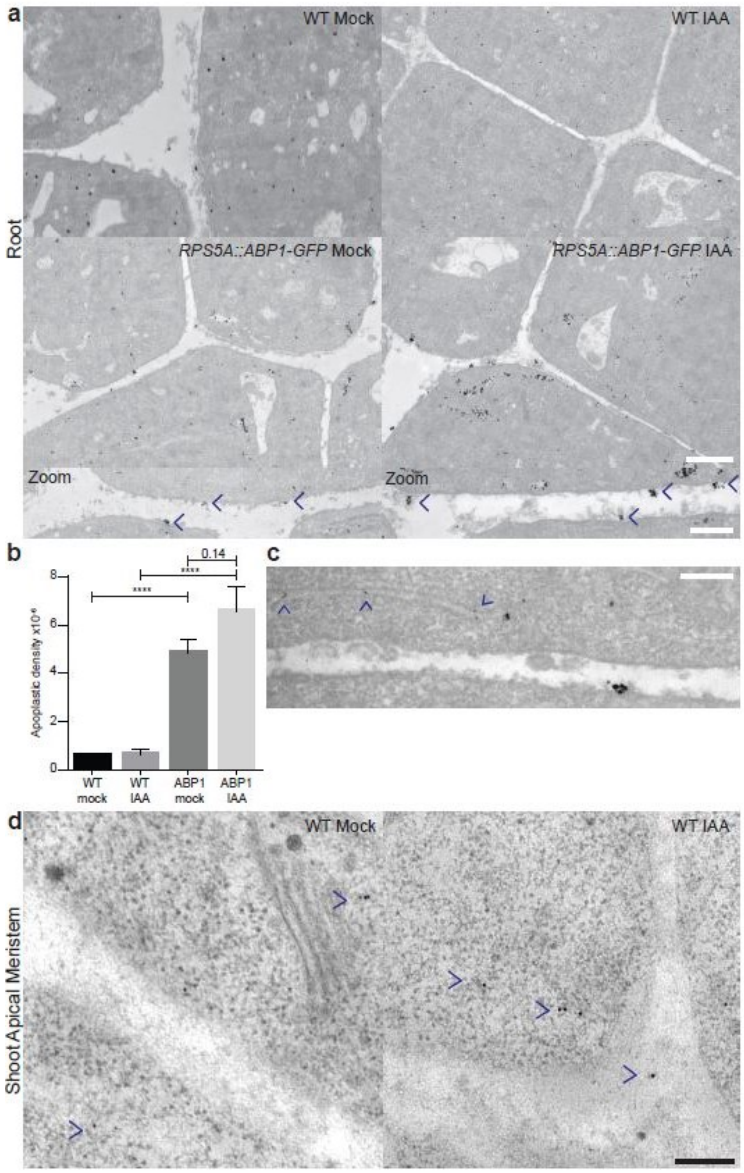

Figure 2.1-7 TEM analysis of apoplastic ABP1 localization.

(a) Example TEM images of *RPS5A::ABP1-GFP* root cells after mock and IAA (1 µM) incubation. Lower 'Zoom' panels are higher magnification images of apoplastic areas from *RPS5A::ABP1-GFP* (IAA) cells showing apoplastic anti-GFP signal. Arrows note gold particles. Scale bars; upper, 1 µm; lower, 500 nm. (b) Quantification of the densities of apoplastic localized anti-GFP gold particles in root cells of WT and RPS5A::ABP1-GFP plants subjected to either mock or 1 µM IAA incubation, as detected by TEM. Plots are mean ± SEM. n: 3 experimental repeats. WT Mock, 37 images; WT IAA, 43 images; ABP1 mock, 45 images; ABP1 IAA, 47 images. Kruskal–Wallis analysis ($\chi^2 = 99.59$, df = 3, P = 1.90E-21) followed by uncorrected unpaired two-sided Wilcoxon rank-sum tests with continuity correction. WT mock versus WT IAA: P = 0.3659, WT mock versus ABP1 mock: P = 1.16E-11, WT IAA versus ABP1 IAA: P = 7.10E-13, ABP1 mock versus ABP1 IAA: P = 0.3118. ****P ≤ 0.0001. (c) Example TEM image of an *RPS5A::ABP1-GFP* root cell showing anti-GFP gold labelling of the ER (arrows). Scale bar, 200 nm. (d) Example TEM images of WT and *ABP1::GFP-ABP1* shoot apical meristem cells labelled with anti-GFP immunogold particles (arrows). Mock or 1 µM IAA incubation. Scale bar, 200 nm.

Figure S3- Global, ultrafast auxin phospho-response and rapid cellular effects.

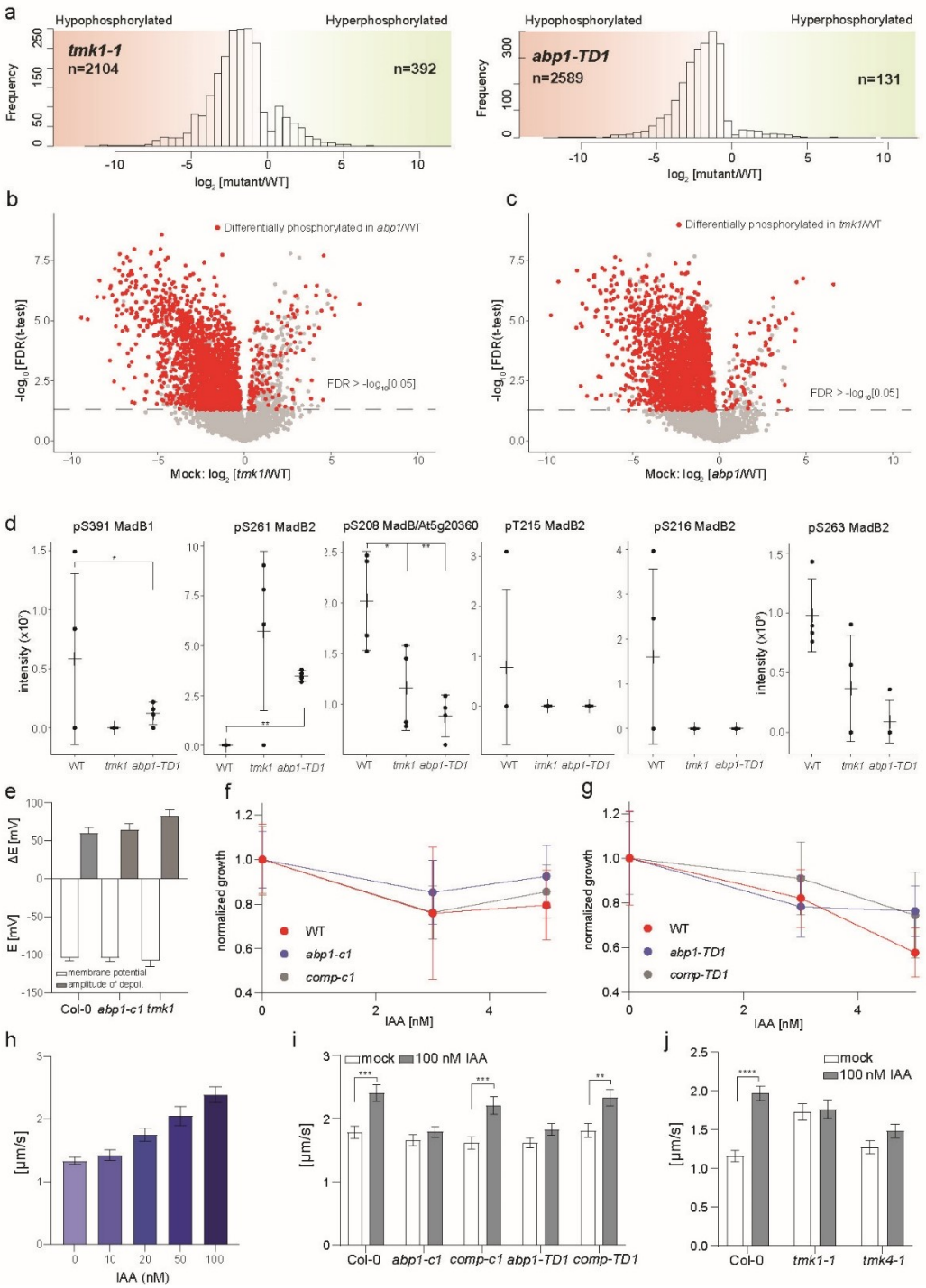

Figure 2.1-8 Global, ultrafast auxin phospho-response and rapid cellular effects.

(a) Ultrafast phosphoproteomics in mock-treated (2 min) *Arabidopsis* roots. Distributions of $\log_2$ fold changes for P-peptides with significantly differential phosphorylation (FDR < 0.05) in *tmk1-1* and *abp1-TD1* as compared to WT. Both mutants exhibit global hypo-phosphorylation. (b) Mock treatment (2 min) of *Arabidopsis* roots. The volcano plot depicts $\log_2$ fold changes (x-axis; *tmk1-1* versus WT) and statistical significance (y axis). Highlighted in red is a subset of significantly regulated P-peptides (FDR < 0.05) which are also significantly regulated in *abp1-TD1*/WT. This shows global hypo-phosphorylation in *tmk1-1* and extensive functional overlap between the two mutants. (c) Mock treatment (2 min) of *Arabidopsis* roots. The volcano plot depicts $\log_2$ fold changes (x-axis; *abp1-TD1* versus WT) and statistical significance (y axis). Highlighted in red is a subset of significantly regulated P-peptides (FDR < 0.05) which are also significantly regulated in *tmk1-1*/WT. This shows global hypo-phosphorylation in *abp1-TD1* and extensive functional overlap between the two mutants. (d) Relative MS intensity for P-peptides pertaining to various *Arabidopsis* MadB paralogs (MadB1, MadB/At5g20360, MadB2/PHOX2). Auxin (IAA, 100 nM, 2 min) treatment, 4 independent biological replicates, mean ± SD. Asterisks indicate FDR-controlled p-values collated from global phosphoproteomic comparisons as described in Materials and Methods. MadB1^{S391} (WT versus *tmk1-1*: no statistics due to low detection, WT versus *abp1-TD1*: P = 0.0354), MadB2^{S261} (WT versus *tmk1-1*: P = 0.1562, WT versus *abp1-TD1*: P = 1.17E-06), MadB^{S208} (WT versus *tmk1-1*: P = 0.0393, WT versus *abp1-TD1*: P = 0.0035), MadB2^{T215} (no statistics due to low detection), MadB2^{S216} (no statistics due to low detection), MadB2^{S263} (WT versus *tmk1-1*: P = 0.0926, WT versus *abp1-TD1*: P = 0.0056). * P ≤ 0.05, ** P ≤ 0.01, ****P ≤ 0.0001. (e) Steady-state membrane potentials (MP) and IAA-induced depolarization (in mV) measured in the mature root zone of WT, *abp1-c1* and *tmk1-1* mutants after 100 nM IAA treatment. Values are means ± SEM (Depolarization amplitudes: WT, n = 9; *abp1-c1*, n = 10; *tmk1-1*, n = 3; Membrane potentials: WT, n = 26; *abp1-c1*, n = 35; *tmk1-1*, n = 11). (f) Auxin sensitivity of *abp1-c1* root growth. Data on the graph represent the normalized growth rate of *abp1-c1* mutant in comparison to *comp-c1* line and WT, mean ± SD (Col-0 DMSO, n = 54; Col-0 3 nM IAA, n = 45; Col-0 5 nM IAA, n = 54; *abp1-c1* DMSO, n = 81; *abp1-c1* 3 nM IAA, n = 90; *abp1-c1* 5 nM IAA, n = 108; *comp-c1* DMSO, n = 90; *comp-c1* 3 nM IAA, n = 81; *comp-c1* 5 nM IAA, n = 81). No statistically significant difference in sensitivity of growth rate to auxin was detected with two-way ANOVA. (g) Auxin sensitivity of *abp1-TD1* root growth. Data on the graph represent the normalized growth rate of *abp1-TD1* mutant in comparison to *comp-TD1* line and Col-4, mean ± SD (Col-4 DMSO, n = 81; Col-4 3nM IAA, n = 81; Col-4 5 nM IAA, n = 90; *abp1-TD1* DMSO, n = 90; *abp1-TD1* 3 nM IAA, n = 72; *abp1-TD1* 5 nM IAA, n = 99; *comp-TD1* DMSO, n = 81; *comp-TD1* 3 nM IAA, n = 72; *comp-TD1* 5 nM IAA, n = 90). No statistically significant difference in sensitivity of growth rate to auxin was detected with two-way ANOVA. (h) Cytoplasmic streaming velocity increases with IAA concentration. WT seedlings were treated with 0, 10, 20, 50 and 100 nM IAA for 30 min. Fast-moving particles in epidermal cells of the root elongation zone were recorded. Error bars represent mean ± SD (n = 72 particles from 24 cells in 8 seedlings for each condition). One-way ANOVA ($F_{4,354} = 16.32$, P = 2.80E-12) with Dunnett's multiple comparison tests indicated in the figure. * P ≤ 0.05, **** P ≤ 0.0001. (i) Auxin-triggered acceleration of cytoplasmic streaming is not observed in *abp1* mutant alleles but is restored in the complemented *abp1* lines. Error bars represent mean ± SD (n = 63 particles from 21 cells in 7 seedlings for each condition). Two-way ANOVA (interaction effect: $F_{4,608} = 2.29$, P = 0.0585; genotype effect: $F_{4,612} = 5.74$, P = 0.0002; treatment effect: $F_{1,612} = 37.26$, P = 1.84E-09) with Šidák's multiple comparison tests indicated in the figure. ** P ≤ 0.01, *** P ≤ 0.001. (j) Auxin-triggered acceleration of cytoplasmic streaming is not observed in *tmk1* and *tmk4* mutants. Unlike *tmk4*, *tmk1* roots have already accelerated cytoplasmic streaming but both mutants are largely auxin-insensitive. Error bars represent mean ± SD (n = 54 particles from 18 cells in 6 seedlings for each condition). Two-way ANOVA (interaction effect: $F_{2,318} = 9.16$, P = 0.0001) with Šidák's multiple comparison tests indicated in the figure. **** P ≤ 0.0001.

Figure S4- ABP1 and TMKs in vasculature formation and regeneration.

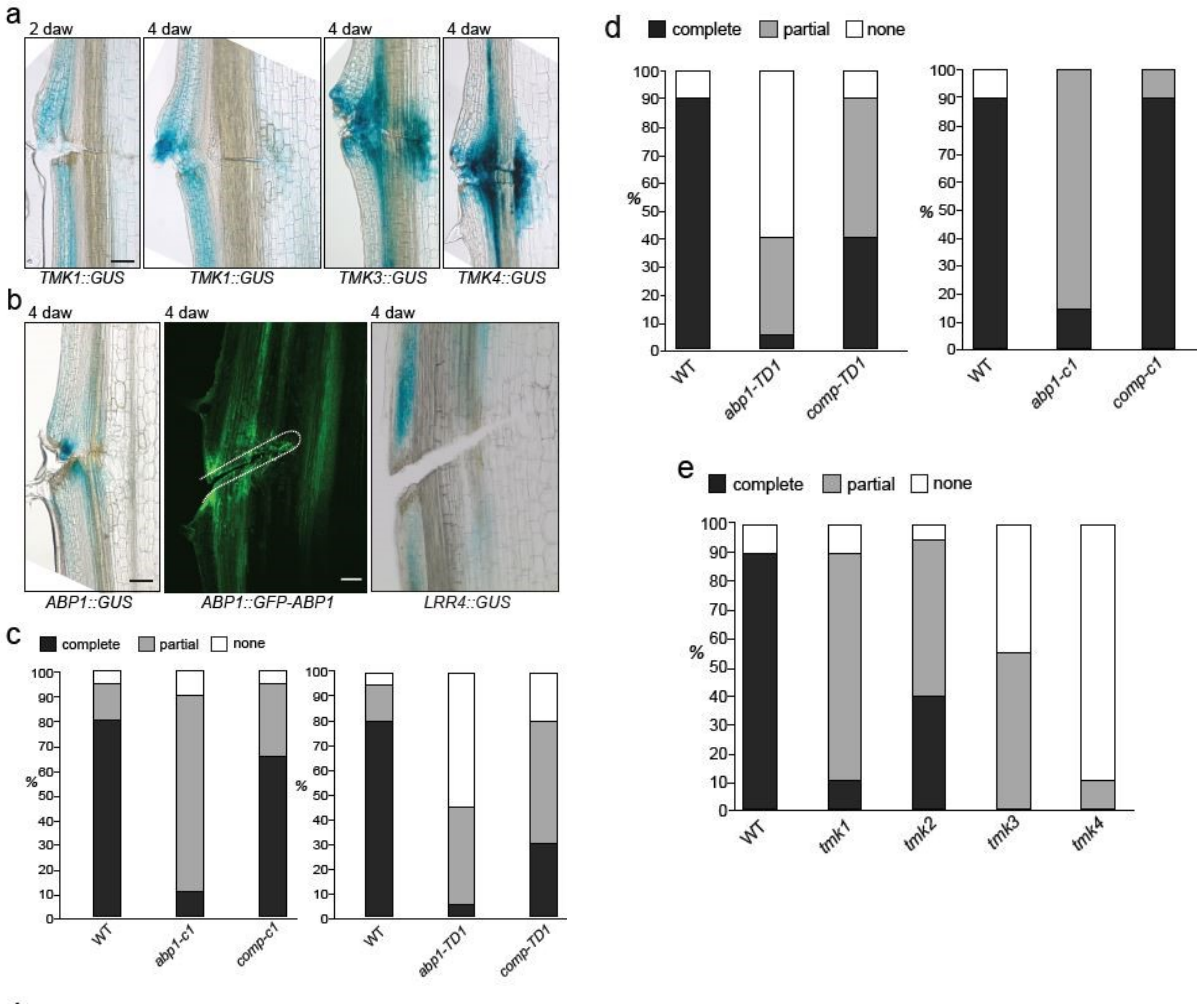

Figure 2.1-9 ABP1 and TMKs in vasculature formation and regeneration.

(a)GUS staining revealed specific upregulation of *TMK1::GUS*, *TMK3::GUS* and *TMK4::GUS* expression around the wound 2 or 4 days after wounding (daw). Representative micrographs from 2 experiments (n = 8 for each). Scale bar, 100 µm. (b) GUS staining revealed specific upregulation of *ABP1::GUS* but not *LRR4::GUS* expression around the wound. *ABP1::GFP-ABP1* confirmed the GUS staining. Representative micrographs from 2 experiments (n = 8 for each). Scale bar, 100 µm. (c) Quantification of vasculature regeneration in wounded *Arabidopsis* stems in *abp1-c1* and *abp1-TD1* mutants as well as corresponding complemented lines (*comp-c1* and *comp-TD1*) confirms that the vasculature regeneration defects are due to disruption of the *ABP1* locus. Total number of samples for each observation, n = 20. (d) Exogenous IAA application (green oval shape) on stems triggered the formation of a channel (visualized by toluidine blue (TBO); indicated by white arrow) from this local source to the existing vascular tissue in WT but not *abp1-TD1* mutant 6 days after application (daa). Scale bar, 100 µm. (e) Quantification of *de novo* vasculature formation from local auxin source (as visualized by TBO) 4 days after application (4 daa) in *abp1-c1* and *abp1-TD1* mutants as well as corresponding complemented lines (*comp-c1* and *comp-TD1*) confirms that the vasculature regeneration defects are due to the *ABP1* locus disruption. Total number of samples for each observation, n = 20. (f) Quantification of *de novo* vasculature formation from local auxin source (as visualized by TBO) in *tmk* mutants. *tmk4* shows stronger defects followed by *tmk3* and *tmk1* whereas *tmk2* has almost normal vasculature formation. Total number of samples for each observation n = 20.

Figure S5- ABP1 and ABP1(M2X) protein characterization, IAA binding analysis and role in regeneration and auxin canalization.

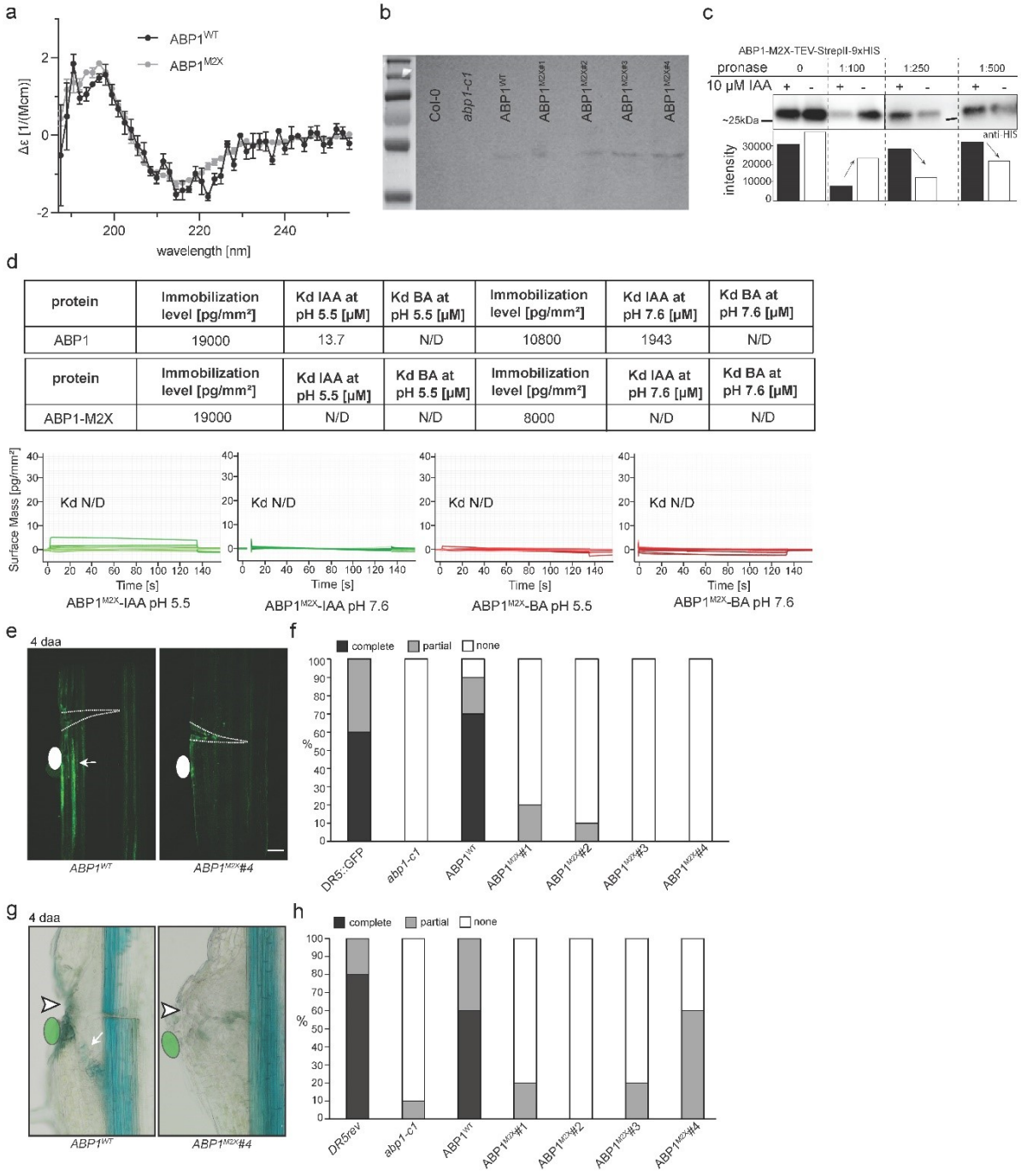

protein	Immobilization level [pg/mm²]	Kd IAA at pH 5.5 [µM]	Kd BA at pH 5.5 [µM]	Immobilization level [pg/mm²]	Kd IAA at pH 7.6 [µM]	Kd BA at pH 7.6 [µM]
ABP1	19000	13.7	N/D	10800	1943	N/D

protein	Immobilization level [pg/mm²]	Kd IAA at pH 5.5 [µM]	Kd BA at pH 5.5 [µM]	Immobilization level [pg/mm²]	Kd IAA at pH 7.6 [µM]	Kd BA at pH 7.6 [µM]
ABP1-M2X	19000	N/D	N/D	8000	N/D	N/D

Figure 2.1-10 ABP1 and ABP1(M2X) protein characterization, IAA binding analysis and role in regeneration and auxin canalization.

(a) Nearly identical Circular Dichroism (CD) spectra of ABP1(WT) and ABP1(M2X) proteins. This and temperatures of transition midpoints derived from Prometheus thermal stability measurements (ABP1(WT): 58.3 °C, ABP1(M2X): 61.4 °C) suggest similar folding of both protein variants. Error bars represent the mean ± SD; n = 3. (b) Western blot detection of ABP1(WT) and ABP1(M2X) proteins in different transgenic lines showing similar size and expression levels. The associated molecular-weight marker is from the same gel and blot. (c) DARTS assay on heterologously expressed and purified ABP1(M2X). Purified protein was mixed with different quantities of pronase enzyme mixture and proteolysis was stopped after 30 min. The resulting degraded protein samples were run on SDS–PAGE and blotted for antibody-aided visualization. Pronase-induced proteolysis of tagged ABP1(M2X) was very variable in the presence of 10 µM IAA not supporting any binding of IAA to ABP1(M2X). The intensity profiles are plotted in the graph below the blots. Representative of 3 independent experiments with similar outcome shown. (d) Overview table and graphs of all ABP1(M2X) GCI-binding analysis. The potential ligands IAA and benzoic acid were evaluated in serial dilution ranging from 91.5 nM to 200 µM. Albeit ABP1 and ABP1(M2X) could be immobilized at the surface to the same level (compared to Extended Data Fig. 1f), only for ABP1(WT), IAA binding kinetics could be observed while for the analyses using ABP1(M2X) no Kd could be estimated. (e) Exogenous IAA application (white oval shape) on *DR5rev::GFP* stems triggered the formation of a DR5-visualized auxin channels (indicated by white arrow) from this local source 4 days after application (daa) in *abp1-c1* transformed with *ABP1::GFP- ABP1*^{WT} but not in any of the *ABP1::GFP-ABP1*^{M2X} lines. Scale bar, 100 µm. (f) Quantification of de novo vasculature formation from local auxin source in *DR5rev::GFP* lines as in (e). Total number of samples for each observation n = 40. (g) Exogenous IAA application (green oval shape) on stems triggered the formation of a channel (visualized by TBO; indicated by white arrow) from this local source 6 daa in *abp1-c1* transformed with *ABP1::GFP- ABP1*^{WT} but not in any of the *ABP1::GFP- ABP1*^{M2X} lines. Scale bar, 100 µm. (h) Quantification of *de novo* vasculature formation from (g). Total number of samples for each observation n = 40.

2.1.8 References

1. Friml, J. Fourteen Stations of Auxin. *Cold Spring Harb. Perspect. Biol.* a039859 (2021) doi:10.1101/cshperspect.a039859.
2. Lavy, M. & Estelle, M. Mechanisms of auxin signaling. *Development* **143**, 3226–3229 (2016).
3. Morffy, N. & Strader, L. C. Structural Aspects of Auxin Signaling. *Cold Spring Harb. Perspect. Biol.* a039883 (2021) doi:10.1101/cshperspect.a039883.
4. Napier, R. The Story of Auxin-Binding Protein 1 (ABP1). *Cold Spring Harb. Perspect. Biol.* a039909 (2021) doi:10.1101/cshperspect.a039909.
5. Fendrych, M. *et al.* Rapid and reversible root growth inhibition by TIR1 auxin signalling. *Nat. Plants* **4**, 453–459 (2018).
6. Dindas, J. *et al.* AUX1-mediated root hair auxin influx governs SCFTIR1/AFB-type Ca2+ signaling. *Nat. Commun.* **9**, (2018).
7. Gallei, M., Luschnig, C. & Friml, J. Auxin signalling in growth: Schrödinger's cat out of the bag. *Curr. Opin. Plant Biol.* **53**, 43–49 (2020).
8. Li, L., Gallei, M. & Friml, J. Bending to auxin: fast acid growth for tropisms. *Trends Plant Sci.* (2021) doi:10.1016/J.TPLANTS.2021.11.006.
9. Kuhn, A. *et al.* Direct ETTIN-auxin interaction controls chromatin states in gynoecium development. *Elife* **9**, (2020).
10. Cao, M. *et al.* TMK1-mediated auxin signalling regulates differential growth of the apical hook. *Nature* **568**, 240–243 (2019).
11. Dubey, S. M., Serre, N. B. C., Oulehlová, D., Vittal, P. & Fendrych, M. No Time for Transcription-Rapid Auxin Responses in Plants. *Cold Spring Harb. Perspect. Biol.* (2021) doi:10.1101/cshperspect.a039891.
12. Adamowski, M. & Friml, J. PIN-dependent auxin transport: Action, regulation, and evolution. *Plant Cell* **27**, 20–32 (2015).
13. Narasimhan, M. *et al.* Systematic analysis of specific and nonspecific auxin effects on endocytosis and trafficking. *Plant Physiol.* (2021) doi:10.1093/plphys/kiab134.
14. Robert, S. *et al.* ABP1 Mediates Auxin Inhibition of Clathrin-Dependent Endocytosis in Arabidopsis. *Cell* **143**, 111–121 (2010).
15. Sachs, T. The induction of transport channels by auxin. *Planta* **127**, 201–206 (1975).
16. Han, H. *et al.* Rapid auxin-mediated phosphorylation of Myosin regulates trafficking and polarity in Arabidopsis. *bioRxiv* 439603 (2021) doi:10.1101/2021.04.13.439603.
17. Li, L. *et al.* Cell surface and intracellular auxin signalling for H + fluxes in root growth. *Nature* **599**, 273–277 (2021).
18. Lin, W. *et al. TMK-based cell surface auxin signaling activates cell wall acidification in Arabidopsis*. http://10.0.82.211/rs.3.rs-203621/v1 (2021) doi:10.21203/rs.3.rs-203621/v1.
19. McLaughlin, H. M., Ang, A. C. H. & Østergaard, L. Noncanonical Auxin Signaling. *Cold Spring Harb. Perspect. Biol.* **13**, (2021).
20. Hertel, R., Thomson, K. S. & Russo, V. E. In-vitro auxin binding to particulate cell fractions from corn coleoptiles. *Planta* **107**, 325–340 (1972).
21. Xu, T. *et al.* Cell Surface ABP1-TMK Auxin-Sensing Complex Activates ROP GTPase Signaling. *Science (80-.).* **343**, 1025–1028 (2014).
22. Gao, Y. *et al.* Auxin binding protein 1 (ABP1) is not required for either auxin signaling

or Arabidopsis development. *Proc. Natl. Acad. Sci.* **112**, 2275–2280 (2015).

23. Grones, P. *et al.* Auxin-binding pocket of ABP1 is crucial for its gain-of-function cellular and developmental roles. *J. Exp. Bot.* **66**, 5055–5065 (2015).
24. Michalko, J., Dravecká, M., Bollenbach, T. & Friml, J. Embryo-lethal phenotypes in early abp1 mutants are due to disruption of the neighboring BSM gene. *F1000Research* **4**, 1104 (2015).
25. Smakowska-Luzan, E. *et al.* An extracellular network of Arabidopsis leucine-rich repeat receptor kinases. *Nature* **553**, 342–346 (2018).
26. Woo, E. J. *et al.* Crystal structure of auxin-binding protein 1 in complex with auxin. *EMBO J.* **21**, 2877–2885 (2002).
27. Tian, H., Klambt, D. & Jones, A. M. Auxin-binding protein 1 does not bind auxin within the endoplasmic reticulum despite this being the predominant subcellular location for this hormone receptor. *J. Biol. Chem.* **270**, 26962–26969 (1995).
28. Gelová, Z. *et al.* Developmental roles of Auxin Binding Protein 1 in Arabidopsis thaliana. *Plant Sci.* **303**, 110750 (2021).
29. Dahlke, R. I. *et al.* Protoplast Swelling and Hypocotyl Growth Depend on Different Auxin Signaling Pathways. *Plant Physiol.* **175**, 982–994 (2017).
30. Jayakannan, M., Bose, J., Babourina, O., Rengel, Z. & Shabala, S. Salicylic acid improves salinity tolerance in Arabidopsis by restoring membrane potential and preventing salt-induced K+ loss via a GORK channel. *J. Exp. Bot.* **64**, 2255–2268 (2013).
31. Paponov, I. A. *et al.* Auxin-Induced Plasma Membrane Depolarization Is Regulated by Auxin Transport and Not by AUXIN BINDING PROTEIN1. *Front. Plant Sci.* **9**, (2019).
32. Serre, N. B. C. *et al.* AFB1 controls rapid auxin signalling through membrane depolarization in Arabidopsis thaliana root. *Nat. Plants* (2021) doi:10.1038/s41477-021-00969-z.
33. Tominaga, M. & Ito, K. The molecular mechanism and physiological role of cytoplasmic streaming. *Curr. Opin. Plant Biol.* **27**, 104–110 (2015).
34. Sauer, M. *et al.* Canalization of auxin flow by Aux/IAA-ARF-dependent feedback regulation of PIN polarity. *Genes Dev.* **20**, 2902–2911 (2006).
35. Mazur, E., Benková, E. & Friml, J. Vascular cambium regeneration and vessel formation in wounded inflorescence stems of Arabidopsis. *Sci. Rep.* **6**, 33754 (2016).
36. Mazur, E. *et al.* Clathrin-mediated trafficking and PIN trafficking are required for auxin canalization and vascular tissue formation in Arabidopsis. *Plant Sci.* **293**, 110414 (2020).
37. Mazur, E., Kulik, I., Hajný, J. & Friml, J. Auxin canalization and vascular tissue formation by TIR1/AFB-mediated auxin signaling in Arabidopsis. *New Phytol.* **226**, 1375–1383 (2020).
38. Dai, N., Wang, W., Patterson, S. E. & Bleecker, A. B. The TMK Subfamily of Receptor-Like Kinases in Arabidopsis Display an Essential Role in Growth and a Reduced Sensitivity to Auxin. *PLoS One* **8**, (2013).
39. Hajný, J., Tan, S. & Friml, J. Auxin canalization: From speculative models toward molecular players. *Curr. Opin. Plant Biol.* **65**, (2022).
40. Wabnik, K. *et al.* Emergence of tissue polarization from synergy of intracellular and extracellular auxin signaling. *Mol. Syst. Biol.* **6**, (2010).

41. Hajný, J. *et al.* Receptor kinase module targets PIN-dependent auxin transport during canalization. *Science* **370**, 550–557 (2020).
42. Yin, K., Han, X., Xu, Z. & Xue, H. Arabidopsis GLP4 is localized to the Golgi and binds auxin in vitro. *Acta Biochim. Biophys. Sin. (Shanghai).* **41**, 478–487 (2009).

2.2 Chapter two: A RAF-like kinase mediates a deeply conserved, rapid auxin response

Adapted and modified from:

Kuhn A, Roosjen M, Mutte S, Dubey SM, Carrasco PC, **Monzer A**, et al. RAF-like protein kinases mediate a deeply conserved, rapid auxin response. *Cell*. 2024;187(1):130-148.e17. doi:10.1016/j.cell.2023.11.021

We know that auxin signaling operates through two major pathways: the well-characterized nuclear pathway, which primarily regulates slow transcriptional responses, and the cell-surface pathway, which mediates rapid cellular changes. However, with algal groups lacking the nuclear auxin response system, a fundamental question arises—do ancestral plants rely on an alternative auxin signaling mechanism? This question became even more pressing following the discovery of a widespread and rapid auxin-triggered phosphoresponse mediated by ABP1 and TMK1. In this study, we investigated multiple land plants and algal species to determine whether this phosphorylation-based auxin signaling mechanism is evolutionarily conserved, shedding light on its role in fast cellular responses such as cytoplasmic streaming.

2.2.1 Introduction

The plant signaling molecule auxin is key to numerous growth and developmental processes in plants[1]. Iconic auxin-dependent processes are the tropic growth responses to light and gravity[2–5], differentiation of vascular strands, and the control of fruit development[6–9]. The dominant naturally occurring auxin is indole 3-acetic acid (IAA), a chemically simple Tryptophan derivative that land plants can synthesize in a two-step pathway, but that is widely found across both prokaryotic and eukaryotic species[10]. Its biological activity in plants as a signaling molecule, acting at nanomolar to micromolar concentrations, is extremely profound. When applied to plants or plant cells, auxin can trigger a wide range of physiological, cellular and molecular changes that likely underly the long-term effects on plant growth and development. While initial discoveries with auxin were made in flowering plants, both the occurrence of IAA and physiological and developmental responses to the molecule have been reported well beyond this group. All land plants studied[11], and a range of algae[12–14] show responses to externally applied auxin, which suggests a very deep origin of the capacity to respond to auxin. The cellular responses to auxin come in essentially two flavors: fast and slow. The fast responses include changes in membrane polarization[15–17], cytoplasmic streaming[18,19], Calcium and proton fluxes[20–24] and remodeling of the cytoskeleton[12,25] and trafficking[26]. Slower responses include cellular growth, division and differentiation[27–30].

Genetic approaches have been incredibly successful in defining a response system that mediates the responses to auxin that control plant growth and development. Using the ability of auxin to inhibit root growth in the flowering plant *Arabidopsis thaliana*, a set of components was identified that mediates auxin's activity in regulating gene expression – the nuclear auxin pathway (NAP)[31–35]. This system revolves around the auxin-triggered proteolysis of a family of transcriptional repressor proteins, thus liberating DNA-bound transcription factors and allowing gene regulation[36]. Through this pathway, auxin controls the expression of hundreds to thousands of genes, and mutations in its components interfere with most, if not all

developmental auxin functions, culminating in embryo lethality in the most strongly affected mutants[37–39].

As increasing numbers of plant genomes have become available, it became possible to reconstruct the occurrence and evolutionary history of the auxin response system. From such analysis, it appeared that the same auxin response system acts to control gene expression and development across land plants[11,40]. However, it is also clear that the closest sister group to land plants – the streptophyte algae – do not carry the NAP, in cases even lacking all its components[11]. Thus, a major unanswered question is how algae can respond to auxin in the absence of the known auxin response system. In addition, the fastest gene expression responses to auxin have been recorded in 5-10 minutes[41,42], but several of the fast responses[18,19,23,43,44] occur within seconds, or at least well within the time needed for gene expression and protein synthesis. Thus, it is likely that the currently known auxin response system represents the "slow" branch, and that a separate, currently unknown system must exist to mediate fast responses. The existence of fast auxin responses in land plants and their algal sisters would predict such a system to be shared between these clades.

Protein phosphorylation is a widespread mechanism for enzymatically modifying the structure and function of pre-existing proteins[45], thus eliminating the need for *de novo* protein synthesis. Given that phosphorylation depends only on the (allosteric) activation of a protein kinase, the reaction is intrinsically rapid. Several well-known examples of phosphorylation-based signaling exist across the kingdoms of life[46–49]. Among these, some are particularly rapid, with Insulin and EGF ligands triggering initial phosphorylation changes by receptor kinases within seconds[48,49], followed by relays and amplification steps with additional protein kinases[49]. Phosphorylation-based signaling is also widespread in plants, and mediates responses to peptide ligands in development and immunity[47], as well as to Brassinosteroids[50–52]. Recently, we found that in Arabidopsis roots, the natural auxin Indole-3-Acetic Acid (IAA) can trigger changes in phosphorylation of numerous proteins within 2 minutes[18,23], which opens the possibility that a phosphorylation-based mechanisms underlies rapid auxin responses. Given that at least one required component for this phosphorylation response, the AUXIN BINDING PROTEIN1 (ABP1)[18] is conserved across land plants and algae[53], it is possible that this fast response also represents the predicted deeply conserved mechanism for auxin response.

Here, we asked if this novel auxin response may represent the elusive, deeply conserved mechanism underlying rapid cellular responses. We first characterized the response in Arabidopsis, and found it to be specific to active auxins, and active within 30 seconds. Importantly, we find that auxin triggers rapid changes in protein phosphorylation in 5 different land plant and algal species, including a core set of conserved targets. We leveraged both dense temporal and comparative datasets to identify a RAF-like kinase that mediates auxin-triggered protein phosphorylation and control of fast cellular responses across species. This work thus identifies an ancient system for rapid responses to the auxin signaling molecule that has profound impact on many cellular pathways and functions.

2.2.2 Results

2.2.2.1 Identification of deeply conserved cellular responses to auxin

Auxin triggers a variety of rapid cellular and physiological responses that are unlikely to be mediated by the NAP. These have predominantly been studied in *Arabidopsis thaliana* (henceforth "Arabidopsis"), and it is unclear if there is a set of deeply conserved rapid cellular and physiological responses to auxin. Among the fast auxin responses that have previously been recorded, two stand out as being potential candidates for being shared outside of land plants, and we first explored their conservation.

Membrane potential reflects the difference between cytoplasmic and apoplastic electrical potentials (Figure 1A). Auxin has a profound effect on membrane potential by triggering instantaneous depolarization of plasma membrane[17,24]. This depolarization is then followed by a hyperpolarization of the membrane[17,23,54,55]. Both membrane depolarization and hyperpolarization depend on auxin's ability to regulate ion fluxes across the plasma membrane, predominantly involving H+-ATPase proton pumps and on the cytoplasmic action of AFB1, a member of the TIR1/AFB canonical auxin receptor family[17]. To first test whether this response is conserved in the plant lineage, we monitored membrane potential after 5 minutes of treatment with 100 nM IAA in Arabidopsis roots, *Marchantia polymorpha* (liverwort; henceforth "Marchantia") rhizoid initials in gemmae and *Klebsormidium nitens* (algae; henceforth "Klebsormidium") filaments using the membrane potential fluorescent probe DISBAC2(3) that has been validated as a tool for reporting changes in membrane potential[17,56]. An increase in apoplastic DISBAC2(3) fluorescence reports membrane depolarization. We observed a significant increase in fluorescence upon auxin treatment in all three species (Figure 1B,C; Suppl Figure 1A,B). Moreover, the increase was quantitatively very similar between species. This indicates that rapid auxin-triggered plasma membrane depolarization is a deeply conserved rapid auxin response.

Cytoplasmic streaming describes the actin cytoskeleton-mediated movement of organelles through the cytoplasm and is thought to have an essential function in the transport of nutrients and proteins within the cell[57]. In plants, cytoplasmic streaming is primarily driven by plant-specific Myosin XI cytoskeletal motor proteins (Figure 1D). We examined the effect of treatment with 100 nM IAA on cytoplasmic streaming by monitoring the movement of fluorescently labeled mitochondria in epidermal cells of Arabidopsis roots within the elongation zone, as well as in Marchantia rhizoid cells (Figure 1E). After particle tracking, we determined the active diffusion rate (K) and diffusive exponent (α) of mobility by fitting mean square displacements, ensemble-averaged per cell, to an anomalous diffusion model[58,59] in both auxin-treated and mock-treated samples. We found consistent streaming in both species (Figure 1F, suppl Movie 1 & 2), but absolute rates differed between species. (Figure 1F; suppl Figure 1C-E). Pretreatment with the actin-depolymerizing drug Lantrunculin B reduced cytoplasmic streaming in both species (suppl Figure 1F,G), confirming that the motion observed is actin-dependent. Importantly, auxin treatment consistently increased the diffusion rate in both species (Figure 1F; suppl Figure 1C; suppl Movie 1,2). Hence, like membrane depolarization, the acceleration of cytoplasmic streaming is a deeply conserved response to auxin.

2.2.2.2 **Identification of a deeply conserved, rapid, phosphorylation-based auxin response**

The finding that there are conserved fast physiological responses to auxin in algae and land plants suggests the existence of a shared mechanism for auxin perception and signal transduction. We previously showed that auxin can trigger changes in protein phosphorylation within 2 minutes in Arabidopsis roots[18,23].

To examine whether this response is conserved beyond Arabidopsis, we selected a set of phylogenetically distant species ranging from bryophytes to green algae for phosphoproteomic analysis. These included the bryophytes Marchantia and *Physcomitrium patens* (moss; henceforth "Physcomitrium"), the streptophyte algae Klebsormidium and *Penium margaritaceum* (henceforth "Penium"), in addition to the angiosperm Arabidopsis. This selection encompasses both early-diverging streptophyte algae (Klebsormidium) and a close sister to land plants (Penium; Zynematophyceae), and covers two clades within the bryophytes: liverworts (Marchantia) and mosses (Physcomitrium). Notably, while sporophytic (root) tissue was sampled for Arabidopsis, gametophytic tissue was sampled for all other species. This is

inevitable given the strongly reduced Arabidopsis gametophyte and the small, transient, or absent sporophyte in all other species. Consequently, the suite of species not only spans phylogeny, but also haploid and diploid generations and a wide array of different cell and tissue types. All species were treated with the same concentration (100 nM) of IAA, followed by phosphopeptide enrichment after two minutes using the same experimental, mass spectrometry and analysis workflow. Strikingly, we find that two minutes of auxin treatment leads to large shifts in the phospho-proteome in all species tested (Figure 2A). The number of differential phosphosites was comparable across species (FDR≥1.301: n=1048 in Arabidopsis; n=670 in Physcomitrium; n=741 in Marchantia; n=719 in Penium; n=1231 in Klebsormidium). In all species except Klebsormidium, hyperphosphorylation upon auxin treatment represented the majority of differential phosphosites (64% in Arabidopsis, 76% in Physcomitrium, 73% in Marchantia and 60% in Penium), while hyper-and hypophosphorylation were more equal in Klebsormidium (47% hyperphosphorylation) (Figure 2A). Thus, rapid, global changes in phospho-proteomes are triggered by auxin at comparable scales in all species tested.

We next asked if the cellular functions and proteins that are targeted by auxin-triggered phosphorylation changes are conserved among the species tested. Estimated divergence times of the species used here from common ancestors is around 850 Mya for algae and land plants, and 500 Mya among the land plants[60]. Given these enormous evolutionary distances, there is substantial sequence divergence within protein families, and large differences in gene family numbers[61]. This makes establishing direct orthology relationships very challenging. Therefore, before comparison of differential phosphoproteins at protein/family level, we first constructed a set of orthogroups that represent the set of genes that originated from a single gene in the last common ancestor of all the species under consideration. We then consider members of the same orthogroup to represent a conserved ancestral function. Among the species tested, Penium has a remarkably large number of orthogroups with multiple members within Penium (Suppl Figure 2A), which is a reflection of the high degree of fragmentation of the genome assembly[62]. In all species, about half of the phosphoproteins are unique to that species, and the other half is shared with one or more other species (Figure 2B). We identified sets of proteins that are commonly regulated among land plants (n=193), bryophytes (n=304) or algae (n=262). In addition, we found an overlap of 11 orthogroups across all organisms (Figure 2B). Given the previous consideration, we also consider orthogroups not represented in Penium to be relevant. When excluding Penium from the analysis we found 29 orthogroups to be shared (Figure 2B,C). Note that, given the large evolutionary distance, and varying degrees of primary sequence conservation, we focused on shared phosphoproteins rather than phosphosites. We next explored functional annotations of shared phosphoproteins for each intersection through Gene Ontology (GO) analysis. There was a large difference between the functions enriched in land plants and algae (Figure 2D). Comparing land plants to only bryophytes showed that some functions are unique to bryophytes ("photosynthesis" and "chlorophyll binding"), but that most are shared. Algae share a set of functional enrichment with land plant plants (or only with bryophytes), but also show a range of algae-specific functions, notably including membrane transporters. Collectively, a large set of processes seems to be targeted by auxin-regulated phosphorylation.

We next focused our attention on the core set of deeply conserved phsophotargets. Analysis of these orthogroups showed that a broad range of cellular functions is subject to auxin regulation (Figure 2C). These include processes at the plasma membrane or endomembranes, such as transmembrane transport and clathrin coat disassembly, but also nuclear organization and posttranslational regulation of gene expression. Furthermore, GO analysis identified responses to external stimuli and hormones, including response to blue light, abscisic acid transport and polar auxin transport. As expected from a phospho-proteomic analysis, protein phosphorylation

was another highly enriched GO-term. Thus, auxin targets both species-specific and deeply conserved phosphorylation responses.

2.2.2.3 **Auxin phospho-response is ultra-rapid and dynamic**

The vast effect of a 2-minute IAA treatment on the phosphoproteome to a low IAA concentration in phylogenetically distant species is striking, and suggests this to be a hormonal response. However, auxin is a weak organic acid derived from Tryptophan, and it is possible that (part of) the response observed is an unspecific response to weak organic acids or auxin-like molecules. To test chemical specificity, we therefore used a panel of related chemicals (all at 100 nM) in the same set-up, and measured phosphoproteomes after 2 minutes of treatment in Arabidopsis roots. None of the synthetic auxin analogs 2,4-Dichlorophenoxy-acetic acid (2,4D), 1-Naphtaleneacetic Acid (1-NAA) or 2-Naphtaleneacetic Acid (2-NAA) triggered phosphorylation changes that showed any correlation to those induced by IAA (Suppl Figure 3A). Likewise, neither Benzoic Acid (BA) nor Formic Acid (FA) induced IAA-like phosphorylation changes (Suppl Figure 3A). As a control, two entirely independent IAA treatments and measurements (Suppl Figure 3B) showed strong correlation. Thus, IAA response is chemically specific. Synthetic auxins have auxinic activity in several physiological assays, and it is therefore striking that 2,4-D, 1-NAA and 2-NAA failed to trigger IAA-like phosphorylation changes. To test if these can act like IAA in this response, albeit less efficiently, we measured phosphoproteomes at a 10-fold higher concentration (1 µM). Indeed, at this concentration, 1-NAA and 2-NAA could induce IAA-like phosphorylation changes, but BA could not (suppl figure 3C). Thus, IAA induces a rapid, chemically specific, hormonal phosphorylation response in Arabidopsis roots. We further confirmed that the changes in phosphopeptide abundance were not correlated to changes in overall protein abundance (Suppl Figure 3D).

To explore the temporal dynamics of the phosphorylation response, we generated a time series of IAA treatments on Arabidopsis roots, ranging from 30 seconds to 10 minutes. To ensure that this time series was not confounded by auxin-independent effects of submerging roots in growth medium, we also sampled solvent mock controls for each time point, and subtracted the phosphosite abundance in the mock treatment from each IAA treatment (Figure 3A). This led to a set of unique phosphoproteomes that could be clearly resolved by Principal Component Analysis (PCA; Figure 3B). Strikingly, even at 30 seconds, IAA triggered changes in abundance of hundreds of phosphosites (Figure 3C), underlining the rapid nature of the response. Compiling all differentially phosphorylated sites across the entire time series, a total of 2962 phosphosites is regulated by IAA (Figure 3C), corresponding to 1770 proteins, representing ~5% of the proteins encoded by the Arabidopsis genome.

We next used the Minardo-Model[63] to order groups of phosphopeptides that show similar trends of phosphorylation (Figure 3C). In each cluster, generalized linear models are derived from individual profiles which, together with Z-scores and post hoc Tukey tests, infers event windows at which the majority of profiles show half-maximal amplitude response. From this analysis, the earliest events likely occur well within 30 seconds after treatment (Figure 3C; Clusters 1-9). This analysis clearly identified a range of temporal patterns in IAA-dependent phosphorylation. These ranged from transient, early or late hyper- or hypo-phosphorylation to gradual hyper- or hypo-phosphorylation, and oscillatory hyper- and hypo-phosphorylation (Figure 3C). GO analysis on the clusters showed clear enrichment of functions in the different phases of the response (Suppl Figure 3E).

The phosphorylation changes reported here offer a rich source of data that allows developing hypotheses for future studies. To facilitate the use of this rich dataset and to help interact with the data, we designed a webtool (AuxPhos; https://weijerslab.shinyapps.io/AuxPhos) and user

interface. AuxPhos allows to search individual proteins by their unique identifier, and to visualize the quantification of its phosphopeptides across the various datasets (wild-type with IAA and various related chemicals; time series; species and diverse mutants). In addition to offering a searchable interface for navigating phosphoproteins, we have implemented AlphaFold2-based protein structural models to visualize phosphosites on predicted protein structures (e.g. Figure 3D). As further phosphoproteomic data will become available, these will be integrated in the tool.

2.2.2.4 **Identification of kinases in auxin-triggered phosphoresponse**

Given the availability of a densely sampled time series and the identification of nearly 3000 phosposites, we asked if the dataset could be used to infer phosphorylation relationships. Moreover, in combination with the auxin-dependent phosphoproteomes in a suite of evolutionary distant species, it has the potential to identify conserved components that mediate rapid auxin responses.

To this end, we filtered the entire Arabidopsis phosphoproteome dataset for phosphosites in the (predicted[64]) activation loops of the full set of Arabidopsis kinases (Figure 4A). This identified 26 kinases that were differentially phosphorylated in their activation loop during the time series (Figure 4B), most of which were hyperphosphorylated and therefore likely activated. We next performed a regression analysis (Figure 4A) where we identified phosphorylation sites that temporally matched or followed the dynamics of activation of each kinase. This led to the generation of an inferred kinase-target network encompassing all 23 regulated kinases and 2140 predicted phosphotargets (Suppl Figure 4). To test the validity of this inference approach, we asked if protein kinases with known phosphotargets were correctly predicted. This analysis is challenging because of the relatively small number of well-documented kinase-substrate relationships with information about the exact phosphosite. Nonetheless, we found several such pairs to conform to their predicted relationship in our dataset (Figure 4C): A Rapidly Accelerated Fibrosarcoma (RAF) -like kinase was connected to its OST1 target, and this OST1 kinase to a bZIP target. In addition, D6PK was connected to PIN7, consistent with PIN phosphorylation by this kinase[65].

We next ranked the 23 kinases according to their weight and position in the phospho-network (Figure 4D), indicated by their degree and their betweenness centrality, parameters that were correlated in this network (Figure 4D). This identified several kinases as potential hubs in this network. These include the D6PK kinase, as well as the LRR-RLK protein LRR1, a group of closely related B4 RAF kinases and PIP5K2. The latter is a phosphoinositide kinase, and it is an open question if the PIP5K activity or the membrane changes it induces are correlated with downstream phosphorylation. In any event, this network analysis offers a prioritized set of auxin-regulated kinases that are strong candidates for mediating rapid responses.

In parallel, to identify kinases that act on the conserved phosphorylation response across species, we analyzed phosphorylation motifs enriched among the conserved phospho-targets. We found that hyperphosporylation was associated with the presence of a proline-directed SP motif (Figure 4E), a motif typically targeted by MAP kinases[66,67]. We next explored if any kinases are found among the conserved IAA-regulated phophotargets. We found three kinases in the core conserved set (Figure 4F): the blue light receptor PHOT1 (Figure 4F) and two RAF-like kinases, representing B3 and B4 subclades of the family[68]. Given that RAF-like kinases were also found as a hub in the network inference in Arabidopsis (Figure 4D), and given that these belong to the MAP kinase family that targets SP motifs, we consider these likely candidates for key components in the response.

RAF-like kinases are serine/threonine kinases that belong to the mitogen activated protein kinase kinase kinase (MAPKKK) family[68]. They are classified into four B clades and seven C

clades according to their homology with the widespread eukaryotic RAF protein kinases. Arabidopsis B2, B3 and B4 clade RAF-like kinases have been implicated in various physiological responses, including responses to hypoxia, osmotic stress and drought[69,70]. The Marchantia B4 RAF-like kinase (PRAF) was implicated in the regulation of carbon fixation[71]. While we found RAF-like kinases of the B2, B3 and B4 clade to be hyperphosphorylated after auxin treatment in Arabidopsis, it seems that only hyperphosphorylation of RAF-like kinases of the B3 and B4 clade upon auxin treatment is conserved (Figure 4F). Moreover, only the B4 RAF kinases were identified as a hub in the kinase network analysis (Figure 4D). Thus, given the multiple lines of evidence suggesting a role for B4 RAF-like Kinases in auxin-triggered phosphorylation, we here focus on these.
The B4 clade of RAF-like Kinases is represented by 7 paralogs in Arabidopsis, 2 in Physcomitrium and single copies in Klebsormidium and Marchantia[72] (Figure 4G). Given the fragmented genome assembly in Penium, we could not unequivocally identify its ortholog. Importantly, most of the B4 RAF-like kinases are hyperphosphorylated in response to auxin treatment across species (Figure 4H), firmly connecting this family to auxin response.

2.2.2.5 B4 RAF-like kinases are conserved components in growth, development and auxin response

Given that no role for B4 RAF-like Kinases in auxin response has been reported, we initially explored requirements for these proteins in auxin-associated growth and development, as well as in response to externally applied auxin. To this end, we analyzed previously established mutants: a septuple mutant of the entire Arabidopsis B4 clade (*raf*^{null}; also referred to as OK^{130} in [70]; here referred to as *raf*), and a null mutant in the single Marchantia ortholog (Mp*praf*^{KO} [71]; here referred to as *praf*). We found that in both species, loss of RAF activity caused growth and developmental phenotypes (Figure 5A-D). While in Arabidopsis we found a range of defects in plant height, rosette area, root growth and germination (Figure 5A-D; Supplementary Figure 5A-F), in Marchantia, these manifested as smaller thallus size and reduced gemmae cup number (Figure 5E,F; Supplementary Figure 5G,H), confirming previously published results[71]. All these phenotypes in both species were either fully or partially complemented by the introduction of individual RAF20 or RAF24 (Arabidopsis) or PRAF (Marchantia) copies, expressed from native genomic fragments, and C-terminally fused to a fluorescent protein (Figure 5A-F; Suppl Figure 5B, D-F, H). The fluorescent signals in these transgenic lines were broadly distributed to both membrane-associated and intracellular punctate structures (Figure 5I,J), perhaps related to the presence of a Phox-Bem1 (PB1) oligomerization domain in these proteins[73].
Essentially all growth phenotypes recorded in *raf* and *praf* mutants reflect processes that are known to involve auxin action[30,74,75]. We therefore tested sensitivity of the Arabidopsis *raf* and Marchantia *praf* mutants to auxin. In Arabidopsis, *raf* mutant roots were slightly less sensitive to growth inhibition by auxin (Figure 5G). Likewise, Marchantia *praf* mutant thallus, although already reduced in size under control conditions, was also less sensitive to auxin-induced growth inhibition (Figure 5H). Thus, in both species, B4 RAF-like kinases act in growth and development, and play a role in auxin response.

2.2.2.6 RAF-like kinases mediate fast auxin phospho-response

Auxin-associated growth and development, as well as Arabidopsis root and Marchantia thallus growth responses to externally applied auxin, is typically associated with changes in auxin-dependent gene expression through the NAP[36,40]. Given the auxin-related phenotypes in *raf* and *praf* mutants, we asked if these are affected in transcriptional responses. We therefore

performed RNA-Seq in Arabidopsis (roots) and Marchantia (thallus) wildtype and (*p*)*raf* mutants that were either treated with 1 µM IAA or control medium for one hour. This concentration of IAA should allow to detect even subtle changes in transcription in mutants. In both species, transcriptomes under untreated conditions look very distinct between mutant and wildtype (Figure 6A,B), suggesting massive effects of loss of RAF function on the "baseline" transcriptome in the absence of externally applied auxin. However, comparing auxin-treated and untreated samples in both species showed substantial auxin-induced changes in transcriptomes in both wildtypes and in mutants (Figure 6A,B). Qualitatively, mutants in both species still showed a typical gene expression response to auxin. Indeed, detailed analysis of individual auxin-regulated genes (Figure 6A,B) showed that mutants did not have an obvious defect in auxin-induced transcription. This suggests that RAF proteins do not have a major role in transcriptional auxin responses.

Given the rapid activation of RAF kinases by auxin (Figure 4B), it is conceivable that these kinases act in auxin response through their role in mediating rapid phosphorylation responses. We tested this hypothesis by subjecting *raf* mutants in Arabidopsis and *praf* mutant in Marchantia to phosphoproteomic profiling after two minutes of treatment with 100 nM IAA or control media. In both species, we found that the number of significant differentially hyperphosphorylated phosphosites after auxin treatment was reduced (666 in Arabidopsis WT; 445 in *raf* mutant; 538 in Marchantia WT; 285 in *praf*; Figure 6C). When comparing the number of phosphosites in wild-types and mutants, we found that 73% of the differential phosphosites in wild-type was lost in the Arabidopsis *raf* mutant, while 51% was lost in the Marchantia *praf* mutant (Figure 6C). We compared phosphoproteomes in non-treated mutants with wild-type controls in both species to identify functions that are deregulated in (*p*)*raf* mutants. In Arabidopsis *raf*, 392 orthogroups were different between mutant and wildtype, while in Marchantia *praf*, 785 orthogroups were differentially phosphorylated (Figure 6D). Many orthogroups that were not significantly affected by auxin in wild-type became differentially phosphorylated upon auxin treatment in the mutants (Figure 6E). This suggests that the mutants in both species not only lack a substantial part of auxin-triggered phosphorylation, but also have a response system that is differently wired in non-treated conditions. It also shows that not all IAA-triggered phosphorylation changes are mediated by RAF-like kinases. These results are consistent with the large transcriptional changes in control-treated mutants, and with the strong phenotypes in the mutants. When comparing targets of B4 RAF-dependent, auxin-triggered phosphorylation changes in the two species, we found a small overlap (24 orthogroups; Figure 6E). Given the evolutionary distance between Marchantia and Arabidopsis, this is remarkable since it suggests that there is indeed a set of conserved fast auxin response under control of a conserved mechanism. These shared, RAF/auxin-dependent targets included proteins associated with a diverse set of cellular processes (Figure 6F; Supplementary Figure 6A). This includes ion transport, membrane dynamics, and auxin export (e.g. PIN's, ABCB's, D6PK), but also featured nuclear processes such as splicing and cytoplasmic processes such as cell plate formation and cytoskeleton organization (e.g. SPIKE1, TOR1, NEK5). Lastly, this analysis also identified previously reported phospho-targets of B4-type RAF kinases (e.g. VCS, VCR, SE).

To explore to what extent the auxin-triggered phosphorylation network is affected in *p*(*raf*) mutants, we compared the phosphorylation state of all kinases that were significantly hypo- or hyperphosphorylated upon auxin treatment in wild-type of both species with their phosphorylation state in the mutants. Notably, most of the auxin-triggered kinase phosphorylation was lost (Figure 6G,H). This suggests that B4 RAF-like kinases directly or indirectly regulate the auxin-triggered phosphorylation of these kinases.

Proteins in the Arabidopsis RAF family have been identified as being hyperphosphorylated upon osmotic treatment[70] and to mediate response to hypoxia[69], while Marchantia PRAF has a role in the response to altered photosynthesis[71]. This suggests that the same kinase is part of multiple response pathways and urges the questions of how specific the auxin-triggered phosphorylation changes are, and how RAF is activated in the context of auxin response. We compared the 2-minute auxin-triggered phosphorylation changes with the set of 973 phosphosites that are osmotic stress-responsive in Arabidopsis[70]. The overlap was very limited (37 phosphosites; Supplementary Figure 6B), and 13 of these overlapping phosphosites depend on RAF (Supplementary Figure 6B). We therefore conclude that the phosphoresponse that we identified here is specific and independent from osmotic stress responses.

We next explored mechanisms of RAF activation. In time-course phosphoproteome data we found that multiple sites on all RAF proteins are modulated upon auxin treatment (Figure 6I), suggesting profound and rapid regulation. To address which auxin binding sites might be upstream of RAF phosphorylation, we analyzed previously recorded[18] phosphoproteomes of mutants in AUXIN BINDING PROTEIN1 (*abp1*[18,76]) and TRANSMEMBRANE KINASE1 (*tmk1*[18,77]), and generated a matched phosphoproteome of a mutant in the AUXIN F-BOX1 receptor (*afb1*[78]). Strikingly, each of the three mutants showed profound changes in their auxin-induced phosphoproteomes (Suppl Figure 6C,E). In all three mutants, a significant fraction of the auxin-triggered changes in phosphorylation were lost (Suppl Figure 6C). We next arrayed all phosphosites in RAF-like kinases and compared their phosphorylation state in the mutant backgrounds (Figure 6J). From this analysis, it emerges that RAF phosphorylation is strongly disturbed in each mutant, and that the *afb1* pattern more closely resembles that of wild-type, whereas *abp1* and *tmk1* more severely disturb RAF phosphorylation (Figure 6J). We, therefore, conclude that ABP1 and TMK1 are required for the phosphorylation of RAF-like kinases.

2.2.2.7 **RAF-like kinases link rapid phospho-response to fast auxin responses**

Given the profound role of RAF-like kinases in mediating fast auxin-triggered phosphorylation changes, we explored whether RAF might mediate rapid physiological and cellular responses to auxin. We first asked if RAF-like kiasnes are involved in rapid growth response sin Arapdopsis. For this, we analyzed both the rapid response to externally applied IAA (Suppl Fig 7A) and gravitropic root bending (Suppl Fig. 7B). Neither of these responses was altered in the *raf* mutant (Suppl Figure 7A,B). In the gravitropism assay, *raf* mutants roots are subtly delayed in bending (Suppl Figure 7B), but this may be a consequence of reduced growth rate (Suppl. Figure 5C). This suggests that RAF-kinases do not play a crucial role in rapid growth responses in Arabidopsis roots. Previously, it has been reported that AFB1 is essential for these responses, which we confirmed (Suppl Figure 7A,B). Therefore, our data place RAF-like kinases in a branch of auxin response distinct from AFB1. This matches the absence of TIR1/AFB1 orthologs in the algae used in phosphoproteomics, and the late emergence of AFB1 in land plant evolution[11].

We next analyzed the response in membrane potential to IAA in (*p*)*raf* mutants. Responses to auxin treatment in membrane depolarization were normal in (*p*)*raf* mutants in both Arabidopsis and Marchantia (Figure 7A,B, Supplementary Figure 7C). We did find that Arabidopsis *raf* mutants showed an altered apoplastic root surface pH profile (Figure 7C,D), perhaps caused by altered developmental zonation, but these displayed a wild-type response to IAA (Figure 7C,D).

We next tested the response of (*p*)*raf* mutants to auxin in the acceleration of cytoplasmic streaming. Strikingly, both Arabidopsis *raf* mutants and Marchantia *praf* mutants are essentially insensitive to the promoting effect of auxin in cytoplasmic streaming (Figure 7E,F; suppl movie 4,5). Already in untreated Arabidopsis *raf* mutant root epidermal cells,

cytoplasmic streaming is significantly reduced (Suppl Figure 7D; suppl movie 6). In Marchantia rhizoid cells, *praf* mutants showed wild-type cytoplasmic streaming velocity in untreated conditions, but mutant cells were insensitive to the promoting effect of auxin (Figure 7F, suppl Figure 7D). The response to IAA in accelerating cytoplasmic streaming in Arabidopsis was fully restored by the introduction of RAF20-YFP, RAF24-YFP (Fig. 7E; suppl Figure 7D), firmly connecting RAF-like kinases to IAA-dependent cytoplasmic streaming. Collectively, we conclude that RAF proteins link rapid phosphorylation changes to a fast cellular response to auxin.

2.2.3 Discussion

In past decades, there have been impressive advances in understanding how auxin is synthesized, transported and degraded, and how it controls plant growth and development by regulating gene expression[36]. There are however several major open questions. Firstly: there is a number of auxin responses that are too rapid to be mediated by gene regulation, for which there is no mechanism yet. Secondly, no known mechanism can account for responses to auxin in algae, that lack the well-known transcriptional auxin response system[11,53], but that we show here to have fast responses that are shared with land plants.

After initially describing a rapid phosphorylation response to auxin in Arabidopsis roots, we now demonstrate that auxin-triggered rapid phosphorylation-dependent signaling is conserved across the green lineage, extending beyond land plants into the streptophyte algae. Coupling dense phososphoproteomic profiling with comparative evolutionary phosphoproteomics, we were able to identify a key protein kinase that mediates both auxin-triggered phosphorylation and a rapid cellular response. This identifies rapid phosphorylation-dependent signaling as a mechanism that can account for both fast and deeply conserved auxin responses.

Although we compared phosphoproteomes in different tissue types, and in both sporophytic (for Arabidopsis) and gametophytic tissue (for all other species), we detected a core set of functions and orthologous protein groups that are shared between all. The most parsimonious explanation is that this core set represents a truly ancient auxin "regulome" that has been retained in all these species to serve core functions. This is not trivial, given the estimated divergence times of between 500-850 Mya[60]. We therefore expect that further sampling of more comparable stages and tissues, such as sporophytic tissue in bryophytes, gametophyte tissue in angiosperms, or fern tissues, will extend this core set of shared phosphotargets. The sample material quantities necessary for reliable proteomic profiling are prohibitive for such comparisons, but methodological innovations in efficient tissue sampling or mass spectrometry may help overcome this limitation. In addition to the core set of phosphotargets, there are numerous lineage/clade/group/organism-specific targets. This suggests profound diversification and neo-functionalization of auxin-triggered phosphorylation pathways. We have compiled all phosphoproteomics data generated in this study in the AuxPhos webtool (https://weijerslab.shinyapps.io/AuxPhos), to allow facile access and expect this to be a starting point for fruitful investigation.

Through dense temporal phosphoproteomic profiling, we identify that Arabidopsis root cells are capable of changing the phosphorylation state of more than 1700 proteins within 10 minutes of treatment with the natural auxin IAA, many of which respond within 30 seconds. We have not explored earlier timepoints, as these become technically impractical to harvest and perhaps effectivity will also be limited by the speed of IAA diffusion into roots. Computational inference suggests that the earliest responses occur around 20 seconds, a timeframe that is consistent with the kinetics of insulin-triggered phosphorylation in animal cells[49]. This auxin-

triggered phosphorylation response is remarkably chemically specific, with natural IAA being substantially more effective than synthetic analogs, and related – but physiologically inactive – compounds being unable to trigger the response. The impressive dynamics of the response in Arabidopsis roots highlight a further variable that complicates comparisons between species. As IAA uptake, diffusion, inactivation, and export rates will differ between organisms (and tissues), treatments with a single concentration at a single time point are likely grossly underestimating similarities.

Through mining both comparative phosphoproteomes, kinase-substrate inference from temporal series, and motif analysis, we identified a family of B4 RAF-like kinases (RAFs) as strong candidates for key components in the phosphoresponse. Exploring mutants in orthologous proteins in Arabidopsis and Marchantia, we could establish that RAF kinases are central to auxin-triggered phosphorylation, and to development and physiological and cellular auxin response. Curiously, transcriptional auxin responses are not impaired, which suggests that the rapid, phosphorylation-based pathway is mechanistically uncoupled from the nuclear auxin pathway. The mutants, even in the absence of auxin treatment, have dramatic phenotypes. While this may in part reflect altered responses to endogenous auxin, it should also be kept in mind that members of the RAF family have been implicated in responses to other triggers (e.g. light, osmotic stress)[69–71]. Disruption of these responses likely also contribute to the strong phenotypes, and dedicated strategies will be required to deconvolute these roles.

Notably, regulation of most kinases that are differentially phosphorylated upon auxin treatment in wild-type Marchantia and Arabidopsis, is lost in (*p*)*raf* mutants, suggesting that RAF kinases may sit at the apex of a multi-tier phosphorylation network. Interestingly, RAF kinase orthologs in mammals, play an important role as master regulators of signaling cascades, for example in EGF signaling[79]. RAF phosphorylation upon auxin treatment occurs within 30 seconds in Arabidopsis (the earliest sampled timepoint). Mammalian RAF kinases can be activated by phosphorylation within seconds to minutes after signal recognition[80,81]. Therefore, the kinetics of RAF activation is consistent with the phospho-activation of their orthologs in animal cells.

Inspired by the finding that algae and land plants share a common set of auxin phosphotargets, we explored if there are also shared cellular and physiological responses. Indeed, cytoplasmic streaming is a deeply conserved response across land plants, while membrane depolarization is deeply conserved across land plants and algae. Both are widespread cellular phenomena that are connected to for example cellular growth, nutrient distribution and acquisition[55,82,83]. It is not clear what function the auxin-regulation of these processes serves, but analysis of these responses in *raf* mutants did help to show a bifurcation of rapid auxin response mechanisms. While auxin-dependent acceleration of cytoplasmic streaming depended on RAF, membrane depolarization did not. Interestingly, *raf* mutants already had lower streaming velocity in the absence of auxin treatment, suggesting the same pathway operates during normal development, perhaps mediating the response to endogenous auxin.

A key question is how the auxin signal is perceived and transmitted onto RAF proteins, given that RAFs do not have a clear ligand-binding domain. The auxin response components ABP1, TMK1 and AFB1 all contribute to auxin-triggered phosphorylation changes in Arabidopsis. RAF phosphorylation was disturbed in all three mutants, but is clear from global phosphoproteomes that the response is not linear, and likely relatively complex. RAF kinases now offer a strong starting point to mechanistically dissect the response pathway, including its receptor. It is encouraging that ABP1 is deeply conserved among land plants and algae[53]. While no clear ortholog is present in Marchantia[84], ABP1 is member of the large Cupin family, and other members of this family in Arabidopsis also appear to function as auxin receptors[85]. This raises the interesting possibility that the broader Cupin family, represented in all domains of life[86], may act as auxin receptors for fast responses, including those mediated by RAF.

One striking aspect of the phosphorylation response we have discovered, is that it clearly predates the origin of the nuclear auxin response pathway[11]. Thus, well before the innovations appeared that led to auxin-dependent gene regulation, algal cells possessed a system to rapidly respond to auxin. The nuclear auxin response did not evolve to replace this system, as the rapid response system has been retained in land plants. Thus, the rapid system likely regulates responses that the nuclear system cannot, and *vice versa*. This could in part reflect the fundamental difference in auxin controlling cellular physiology and cell identity and fate, which happen at very different timescales. The description of this response and its deep origin, and the identification of a key component, now opens avenues to genetically and biochemically characterize these pathways in the future. This will likely deepen our understanding of the origins of auxin signaling and help reveal the ancestral role of auxin within the green lineage.

2.2.4 Material and methods

Plant material and culture conditions

All plants were cultured under 90-100 µmol photons m^{-2} s^{-1} white light with a 16 h light / 8 dark cycle at 22 °C and 75% humidity. *Arabidopsis thaliana* wild type Columbia-0 (Col-0) and all Arabidopsis mutants and transgenics were cultured on half strength Murashige and Skoog (MS) basal medium [87] at pH 5.7 supplemented with 0.8 % agar. All Arabidopsis mutants use were previously published: *tmk1-1* (SALK_016360) [77], *abp1-td1* [88], *afb1-3* [89], *raf*^{null} (published as OK^{130null}) [70].

Marchantia polymorpha wild type strain Takaragaike-1 (Tak-1) and all Marchantia mutants and transgenics were cultured on half strength Gamborg's B5 medium (B5 medium, [90]) pH 5.7 supplemented with 1% agar. The Marchantia *praf*^{ko} mutant was previously published as *Mppraf*^{ko} [71].

Klebsormidium nitens (NIES-2285) and *Physcomitrium patens* (Gransden strain) was cultured on BCD medium [91] supplemented with 1 % agar under the same condition as M. polymorpha.

Penium margaritaceum was cultured in liquid Woods Hole medium [92] at pH 7.2 under gentle agitation (60RPM) at 20 °C with a 16 h light / 8 dark cycle, 30 – 50 µmol photons m^{-2} s^{-1} light in 50 ml Erlenmeyer flasks.

Generation of transgenics

Primers used in this study can be found in Supplementary Table 1. Arabidopsis MARK reporter lines for RAF20 and RAF24 under their endogenous promoter were generated by amplifying the genomic fragment including the 3.5 kb region upstream of the start codon using the appropriate primers for each gene. Fragments were cloned into a pGIIK LIC-YFP (pPLV17) vector [93] using the HiFi cloning kit (ThermoFisher).

For the Marchantia PRAF reporter line, a DNA fragment for an Arabidopsis-codon-optimized mCitrine coding sequence (CDS) was synthesized (IDT) and used to amplify a GGS□2 linker-containing fragment by PCR with a primer set, pUGW2_Aor_GGS2_mCit_IF_F and pUGW2_Aor_mCit_IF_R, which was then cloned into the Aor51HI site in pUGW2 35S[94] using the In-Fusion cloning kit (TaKaRa Bio). The 2.5-kb HindIII-SacI fragment in the resulting plasmid, including the Gateway cassette followed by the GGS□2 linker-attached mCitrine CDS, was ligated with the HindIII- and SacI-digested pMpGWBx00 [94] to generate pMpGWBx47. The MpMARK/PRAF genomic sequence covering its promoter and CDS (without stop codon) in pENTR/D-TOPO_PRAF [71] was transferred to pMpGWB347 to generate pMpGWB347-PRAF. Agrobacterium GV2260 containing pMpGWB347-PRAF was used to transform *praf*^{ko} plants (Koide et al. 2020) by the thallus transformation method [95].

Imaging of transgenic lines plants for RAF-localization analysis

Marchantia gemmae expressing PRAF-mCitrine under endogenous promoter and 7 day-old Arabidopsis roots expressing RAF20-YFP or RAF24-YFP under their respective endogenous promoter were imaged using a Leica SP5 or SP8 confocal microscope equipped with an Argon laser (SP5) or a white light laser (SP8). Both, mCitrine and YFP were excited at 514 nm, and emission was collected between 525-575 nm. Images were analyzed using ImageJ (Version 1.52).

Phosphopeptide enrichment

For phosphopeptide enrichment, ground Arabidopsis roots powder was suspended in an extraction buffer with 100 mM Tris-HCl pH 8.0, 7 M Urea, 1% Triton-X, 10 mM DTT, 10 U/ml DNase I (Roche), 1 mM $MgCl_2$, 1% benzonase (Novagen), 1xphosphoSTOP (Pierce) and 1x cocktail protease inhibitor (Pierce). The suspended lysate was sonicated using a cooled (4°C) waterbath sonicator (Qsonica) using 30 cycles of 30 seconds ON and 30 seconds OFF at 90% amplitude. Lysate was subsequently spun down using a cooled (4°C) tabletop centrifuge at 20.000xg for 30 minutes. After centrifugation supernatant was collected and an extra 1% (v:v) of benzonase was added and incubated for 30 minutes at room temperature. Acrylamide was added to 50 mM and incubated for an extra 30 minutes at room temperature. After alkylation, proteins were precipitated using methanol/chloroform. To the lysate, 4 volumes of methanol, 1 volume of chloroform and 3 volumes of milliQ was added with rigorous vortexing in between. Lysate was centrifuged for 10 minutes at 5000 rpm. After centrifugation, the top layer was discarded and 3 volumes of methanol were added to further precipitate the protein layer by centrifugation for 10 minutes at 5000 rpm. After centrifugation, the supernatant was discarded and protein pellet was air dried. Proteins were next resuspended in 50 mM ammonium bicarbonate (ABC) and sonicated using a cooled (4°C) waterbath sonicator (Qsonica) using 30 cycles of 30 seconds ON and 30 seconds OFF at 90% amplitude. After sonication, protein concentration was measured by Bradford reagent (Biorad). For every biological replicate 500 µg protein was digested with sequencing grade trypsin (1:100 trypsin:protein; Roche) overnight at room temperature. Next, peptides were desalted and concentrated using home-made C18 microcolumns. For peptide desalting and concentrating, disposable 1000 µl pipette tips were fitted with 4 plugs of C18 octadecyl 47 mm Disks 2215 (Empore™) material and 1 mg:10 µg of LiChroprep® RP-18 (Merck) : peptides. Tips were sequentially washed with 100 % methanol, 80 % Acetonitrile (CAN) in 0.1% formic acid and twice equilibrated with 0.1 % formic acid. All chromatographic steps were performed by centrifugation for 4 minutes at 1500xg. After equilibration, peptides were loaded for 20 minutes at 400xg. Bound peptides were washed with 0.1% formic acid and eluted with 80 % ACN in 0.1 % formic acid for 4 minutes at 1500xg. Eluted peptides were suspended in loading buffer (80 % acetonitrile, 5 % tri-fluor acetic acid (TFA)). For phosphopeptide enrichment, MagReSyn® Ti-IMAC beads (Resyn bioscience) were used. For every reaction, a 1:4 peptide:bead ratio was used. Beads were equilibrated in loading buffer, resuspended peptides were added and incubated for 20 minutes at room temperature with slow mixing. After 20 minutes, bead-bound phosphopeptides were washed once in loading buffer, once in 80 % acetonitrile, 1 % TFA, and once in 10 % acetonitrile, 0.2 % TFA. After washing, phosphopeptides were eluted twice with x ul 1 % NH_4OH. After the last elution, phosphopeptides were acidified using 10 % formic acid. Phosphopeptides were subsequently concentrated using home-made C18 microcolumns. For peptide desalting and concentrating, disposable 200 µl pipette tips were fitted with 2 plugs of C18 octadecyl 47 mm Disks 2215 *(Empore™)* material and 1mg:10 µg of LiChroprep® RP-18 (Merck) : peptides. Tips were sequentially washed and equilibrated as described above. After equilibration, peptides were

loaded for 20 minutes at 400xg. Bound peptides were washed with 0.1 % formic acid and eluted with 80 % ACN in 0.1 % formic acid for 4 min at 1500xg. Eluted peptides were subsequently concentrated using a vacuum concentrator for 30-60 minutes at 45˚C and resuspended in 15µl of 0.1 % formic acid.

Filter aided sample preparation and peptide fractionation

For FASP 30kDa cut-off amicon filter units (Merck Millipore) were used. Filters were first washed by appling 50µl urea buffer UT buffer (8M Urea and 100mM Tris pH8.5) and centrifuging for 10 minutes on 11000 RPM at 20˚C. The desired amount of protein sample (100µg) was next mixed with UT buffer until a volume of 200 µl, applied to the filter and centrifuged for 15 minutes on 11000 RPM at 20˚C. Filter was washed with UT buffer by centrifugation for 15 minutes on 11000RPM at 20˚C. Retained proteins were alkylated with 50mM acrylamide (Sigma) in UT buffer for 30 minutes at 20˚C while gently shaking. Filter was centrifuged and after that washed trice with UT buffer for 15 minutes on 11000RPM at 20˚C. Next filter was washed trice in 50mM ABC buffer. After last wash proteins were cleaved by adding sequencing grade trypsin (Roche) in a 1:100 trypsin:protein ratio. Digestion was completed overnight. The following day the filter was placed into a new tube and peptides were eluted by centrifuging for 15 minutes on 11000RPM at 20˚C. Further elution was completed by adding two times 50mM ABC buffer and centrifuging for 10 minutes on 11000RPM at 20˚C.

FASP digested peptides (10 µg) were submitted to offline in stage-tip high pH reversed phase (Hp-RP) fractionation. For Hp-RP tips, 2 plugs of C18 octadecyl 47mm Disks 2215 *(Empore™) material and 1mg:10 µg of LiChroprep® RP-18 (Merck) : peptide were added to a 200 µl tip. Tips were washed with methanol for 4 minutes at 1000xg. Next buffer containing 0.1% formic acid and 80% acetonitrile was added and centrifuged for 4 minutes at 1000xg. Final equilibration was achieved with two washes of 0.1% formic acid and two washes of 20mM ammonium formate (Optima®) pH10 for 4 minutes at 1000xg. Peptides were suspended in 20mM ammonium formate pH10 before loading onto Hp-RP tip. Sample was loaded by centrifugation for 20 minutes at 400xg. Peptides were subsequently eluted with ammonium formate buffers containing 5%,8%,11%,18% and 40% ACN.*

Mass spectrometry

For nano liquid chromatography–tandem mass spectrometry (LC–MS/MS) analysis 5 ul of peptide samples were loaded directly onto a 0.10 * 250 mm ReproSil-Pur 120 C18-AQ 1.9 µm beads analytical column (prepared in-house) at a constant pressure of 825 bar (flow rate of circa 700 nL/min) with 1 ml/l HCOOH in water and eluted at a flow of 0.5 ul/min with a 50 min linear gradient from 9% to 34% acetonitril in water with 1 ml/l formic acid with a Thermo EASY nanoLC1000. An electrospray potential of 3.5 kV was applied directly to the eluent via a stainless steel needle fitted into the waste line of a micro cross that was connected between the nLC and the analytical column. Full scan positive mode FTMS spectra were measured between m/z 380 and 1400 on an Exploris 480 (Thermo electron, San Jose, CA, USA) in the Orbitrap at resolution (60000). MS and MSMS AGC targets were set to 300%, 100% respectively or maximum ion injection times of 50 ms (MS) and 30 ms (MSMS) were used. HCD fragmented (Isolation width 1.2 m/z, 28% normalized collision energy) MSMS scans of 2-5+ charged peaks in the MS scan were recorded in data dependent mode in a cycle time of 1.1 s (Resolution 15000, threshold 2e4, 15 s exclusion duration for the selected m/z +/- 10 ppm).

The MaxQuant quantitative proteomics software package was used to analyse LC–MS data with all MS/MS spectra. The following settings were used: peptide and protein FDR ≤ 0.01;

the proteome of *A. thaliana* (UniProt ID UP000006548) was used as the protein database; maximum missed cleavage was set at 2; variable modifications Oxidation (M), Acetyl (protein N-term), Deamidation (NQ), pPhospho (STY); fixed modification AcrylAmide (C); match between runs and label-free quantification options were selected.

Data analysis

Maxquant output was analyzed using Perseus or R. For time series analysis, the Maxquant output PhosphoSTY tab was imported in Perseus [96]. Data was filtered for reverse, contaminants, only identified by site and localization probability of ≥0.75. Intensity values were log2 transformed and filtered to contain at least 75% valid values in each group. Values were subsequently normalized by median column subtraction. Remaining missing values were imputed from a normal distribution using standard settings in Perseus (width: 0.3, down shift: 1.8). An FDR permutation-based ANOVA test was performed to identify significantly changing phosphosite profiles (FDR ≤0.01). To adjust for treatment response, all log2-transformed profiles from mock treatments were merged with the auxin-responsive profiles. Mock values were subsequently subtracted from auxin-responsive profiles to obtain normalized auxin-responsive phosphosite profiles.

Next, temporal ordering/cluster identification of the phosphosite profiles were done using the Minardo-Model in R[63]. Cluster number was determined in a way that most profiles followed the cluster centroid, resulting in 24 clusters.

Gene ontology enrichment was performed using the database for annotation, visualization and integrated discovery (DAVID)[97,98]. For this, UniProt accession codes were used with duplicates removed. As a background, the full *Arabidopsis thaliana* proteome was used. Next REVIGO[99] and R were used to reduce overlapping GO-terms.

For kinase network analysis, log2-transformed phosphosite profiles of kinases with phosphosites in the activation loop (as described in[64]) were compared against all FDR significant (FDR≤0.01) profiles using Pearson correlation and Euclidean distance (to also include time offset profiles). Profiles passing a Pearson correlation threshold of ≥0.6 and Euclidian distance threshold of ≤2.5 were extracted for further network analysis. For network analysis, UniProt accession codes were taken as an input for Cytoscape. Network analysis was performed in Cytoscape using standard settings. The degree and betweenness centrality were used to determine signaling hub importance.

Adobe illustrator and R, using standard packages, were used for visualization.

R shiny app

All the phosphosites and the corresponding enrichment data have been imported into the R environment as CSV files. DataTables, reshape2 and dplyr packages were used for data visualization and data wrangling. 3D protein structures of *Arabidopsis thaliana* proteome predicted through the AlphaFold2 program were downloaded from the AlphaFold database hosted at EBI (https://alphafold.ebi.ac.uk/download). These structures were rendered and visualized using the r3dmol package while the plots were generated using ggplot2 package in R.

Phosphoproteomics other species

For other species phosphoproteomics was carried out as described in above with the following adjustments:the same work flow was used with the following adjustments: *Klebsormidium nitens*, *Physcomitrium patens* and *Marchantia polymorpha* were grown for 10 days on plates as described above, then treated with 100 nM IAA or DMSO in the respective growth medium for 2 minutes, harvested and frozen in liquid nitrogen. *Penium margaritaceum* was grown for 15 days as described above. Cells were collected by centrifugation at 1620 g for 2 min and

washed 3 times with 10 ml of WHM to remove any residual extracellular polysaccharides from the cell surface. The pellet was resuspended in 10 ml of media and cells were treated with 100 nM IAA or DMSO for 2 min, harvested by centrifugation at 1620 g for 2 min and frozen in liquid nitrogen. Sample preparation and data analysis was carried out as described in (Roosjen, Kuhn et al., accompanying manuscript) with the following adjustments: for *Marchantia polymorpha* the UP000244005 proteome was used, for *Physcomitrium patens* the UP000006727 proteome was used, for *Klebsormidium nitens* the UP000054558 proteome was used and for *Penium margaritaceum* the proteome from a whole genome assembly was used [62].

Orthogroup construction

Identification of orthogroups i.e., common orthologous sequences between multiple species were estimated using Orthofinder [101]. Proteomes used for this analysis include: *Arabidopsis thaliana* (Araport11), *Marchantia polymorpha* (v6.1), *Physcomitrium patens* (v3.3), *Klebsormidium nitens* (v1.1) and *Penium margaritaceum* (v1).

Cytoplasmic streaming

Cytoplasmic streaming was recorded using a Leica SP5 or SP8 confocal microscope equipped with HyD detectors using Apo λ 63×/1.10 water immersion objective plus 6x digital zoom in an 256x256 pixel format. Cytoplasmic streaming was recorded and analyzed for Arabidopsis epidermal cells of the root elongation zone and Marchantia rhizoid cells using the following method: Seven day old Arabidopsis plate-grown seedlings were taken into the microscopy room and mitochondria were stained by transferring the seedling into a petri dish with liquid ½ MS medium containing 1 µM Rhodamine 123 for 5 minutes. Subsequently, seedlings were washed with liquid ½ MS without Rhodamine 123. Seedlings were then transferred to microcopy slides in a drop of liquid ½ MS containing 100 nM IAA or DMSO, covered by a coverslip and left on the microscope stage to adapt to the environment for 30 minutes. Cytoplasmic streaming was recorded in at least 5 epidermal cells of the root elongation zone per root at a frame rate of 5.3 frames per second for 30 seconds (159 frames).
Prior to the experiment, Marchantia thallus was grown from gemmae for two days in liquid B5 medium in a petridish. After two days of cultivation Rhodamine 123 was added to a final concentration of 1 µM and Triton-X-100 was added to a final concentration of 0.01%. Marchantia samples were stained for 30 minutes and then washed three time with liquid B5 medium containing 0.01% Triton-X-100 without Rhodamine 123. Samples were then transferred to microscopy slides and cytoplasmic streaming in rhizoid cells was recorded as described for Arabidopsis.

Data analysis for cytoplasmic streaming

Data analysis was performed in MatLab (version: 2021b). First, static background signal was removed from the raw fluorescence images using a moving window median filter (averaging window = 25 frames) and motile objects smoothed with a 2-pixel Gaussian blur filter. Moving objects were tracked using an established particle tracking algorithm [102], keeping only those trajectories whose length exceeds 3 seconds. For each cell, from the individual trajectories of the remaining moving objects, typically between 30 to 60 per time series, an ensemble-averaged mean-squared displacement was computed:

$$\Delta r^2(\tau) = < |r(t+\tau) - r(t)|^2 >$$

Per cell, these mean-squared displacements were fitted to the anomalous diffusion model (ADM) [58,59], a generalization of Einstein's diffusion model to describe complex non-Fickian motion of organelles in the visco-elastic liquid of the cellular cytosol, which is composed of an unknown mixture of passive (Brownian) and active (streaming) transport in a crowded and heterogeneous medium:

$$\Delta r^2(\tau) = K\tau^{\alpha}$$

where τ is the correlation time. In the ADM, the generalized diffusion power law exponent α provides information on the average nature of the transport processes: $\alpha < 1$ is indicative of sub-diffusive motion, characteristic of Brownian motion in a visco-elastic liquid, $\alpha = 1$ indicates pure Brownian motion in a viscous liquid and > 1 , known as super-diffusion, indicates transport with an active, e.g., motor-protein driven, component. Intermediate values of the power law exponent α provide insight into the relative balance of these different processes on the organellar motion. The transport rate constant K (in units mm/s^{a}) informs about the average transport rate: the larger the value of K the faster the organellar transport in the cells. Our analysis yields one average value for α and K per cell; the significance of the differences between control and treatment was assessed with a two-sided Wilcoxon signed rank test.

Membrane potential measurement using $DISBAC_2(3)$

Membrane potential was measured using the $DISBAC_2(3)$ probe as previously described for Arabidopsis[17]. DISBAC2(3) (2 µM) was added to buffered ½ MS liquid medium with 1% (w/v) sucrose containing either 0 or 100 nM IAA. Five-day-old Arabidopsis seedlings were transferred to a sealable single-layer PDMS silicone chip[17]. The PDMS silicone chip containing the seedlings was then placed on a vertical spinning disk microscope for a 20-min recovery. During the recovery process, the seedlings were treated with control medium at a flow rate of 3 µl/min. Seedlings were imaged every 30 seconds with a x20/0.8 objective. DISBAC2(3) was excited with a 515-nm laser, and the emission was filtered with a 535/30-nm bandpass filter. DISBAC2(3) fluorescence was measured at the border between epidermis and cortical cells of the transition zone by selecting 5-6 or 3-4 cells for Col-0 and *raf*^{null}, respectively.

Membrane potential of Marchantia and Klebsormidium was measured using the same probe with the following modifications to the protocol: Marchantia gemmae were removed from gemmae cups and placed liquid B5 with 0.01%Triton-X-100 supplemented with 15 µM $DISBAC_2(3)$, vacuum infiltrated for 5 minutes and transferred to a cover slip followed by incubation for 30 minutes before imaging. Imaging was performed on an inverted Leica SP8 confocal microscope using the same setting as for Arabidopsis. Klebsormidium was grown for 10 days as described above. A small amount of Klebsormidium was then scraped off the plate and dissolved in liquid BCD medium supplemented with 15 µM $DISBAC_2(3)$ followed by incubation for 30 minutes before imaging.

Root surface pH profile

Root surface pH was measured using the ratiometric Fluorescein-5-(and-6)-Sulfonic Acid, Trisodium Salt (FS) (Invitrogen™ F1130)[103]. Five-day-old Arabidopsis seedlings were transferred to unbuffered ½ MS medium containing 50 µM FS dye and either 0 or 100 nM IAA. Seedlings were allowed to recover on a vertical spinning disk microscope for 20 minutes after transfer to the microscope chamber. Imaging was performed using a vertical stage Zeiss Axio Observer 7 microscope coupled to a Yokogawa CSU-W1-T2 spinning disk unit with 50 µm pinholes, equipped with a VS-HOM1000 excitation light homogenizer (Visitron Systems).

Images were acquired using VisiView software (Visitron Systems, v.4.4.0.14). We used a Zeiss Plan-Apochromat ×10/0.45 objective. FS was excited by 405 and 488 nm laser. The 488/405 nm fluorescence emission ratio along the root was calculated using the ATR software[103].

Gravitropic response

5-day-old seedlings were placed on the top of a thin layer of growth medium (½ MS, 1% (w/v) sucrose, 1% plant agar, Duchefa) in a 3D-printed microscopy chambered coverslip. The chamber was placed vertically on the vertical stage microscope for 45 minutes to recover, after which the chamber was rotated 90 degrees. Roots were imaged every minute for 1 hour. The angles of the root tips were measured using ACORBA v1.2 software.

Phenotyping

Arabidopsis *plant height* was determined from respectively 48 individual wild type and *raf*^{null}, RAF20 and RAF24 complementation lines senescing plants, seven weeks after germination. *Rosette area* was determined from respectively 90 individual wild type and *raf*^{null} plants plants 28 days after germination. Plants were photographed individually using a Canon EOS 250D camera with EFS 18-135mm Macro Lens. Rosette area was then measured in ImageJ (Version 1.52) using the Polygon selection tool. To compare the *germination efficiency* between *raf*^{null} mutants and wild type, seeds for each genotype were surface sterilized, stratified in a 0.1% agarose solution for two days at 4 ˚C and paced on half strength MS plates (0.8% Agar). Plates were grown vertically for 9 days and germinated seeds were scored at day 1, 2, 3, 4, 7 and 9. Germination percentages were calculated for each day. The experiment was repeated three times individually and data were combined for analysis.

Germination

Seedlings of Arabidopsis wild type, *raf*^{null} , RAF20 and RAF24 complementation lines were germinated on half strength MS and vertically grown for 7 days. After seven days, 16 seedlings with representative root length for each genotype were transferred to new square petri dishes either containing 10 nM IAA, 100 nM IAA, 1000nM IAA or a mock treatment representing an equal amount of solvent (DMSO). *Root length* was captured by photographing the plates immediately after transferring the seedlings, after 24 hour, after 48 hours and after 120 hours, using a Canon EOS 250D camera with EFS 18-135mm Macro Lens. Root length was then measured in ImageJ using the segmented line tool and growth rates calculated.

Marchantia phenotyping

To compare the *thallus growth* between Marchantia *praf*^{ko} mutants (n=44) and wild type (n=50), thalli were grown from gemmae on half strength Gamborg B5 medium. Plates were grown for 29 days and projected thallus area was captured by photographing the plates immediately after transferring the gemmae, after 2, 4, 7, 9, 11, 14, 16, 18, 22 and 29 days, using a Canon EOS 250D camera with EFS 18-135mm Macro Lens. Thallus area was then measured in ImageJ (Version 1.52) using the Polygon selection tool. For *auxin sensitivity* assays, Marchantia *praf*^{ko} mutant (n=10) or wild-type (n=10) gemmae were grown on half strength Gamborg B5 medium supplemented the indicated concentration of IAA and grown for 10 days. At day 10, thallus size was captured by photographing the plates using a Canon EOS 250D with EFS 18-135mm Macro Lens. Thallus area was then measured in ImageJ (Version 1.52) using the Polygon selection tool. *Gemma cup number* was determined on *praf*^{ko} mutants (n=20) and wild type (n=20) thalli after 24 days of growth on half strength Gamborg B5 medium.

Transcriptomic analysis

Arabidopsis thaliana wild-type (Col-0) and mutant (*raf*^{null}) seeds were sown on half-strength MS medium covered with nylon mesh and vertically grown for 7 days. Plants were then submerged in liquid half-strength MS medium containing either 1 µM IAA or the equivalent amount of solvent (DMSO). Plates were kept horizontally for about 30 seconds and then kept vertically for 1 hour to incubate. After incubation, root tips were harvested using a scalpel and immediately frozen in liquid nitrogen.
Marchantia polymorpha wild-type (Tak-1) and mutant (*praf*^{ko}) gemmae were placed on B5 solid medium covered with nylon mesh (100 mm pore) and grown for 9 days. After growing, plants were submerged in liquid B5 medium and cultured for 1 day. After pre-cultivation, IAA was added to a final concentration of 1 µM or an equivalent amount of DMSO was added and plants were incubated for 1 hour. Using a scalpel, thalli were harvested from the mesh, blotted on paper towels and immediately frozen in liquid nitrogen.
After harvesting, all frozen samples were ground into fine powder using a pre-cooled mortar and pestle. Total RNA form all samples was extracted using a RNeasy Plant Mini Kit (QIAGEN). Total RNA was treated with RNase-free DNase I set (QIAGEN). RNA-seq library construction and RNA sequencing were performed by BGI Tech Solutions (Hong Kong).

RNAseq data analysis
Up to 20 million paired-end 150 bp reads were collected for each sample. Quality assessment for raw reads was performed using FastQC (www.bioinformatics.babraham.ac.uk/projects/fastqc). For both *Arabidopsis thaliana* (Araport11[104]) and *Marchantia polymorpha* (v6.1[105]), reads were mapped onto the respective genomes using HISAT2 (v2.1.0; [106]) with additional parameters "--trim5 10 –dta". Alignment (SAM/BAM) files were sorted and indexed using SAMTOOLS (v1.9[107]). FeatureCounts (v2.0.0[108]) was used to count the reads mapped on to each gene, with the parameters "-t 'exon' -g 'gene_id' -Q 30 --primary -p -B -C" for Arabidopsis transcipts and "t 'gene' -g 'ID' -Q 30 --primary -p -B -C" for Marchantia transcripts. DEseq2 [109] was used to normalize the raw counts and perform the differential expression analysis with a design matrix including the interaction term (Padj<0.05). Data processing and statistical analysis was performed using R (https://www.r-project.org/). Sequenced raw reads were deposited in NCBI Sequence Read Archive (SRA) under the project accession number PRJNA881051.

2.2.5 Acknowledgments

We are grateful to Asuka Shitaku and Eri Koide for generating and sharing the Marchantia PRAF-mCitrine line, to Peng-Cheng Wang for sharing the Arabidopsis *raf* mutants. We are grateful to Mark Estelle for making the *afb1* mutant available, and to our team members for discussions and helpful advice. This work was supported by funding from the Netherlands Organization for Scientific Research (NWO): VICI grant 865.14.001 and ENW-KLEIN OCENW.KLEIN.027 grants to D.W. and VENI grant VI.VENI.212.003 to A.K.; the European Resaerch Council AdG DIRNDL (contract number 833867) to D.W., CoG CATCH to J.S., StG CELLONGATE (contract 803048) to M.F. and AdG ETAP (contract 742985) to J.F.; MEXT KAKENHI Grant number JP19H05675 to T.K.; JSPS KAKENHI Grant Number JP20H03275 to R.N., Takeda Science Foundation to R.N. and the Austrian Science Fund (FWF, P29988) to J.F..

2.2.6 Contributions

Conceptualization: A.K., M.R., D.W.; Methodology: A.K., M.R., P.C.C., S.M., S.M.D., J.S.; Formal analysis: M.R., A.K., P.C.C., S.M., S.M.D., A.M., M.F., J.S..; Investigation: A.K.,

M.R., P.C.C., S.M., S.M.D., A.M.; Resources: R.N., T.K.; Writing – Original Draft: A.K., D.W.; Writing – Review & Editing: all authors; Visualization: A.K., M.R., P.C.C., S.M., S.M.D.; Supervision: M.F., J.S., J.F., D.W.; Funding Acquisition: A.K., M.F., J.F., J.S., D.W..

2.2.7 Figures

Figure 1- Auxin triggers fast cellular and physiological responses across the plant kingdom

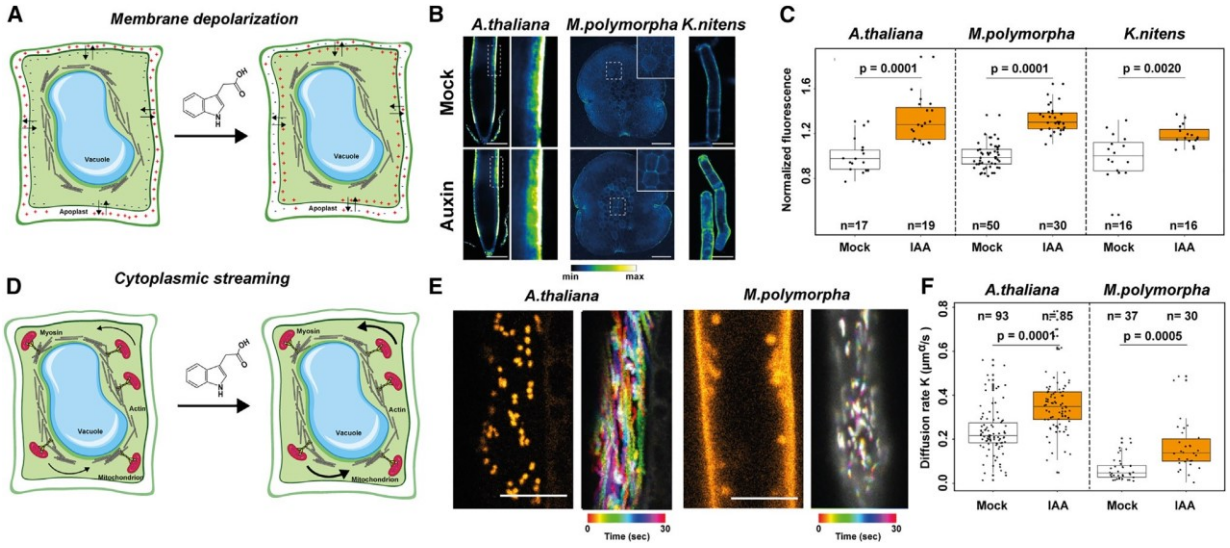

Figure 2.2-1 Auxin triggers fast cellular and physiological responses across the plant kingdom.

(A) Scheme depicting membrane polarity. (B) Representative images of membrane depolarization measured using DISBAC2(3) fluorescence in control (mock) and IAA-treated Arabidopsis root cells, Marchantia rhizoid initial cells and Klebsormidium cells, and (C) quantification of normalized fluorescence intensities across replicates. (D) Scheme depicting cytoplasmic streaming. (E) Representative images of Arabidopsis root epidermis cells and Marchantia rhizoid cells stained with the mitochondria stain Rhodamine 123. (F) Diffusion rate K (μm$^{\alpha}$/s) in control (mock) and IAA-treated Arabidopsis root cells and Marchantia rhizoid cells. Boxplots are shown along individual measurements, number of observations (n) is indicated, and significance (Student's t-test) is shown.

Figure 2- Comparative phosphoproteomics identifies a rapid and conserved auxin response

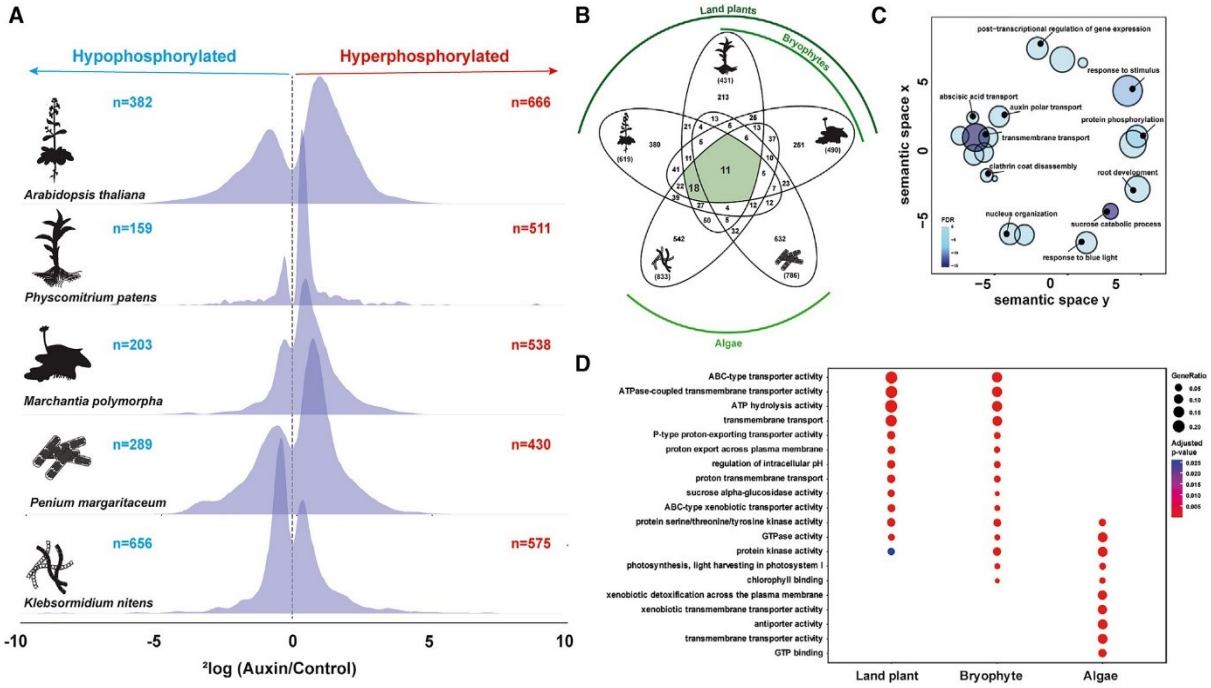

Figure 2.2-2 Comparative phosphoproteomics identifies a rapid and conserved auxin response

(A) Distribution histograms of significantly differential phosphosites (FDR≤0.05) comparing 2 minutes of 100 nM IAA (Auxin) treatment with mock treatment across 5 species, as indicated on the left (including pictograms). Numbers of hyper- or hypo-phosphorylated sites are indicated. (B) Venn diagram depicting the orthogroups found as differentially phosphorylated upon auxin treatment in all 5 species, as well as in intersections among the species used. (C) Reduced GO analysis (Revigo) of the 29 shared orthogroups (marked green in panel B). Circle sizes correspond to gene count within orthogroups. (D) GO-term analysis depicting enrichment of terms within land plants, bryophytes and algae.

Figure 3- Dynamics of auxin phosphoresponse in *Arabidopsis*

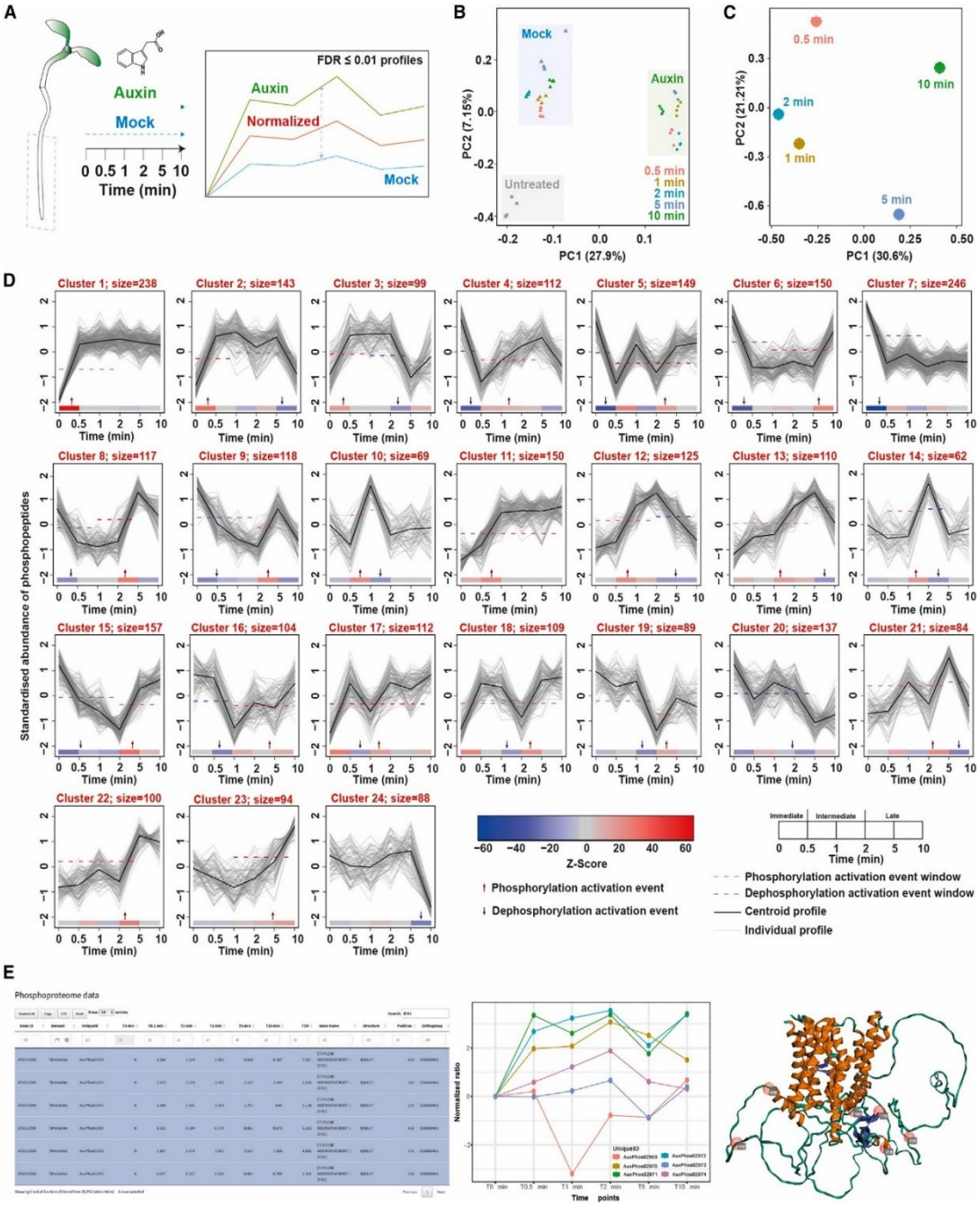

Figure 2.2-3 Dynamics of auxin phosphoresponse in Arabidopsis

(A) Schematic overview of treatment, time and analysis procedure. Roots of Arabidopsis seedlings were treated with 100 nM IAA or mock medium as treatment control for various timepoints. Datasets were individually analyzed and intensities of treatment control were subtracted from the auxin responsive profiles (FDR ≥ 0.01) resulting in normalized auxin-responsive profiles. (B) Principal component analysis of normalized auxin-responsive profiles. (C) Time series ordering of all FDR ≥ 0.01 log2 Z-scored normalized auxin-responsive profiles using the Minardo-model. Clusters are ordered based on earliest phosphorylation event. Phosphorylation event is based on the median time at which all individual profiles in a cluster cross half-maximal abundance within each event window (identified by the red or blue dashed line in graph and red and blue arrows on x-axis, respectively). (D) Screenshots of the R shiny app Auxphos. Selected profiles of a single protein can be selected, visualized in a plot and phosphosites are mapped on a 3D predicted protein structure using AlphaFold2.

Figure 4- Inference of kinase-substrate relationships and comparative phosphoproteomics identify B4 RAF-like kinases

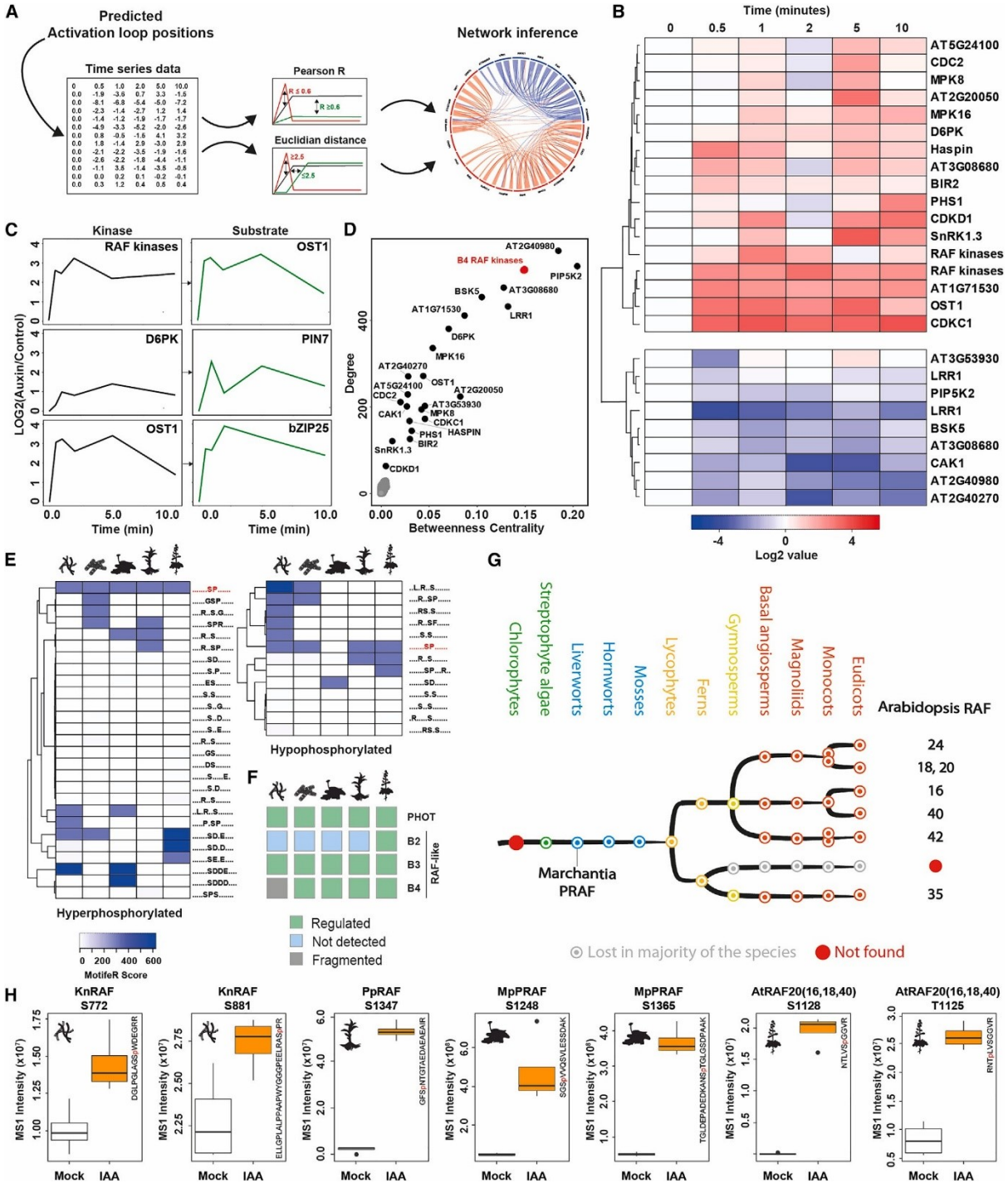

Figure 2.2-4 Inference of kinase-substrate relationships and comparative phosphoproteomics identify B4 RAF-like kinases

(A) Schematic overview of the kinase network inference approach. Phosphosites in predicted activation loops are selected from the time series data. The time series profile of the individual activation loop phosphosites are next analysed using correlation analysis (Pearson R and Euclidian distance). Profiles of phosphosites passing the threshold (Pearson R $\geq$0.6, Euclidian distance $\leq$2.5) are considered as potential substrates, and used to build a network. (B) Heatmap depicting the normalized intensity profiles of phosphopeptides in the activation loop of kinases along the time series. (C) Plots showing normalized phosphopeptide abundance profiles along auxin time series of known kinase-substrate pairs recovered in the network inference approach. (D) Network position of auxin-regulated kinases analyzed in the inference approach. Plot depicts degree (i.e. how many edges/interactions a node has) and betweenness centrality. The latter is a measurement of hub importance/centrality of a node. (E) Clustering of phosphomotif enrichment scores (using motifeR) of significantly differential (FDR$\leq$0.05) phosphosites in all tested species. (F) Heatmap depicting measured significantly differential phosphosites (FDR$\leq$0.05) of two kinase families, PHOT and RAF-like kinases, in all species tested. (G) Inferred phylogeny of the B4 RAF-like kinase. Arabidopsis numbering is indicated on the top. Every node represents an inferred ancestral gene copy at each divergence event. The phylogenetic tree underlying this abstraction can be found at interactive Tree of Life (iTOL): https://itol.embl.de/shared/dolfweijers. Arabidopsis and Marchantia copies are indicated. (H) Raw MS1 intensities of B4 RAF-like kinase orthologues in mock- and IAA-treated samples. Phosphorylated residues and peptide sequence are indicated.

Figure 5- Phenotypes of *raf* mutants

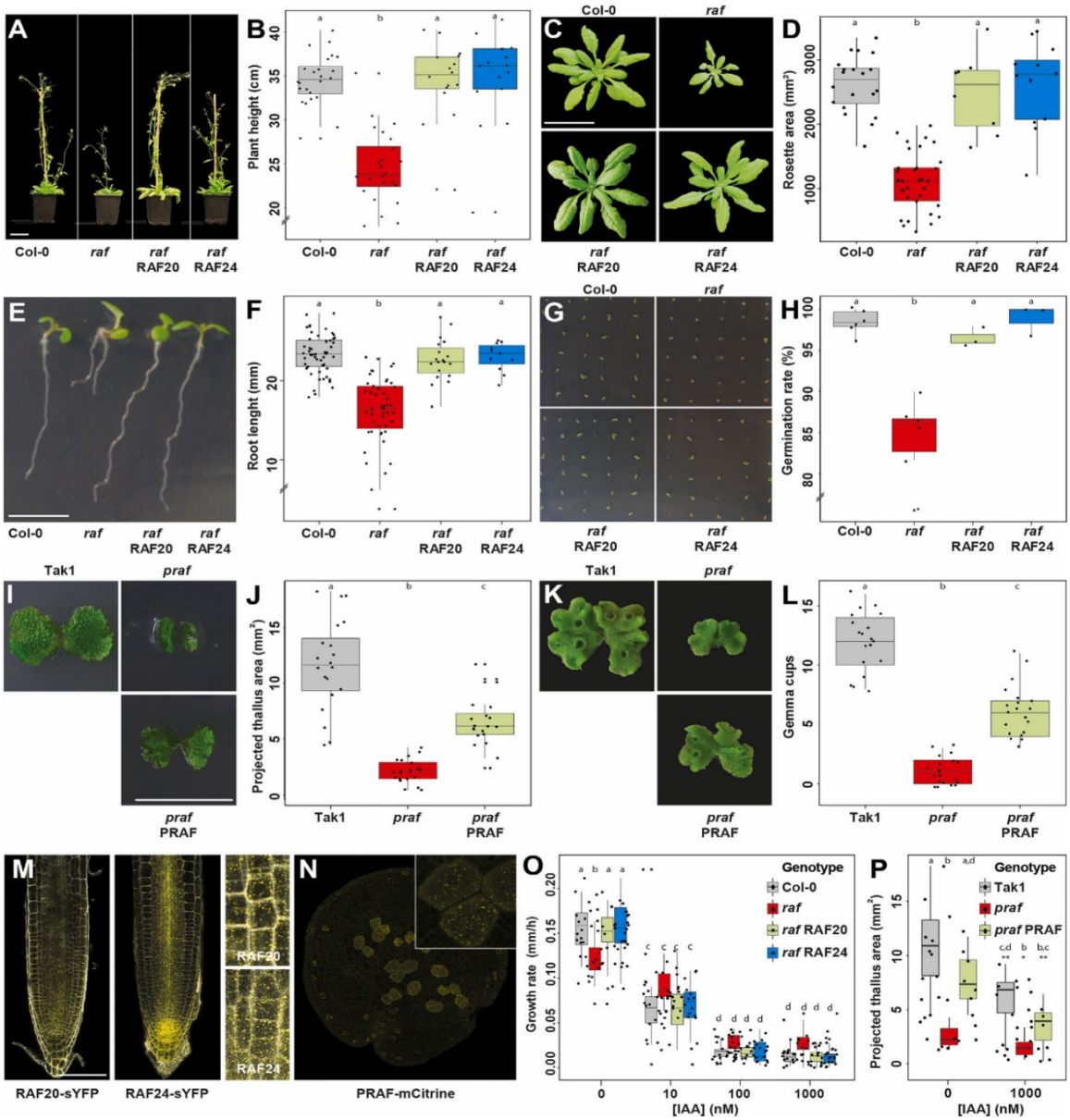

Figure 2.2-5 Phenotypes of raf mutants

(A–H) Characterization of phenotypes related to growth and development in Arabidopsis wild type (Col-0), raf mutant, and complemented raf mutant (with RAF20 of RAF24 transgene) and (I–L) in Marchantia wild type (Tak-1), praf mutant, and complemented praf mutant (with PRAF transgene). (A) Flowering plants and (B) quantification of shoot height. (C) Rosettes of 28-day-old plants and (D) quantification of rosette area. (E) 7-day-old seedlings and (F) quantification of root length. (G) Germinating seeds after 3 days and (H) quantification of germination rate. (I) Young thallus and (J) quantification of projected thallus area. (K and L) (K) Older thallus and (L) quantification of gemmae cup number. (M) Localization of pRAF20-RAF20-sYFP and pRAF24-RAF24-sYFP in Arabidopsis root tips (left: overview; right: magnifications).(N) Localization of PRAF-PRAF-mCitrine in Marchantia gemma (inset: magnification).(O) Root growth response to different concentrations of IAA in Arabidopsis wild type (Col-0), raf mutant, and complemented raf mutant (with RAF20 of RAF24 transgene). Projected thallus area of Marchantia type (Tak-1), praf mutant, and complemented praf mutant (with PRAF transgene) in the presence or absence of IAA. Dots in all graphs represent individual plants; scale bars are 5 cm (A) 5 cm (C), 10 mm (E), 10 mm (I), and 100 mm (M).

Figure 6- RAF-like kinases mediate auxin posphoresponse across land plant species

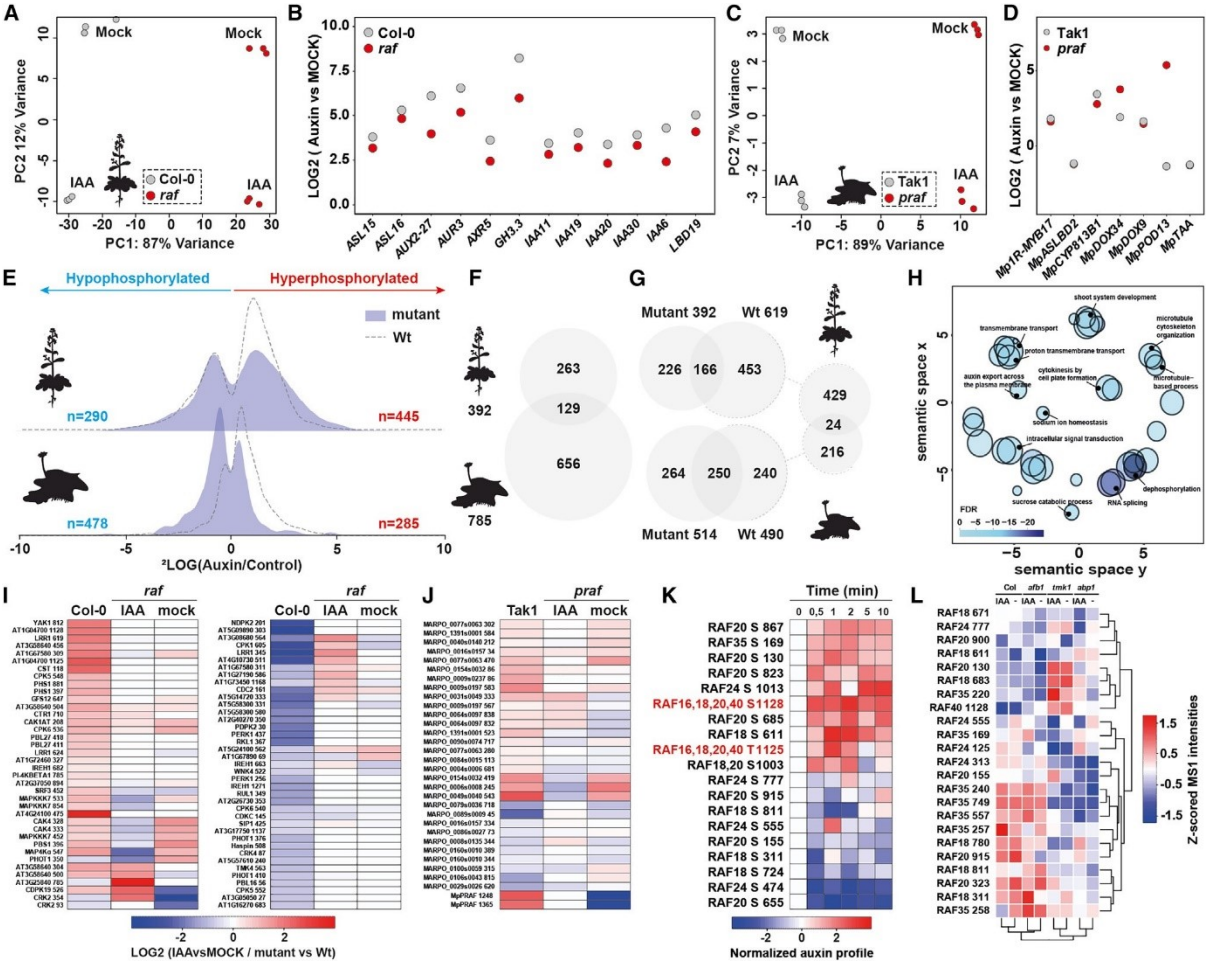

Figure 2.2-6 RAF-like kinases mediate auxin posphoresponse across land plant species

(A–D) RNA-seq analysis on wild type (Arabidopsis Col-0; Marchantia Tak-1) and raf (Arabidopsis, roots) and praf (Marchantia, gemmae) mutants treated with mock control or 1 mM IAA for 1 h. (A and C) PCA plots and (B and D) expression levels of individual, auxin-regulated genes.
(E) Distribution histograms of significant differential phosphosites (FDR % 0.05) comparing 2 min of 100 nM IAA (auxin) treatment with mock treatment in wild type (dashed lines) and (p)raf mutant (solid area) in Arabidopsis roots (top) and Marchantia gemmae (bottom). Number of differential phosphosites is indicated. (F) Venn diagrams indicating orthogroup overlap of differential phosphosites (FDR % 0.05) in (p)raf mutants in Arabidopsis and Marchantia compared with respective wild types under mock condition. (G) Venn diagrams indicating orthogroup overlap of differential phosphosites (FDR % 0.05) in (p)raf mutants and wild types in Arabidopsis and Marchantia under IAA-treated conditions.(H) Gene ontology analysis on the overlapping and conserved auxin- and (P)RAF-dependent proteins.
(I and J) Heatmap showing differential phosphorylation in Arabidopsis (I) and Marchantia (J) (p)raf null mutants of all kinases that are auxin-regulated in wild type. (K) Heatmap showing phosphorylation profiles, normalized to the t = 0 time point, of Arabidopsis RAF kinases. Profiles marked in red are phosphosites located in the activation loop.
(L) Z scored MS1 intensities off all measured phosphosites of Arabidopsis RAF kinases in wild type, afb1-3, tmk1-1, and abp1-TD1 mutants with or without IAA.

Figure 7- RAF-like kinases link phospho-response to a fast auxin response

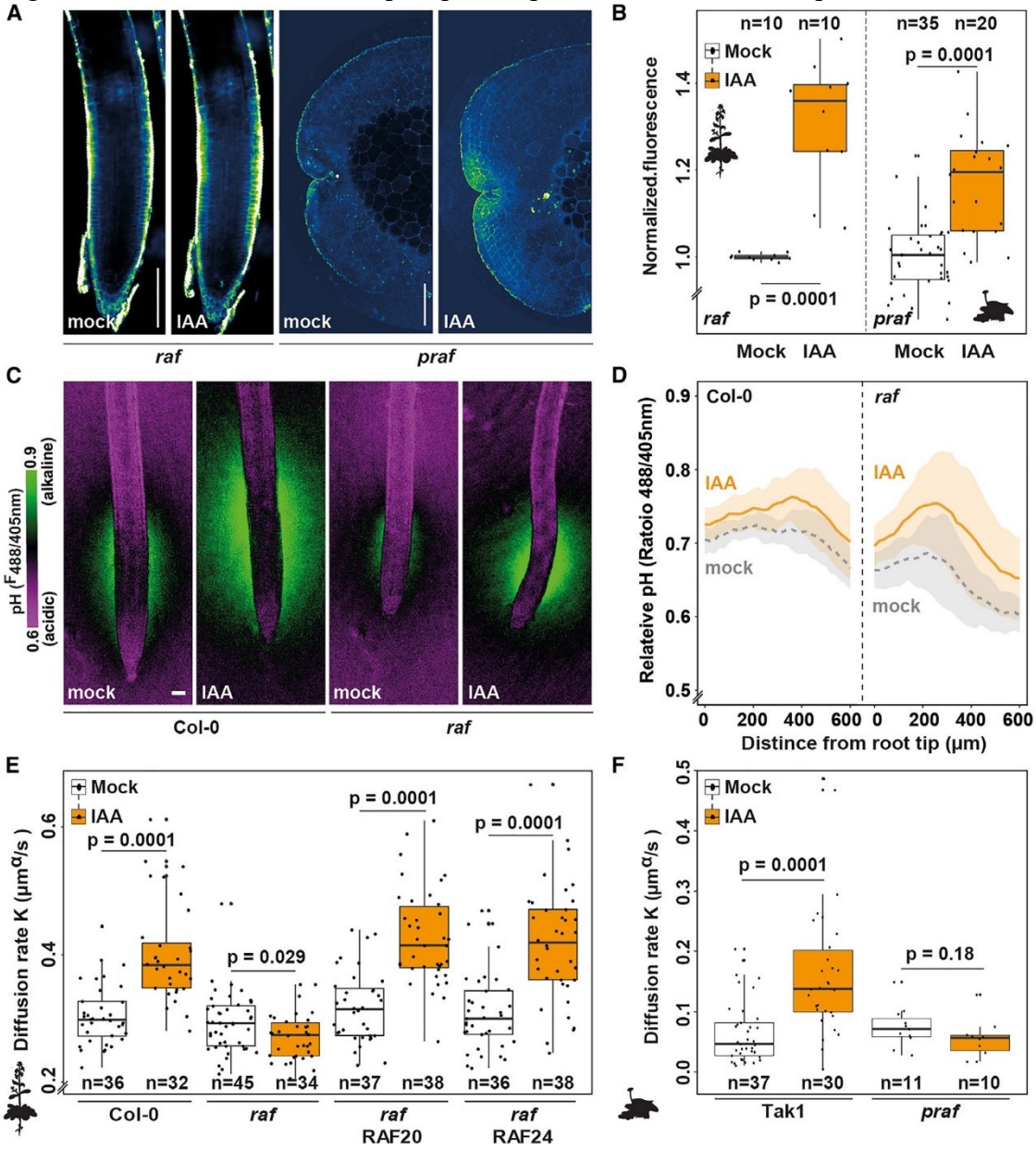

Figure 2.2-7 RAF-like kinases link phospho-response to a fast auxin response

(A and B) (A) Representative images and (B) quantification of membrane depolarization measured using DISBAC2(3) fluorescence in control (mock) and IAAtreated Arabidopsis raf mutant roots and Marchantia praf mutant rhizoid initial cells. Note that roots in (A) are the same before and after IAA treatment, and gemmae are different ones with and without IAA. Wild types for (B) are in Figure 2A. Quantification is normalized DISBAC2(3) fluorescence (IAA/mock). (C and D) (C) Arabidopsis wild type (Col-0; n = 12 roots) and raf mutant (n = 11 roots) root surface pH visualized using the ratiometric pH-sensitive FS dye treated with mock or 100 nM IAA and (D) quantification of the F488/405 nm fluorescence emission ratio along the root surface. Shaded areas represent standard deviations. (E and F) Cytoplasmic streaming in mock and IAA-treated root epidermis cells in Arabidopsis wild type (Col-0), raf null mutants, and raf mutant complemented with RAF20 or RAF24 transgenes (E) and Marchantia praf mutant and wild-type (Tak-1) rhizoid cells (note: the same wild-type data are shown in Figure 1F). Displayed is the diffusion rate K (mma/s). Boxplots are shown along individual measurements, number of observations (n) is indicated, and significance (Student's t test) is shown. Scale bars are 100 mm (A) and 50 mm (C)

Figure S1- Characterization of cytoplasmic streaming, related to Figure 1

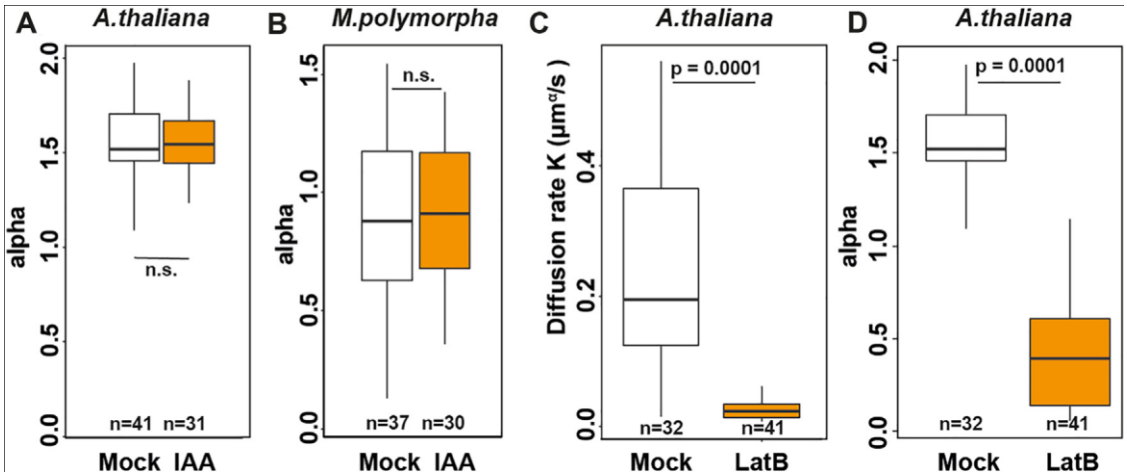

Figure 2.2-8 Characterization of cytoplasmic streaming, related to Figure 1

(A and B) (A) Quantification of the diffusive component (a) of cytoplasmic streaming in wild-type Arabidopsis roots and (B) Marchantia rhizoid cells with and without auxin treatment.
(C and D) Diffusion rate (K; C) and diffusive exponent (a; D) of cytoplasmic streaming in wild-type Arabidopsis roots treated with mock medium or latrunculin B.
Boxplots are shown along individual measurements, number of observations (n) is indicated, and significance (Student's t test) is shown.

Figure S2- Comparative analysis of auxin-triggered changes in phosphoproteomes across species, related to Figure 2

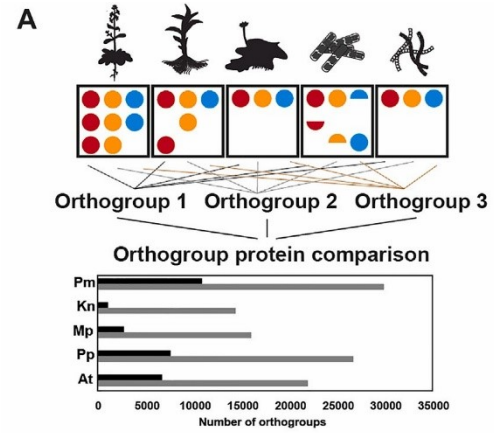

B

Orthogroup	ATG code	Description
OG0000102	AT1G08720	Serine/threonine-protein kinase EDR1
OG0000257	AT1G06070	bZIP transcription factor
OG0000323	AT1G07350	Serine/arginine-rich splicing factor SR45a
OG0000502	AT2G16640	Translocase of chloroplast 132
OG0000557	AT1G23860	Serine/arginine-rich splicing factor RSZ21
OG0000647	AT3G45780	Phototropin-1
OG0001209	AT3G60240	Eukaryotic translation initiation factor 4G
OG0001903	AT1G13020	Eukaryotic translation initiation factor 4B2
OG0002206	AT1G21160	Eukaryotic translation initiation factor 5B
OG0002707	AT3G48860	Coiled-coil domain-containing protein SCD2
OG0003358	AT1G13950	Eukaryotic translation initiation factor 5A-1

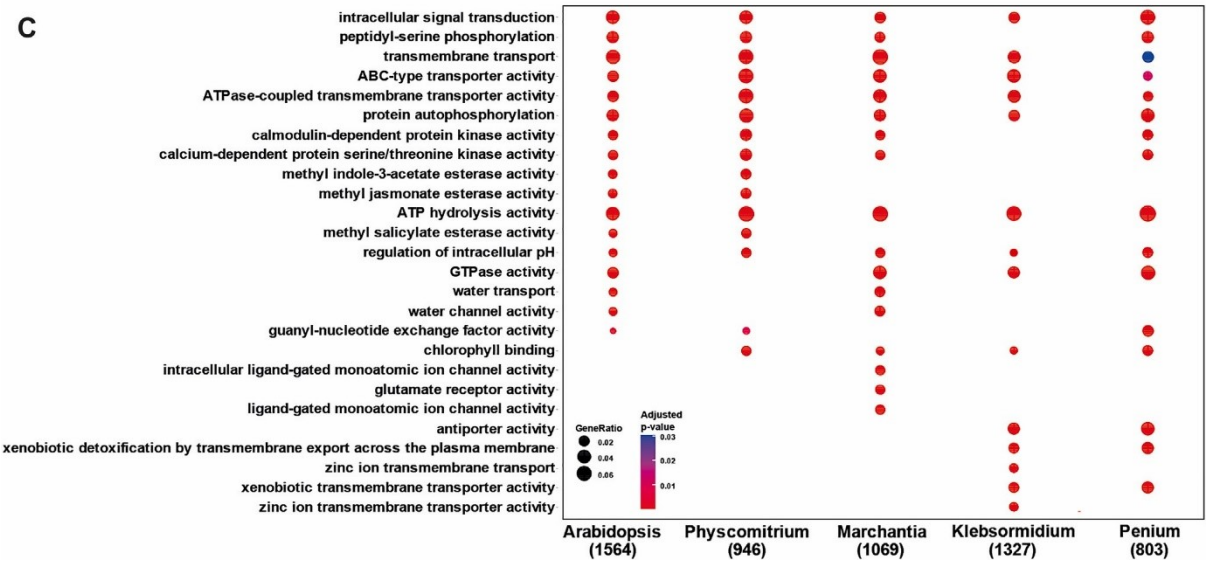

Figure 2.2-9 Comparative analysis of auxin-triggered changes in phosphoproteomes across species, related to Figure 2

(A) Strategy for orthogroup construction based on protein sequence across the 5 species used here (top). The lower panel shows the number proteins in shared(black) and unique (gray) orthogroups in each species. (B) List of the 11 orthogroups shared between all species, alongside ATG code of an Arabidopsis member in each orthogroup and its functional description. (C) GO-term analysis of FDR significant orthogroups of all species tested identified in phosphoproteomics.

Figure S3- Specificity and dynamics of auxin-triggered phosphor-response, related to Figure3

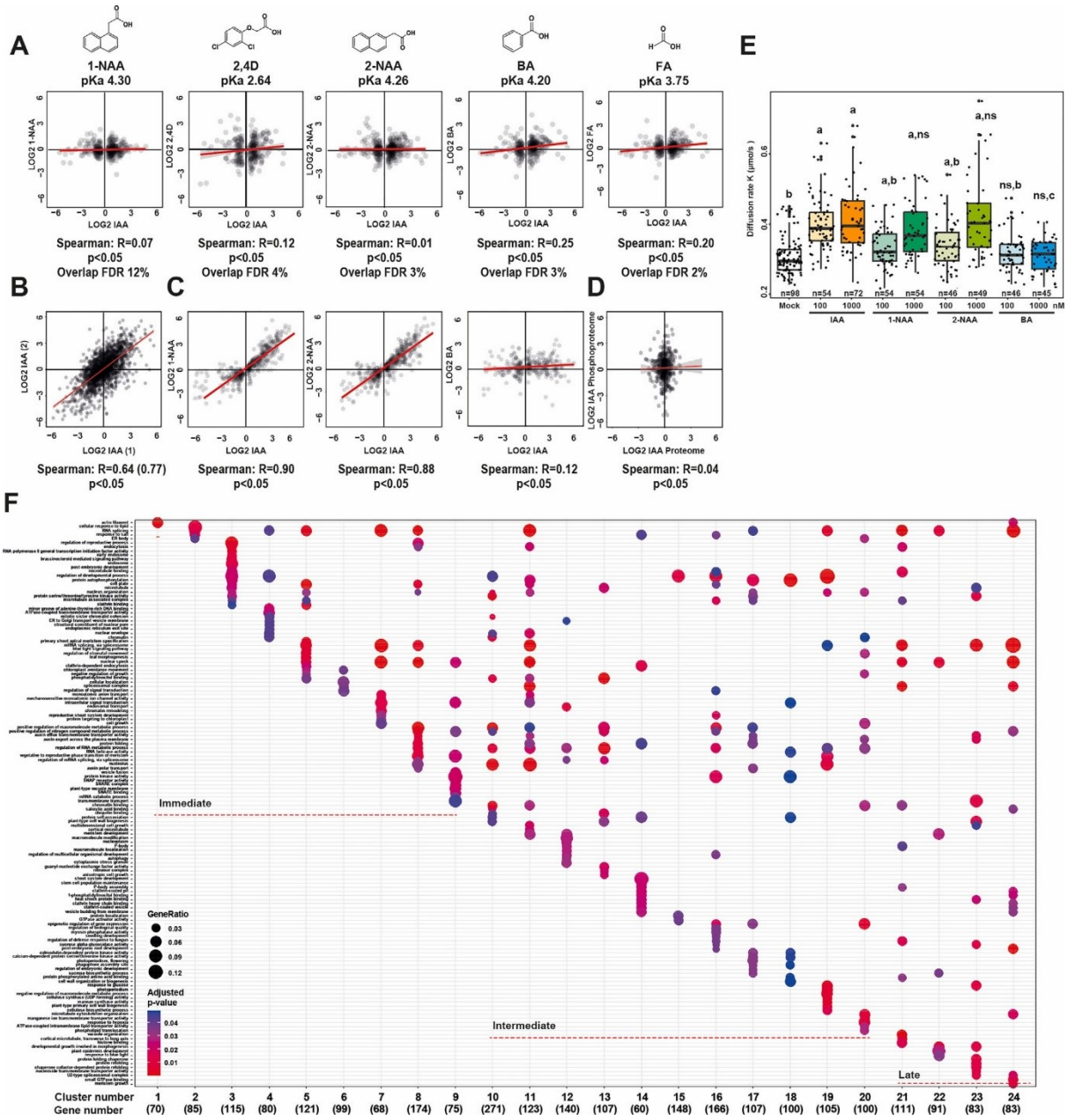

Figure 2.2-10 Specificity and dynamics of auxin-triggered phosphor-response, related to Figure3

(A) Plots comparing differential phosphosites (FDR ≤0.05) in 2 minutes 100 nM IAA treatment (x-axes) with fold-change of corresponding phosphosites in similar treatments with other compounds. Structures and pKa values are given for each compound. Red line indicates regression line (with confidence interval in grey), and Spearman correlation value is indicated in each plot. (B) Correlation plot of two independent IAA phosphoproteome experiments. Spearman correlation of all sites is 0.64 while it is 0.77 when considering only differential sites at FDR≤0.05. (C) Plots comparing differential phosphosites (FDR ≤0.05) in 2 minutes 100 nM IAA treatment (x-axes) with fold-change of corresponding phosphosites in 2 minutes treatment of 1 µM of other compounds. Structures and pKa values are given for each compound. Red line indicates regression line (with confidence interval in grey), and Spearman correlation value is indicated in each plot. (D) Correlation between fold-changes in IAA-trigged shotgun proteome (x-axis) and phosphoproteome (y-axis) both treated with 100 nM IAA for 2 minutes. Red line is regression line with confidence interval (grey). (E) GO-term analysis of each cluster identified in Figure 3C.

Figure S4- Inferred kinase-substrate network, related to Figure 4

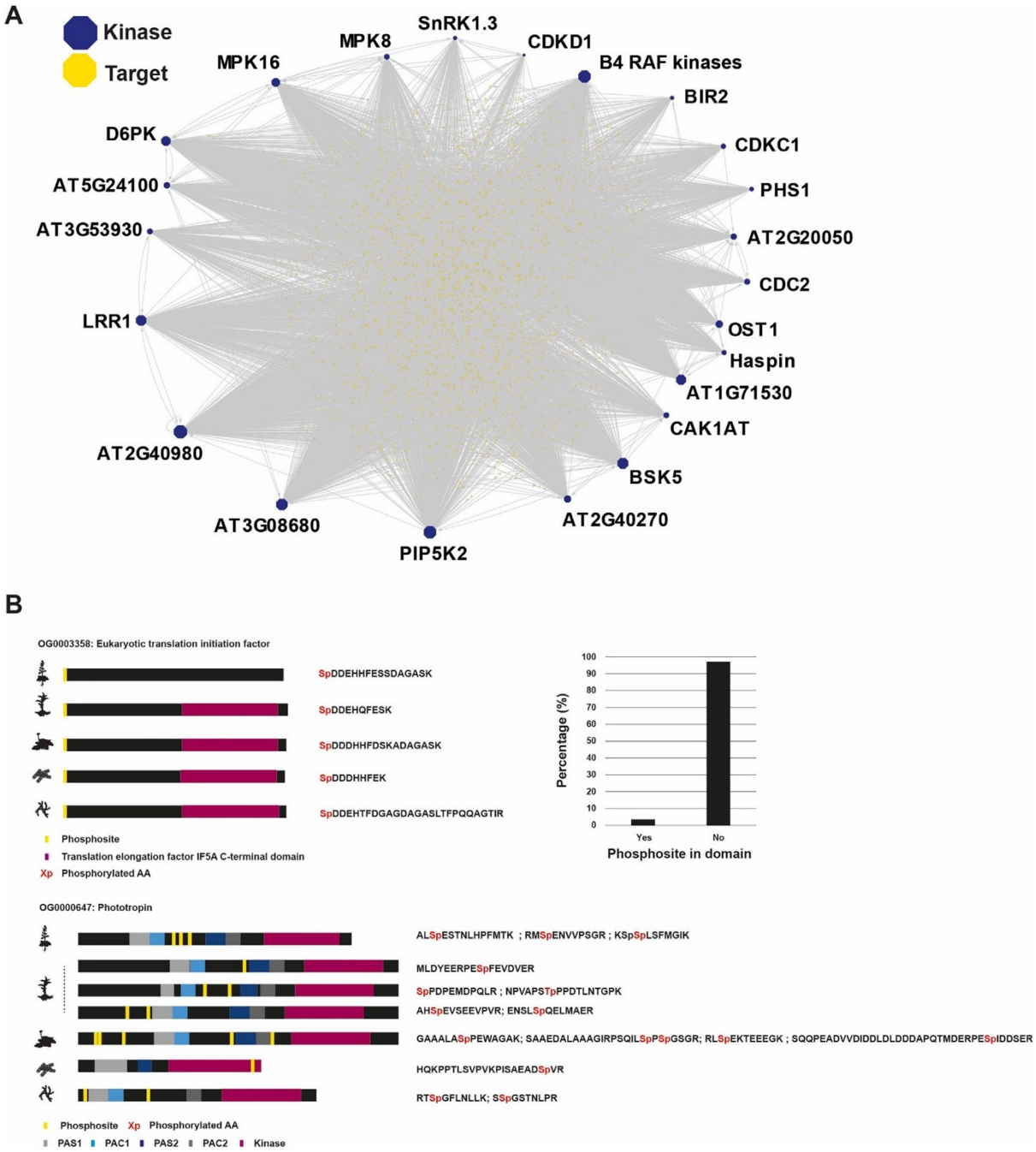

Figure 2.2-11 Inferred kinase-substrate network, related to Figure 4

(A) Kinase network of the 23 identified kinases with phosphoregulation in their activation loop. Kinases are depicted in blue, whereas substrates are depicted in yellow. Sizes of hexagons are based on degree. (B) Comparison of the location and sequence of phosphosites among phospho-targets conserved in all species tested. Displayed are the domain structures of theproteins and the position of the phosphosites within the protein of two examples (left). The posphopeptide sequence is shown, and the phosphorylated amino acid is highlighted (middle). Quantification of the fraction of phosphosites located in a domain or not is given for all phosphosites in conserved phospho-targets (right).

Figure S5- Phenotypic analysis of raf mutants in Arabidopsis and Marchantia, related to Figure 5

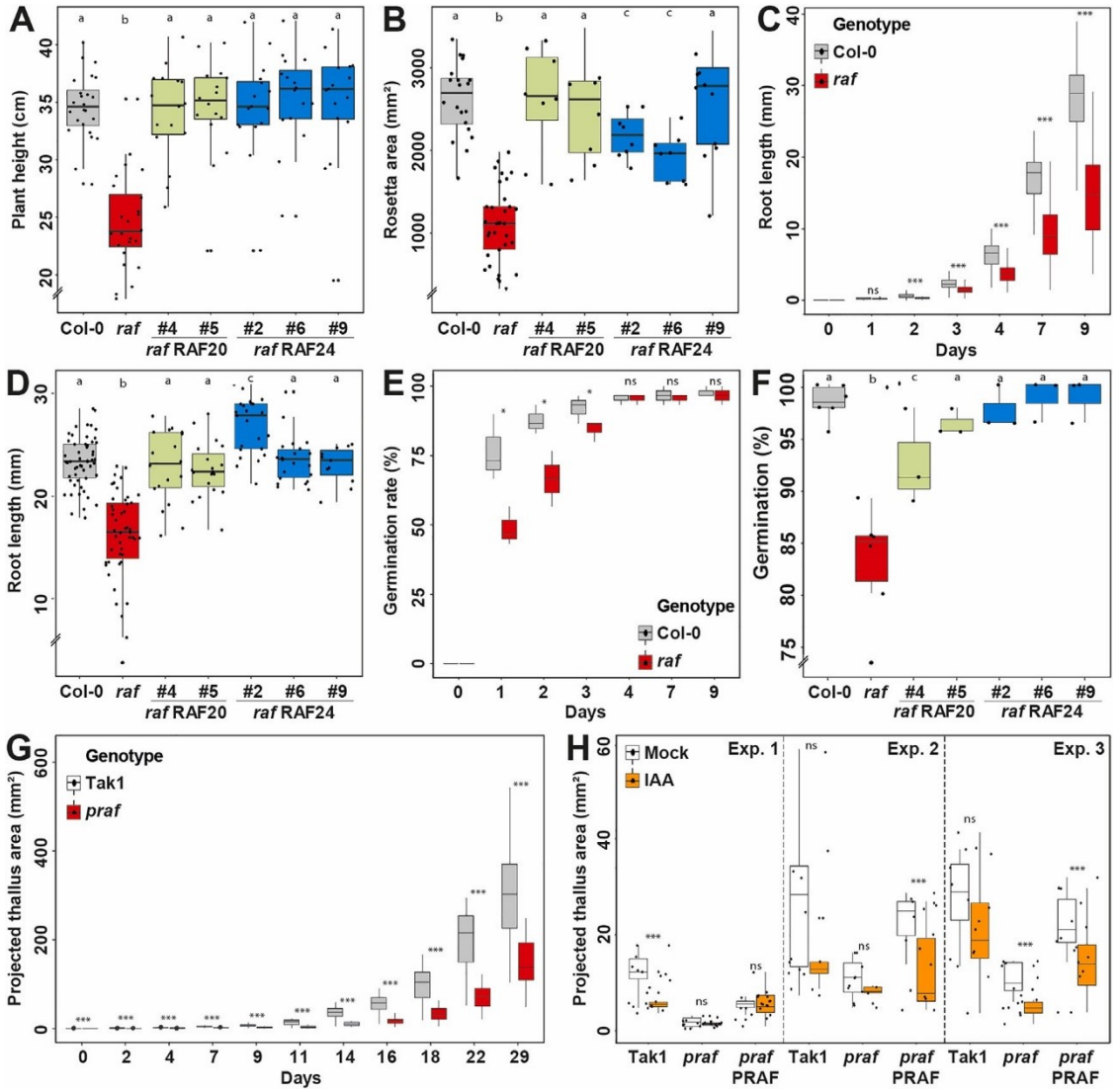

Figure 2.2-12 Phenotypic analysis of raf mutants in Arabidopsis and Marchantia, related to Figure 5

(A–F) Characterization of phenotypes related to growth and development in Arabidopsis wild type (Col-0), raf mutant, and complemented raf mutant (with RAF20 of RAF24 transgene; multiple independent lines each) and (G) in Marchantia wild type (Tak1) and praf mutant. (A) Flowering plant height, (B) rosette area, (C) root length followed over 9 days in wild type and mutant and at 7 days in all genotypes (D). (E) Germination rate over 9 days in wild type and mutant and after 3 days in all genotypes (F). (G) Projected thallus area in wild-type and mutant Marchantia thallus, followed over 29 days. (H) Quantification of IAA-induced thallus growth inhibition in wild-type Marchantia (Tak1), praf mutant, and praf mutant complemented with PRAF transgene, across three independent experiments. (A, B, D, F, and H) Boxplots are shown along individual measurements and (A, B, D, and F) significance (Student's t test) is shown, ''a'' indicates no significant difference to mutant, ''b'' indicates significant difference to wild type, and ''c'' indicates significant difference to both wild type and mutant ($p < 0.001$, ns, not significant). (C, E, and G) Boxplots are shown along individual measurements, and significance (Student's t test) is shown (*** $p < 0.001$). (H) Significance (Student's t test) is shown to corresponding 0 nM IAA treatment (*** $p < 0.001$, ** $p < 0.01$, * $p < 0.05$, ns, not significant).

Figure S6- Analysis of raf mutant phosphoproteomes, related to Figure 6

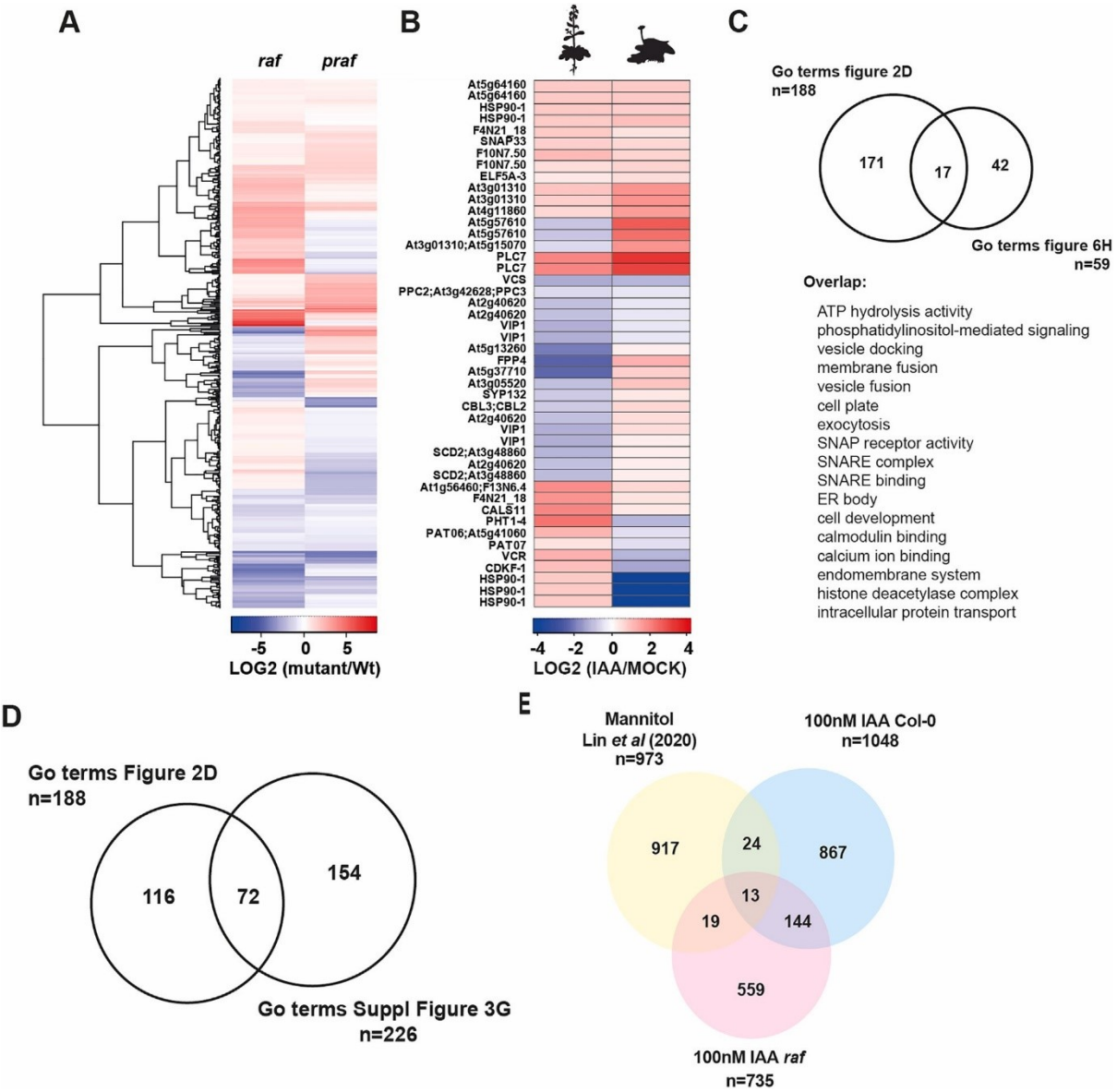

Figure 2.2-13 Analysis of raf mutant phosphoproteomes, related to Figure 6

(A) Overlap of potential RAF targets in Arabidopsis and Marchantia, based on differential phosphorylation in raf and praf phosphoproteomes under mock conditions, compared with wild types.
(B) Differential phosphorylation patterns upon IAA treatment in wild-type Arabidopsis and Marchantia (2 min) of orthologous proteins commonly dependent onRAF in both species. Note that some orthogroups contain more than one member in Arabidopsis.
(C) Venn diagram showing the overlap between GO-terms enriched for land plants, bryophytes, and algae (Figure 2D) and GO-terms enriched for overlapping and conserved auxin- and (P)RAF-dependent phosphorylated proteins (Figure 6H). The list shows the overlapping GO terms.
(D) Venn diagram displaying the overlap between GO-terms enriched for land plants, bryophytes, and algae (Figure 2D) and GO-terms enriched for all clusters of the time series (Figures 3C and S3G). The description of overlapping GO terms can be found in Data S1.
(E) Venn diagram showing overlap between phosphosites differentially regulated (%0.05) in mannitol-treated Arabidopsis plants, 100 nM IAA treated Col-0 and 100 nM treated raf mutant.

Figure S7- RAF-like kinases link rapid phospho-response to fast auxin responses, related to Figure 7

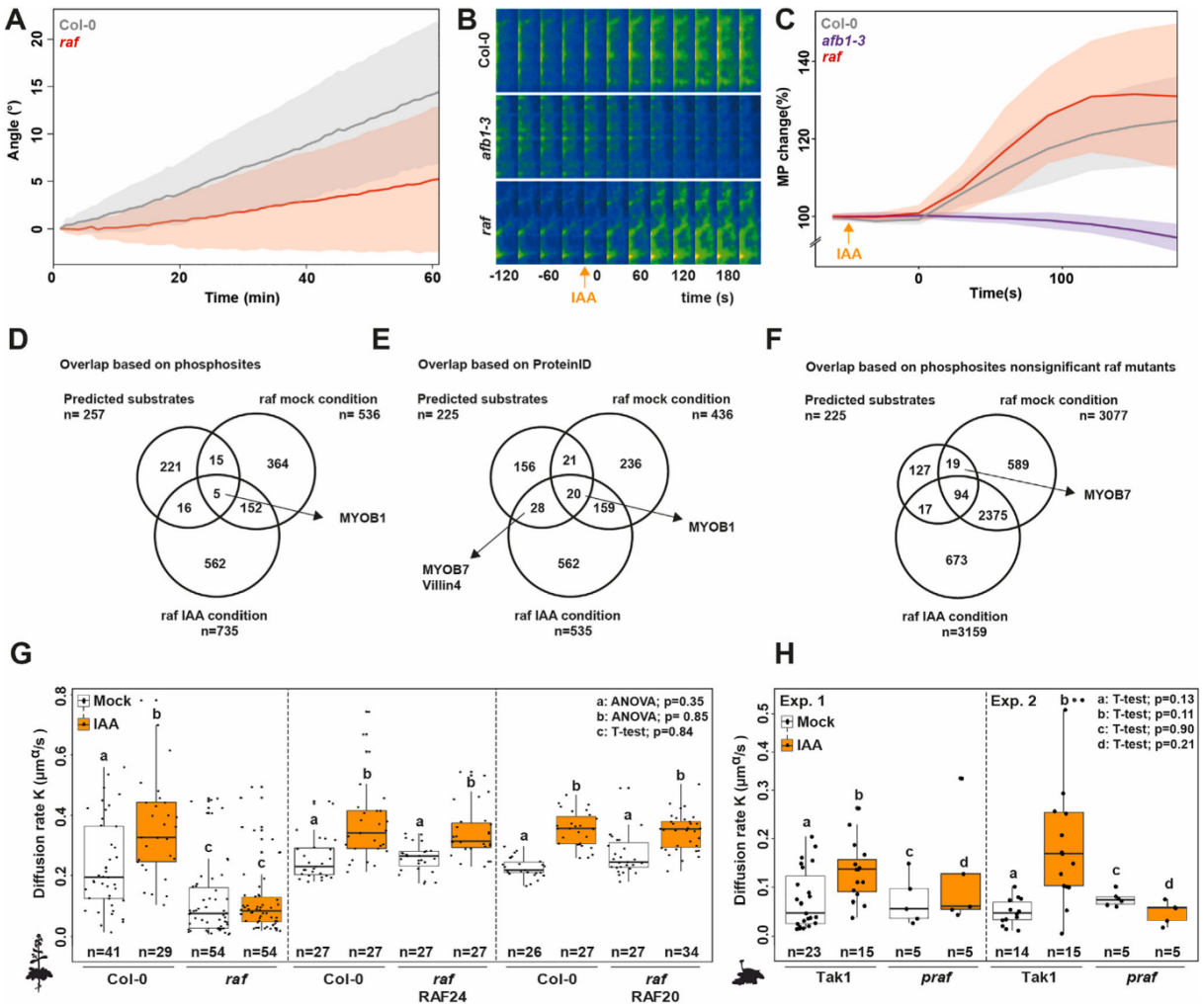

Figure 2.2-14 RAF-like kinases link rapid phospho-response to fast auxin responses, related to Figure 7

(A) Angle of root tip bending of Arabidopsis wild type (Col-0) and raf mutant seedlings after gravitropic stimulation over time. Solid lines show average, and shaded areas confidence intervals across 26–28 roots for each genotype.
(B and C) (B) Representative images and (C) quantification of changes in of DISBAC2(3) fluorescence intensity in the elongation zone of roots from wild type (Col-0), afb1-3, and raf mutant before and after IAA treatment. Solid lines show average, and shaded areas confidence intervals across 10 roots for each genotype. (D–F) Venn diagrams showing overlap between predicted RAF-substate phosphosites (D) or phosphoproteins (E and F) and (D) phosphosites or (E) phosphoproteins differentially regulated (%0.05), and (F) all proteins detected but not significantly enriched in raf mutants under mock of IAA conditions.
(G and H) Cytoplasmic streaming in mock and mock- or IAA-treated root epidermal cells in Arabidopsis wild type (Col-0), raf mutants, and raf mutant complemented with RAF20 or RAF24 transgenes (G) and Marchantia wild-type (Tak1, H) and praf mutant rhizoid cells. Displayed is the diffusion rate K (mm^a/s). Boxplots are shown along individual measurements, number of observations (n) is indicated, and significance (Student's t test or ANOVA) is shown. Dashed lines indicated independent experiments (note that for E, a selection of the data has been compiled and shown in Figures 1 and 7).

2.2.8 References

1. Friml, J. (2022). Fourteen Stations of Auxin. Cold Spring Harb Perspect Biol *14*, a039859. 10.1101/cshperspect.a039859.
2. Friml, J., Wiśniewska, J., Benková, E., Mendgen, K., and Palme, K. (2002). Lateral relocation of auxin efflux regulator PIN3 mediates tropism in Arabidopsis. Nature *415*, 806–809. 10.1038/415806a.
3. Tao, Y., Ferrer, J.-L., Ljung, K., Pojer, F., Hong, F., Long, J.A., Li, L., Moreno, J.E., Bowman, M.E., Ivans, L.J., et al. (2008). Rapid Synthesis of Auxin via a New Tryptophan-Dependent Pathway Is Required for Shade Avoidance in Plants. Cell *133*, 164–176. 10.1016/j.cell.2008.01.049.
4. Went, F.W., and Thimann, K.V. (1937). Phytohormones (MacMillan Company).
5. Went, F.W. (1928). Wuchsstoff und Wachstum. Recueil des travaux botaniques néerlandais *25*, 1–116.
6. Sessions, R.A., and Zambryski, P.C. (1995). Arabidopsis gynoecium structure in the wild and in ettin mutants. Development *121*, 1519–1532. 10.1242/dev.121.5.1519.
7. Nemhauser, J.L., Feldman, L.J., and Zambryski, P.C. (2000). Auxin and ETTIN in Arabidopsis gynoecium morphogenesis. Development *127*, 3877–3888. 10.1242/dev.127.18.3877.
8. Scarpella, E., Marcos, D., Friml, J., and Berleth, T. (2006). Control of leaf vascular patterning by polar auxin transport. Genes Dev *20*, 1015–1027. 10.1101/gad.1402406.
9. De Rybel, B., Adibi, M., Breda, A.S., Wendrich, J.R., Smit, M.E., Novák, O., Yamaguchi, N., Yoshida, S., Van Isterdael, G., Palovaara, J., et al. (2014). Integration of growth and patterning during vascular tissue formation in *Arabidopsis*. Science (1979) *345*. 10.1126/science.1255215.
10. Morffy, N., and Strader, L.C. (2020). Old Town Roads: routes of auxin biosynthesis across kingdoms. Curr Opin Plant Biol *55*, 21–27. 10.1016/j.pbi.2020.02.002.
11. Mutte, S.K., Kato, H., Rothfels, C., Melkonian, M., Wong, G.K.-S., and Weijers, D. (2018). Origin and evolution of the nuclear auxin response system. Elife *7*. 10.7554/eLife.33399.
12. JIN, Q., SCHERP, P., HEIMANN, K., and HASENSTEIN, K. (2008). Auxin and cytoskeletal organization in algae. Cell Biol Int *32*, 542–545. 10.1016/j.cellbi.2007.11.005.
13. Park, W.-K., Yoo, G., Moon, M., Kim, C.W., Choi, Y.-E., and Yang, J.-W. (2013). Phytohormone Supplementation Significantly Increases Growth of Chlamydomonas reinhardtii Cultivated for Biodiesel Production. Appl Biochem Biotechnol *171*, 1128–1142. 10.1007/s12010-013-0386-9.
14. Vance, B.D. (1987). Phytohormone effects on cell division inChlorella pyrenoidosa chick (TX-7-11-05) (chlorellaceae). J Plant Growth Regul *5*, 169–173. 10.1007/BF02087185.
15. Etherton, B. (1970). Effect of Indole-3-acetic Acid on Membrane Potentials of Oat Coleoptile Cells. Plant Physiol *45*, 527–528. 10.1104/pp.45.4.527.
16. Bates, G.W., and Goldsmith, M.H.M. (1983). Rapid response of the plasma-membrane potential in oat coleoptiles to auxin and other weak acids. Planta *159*, 231–237. 10.1007/BF00397530.
17. Serre, N.B.C., Kralík, D., Yun, P., Slouka, Z., Shabala, S., and Fendrych, M. (2021). AFB1 controls rapid auxin signalling through membrane depolarization in Arabidopsis thaliana root. Nat Plants *7*, 1229–1238. 10.1038/s41477-021-00969-z.
18. Friml, J., Gallei, M., Gelová, Z., Johnson, A., Mazur, E., Monzer, A., Rodriguez, L., Roosjen, M., Verstraeten, I., Živanović, B.D., et al. (2022). ABP1–TMK auxin

perception for global phosphorylation and auxin canalization. Nature *609*, 575–581. 10.1038/s41586-022-05187-x.

19. Ayling, S., and Clarkson, D. (1996). The Cytoplasmic Streaming Response of Tomato Root Hairs to Auxin; the Role of Calcium. Functional Plant Biology *23*, 699. 10.1071/PP9960699.
20. Monshausen, G.B., Miller, N.D., Murphy, A.S., and Gilroy, S. (2011). Dynamics of auxin-dependent Ca2+ and pH signaling in root growth revealed by integrating high-resolution imaging with automated computer vision-based analysis. The Plant Journal *65*, 309–318. 10.1111/j.1365-313X.2010.04423.x.
21. Barbez, E., Dünser, K., Gaidora, A., Lendl, T., and Busch, W. (2017). Auxin steers root cell expansion via apoplastic pH regulation in *Arabidopsis thaliana*. Proceedings of the National Academy of Sciences *114*. 10.1073/pnas.1613499114.
22. Shih, H.-W., DePew, C.L., Miller, N.D., and Monshausen, G.B. (2015). The Cyclic Nucleotide-Gated Channel CNGC14 Regulates Root Gravitropism in Arabidopsis thaliana. Current Biology *25*, 3119–3125. 10.1016/j.cub.2015.10.025.
23. Li, L., Verstraeten, I., Roosjen, M., Takahashi, K., Rodriguez, L., Merrin, J., Chen, J., Shabala, L., Smet, W., Ren, H., et al. (2021). Cell surface and intracellular auxin signalling for H+ fluxes in root growth. Nature *599*, 273–277. 10.1038/s41586-021-04037-6.
24. Senn, A.P., and Goldsmith, M.H.M. (1988). Regulation of Electrogenic Proton Pumping by Auxin and Fusicoccin as Related to the Growth of *Avena* Coleoptiles. Plant Physiol *88*, 131–138. 10.1104/pp.88.1.131.
25. Arieti, R.S., and Staiger, C.J. (2020). Auxin-induced actin cytoskeleton rearrangements require AUX1. New Phytologist *226*, 441–459. 10.1111/nph.16382.
26. Narasimhan, M., Gallei, M., Tan, S., Johnson, A., Verstraeten, I., Li, L., Rodriguez, L., Han, H., Himschoot, E., Wang, R., et al. (2021). Systematic analysis of specific and nonspecific auxin effects on endocytosis and trafficking. Plant Physiol *186*, 1122–1142. 10.1093/plphys/kiab134.
27. Heisler, M.G., Ohno, C., Das, P., Sieber, P., Reddy, G. V., Long, J.A., and Meyerowitz, E.M. (2005). Patterns of Auxin Transport and Gene Expression during Primordium Development Revealed by Live Imaging of the Arabidopsis Inflorescence Meristem. Current Biology *15*, 1899–1911. 10.1016/j.cub.2005.09.052.
28. Dubrovsky, J.G., Sauer, M., Napsucialy-Mendivil, S., Ivanchenko, M.G., Friml, J., Shishkova, S., Celenza, J., and Benková, E. (2008). Auxin acts as a local morphogenetic trigger to specify lateral root founder cells. Proceedings of the National Academy of Sciences *105*, 8790–8794. 10.1073/pnas.0712307105.
29. Reinhardt, D., Pesce, E.-R., Stieger, P., Mandel, T., Baltensperger, K., Bennett, M., Traas, J., Friml, J., and Kuhlemeier, C. (2003). Regulation of phyllotaxis by polar auxin transport. Nature *426*, 255–260. 10.1038/nature02081.
30. Thimann, K. V. (1938). HORMONES AND THE ANALYSIS OF GROWTH. Plant Physiol *13*, 437–449. 10.1104/pp.13.3.437.
31. Kepinski, S., and Leyser, O. (2005). The Arabidopsis F-box protein TIR1 is an auxin receptor. Nature *435*, 446–451. 10.1038/nature03542.
32. Dharmasiri, N., Dharmasiri, S., and Estelle, M. (2005). The F-box protein TIR1 is an auxin receptor. Nature *435*, 441–445. 10.1038/nature03543.
33. Tan, X., Calderon-Villalobos, L.I.A., Sharon, M., Zheng, C., Robinson, C. V., Estelle, M., and Zheng, N. (2007). Mechanism of auxin perception by the TIR1 ubiquitin ligase. Nature *446*, 640–645. 10.1038/nature05731.

34. Gray, W.M., Kepinski, S., Rouse, D., Leyser, O., and Estelle, M. (2001). Auxin regulates SCFTIR1-dependent degradation of AUX/IAA proteins. Nature *414*, 271–276. 10.1038/35104500.
35. Kim, J., Harter, K., and Theologis, A. (1997). Protein–protein interactions among the Aux/IAA proteins. Proceedings of the National Academy of Sciences *94*, 11786–11791. 10.1073/pnas.94.22.11786.
36. Weijers, D., and Wagner, D. (2016). Transcriptional Responses to the Auxin Hormone. Annu Rev Plant Biol *67*, 539–574. 10.1146/annurev-arplant-043015-112122.
37. Prigge, M.J., Platre, M., Kadakia, N., Zhang, Y., Greenham, K., Szutu, W., Pandey, B.K., Bhosale, R.A., Bennett, M.J., Busch, W., et al. (2020). Genetic analysis of the Arabidopsis TIR1/AFB auxin receptors reveals both overlapping and specialized functions. Elife *9*. 10.7554/eLife.54740.
38. Hamann, T., Benkova, E., Bäurle, I., Kientz, M., and Jürgens, G. (2002). The *Arabidopsis BODENLOS* gene encodes an auxin response protein inhibiting MONOPTEROS-mediated embryo patterning. Genes Dev *16*, 1610–1615. 10.1101/gad.229402.
39. Hardtke, C.S., and Berleth, T. (1998). The Arabidopsis gene MONOPTEROS encodes a transcription factor mediating embryo axis formation and vascular development. EMBO J *17*, 1405–1411. https://doi.org/10.1093/emboj/17.5.1405.
40. Kato, H., Mutte, S.K., Suzuki, H., Crespo, I., Das, S., Radoeva, T., Fontana, M., Yoshitake, Y., Hainiwa, E., van den Berg, W., et al. (2020). Design principles of a minimal auxin response system. Nat Plants *6*, 473–482. 10.1038/s41477-020-0662-y.
41. Abel, S., and Theologis, A. (1996). Early Genes and Auxin Action. Plant Physiol *111*, 9–17. 10.1104/pp.111.1.9.
42. McClure, B.A., Hagen, G., Brown, C.S., Gee, M.A., and Guilfoyle, T.J. (1989). Transcription, organization, and sequence of an auxin-regulated gene cluster in soybean. Plant Cell *1*, 229–239. 10.1105/tpc.1.2.229.
43. Fendrych, M., Akhmanova, M., Merrin, J., Glanc, M., Hagihara, S., Takahashi, K., Uchida, N., Torii, K.U., and Friml, J. (2018). Rapid and reversible root growth inhibition by TIR1 auxin signalling. Nat Plants *4*, 453–459. 10.1038/s41477-018-0190-1.
44. Dindas, J., Scherzer, S., Roelfsema, M.R.G., von Meyer, K., Müller, H.M., Al-Rasheid, K.A.S., Palme, K., Dietrich, P., Becker, D., Bennett, M.J., et al. (2018). AUX1-mediated root hair auxin influx governs SCFTIR1/AFB-type Ca2+ signaling. Nat Commun *9*, 1174. 10.1038/s41467-018-03582-5.
45. Jin, J., and Pawson, T. (2012). Modular evolution of phosphorylation-based signalling systems. Philosophical Transactions of the Royal Society B: Biological Sciences *367*, 2540–2555. 10.1098/rstb.2012.0106.
46. Nurnberger, T., Brunner, F., Kemmerling, B., and Piater, L. (2004). Innate immunity in plants and animals: striking similarities and obvious differences. Immunol Rev *198*, 249–266. 10.1111/j.0105-2896.2004.0119.x.
47. Couto, D., and Zipfel, C. (2016). Regulation of pattern recognition receptor signalling in plants. Nat Rev Immunol *16*, 537–552. 10.1038/nri.2016.77.
48. Oyama, M., Kozuka-Hata, H., Tasaki, S., Semba, K., Hattori, S., Sugano, S., Inoue, J., and Yamamoto, T. (2009). Temporal Perturbation of Tyrosine Phosphoproteome Dynamics Reveals the System-wide Regulatory Networks. Molecular & Cellular Proteomics *8*, 226–231. 10.1074/mcp.M800186-MCP200.

49. Humphrey, S.J., Azimifar, S.B., and Mann, M. (2015). High-throughput phosphoproteomics reveals in vivo insulin signaling dynamics. Nat Biotechnol *33*, 990–995. 10.1038/nbt.3327.
50. Kinoshita, T., Caño-Delgado, A., Seto, H., Hiranuma, S., Fujioka, S., Yoshida, S., and Chory, J. (2005). Binding of brassinosteroids to the extracellular domain of plant receptor kinase BRI1. Nature *433*, 167–171. 10.1038/nature03227.
51. Wang, X., Kota, U., He, K., Blackburn, K., Li, J., Goshe, M.B., Huber, S.C., and Clouse, S.D. (2008). Sequential Transphosphorylation of the BRI1/BAK1 Receptor Kinase Complex Impacts Early Events in Brassinosteroid Signaling. Dev Cell *15*, 220–235. 10.1016/j.devcel.2008.06.011.
52. Ryu, H., Kim, K., Cho, H., Park, J., Choe, S., and Hwang, I. (2007). Nucleocytoplasmic Shuttling of BZR1 Mediated by Phosphorylation Is Essential in *Arabidopsis* Brassinosteroid Signaling. Plant Cell *19*, 2749–2762. 10.1105/tpc.107.053728.
53. Carrillo-Carrasco, V.P., Hernandez-Garcia, J., Mutte, S.K., and Weijers, D. (2023). The birth of a giant: evolutionary insights into the origin of auxin responses in plants. EMBO J *42*. 10.15252/embj.2022113018.
54. Ren, H., Park, M.Y., Spartz, A.K., Wong, J.H., and Gray, W.M. (2018). A subset of plasma membrane-localized PP2C.D phosphatases negatively regulate SAUR-mediated cell expansion in Arabidopsis. PLoS Genet *14*, e1007455. 10.1371/journal.pgen.1007455.
55. Takahashi, K., Hayashi, K., and Kinoshita, T. (2012). Auxin Activates the Plasma Membrane H+-ATPase by Phosphorylation during Hypocotyl Elongation in Arabidopsis . Plant Physiol *159*, 632–641. 10.1104/pp.112.196428.
56. Renier, M., Tamanini, A., Nicolis, E., Rolfini, R., Imler, J.-L., Pavirani, A., and Cabrini, G. (1995). Use of a Membrane Potential-Sensitive Probe to Assess Biological Expression of the Cystic Fibrosis Transmembrane Conductance Regulator. Hum Gene Ther *6*, 1275–1283. 10.1089/hum.1995.6.10-1275.
57. Tominaga, M., and Ito, K. (2015). The molecular mechanism and physiological role of cytoplasmic streaming. Curr Opin Plant Biol *27*, 104–110. 10.1016/j.pbi.2015.06.017.
58. Metzler, R., Jeon, J.-H., Cherstvy, A.G., and Barkai, E. (2014). Anomalous diffusion models and their properties: non-stationarity, non-ergodicity, and ageing at the centenary of single particle tracking. Phys. Chem. Chem. Phys. *16*, 24128–24164. 10.1039/C4CP03465A.
59. Regner, B.M., Vučinić, D., Domnisoru, C., Bartol, T.M., Hetzer, M.W., Tartakovsky, D.M., and Sejnowski, T.J. (2013). Anomalous Diffusion of Single Particles in Cytoplasm. Biophys J *104*, 1652–1660. 10.1016/j.bpj.2013.01.049.
60. Yoon, H.S., Hackett, J.D., Ciniglia, C., Pinto, G., and Bhattacharya, D. (2004). A Molecular Timeline for the Origin of Photosynthetic Eukaryotes. Mol Biol Evol *21*, 809–818. 10.1093/molbev/msh075.
61. Leebens-Mack, J.H., Barker, M.S., Carpenter, E.J., Deyholos, M.K., Gitzendanner, M.A., Graham, S.W., Grosse, I., Li, Z., Melkonian, M., Mirarab, S., et al. (2019). One thousand plant transcriptomes and the phylogenomics of green plants. Nature *574*, 679–685. 10.1038/s41586-019-1693-2.
62. Jiao, C., Sørensen, I., Sun, X., Sun, H., Behar, H., Alseekh, S., Philippe, G., Palacio Lopez, K., Sun, L., Reed, R., et al. (2020). The Penium margaritaceum Genome: Hallmarks of the Origins of Land Plants. Cell *181*, 1097-1111.e12. 10.1016/j.cell.2020.04.019.

63. Kaur, S., Peters, T.J., Yang, P., Luu, L.D.W., Vuong, J., Krycer, J.R., and O'Donoghue, S.I. (2020). Temporal ordering of omics and multiomic events inferred from time-series data. NPJ Syst Biol Appl *6*, 22. 10.1038/s41540-020-0141-0.
64. Montes, C., Wang, P., Liao, C., Nolan, T.M., Song, G., Clark, N.M., Elmore, J.M., Guo, H., Bassham, D.C., Yin, Y., et al. (2022). Integration of multi-omics data reveals interplay between brassinosteroid and Target of Rapamycin Complex signaling in Arabidopsis. New Phytologist *236*, 893–910. 10.1111/nph.18404.
65. Weller, B., Zourelidou, M., Frank, L., Barbosa, I.C.R., Fastner, A., Richter, S., Jürgens, G., Hammes, U.Z., and Schwechheimer, C. (2017). Dynamic PIN-FORMED auxin efflux carrier phosphorylation at the plasma membrane controls auxin efflux-dependent growth. Proceedings of the National Academy of Sciences *114*. 10.1073/pnas.1614380114.
66. Songyang, Z., Lu, K.P., Kwon, Y.T., Tsai, L.H., Filhol, O., Cochet, C., Brickey, D.A., Soderling, T.R., Bartleson, C., Graves, D.J., et al. (1996). A structural basis for substrate specificities of protein Ser/Thr kinases: primary sequence preference of casein kinases I and II, NIMA, phosphorylase kinase, calmodulin-dependent kinase II, CDK5, and Erk1. Mol Cell Biol *16*, 6486–6493. 10.1128/MCB.16.11.6486.
67. Lewis, T.S., Shapiro, P.S., and Ahn, N.G. (1998). Signal Transduction through MAP Kinase Cascades. In, pp. 49–139. 10.1016/S0065-230X(08)60765-4.
68. (Kazuya Ichimura et al.), M.G., Ichimura, K., Shinozaki, K., Tena, G., Sheen, J., Henry, Y., Champion, A., Kreis, M., Zhang, S., Hirt, H., et al. (2002). Mitogen-activated protein kinase cascades in plants: a new nomenclature. Trends Plant Sci *7*, 301–308. 10.1016/S1360-1385(02)02302-6.
69. Shahzad, Z., Canut, M., Tournaire-Roux, C., Martinière, A., Boursiac, Y., Loudet, O., and Maurel, C. (2016). A Potassium-Dependent Oxygen Sensing Pathway Regulates Plant Root Hydraulics. Cell *167*, 87-98.e14. 10.1016/j.cell.2016.08.068.
70. Lin, Z., Li, Y., Zhang, Z., Liu, X., Hsu, C.-C., Du, Y., Sang, T., Zhu, C., Wang, Y., Satheesh, V., et al. (2020). A RAF-SnRK2 kinase cascade mediates early osmotic stress signaling in higher plants. Nat Commun *11*, 613. 10.1038/s41467-020-14477-9.
71. Koide, E., Suetsugu, N., Iwano, M., Gotoh, E., Nomura, Y., Stolze, S.C., Nakagami, H., Kohchi, T., and Nishihama, R. (2020). Regulation of Photosynthetic Carbohydrate Metabolism by a Raf-Like Kinase in the Liverwort Marchantia polymorpha. Plant Cell Physiol *61*, 631–643. 10.1093/pcp/pcz232.
72. Bowman, J.L., Kohchi, T., Yamato, K.T., Jenkins, J., Shu, S., Ishizaki, K., Yamaoka, S., Nishihama, R., Nakamura, Y., Berger, F., et al. (2017). Insights into Land Plant Evolution Garnered from the Marchantia polymorpha Genome. Cell *171*, 287-304.e15. https://doi.org/10.1016/j.cell.2017.09.030.
73. Bienz, M. (2014). Signalosome assembly by domains undergoing dynamic head-to-tail polymerization. Trends Biochem Sci *39*, 487–495. 10.1016/j.tibs.2014.08.006.
74. Benková, E., Michniewicz, M., Sauer, M., Teichmann, T., Seifertová, D., Jürgens, G., and Friml, J. (2003). Local, Efflux-Dependent Auxin Gradients as a Common Module for Plant Organ Formation. Cell *115*, 591–602. 10.1016/S0092-8674(03)00924-3.
75. Flores-Sandoval, E., Eklund, D.M., and Bowman, J.L. (2015). A Simple Auxin Transcriptional Response System Regulates Multiple Morphogenetic Processes in the Liverwort Marchantia polymorpha. PLoS Genet *11*, e1005207. 10.1371/journal.pgen.1005207.
76. Gelová, Z., Gallei, M., Pernisová, M., Brunoud, G., Zhang, X., Glanc, M., Li, L., Michalko, J., Pavlovičová, Z., Verstraeten, I., et al. (2021). Developmental roles of

Auxin Binding Protein 1 in Arabidopsis thaliana. Plant Science *303*, 110750. 10.1016/j.plantsci.2020.110750.
77. Dai, N., Wang, W., Patterson, S.E., and Bleecker, A.B. (2013). The TMK Subfamily of Receptor-Like Kinases in Arabidopsis Display an Essential Role in Growth and a Reduced Sensitivity to Auxin. PLoS One *8*, e60990-.
78. Wang, Y., Goertz, N.J., Rillo, E., and Yang, M. (2022). Negative regulation of seed germination by maternal AFB1 and AFB5 in Arabidopsis. Biosci Rep *42*. 10.1042/BSR20221504.
79. Moscat, J., Diaz-Meco, M.T., Albert, A., and Campuzano, S. (2006). Cell Signaling and Function Organized by PB1 Domain Interactions. Mol Cell *23*, 631–640. 10.1016/j.molcel.2006.08.002.
80. Blagoev, B., Ong, S.-E., Kratchmarova, I., and Mann, M. (2004). Temporal analysis of phosphotyrosine-dependent signaling networks by quantitative proteomics. Nat Biotechnol *22*, 1139–1145. 10.1038/nbt1005.
81. Winston, B.W., Lange-Carter, C.A., Gardner, A.M., Johnson, G.L., and Riches, D.W. (1995). Tumor necrosis factor alpha rapidly activates the mitogen-activated protein kinase (MAPK) cascade in a MAPK kinase kinase-dependent, c-Raf-1-independent fashion in mouse macrophages. Proceedings of the National Academy of Sciences *92*, 1614–1618. 10.1073/pnas.92.5.1614.
82. Tominaga, M., Kimura, A., Yokota, E., Haraguchi, T., Shimmen, T., Yamamoto, K., Nakano, A., and Ito, K. (2013). Cytoplasmic Streaming Velocity as a Plant Size Determinant. Dev Cell *27*, 345–352. 10.1016/j.devcel.2013.10.005.
83. Du, M., Spalding, E.P., and Gray, W.M. (2020). Rapid Auxin-Mediated Cell Expansion. Annu Rev Plant Biol *71*, 379–402. 10.1146/annurev-arplant-073019-025907.
84. Kato, H., Ishizaki, K., Kouno, M., Shirakawa, M., Bowman, J.L., Nishihama, R., and Kohchi, T. (2015). Auxin-Mediated Transcriptional System with a Minimal Set of Components Is Critical for Morphogenesis through the Life Cycle in Marchantia polymorpha. PLoS Genet *11*, e1005084. 10.1371/journal.pgen.1005084.
85. Yu, Y., Tang, W., Lin, W., Li, W., Zhou, X., Li, Y., Chen, R., Zheng, R., Qin, G., Cao, W., et al. (2022). ABLs and TMKs are co-receptors for extracellular auxin. bioRxiv, 2022.11.28.518138. 10.1101/2022.11.28.518138.
86. Khuri, S., Bakker, F.T., and Dunwell, J.M. (2001). Phylogeny, Function, and Evolution of the Cupins, a Structurally Conserved, Functionally Diverse Superfamily of Proteins. Mol Biol Evol *18*, 593–605. 10.1093/oxfordjournals.molbev.a003840.
87. Murashige, T., and Skoog, F. (1962). A revised medium for rapid growth and bio assays with tobacco tissue cultures. Physiol Plant *15*, 473–497.
88. Gao, Y., Zhang, Y., Zhang, D., Dai, X., Estelle, M., and Zhao, Y. (2015). Auxin binding protein 1 (ABP1) is not required for either auxin signaling or *Arabidopsis* development. Proceedings of the National Academy of Sciences *112*, 2275–2280. 10.1073/pnas.1500365112.
89. Savaldi-Goldstein, S., Baiga, T.J., Pojer, F., Dabi, T., Butterfield, C., Parry, G., Santner, A., Dharmasiri, N., Tao, Y., Estelle, M., et al. (2008). New auxin analogs with growth-promoting effects in intact plants reveal a chemical strategy to improve hormone delivery. Proceedings of the National Academy of Sciences *105*, 15190–15195. 10.1073/pnas.0806324105.
90. Gamborg, O.L., Miller, R.A., and Ojima, K. (1968). Nutrient requirements of suspension cultures of soybean root cells. Exp Cell Res *50*, 151–158. 10.1016/0014-4827(68)90403-5.

91. Cove, D.J., Perroud, P.-F., Charron, A.J., McDaniel, S.F., Khandelwal, A., and Quatrano, R.S. (2009). Culturing the Moss Physcomitrella patens. Cold Spring Harb Protoc *2009*, pdb.prot5136. 10.1101/pdb.prot5136.
92. Domozych, D.S., Sørensen, I., Popper, Z.A., Ochs, J., Andreas, A., Fangel, J.U., Pielach, A., Sacks, C., Brechka, H., Ruisi-Besares, P., et al. (2014). Pectin Metabolism and Assembly in the Cell Wall of the Charophyte Green Alga Penium margaritaceum. Plant Physiol *165*, 105–118. 10.1104/pp.114.236257.
93. de Rybel, B., van den Berg, W., Lokerse, A.S., Liao, C.-Y., van Mourik, H., Möller, B., Llavata-Peris, C.I., and Weijers, D. (2011). A Versatile Set of Ligation-Independent Cloning Vectors for Functional Studies in Plants. Plant Physiol *156*, 1292–1299. 10.1104/pp.111.177337.
94. Ishizaki, K., Nishihama, R., Ueda, M., Inoue, K., Ishida, S., Nishimura, Y., Shikanai, T., and Kohchi, T. (2015). Development of Gateway Binary Vector Series with Four Different Selection Markers for the Liverwort Marchantia polymorpha. PLoS One *10*, e0138876. 10.1371/journal.pone.0138876.
95. KUBOTA, A., ISHIZAKI, K., HOSAKA, M., and KOHCHI, T. (2013). Efficient *Agrobacterium* -Mediated Transformation of the Liverwort *Marchantia polymorpha* Using Regenerating Thalli. Biosci Biotechnol Biochem *77*, 167–172. 10.1271/bbb.120700.
96. Tyanova, S., Temu, T., Sinitcyn, P., Carlson, A., Hein, M.Y., Geiger, T., Mann, M., and Cox, J. (2016). The Perseus computational platform for comprehensive analysis of (prote)omics data. Nat Methods *13*, 731–740. 10.1038/nmeth.3901.
97. Sherman, B.T., Hao, M., Qiu, J., Jiao, X., Baseler, M.W., Lane, H.C., Imamichi, T., and Chang, W. (2022). DAVID: a web server for functional enrichment analysis and functional annotation of gene lists (2021 update). Nucleic Acids Res *50*, W216–W221. 10.1093/nar/gkac194.
98. Huang, D.W., Sherman, B.T., and Lempicki, R.A. (2009). Systematic and integrative analysis of large gene lists using DAVID bioinformatics resources. Nat Protoc *4*, 44–57. 10.1038/nprot.2008.211.
99. Supek, F., Bošnjak, M., Škunca, N., and Šmuc, T. (2011). REVIGO Summarizes and Visualizes Long Lists of Gene Ontology Terms. PLoS One *6*, e21800. 10.1371/journal.pone.0021800.
100. Perez-Riverol, Y., Bai, J., Bandla, C., García-Seisdedos, D., Hewapathirana, S., Kamatchinathan, S., Kundu, D.J., Prakash, A., Frericks-Zipper, A., Eisenacher, M., et al. (2022). The PRIDE database resources in 2022: a hub for mass spectrometry-based proteomics evidences. Nucleic Acids Res *50*, D543–D552. 10.1093/nar/gkab1038.
101. Emms, D.M., and Kelly, S. (2019). OrthoFinder: phylogenetic orthology inference for comparative genomics. Genome Biol *20*, 238. 10.1186/s13059-019-1832-y.
102. Gao, Y., and Kilfoil, M.L. (2009). Accurate detection and complete tracking of large populations of features in three dimensions. Opt Express *17*, 4685. 10.1364/OE.17.004685.
103. Serre, N.B., Wernerova, D., Vittal, P., Dubey, S.M., Medvecka, E., Jelinkova, A., Petrasek, J., Grossmann, G., and Fendrych, M. (2022). The AUX1-AFB1-CNGC14 module establishes longitudinal root surface pH profile. bioRxiv.
104. Cheng, C., Krishnakumar, V., Chan, A.P., Thibaud-Nissen, F., Schobel, S., and Town, C.D. (2017). Araport11: a complete reannotation of the *Arabidopsis thaliana* reference genome. The Plant Journal *89*, 789–804. 10.1111/tpj.13415.
105. Montgomery, S.A., Tanizawa, Y., Galik, B., Wang, N., Ito, T., Mochizuki, T., Akimcheva, S., Bowman, J.L., Cognat, V., Maréchal-Drouard, L., et al. (2020).

Chromatin Organization in Early Land Plants Reveals an Ancestral Association between H3K27me3, Transposons, and Constitutive Heterochromatin. Current Biology *30*, 573-588.e7. 10.1016/j.cub.2019.12.015.

106. Kim, D., Langmead, B., and Salzberg, S.L. (2015). HISAT: a fast spliced aligner with low memory requirements. Nat Methods *12*, 357–360. 10.1038/nmeth.3317.
107. Li, H., Handsaker, B., Wysoker, A., Fennell, T., Ruan, J., Homer, N., Marth, G., Abecasis, G., and Durbin, R. (2009). The Sequence Alignment/Map format and SAMtools. Bioinformatics *25*, 2078–2079. 10.1093/bioinformatics/btp352.
108. Liao, Y., Smyth, G.K., and Shi, W. (2014). featureCounts: an efficient general purpose program for assigning sequence reads to genomic features. Bioinformatics *30*, 923–930. 10.1093/bioinformatics/btt656.
109. Love, M.I., Huber, W., and Anders, S. (2014). Moderated estimation of fold change and dispersion for RNA-seq data with DESeq2. Genome Biol *15*, 550. 10.1186/s13059-014-0550-8.

2.3 Chapter three: ABP1/ABL3-TMK1 cell-surface auxin signaling directly targets PIN2-mediated auxin fluxes for root gravitropism

Adapted and modified from:

Rodriguez L, Fiedler L, Zou M, Giannini C, **Monzer A,** et al. ABP1/ABL3-TMK1 cell-surface auxin signaling directly targets PIN2-mediated auxin fluxes for root gravitropism. Published online November 30, 2022. doi:10.1101/2022.11.30.518503

In the previous chapters, we established that the ABP1-TMK1 pathway mediates auxin-induced phosphorylation events. A key group of targets in this cascade are the PIN transporters, which are essential for directing auxin flows that drive various developmental processes. In this study, we focus on PIN2—a crucial auxin transporter in root gravitropism. We investigate how TMK1-mediated phosphorylation modulates PIN2 function, shedding light on the positive feedback between cell-surface auxin signaling and PIN-mediated transport, which reinforces auxin asymmetry during root bending.

2.3.1 Introduction

Plant developmental mechanisms differ fundamentally from those of animals. With cells encapsulated in rigid cell walls without the possibility of migration, plants mainly rely on oriented cell divisions and expansions and have the capacity to self-organize complex tissues. Being rooted in the soil, plants are also highly adapted to cope with changing environments. Much of the adaptability and self-organization is mediated by the phytohormone auxin with examples including the formation of an embryonic axis, regular arrangement of leaves and flowers, establishment of leaf vein patterns, or flexible vasculature regeneration around a wound[1]. Auxin also acts as a key endogenous signal positioning sessile plants in their environment during directional growth responses such as gravitropism and phototropism[2]. Both self-organizing development and translation of environmental signals into directional growth rely on mechanistically elusive feedback between auxin signaling and polar auxin transport[3,4]. Directional cell-to-cell auxin transport is a plant-specific mechanism[5] dependent upon plasma membrane-localized transporters[6,7]. Chief among these are AUX1/LAX importers[8] and PIN auxin exporters. The latter inhabit polarized plasma membrane domains to determine vectorial auxin fluxes through tissues[9,10]. Inside cells, auxin triggers a well-studied transcriptional pathway through predominantly nuclear TIR1/AFB receptors. This leads to developmental reprogramming[11,12] and contributes to growth regulation[13]. Historically, several auxin responses showed such rapidity that transcriptional cascades did not suffice for their explanation. While several of these were later found to also depend on TIR1/AFB receptors, other responses require extracellular (apoplastic) auxin perception[14]. This has been formalized recently as comprising AUXIN-BINDING PROTEIN1 (ABP1), ABP1-LIKEs (ABLs), and TRANSMEMBRANE KINASEs (TMKs) [ABP1/ABL-TMK] co-receptor complexes at the cell-surface[15–17].

Sensitive phospho-proteomic pipelines recently revealed that auxin triggers a global phosphorylation response via ABP1 and TMK1[17,18]. Notably, the lack of auxin-induced phosphorylation in *abp1* and *tmk1* mutants correlates with strong defects in auxin canalization[17], a mysterious process underlying self-organized plant development including regeneration of vasculature and formation of polarized auxin-transporting channels from a local auxin source. Canalization also requires TIR1/AFB receptors[19], suggesting that both

intracellular and apoplastic signaling contribute to auxin feedback regulation of PIN-dependent auxin transport. This is consistent with computational predictions exploring potential mechanism of PIN polarization by auxin feedback[20], however, no such mechanism linking auxin signaling and transport has been discovered.
Feedback between auxin and its transport has also been proposed for gravitropic root bending. Contrary to canalization, this would not involve adjustments of PIN polarity but rather the stabilization of the root-specific PIN2 transporter[21]. Among the latest novelties in the quest of plants to grow upright is evolution of fast root gravitropism, which was enabled by functional innovations in the PIN2 protein[22]. Fast gravitropism occurs through directional auxin transport from the site of gravity perception towards the elongation zone where growth response takes place. After gravity sensing in the columella at the root tip[23], auxin flux becomes redirected to the lower root side[24,25]. This initial asymmetry is then propagated by AUX1- and PIN2-mediated transport[26,27] from the root tip to the elongation zone and translated into root bending through local inhibition of cell elongation[28].
During the gravitropic response, PIN2 distribution itself becomes asymmetric with increased and decreased PIN2 stability at the lower and upper root sides, respectively[21,29]. Such lateral PIN2 gradient not only propagates but also reinforces the initial root tip auxin asymmetry, contributing to the robustness of root bending as well as to the fine-tuning of gravitropism by other hormonal cues[30]. How auxin regulates its own transport via PIN2 in the context of root gravitropism remains an outstanding question.
In search of a possible mechanism for cell-surface auxin signaling effect on auxin transport, we mined the auxin-inducible ABP1-TMK1-mediated phospho-proteome and identified enrichment of PINs with PIN2 as the main target. We find that an auxin-induced interaction of TMK1 with PIN2 and its phosphorylation are directly responsible for the PIN2 gradient that reinforces gravitropic root bending. This pathway perceives auxin through the newly identified root-expressed ABL3 receptor acting redundantly with ABP1. Our findings identify a direct mechanism for feedback regulation between auxin signaling and auxin transport.

2.3.2 Results

2.3.2.1 ABP1-TMK1 cell-surface auxin signaling induces phosphorylation of PIN auxin transporters

To identify components of feedback regulation of auxin transport downstream of ABP1-TMK1 auxin signaling, we took advantage of a rapid phospho-proteomic dataset (100 nM IAA, 2 min) recorded in roots of *Arabidopsis thaliana* (Arabidopsis) wild-type (WT) or the respective mutants[17]. We queried proteins concurrently hypo-phosphorylated in both *abp1-TD1* and *tmk1-1* mutants for molecular function using a gene ontology (GO) analysis. When partitioned by significance, the most dominant terms were rather general and included “binding” or “protein binding”. On the other hand, partitioning significant terms by effect size (fold enrichment) always recovered “auxin efflux transmembrane transporter activity” as the most strongly enriched GO term (Figure S1A and S1B). Inspection of the corresponding enriched phospho-proteins showed the presence of PINs and ABCB/ABCG transporters. We further focused on PINs as dominant auxin transporters with many established developmental roles.
There were in total nine PIN phospho-sites significantly downregulated in both *abp1-TD1* and *tmk1-1* (Figure 1A and Figure S1C). To verify the genetic specificity of these results, we examined in parallel a recent matched auxin phosphorylation dataset[18] from the mutant of the intracellular AFB1 auxin receptor[31]. Except for PIN1^{S337}, none of the ABP1-TMK1-dependent PIN phospho-sites were deregulated in *afb1-3* (Figure 1A). This suggests that auxin activates PIN phosphorylation specifically through the cell-surface ABP1-TMK1 module independently

of intracellular TIR1/AFB signaling. Two of the nine PIN phospho-sites mapped to PIN1, five to PIN2, and two to PIN3 (Figure 1A). Notably, all these targeted hydrophilic PIN loops, the expected location for post-translational modifications regulating PIN function[32]. The two PIN1 sites, PIN1^{S271} and PIN1^{S337}, were previously ascribed to shoot functions as targets of the D6PK protein kinase[33] and the MKK7-MPK6 module[34], respectively. Another previously studied phospho-site was PIN2^{S439}, which participates in root adaptation to varying nitrogen sources[35,36].

Given that cell-surface auxin signaling mutants show perturbed phospho-proteomes even under mock conditions[17,18], we next assessed auxin inducibility of these phospho-sites in WT roots. Notably, four out of five PIN2 phospho-sites strongly responded to 100 nM IAA within 30 seconds of treatment (Figure 1B). The PIN3^{S389} phospho-site showed a similar behavior. Conversely, while the auxin profile of PIN1^{S337} also significantly deviated from mock conditions, the site only underwent a delayed negative fluctuation (Figure S1D). This correlates with PIN1^{S337} not being specifically targeted by ABP1-TMK1 (Figure 1A). We also confirmed average to low evolutionary conservation of PIN1^{S337} (Figure S1E), altogether suggesting minor biological relevance of this particular site for the ABP1-TMK1 auxin phospho-response. When extending evolutionary conservation analysis to the remaining PIN phospho-sites, we observed moderate conservation of PIN1^{S271} and poor conservation of the auxin-inducible PIN3^{S389} (Figure S1E and S1F). On the other hand, four out of five PIN2 phospho-sites showed high ConSurf scores and perfect conservation in PIN2 orthologs from Arabidopsis to Gymnosperms (Figure 1C and 1D).

Given that rapid auxin phospho-response represents an ancient auxin pathway[18], we next asked whether PIN phosphorylation is conserved across the green lineage. Unlike in Arabidopsis, we found no significantly regulated PIN phospho-sites in the WT auxin phospho-proteomes (100 nM IAA, 2 min) of two bryophytes (*Physcomitrium*, *Marchantia*) and two streptophyte algae (*Penium*, *Klebsormidium*). This suggests a co-option of an ancestral auxin response for PIN phosphorylation after the divergence of Bryophyta from the green lineage, potentially already in the common ancestor of vascular plants.

These analyses identified PIN auxin transporters, particularly PIN2, as prominent targets of ultrafast ABP1-TMK1-mediated auxin phospho-response, representing a recent evolutionary innovation.

2.3.2.2 ABP1-TMK1-dependent PIN2 phospho-sites are crucial for PIN2 stability and root gravitropism

In further investigations, we focused on PIN2, as it was most extensively targeted, its phosphorylation strongly responded to auxin, and it showed remarkable conservation at the majority of its phospho-sites.

To test the physiological relevance of ABP1-TMK1-dependent PIN2 phosphorylation, we mutated the five candidate phospho-sites (Figure 2A and 2B) to either aspartate or alanine and introduced the resultant phospho-variants in the agravitropic *eir1-4* mutant[21] under the native PIN2 promoter. This yielded *PIN2::PIN2^{WT}-GFP;eir1-4* (*PIN2^{WT}-GFP*), *PIN2::PIN2$^{5\text{-}MIMIC}$-GFP;eir1-4* (*PIN2$^{5\text{-}MIMIC}$-GFP*) and *PIN2::PIN2$^{5\text{-}DEAD}$-GFP;eir1-4* (*PIN2$^{5\text{-}DEAD}$-GFP*). Given the rapidity of the auxin effect on PIN2 phosphorylation (Figure 1B), we specifically focused on early stages of gravitropic root bending. While *PIN2^{WT}-GFP* complemented *eir1-4* close to WT levels, the phospho-mimic *PIN2$^{5\text{-}MIMIC}$-GFP* provided only partial rescue (Figure 2C); an effect highly reproducible among independent lines. The phospho-dead *PIN2$^{5\text{-}DEAD}$-GFP* showed a weaker effect, which was pronounced during the first two hours of bending and then slowly dissipated (Figure 2C). Interestingly, the *PIN2$^{5\text{-}MIMIC}$-GFP* phenotype extended beyond early gravitropic stages and was apparent even 12 hours after gravistimulation (Figure S2A),

suggesting that chronic ABP1-TMK1-like phosphorylation of PIN2 strongly perturbs root gravitropism. These results collectively demonstrate the importance of ABP1-TMK1-dependent phospho-sites for the physiological function of PIN2 in root gravitropism.
Phosphorylation of PIN2 by AGC3 kinases at PIN2^{S237}, PIN2^{S258}, and PIN2^{S310} was previously established as regulating polar PIN2 localization[37]. However, the five ABP1-TMK1-dependent PIN2 phospho-sites were non-overlapping (Figure 2A). Indeed, we observed stereotypical polarity of apical PIN2 in epidermal cells and basal PIN2 in young cortical cells in our *PIN2$^{5\text{-}MIMIC}$-GFP* and *PIN2$^{5\text{-}DEAD}$-GFP* phospho-lines (Figure S2B). While the PIN2 phospho-lines showed no obvious polarity defects, we did observe significant differences in their GFP signal intensity. Despite direct comparison of independent T-DNA insertion lines being problematic due to local chromatin effects of individual insertion sites on transgene expression[38], we observed reproducible differences stronger than insertion-dependent variation when selecting T1 transformants and these were also apparent in independent, single-insert, GFP-positive T3 lines (Figure 2D). The *PIN2$^{5\text{-}DEAD}$-GFP* variants showed a highly consistent strong destabilization compared to *PIN2^{WT}-GFP* roots. On the other hand, *PIN2$^{5\text{-}MIMIC}$-GFP* showed increased stability compared to *PIN2^{WT}-GFP* (Figure 2D). This latter effect was less pronounced and less consistent across many independent lines, albeit still significant (Figure 2E).
Altogether, our results show that ABP1-TMK1-dependent PIN2 phospho-sites are relevant for steady-state PIN2 stability and root gravitropism, suggesting a role of cell-surface auxin signaling in these processes.

2.3.2.3 Root-expressed ABL3 auxin receptor acts redundantly with ABP1 in root gravitropism

Next, we investigated the genetic basis of PIN2 phosphorylation by cell-surface auxin signaling. It recently became recognized that apoplastic auxin perception shows multi-level redundancy[39,40]. This includes a presumably abundant pool of poorly understood ABP1/ABL auxin receptors communicating with four possible TMKs, together activating global phosphorylation reprogramming of the cellular proteome[15,17,18]. Although we identified PINs as major phospho-targets of this signaling pathway (Figure 1A), the precise composition and redundancy of the upstream auxin signaling complexes remain elusive.
TMKs form a redundant family with single mutants having rather subtle phenotypes and higher-order mutants showing strong defects in growth and development[41]. To study TMK expression in roots we used global transcriptomic data and generated *TMK1::GUS*, *TMK2::GUS*, *TMK3::GUS,* and *TMK4::GUS* lines reporting the corresponding promoter activities. The dominant family member highly expressed in roots was *TMK1*, followed by *TMK3* and *TMK4* with lower expression levels (Figure S3A-D). To examine the role of TMK1 in root gravitropism, we performed sensitive phenotyping of the *tmk1-1* mutant (Figure 3A, Figure S3F, and Figure S4D). This revealed an early root-bending defect that was complemented by a *TMK1::gTMK1-GFP* construct (Figure S3F). These data support TMK1 as the dominant TMK upstream of PIN2 phosphorylation.

Unlike *tmk1-1*, the well-established *abp1* mutant lines (*abp1-C1*, *abp1-TD1*) do not show any appreciable defects in gravitropism[42]. Nevertheless, complementation of *abp1-TD1* by native expression of an auxin-binding-deficient ABP1 variant exerts a dominant negative effect on root gravitropism, indicating the existence of unknown redundant ABLs interacting with TMK1 in the root[15]. A recent report[15] described the redundant action of ABP1 with two auxin receptors, ABL1 and ABL2. The *abp1;abl1;abl2* triple mutant shows normal gravitropism, however, consistent with the predominantly shoot-specific expression of *ABL1* and *ABL2* (Figure S4A).

Sensitive gravitropic phenotyping led us to identify a T-DNA insertion knock-out of an ABL1/ABL2 paralog, which we named ABP1-LIKE 3 (ABL3). The *abl3-1* mutation phenocopied the early root gravitropism defects of *tmk1-1* but only in a double mutant constellation with either *abp1-C1* (Figure 3A and 3B) or *abp1-TD1* (Figure S4D and S4E). The double mutant phenotype was reproduced with an independent T-DNA insertion line, *abl3-2* (Figure S4F). We confirmed *ABL3* (AT4G14630) expression in the root by mining public RNAseq data and using an *ABL3::GUS* line (Figure S4A-C). The ABL3 protein encompasses 222 residues and does not harbor a KDEL endoplasmic reticulum retention sequence. Superimposition of Arabidopsis ABL3 AlphaFold2 structure with the 1-NAA-bound maize ABP1 crystal structure revealed a plausible auxin-binding cleft in AtABL3 (Figure 3C). This also highlighted that ABL3 conforms to the ancient cupin fold of ABP1[43]. Importantly, ABL3 showed perfect conservation of three metal-coordinating residues known to be indispensable for auxin binding in ABP1, ABL1, and ABL2 (Figure 3C). The sequence surrounding these residues resembled ABL1 and ABL2 more than ABP1 (Figure S4G), as expected from members of the same GLP family[16].

Next, we tested whether ABL3 binds auxin using a cellular thermal shift assay (CETSA) followed by western blotting. The natural auxin IAA conferred protection from thermal denaturation on ABL3-HA in protein extracts from Arabidopsis root protoplasts transformed with *35S::ABL3-HA* (Figure 3D). Likewise, IAA protected ABL3-6xHIS-3xFLAG (or ABL3-HF) in protein extracts from Arabidopsis seedlings stably transformed with *35S::ABL3-HF* (Figure S4H). These results qualify ABL3 as an auxin-binding protein.

To transmit signals from auxin-bound ABL3, TMK1 would be expected as an ABL3 interaction partner. Indeed, in tobacco leaves, TMK1-HA co-immunoprecipitated with ABL3-mCherry but not with anti-mCherry beads alone (Figure 3E). Reciprocally, we further confirmed this interaction in Arabidopsis root protoplasts where ABL3-HA co-immunoprecipitated with TMK1-mCherry but not with anti-mCherry beads alone (Fig. S4I).

Thus, we identified ABL3 as a root-expressed auxin-binding protein interacting with TMK1 and acting redundantly with ABP1 in root gravitropism. These observations are consistent with the notion that the cell-surface ABP1/ABL3-TMK1 module represents a root-specific pathway targeting PIN2 phosphorylation for early stages of gravitropic root bending.

2.3.2.4 **Exogenous and endogenous auxin activates TMK1 and downstream ROP signaling in roots**

Despite recent progress, the cellular and molecular readouts of cell-surface TMK1-dependent auxin signaling remain poorly established. Previous data showed that the cytoplasmic part of TMK1 harbors an ABP1-dependent phospho-site[17]. Furthermore, the TMK1 kinase domain shows a capacity to auto-phosphorylate[44], and research on other leucine-rich repeat receptor-like kinases (LRR-RLKs) suggests that phosphorylation of their cytoplasmic domains leads to LRR-RLK activation[45,46].

Therefore, we examined TMK1 phosphorylation in response to auxin. We immunoprecipitated TMK1-FLAG from auxin-treated (IAA, 10 nM, 1 hour) *TMK1::TMK1-FLAG*;*tmk1-1* roots. After confirming successful IP with an anti-FLAG antibody, we stripped and re-probed the membranes with a Phos-tag Biotin Probe that coordinates tetrahedral phosphate moieties. We observed significant induction of TMK1 phosphorylation by auxin, presumably corresponding to increased TMK1 activity (Figure 4A and S5A).

As a downstream response, we investigated the root-specific activation of small GTPases from the ROP family implicated downstream of ABP1/ABL-TMKs. Previous ROP activation assays relied extensively on ROP overexpression, used the synthetic auxin 1-NAA, and were usually performed with leaf tissue[15,47,48]. We specifically asked if the natural auxin IAA activates ROPs

in roots under non-overexpressing conditions. Immunoblotting microsomal protein extracts from auxin-treated (IAA, 5 nM, 0–120 minutes) roots with an anti-ROP6 antibody revealed auxin-induced enrichment of ROP6 in WT but not *tmk1-1* (Figure 4B and S5B). Given that membrane association is a prerequisite for ROP activation[49], enrichment in the microsomal fraction likely reports TMK1-dependent ROP6 activation by auxin. Interestingly, we also observed that auxin stabilized TMK1 itself (Figure 4A-B and S5B) but did not induce *TMK1* mRNA over time (IAA, 10 or 100 nM, 0–120 minutes: Figure S5C). Such TMK1 stabilization at the membrane might be related to the recently reported auxin-mediated TMK1 nano-clustering effect[50].

We next used an orthogonal method to study ROP activation by auxin. As usual for small GTPases, only GTP-bound (active) but not GDP-bound (inactive) ROP proteins engage in protein-protein interactions with their effectors. We purified the Cdc42/Rac-interactive binding motif (CRIB) domain of the RIC1 ROP effector from bacteria and used it to pull down active ROPs from native root protein extracts. Immunoblotting with an anti-ROP2 antibody revealed a strong auxin-induced (IAA, 100 nM, 10 minutes) ROP2 activation in WT but much weaker activation in *tmk1-1*, *abp1-C1*, or *abp1-TD1* roots (Figure 4C and S5D). This confirms that auxin activates root ROP2 through the ABP1-TMK1 module.

To test whether the above observations remain valid also when auxin levels are changed endogenously, we repeated TMK1-FLAG immunoprecipitation followed by a Phos-tag Biotin Probe blotting on gravistimulated roots. This revealed a significant increase in TMK1 phosphorylation (Figure 4D and S5E), indicating that gravistimulation activates TMK1. Accordingly, gravistimulation also induced a TMK1-dependent enrichment of ROP6 in the microsomal fraction (Figure 4E and S5F).

Overall, these data show that both exogenous and endogenous manipulations of auxin levels promote TMK1 phosphorylation and activation of downstream ROP GTPase signaling.

2.3.2.5 **Asymmetric activation of TMK1 and downstream ROP signalling in root gravitropism**

Having established auxin-induced TMK1 activation in the root (see Figure 4 and S5) and the importance of ABP1-TMK1-dependent PIN2 phosphorylation for its stability and in early gravitropic root bending (see Figure 1, 2, S1, and S2), we assessed the role of these regulations in root gravitropism.

Our experiments with native ROP activation suggested auxin-responsive ROP signaling as a suitable proxy for TMK1 activity in the root tissue (Figure 4 and S5). However, blotting-based assays do not provide sufficient spatiotemporal resolution. For this reason, we constructed an *in situ* ROP sensor by inserting (i) ROP2 and (ii) the CRIB domain of the ROP effector RIC1 on opposite ends of a circularly permuted GFP (cpGFP). The cpGFP fluorescence should decrease when activated GTP-bound ROP2 interacts with the nearby CRIB domain (Figure S6D). Expression of CRIB-cpGFP-ROP2 and ROP2-mCherry from the same cassette yielded a ratiometric ROP sensor, which we called the CpGFP ROP Activity Probe (CRAP). As expected, the 561/488 nm CRAP ratio sensitively reported auxin (IAA, 10 nM) pulses in *CRAP;WT* roots in a microfluidic root chip setup (Figure S6E).

Strikingly, within 5 minutes of gravistimulation, CRAP-expressing roots developed asymmetric signal distribution with significantly more ROP activation at the lower side of the root (Figure S6F and Figure 5A). A GDP-locked CRAP (CRIB-cpGFP-ROP2^{T20N}) failed to show this asymmetry, confirming that CRAP indeed reports ROP activation rather than e.g. local fluctuations of the cpGFP root microenvironment (Figure S6F). This identifies a novel asymmetric rapid response to gravity-induced auxin flux redirection in roots, as confirmed by the lack of CRAP asymmetry after inhibition of auxin transport by NPA (Figure S6I).

Given that auxin-induced ROP activation is TMK1-dependent (Figure 4 and S5), the gravitropic CRAP gradient likely mirrors asymmetric TMK1 activation by auxin flow from the root rip. Indeed, the *tmk1-1* mutation abolished asymmetric ROP activation in *CRAP;tmk1-1* roots (Figure 5B). These data collectively establish rapid asymmetric activation of the TMK1 kinase and downstream ROP signaling by redirection of auxin fluxes during gravitropic root bending.

2.3.2.6 Asymmetric TMK1 activation mediates PIN2 asymmetry in root gravitropism

The rapid TMK1 activation along the lower root side corresponds well with the timeframe in which auxin induces PIN2 phosphorylation through TMK1 (Figure 1B), inferring that asymmetric TMK1 activation likely results in asymmetric PIN2 phosphorylation. Given that TMK1-regulated phospho-sites mediate PIN2 stability (see Figure 2), we decided to follow the fate of PIN2-GFP in gravistimulated roots. We observed asymmetric PIN2-GFP stabilization at the lower root side, as shown before[21,29,51], and this was completely abolished in the *tmk1-1* mutant (Figure 5C and 5D).

We further assessed the role of TMK1 and its kinase activity by cloning a kinase-dead TMK1 construct carrying a mutation in the ATP-binding site and generating *UBQ10::TMK1^{K616R}-mCherry* (TMK1^{DN}) in a WT background. Notably, TMK1^{DN} expression perturbed the gravity-induced PIN2-GFP asymmetry (Figure S6G). Accordingly, it also conveyed an early defect in gravitropic root bending (Figure S6A and S6B), phenocopying the *tmk1-1* mutant (Figure 3A, S3F and S4D). The TMK1^{DN}-expressing plants showed unperturbed levels of the endogenous TMK1 protein (Figure S6C), ruling out transgene-induced silencing of the endogenous *TMK1* gene. This shows that TMK1^{DN} causes a dominant negative phenotype, underscoring the importance of TMK1 kinase activity for both, gravity-induced PIN2 asymmetry and rapid bending response.

The requirement of TMK1 for the PIN2-GFP gradient suggests that TMK1 stabilizes PIN2 to enhance PIN2-mediated auxin flux from the root tip along the lower root side. To test this, we monitored the *DR5rev::GFP* auxin response reporter, which revealed a significantly decreased gravity-induced auxin asymmetry in *tmk1-1* compared to WT (Figure 5E and 5F, Figure S6H). Accordingly, inhibition of PIN-mediated auxin transport by NPA interfered not only with CRAP-reported asymmetric TMK1 activation (Figure S6I) but also the PIN2-GFP asymmetry (Figure S6J), confirming that polar auxin transport itself contributes to asymmetric TMK1 activation and subsequent PIN2 stabilization for further asymmetric auxin flow reinforcement. Altogether, these data identify a positive feedback loop, in which, following gravistimulation, PIN2 redistributes auxin from the root tip to the lower root side, activating the TMK1 kinase, which promotes PIN2 phosphorylation and stabilization, channeling even more auxin along the lower root side and reinforcing the original gravity-induced auxin flow asymmetry.

2.3.2.7 Auxin induces TMK1 interaction with PIN2 and phosphorylation of its hydrophilic loop

Our hitherto results demonstrate a strong functional relevance of TMK1-dependent PIN2 phosphorylation during root gravitropism. Co-localization of TMK1-GFP and PIN2-mCherry expressed from native promoters suggested a possibility for their direct interaction (Figure S7A). To test this, we immunoprecipitated TMK1-FLAG from *TMK1::TMK1-FLAG;tmk1-1* roots and used an anti-PIN2 antibody for detection of native PIN2. PIN2 did not co-immunoprecipitate with TMK1-FLAG in untreated samples. On the other hand, in auxin-treated roots (IAA, 5 or 20 nM, 15 or 30 minutes), PIN2 co-immunoprecipitated with TMK1-FLAG in a time-dependent and auxin concentration-dependent manner (Figure 6A and S7B).

This suggests that auxin promotes the formation of a TMK1-PIN2 complex at the plasma membrane.
To verify the biochemical evidence for TMK1-PIN2 interaction, we performed fluorescence lifetime imaging on FRET-pair-tagged proteins (FRET-FLIM), a technique that quantitatively reports protein interactions. We introduced *35S::TMK1-GFP* and *35S::PIN2-mCherry* in Arabidopsis root protoplasts and measured the fluorescence lifetime of the GFP signal. PIN2-mCherry strongly reduced the lifetime of TMK1-GFP, demonstrating an interaction between TMK1 and PIN2 (Figure 6B). Notably, a truncated $TMK1^{\Delta KD}$-GFP variant without a kinase domain caused a significant ~35 % drop in the interaction strength compared to TMK1-GFP. The interaction of an unrelated receptor-like kinase FLS2-GFP with PIN2-mCherry was ~60 % weaker than that of TMK1-GFP (Figure 6B and S7C). These results establish both the contribution of the TMK1 kinase domain and the specificity of the TMK1-PIN2 interaction.
An auxin-induced TMK1-PIN2 interaction provides a plausible mechanism for the TMK1-dependent PIN2 phosphorylation observed in phospho-proteomic data (Figure 1 and S1). To test this, we performed an *in vitro* phosphorylation assay with ^{32}P-ATP as a phosphate donor. We incubated a purified N-terminally HIS-tagged PIN2 hydrophilic loop (HIS-PIN2-HL) with TMK1-3HA immunoprecipitated from a root protein extract. The results showed that intact TMK1-3HA but not the kinase-dead version $TMK1^{K616R}$-3HA was able to phosphorylate HIS-PIN2-HL (Figure 6C). We did not observe any auxin effect in this kinase assay (Figure S7D), presumably due to saturation of TMK1-3HA activity by endogenous auxin during immunoprecipitation from TMK1-3HA roots.
Taken together, these data demonstrate that the receptor-like kinase TMK1 interacts, in an auxin-dependent manner, with the PIN2 auxin efflux carrier and phosphorylates its hydrophilic loop to stabilize it.

2.3.3 Discussion

2.3.3.1 Co-option of ancient auxin phospho-response for auxin feedback on its transport in vascular plants

Previous work indicated that while the rapid ABP1-TMK1-mediated auxin phospho-response is relevant for some rapid cellular auxin effects, specifically cytoplasmic streaming and apoplast acidification[13,17,18,52], *abp1* and *tmk* mutants also show severe phenotypes in the long-term establishment of auxin- and auxin transport-positive channels after wounding and from externally applied auxin source, leading to vasculature formation[17]. The underlying mechanism of this so-called auxin canalization is largely unclear but at its center lies feedback regulation between auxin signaling and directional auxin transport[3,4].
Here, mining of a root ABP1-TMK1 phospho-proteome revealed PIN auxin transporters as major phospho-targets of the ABP1-TMK1 cell-surface auxin perception. It follows that PIN phosphorylation by ABP1-TMK1 likely modulates directional auxin transport to delineate auxin channels for subsequent vascular differentiation and eventually other processes involving feedback regulation of auxin transport. Consistently, a 15-year-old model predicted extracellular auxin perception as a key signaling input parameter for auxin canalization[20]. Although the auxin phospho-response evolved in unicellular algae[18], we find that it began targeting PINs only after the divergence of Bryophyta from the green lineage, likely in the common ancestor of vascular plants. The ABP1-TMK1-mediated PIN phosphorylation thus represents a recent evolutionary novelty that arose through the co-option of ancient rapid auxin response, presumably to enable the formation and regeneration of vasculature.

2.3.3.2 ABP1-TMK1-mediated phosphorylation encodes PIN2 stability

Focusing on the dominant phospho-target PIN2, we report five ABP1-TMK1-dependent phospho-sites, the majority of which are induced by auxin and remarkably conserved. Strikingly, neither of these overlaps with previously published polarity-regulating PIN2 phospho-sites[37]. Indeed, both PIN2 stability and the physiological function of PIN2 in root gravitropism require ABP1-TMK1-dependent phospho-sites, implying the existence of two PIN2 phospho-codes; one for stereotypical maintenance of PIN2 polarity via AGC3 kinases[37], and the other for dynamic adjustments of PIN2 stability in response to auxin.

2.3.3.3 ABL3: Root-expressed auxin receptor acting redundantly with ABP1 in root gravitropism

Overall lack of *tmk1*-like phenotypes in *abp1* mutants, despite the strong similarity of phospho-proteomic signatures between *abp1* and *tmk1*[17], contributed to the historical controversy surrounding ABP1. Indeed, while we confirmed an early gravitropic phenotype in the *tmk1* mutant, *abp1* mutant alleles show normal root bending, as reported before[42]. Hidden genetic redundancy with distant but structurally conserved ABL proteins has been invoked to explain this discrepancy, however, the recently identified ABL1 and ABL2 show minimal expression in the root, and the *abp1;abl1;abl2* triple mutant shows normal gravitropism[15].

We identified the first root-expressed ABL protein, ABL3, through genetic redundancy with ABP1, and as an auxin binder and TMK1 interactor. Notably, ABL3 is paralogous to both ABL1 and ABL2 because they all belong to the 32-member Arabidopsis GLP family, which is distantly related to ABP1 by the ancient cupin fold[43]. ABP1 and ABL3 likely form part of an auxin-sensing complex docking on TMK1 in the root, providing a plausible model for auxin perception upstream of PIN2 phosphorylation.

While the field so far only scratched the surface of the real diversity of potential cell surface auxin receptors, this paints a picture in which specialized expression patterns of ABL auxin receptors confer specific functions on the rather ubiquitously expressed TMKs. There are likely more root-expressed ABLs awaiting discovery because *tmk1* and *abp1;abl3* mutants show a weaker phenotype than both the dominant-negative *ABP1::ABP1-5;abp1-TD1* line[15] and higher-order *tmk* mutants[53,54].

2.3.3.4 Model for TMK1-based auxin feedback on PIN2-mediated transport in root gravitropism

The PIN2 transporter evolved as a specific component of efficient root gravitropism in seed plants[22] and it is well documented that its abundance during gravistimulation becomes asymmetric with more PIN2 found at the lower root side[21,29]. This reinforces an initial auxin gradient and contributes to the robustness of root bending[30]. Nonetheless, the molecular mechanism behind this regulation has remained unknown since its discovery almost 20 years ago. Here, the wealth of our data together argues for a model encompassing auxin feedback on its transport.

A change in the gravity vector is sensed in the root columella, which establishes an initial auxin flow redirection to the lower side of the root[23]. This initial auxin asymmetry activates the TMK1 kinase specifically at the lower root side. Activated TMK1 then interacts with PIN2 in the epidermis and phosphorylates its hydrophilic loop at several conserved stability-regulating phospho-sites, leading to PIN2 stabilization in these cells. The resulting PIN2 abundance gradient further enhances auxin transport along the lower root side to the elongation zone, where it activates intracellular TIR1/AFB auxin signaling for growth inhibition and downward

root bending. This demonstrates the existence of a positive feedback loop representing the first direct molecular mechanism for auxin feedback on its transport.

2.3.4 Conclusion

We identified a mechanism for positive feedback between auxin and its own transport. It comprises the phosphorylation of PIN auxin transporters by the TMK1 kinase downstream of ABP1-mediated cell surface auxin perception. In the case of PIN2, the input for TMK1 activation likely comes from auxin perception by the ABP1 and ABL3 receptors, resulting in TMK1 autophosphorylation and activation. This triggers the formation of a TMK1-PIN2 complex leading to PIN2 phosphorylation and stabilization. Such positive feedback regulation is required in the case of PIN2 for robust asymmetric auxin fluxes during root gravitropism and in the case of PIN1 for canalization-guided flexible vascular tissue formation and regeneration[55]. The TMK-based auxin feedback regulation may represent a more general mechanism acting in various developmental contexts with different PIN transporters, thereby mediating specialized aspects of adaptive and self-organized plant growth and development. This mechanism evolved recently in vascular plants through the co-option of an ancestral auxin phospho-response from unicellular algae[18] and it likely diversified to guide the auxin-mediated development of morphologically complex plants.

2.3.5 Material and methods

Molecular cloning, plant material, and growth conditions

All mutant alleles were in the *Columbia-0* (*Col-0*) background except *abp1-TD1*, which was in *Columbia-4* (*Col-4*). The T-DNA insertion lines *eir1-4* (SALK_091142) and *tmk1-1* (SALK_016360) were previously reported[21,58], as was *abp1-C1* and *abp1-TD1*[59]. The T-DNA insertion line SAIL_441_G04, which harbors four insertions, was obtained from NASC and crossed with Col-0. Insertion-specific primers (Supplementary Table 3) were then used to out-segregate the SAILSEQ_441_G04.2 insertion in *ABL3*/AT4G14630 from SAILSEQ_441_G04.0 (AT4G09510), SAILSEQ_441_G04.1 (AT4G02930) and SAILSEQ_441_G04.3 (AT5G09590), yielding *abl3-1*. To obtain *abp1-C1;abl13-1* and *abp1-TD1;abl3-1*, we crossed the respective *abp1* mutants with *abl3-1*.

PIN2::PIN2-GFP, *DR5rev::GFP*, *TMK1::TMK1-FLAG*;*tmk1-1*, *TMK1::GUS*, *TMK2::GUS*, *TMK3::GUS*, and *TMK4::GUS* were described before[17,58,60,61]. We generated *PIN2::PIN2-GFP*;*tmk1-1* and *DR5rev::GFP*;*tmk1-1* by genetic crosses with *tmk1-1*. Shuta Asai kindly provided the *ABL3::GUS* and *35S::ABL3-6xHIS-3xFLAG* lines[62]. To generate *TMK1::TMK1-GFP* and *35S::TMK1$^{\Delta KD}$-GFP*, the *TMK1* full length or *TMK1$^{\Delta KD}$* (amino acid 1-587) genomic DNA without a stop codon were amplified from *Col-0* DNA through PCR with *TMK1-FL-B1-F* and *TMK1-FL-B2-R/TMK1-ΔKD-B2-R* primers (Supplemental Table 3), respectively. The resulting *TMK1* sequences were inserted into pDONR221 by a BP reaction. Next, for the *TMK1::TMK1-GFP* construct, *pDONR P4-P1R pTMK1*, *pDONR221 gTMK1,* and *pDONR P2R-P3 GFP*; for *35S::TMK1$^{\Delta KD}$-GFP*, *pDONR P4-P1R p35S*, *pDONR221 gTMK1$^{\Delta KD}$* and *pDONR P2R-P3 GFP* were recombined into pB7m34GW vector by a MultiSite Gateway LR reaction. To generate *UBQ10::TMK1^{K616R}-2xmCherry*, *TMK1^{K616R}noSTOP/pDONR221* was obtained by site-directed mutagenesis, amplifying *pDONR221 TMK1* with the *TMK1KD-K616F* and *TMK1KD-K616R* primer pair. *pDONR221-TMK1^{K616R}* was then recombined by LR reaction with *pDONR P4-P1R pUBQ10*[63], *pDONR P2R-P3 2xmCHERRY-4xMyc*[64] and pH7m34GW[65] to obtain *UBQ10::TMK1^{K616R}-2xmCherry* in pH7m34GW.

To clone PIN2 phospho-lines, Gibson Assembly was used to insert EGFP into the PIN2 coding sequence between Thr405 and Arg406 (according to[35]) and to assemble this fragment with an

attL sites-containing pDONR221 backbone (Supplemental Table 3), yielding *pDONR22 PIN2^{WT}-EGFP*. For 5-mimic and 5-dead constructs, we used gene synthesis (Integrated DNA Technologies, IDT) to obtain 1533-bp blocks containing EGFP and flanking PIN2 CDS sequences with Ser179, Ser183, Thr233, Ser393, Ser439 triplets mutated to either GAC (Asp, 5-mimic) or GCC (Ala, 5-dead) (Supplementary table 3). These were Gibson-Assembled with a fragment amplified from the *pDONR221 PIN2^{WT}-EGFP* plasmid (Supplementary table 3), yielding *pDONR221 PIN2$^{5\text{-}MIMIC}$-EGFP* and *pDONR221 PIN2$^{5\text{-}DEAD}$-EGFP*. Finally, the pDONR221 plasmids were recombined with pDONR-P4-P1R-pPIN2[22] into pB7m24GW.3 by a multisite LR reaction (Gateway), and the *eir1-4*[21] mutant (*pin2* null) was used for line construction.

The CRAP sensor was cloned using a combination of Gibson Assembly (NEBuilder® HiFi DNA Assembly Master Mix, E2621L) and the GreenGate approach. First, each GreenGate block was generated by fusing two PCR fragments – vector backbone and the respective CDS. ROP2 promoter fragment was subcloned into pGGA backbone fragment digested by BSAI. To obtain a non-ratiometric CRAP sensor, the following fragments were fused: pGGA-ROP2p. + pGGB-CRIB + pGGC-cpGFP + pGGD-ROP2+pGGE009(UBI10term.) + pGGF-HYG. Resulting destination vector was sequenced and used as a template for cloning the entire CRAP CDS into pGGD vector. This vector was then used in the GreenGate reaction to add the mCHERRY ratiometric control: pGGA-ROP2p + pGGB-mCHERRY-ROP2_UBI10term. + pGGC015(mCHERRY)-pGGD-CRAP-pGGE-HSP18.2term + pGGF005(HYG). ROP2-UBI10 fragment was amplified from the non-ratiometric CRAP sensor. Point mutagenesis to generate the dominant negative T20N mutation into ROP2 was performed as a single fragment Gibson Assembly with point-mutated compatible cohesive ends. The common building blocks were obtained from[66] (pGGC015, pGGE-009, pGGF005). The pGGZ001 block with exchanged bacterial selection cassette to kanamycin and pGGE-HSP18term was kindly provided by Dr. Andrea Bleckmann. The CRAP sensor was dipped into Col-0 to obtain *CRAP;WT*, which was then crossed to *tmk1-1* to obtain *CRAP;tmk1-1*.

To obtain seedlings co-expressing TMK1-GFP and PIN2-mCherry, we crossed *TMK1::TMK1-GFP;tmk1-1*[67] with *PIN2::PIN2-mCherry;eir-1-4* (kind gift by Christian Luschnig) and subsequently worked with the F1 generation.

All constructs were transformed into the *Agrobacterium tumefaciens* strain pGV3101 by electroporation and further into plants by the floral dip method. After selection for single insertions, two homozygous T3 lines were used for further work.

Arabidopsis seeds were surface-sterilized with 70% (v/v) ethanol for 20 min, followed by commercial bleach (2.5% [v/v] sodium hypochlorite) containing 0.05% (v/v) Triton X-100 for 10 min, and finally washed four times with sterile distilled water. Seed stratification was conducted in the dark at 4°C for 2 days. Unless indicated otherwise, seedlings were grown at 22°C on ½ MS plates with 1% agar and 1% sucrose, or in soil with 16h light/8h dark cycles, photoperiod at 80 to 100 mE m^{-2} sec^{-1}.

Bioinformatics

Phospho-proteomic analyses used data from[17,18]. Time-course profiles of auxin-induced phosphorylation were obtained with the AuxPhos tool (https://weijerslab.shinyapps.io/AuxPhos)[18]. Evolutionary rates for PIN1, PIN2, and PIN3 amino acids were calculated as ConSurf[68,69] conservation scores and projected on the respective AlphaFold structures for visualization. Multiple sequence alignment of PIN2 orthologs (Uniprot IDs: Q9LU77, F6GXI9, E5KGD3, A0A251QTL1, A0A1D6P5D8, Q651V6, W1PK04, B5TXD0) or ABP1/ABLs (Uniprot IDs: P33487, P13689, P94040, P94072, Q9LEA7) was done with the MUSCLE tool available from EMBL-EBI[70] and visualized in Jalview[71].

For gene ontology enrichment, the "mock ABP1-TMK1 phospho-proteome" comprised Ensembl protein IDs of proteins concurrently hypo-phosphorylated in both *abp1-TD1* and *tmk1-1* mutants under mock conditions or—in the case of the "auxin-treated ABP1-TMK1 phospho-proteome"—auxin (2 min, 100 nM IAA) conditions[17]. These were submitted to the PANTHER extension of the TAIR database[72,73] and queried for molecular function with all *Arabidopsis thaliana* proteins as a reference list. Annotation version and release date: [GO Ontology database DOI: 10.5281/zenodo.12173881 Released 2024-06-17]. Enrichment calculation was using Fisher's Exact Test with a Bonferroni correction ($p<0.05$). The resultant terms were processed in REVIGO[74] (parameters: medium list size of 0.7, clustering variables: p-value or fold enrichment, removal of obsolete GO terms, whole Uniprot reference set, SimRel semantic similarity) and visualized as treemaps with arbitrary coloring.
Plant pictograms were obtained from the Bioicons project under the MIT license. Attributions: Arabidopsis_thaliana icon by DBCLS https://togotv.dbcls.jp/en/pics.html is licensed under CC-BY 4.0 Unported https://creativecommons.org/licenses/by/4.0/. Zea_mays_cartoon icon by Daniel Carvalho https://figshare.com/authors/Plant_Illustrations/3773596 is licensed under CC-BY 4.0 Unported https://creativecommons.org/licenses/by/4.0/. DicotSeedling icon https://github.com/ginavong by Gina-Vong is licensed under CC0 https://creativecommons.org/publicdomain/zero/1.0/. The conifer branch pictogram was obtained from free-for-use Pixabay repository.
The crystal structure of maize ABP1 (PDB ID: 1LRH) was superimposed with the AlphaFold2 structure of ABL3 (Uniprot ID: Q9LEA7) with the "super" command in Pymol. Tissue-specific expression profiles for *ABL1*, *ABL2*, *ABP1*, *ABL3*, *TMK1*, *TMK2*, *TMK3* and *TMK4* were compiled using a database of ~20,000 public Arabidopsis RNAseq experiments[57].

RT-qPCR

Total RNA was prepared from max. 100mg of roots of 4-day-old seedlings according to the RNeasy Plant Mini Kit (Qiagen). cDNA was synthesized from 1µg of total mRNA using the QuantiNova Reverse Transcription Kit (Qiagen). Mutant expression analyses used four biological replicates and the samples were pipetted in three technical replicates into a 384-well plate using an automated JANUS Workstation (PerkinElmer). According to the manufacturer's instructions, 5 µL reaction volume contained 2.5 µL Luna® Universal qPCR mastermix (NEB). RT-qPCR analyses were performed using the Real-time PCR Roche Lightcycler 480 and the expression of PP2AA3 (At1G13320) was used as in[75]. For each of the evaluated genes, three different primer pairs were tested (Supplemental Table 3).

Fluorescence lifetime imaging

FRET-FLIM experiments were performed in protoplast systems isolated from Arabidopsis root cell suspension as described previously[76]. 10 µg of plasmid DNA (*TMK1-GFP, TMK1$^{\Delta KD}$-GFP, PIN2-mCherry, FLS2-GFP*) were used for protoplast transfection, followed by incubation in a sterile 24-well microtiter plate overnight in the dark at room temperature. FRET-FLIM experiments were performed using a TriM Scope II inverted 2-photon microscope equipped with a FLIM X16 TCSPC Detector for time-correlated single photon counting (LaVision BioTec). Fluorescence lifetime image stacks (150 slices, with 0,082 ns time interval) were acquired. Image analyses were done in Fiji by performing a threshold mask from the sum projection of each stack and by averaging all the pixels at each time point of the stack. To yield an exponential decay with offset, the intensity at time point 0 was normalized.

GUS staining

4-day-old seedlings were stained in 0.1 M sodium phosphate buffer (pH 7.0) containing 0.1% X-GlcA sodium salt, 1 mM $K_3[Fe(CN)_6]$, 1 mM $K_4[Fe(CN)_6]$ and 0.05% Triton X-100 for 20 min (*TMK1::GUS*), 2 h (*TMK4::GUS*, *TMK2::GUS*, *ABL3::GUS*) or 6 h (*TMK3::GUS*) at 37°C. Further, samples were incubated overnight in 80% (v/v) ethanol at room temperature. Tissue clearing was conducted as previously described[77]. DIC microscopy for analysis of the GUS staining assay was performed using an Olympus BX53 microscope equipped with 10x and 20x air objectives and a DP26 CCD camera.

Root gravitropic assays

For sensitive phenotyping of the gravitropic response, seeds were germinated on sucrose-free ½ MS plates with 1% agar[26,78,79]. 5-day-old seedlings were transferred to fresh plates and incubated in a vertical position for 40 minutes for recovery. After rotation by 90°, the roots were imaged every 30 min on a vertical flatbed scanner (Epson Perfection V370 Photo). Image time series were stabilized using the StackReg Fiji plugin. Root curvature was analyzed with the Manual Tracking Fiji plugin and angles were calculated from root tip positions over time in Microsoft Excel.

Imaging of transgenic lines

Confocal microscopy was performed on a vertical Zeiss LSM800 microscope[80] equipped with a 20X Plan Apochromat air objective (NA = 0.8). GFP- and mCherry-tagged proteins [PIN2-GFP, TMK1-GFP, CRAP (mCherry/GFP), DR5rev::GFP] were excited at 488 and 561 nm, respectively, with emission collected in the following ranges: 490-576 nm or 560-700 nm, respectively.

PIN2-GFP phospho-lines were imaged by taking 12 Z-sections through the volume of each root. These were processed through "maximum intensity" projection in Fiji and total GFP signal was quantified across PIN2-expressing regions.

For imaging of *PIN2::PIN2-GFP* and *DR5rev::GFP* asymmetric distribution, 5-day-old seedlings were placed in a 1-well chambered coverglass (VWR, Kammerdeckglaser, Lab-Tek, Nunc, catalog number 734-2056) with a block of solid ½ MS medium[80], optionally supplemented with mock or 10 µM NPA according to the experiment. For recovery, the chamber was incubated vertically in darkness for 2 h before imaging. Ten Z-sections spaced 1 µm for *PIN2::PIN2-GFP* line and 4.5 µm for *DR5rev::GFP* were collected in the median root section before and after 90° rotation at the indicated time points. The "sum slices" intensity projection in Fiji was then applied. Marking epidermal and cortical regions together, the mean grey value was quantified as per[29].

The CRAP sensor was validated by auxin treatments in a microfluidic vRootchip setup described previously[13,28]. For CRAP sensor imaging during gravistimulation, 5-day-old seedlings were placed vertically in a 1-well chambered coverglass with a block of solid 1/2 MS medium. The coverglass was fitted inside a rotational stage. Seedlings were gravistimulated by turning the stage by 90°, achieving horizontal root position, and subsequently flipping the stage by 180°. Each root was imaged every 8.94 s for 15 min three times (with 180° flips in between) as technical replicates. GFP and mCherry were imaged simultaneously as a single track. Mean grey values at the lower and upper root sides were quantified, averaging the three technical replicates for each single root. Next, the 561/488 nm ratio indicative of ROP activity was calculated for the upper and lower root sides. Finally, to compare ROP activity between the two sides, the lower root side ratio was divided by the upper root side ratio and plotted over time. For visual representation, a root with a strong CRAP asymmetry was used. The last 10 time points of the 15-min imaging time course were averaged, and the pixel ratios reflecting CRAP activation were calculated as [mCherry - mCherry background] / [GFP - GFP

background]. For plotting, the alpha value was derived from intensity and the Gaussian difference of the mCherry reference channel to suppress artefacts from numeric instability in low-intensity regions.

Protein extraction and western blot analysis

Roots from 4-day-old seedlings expressing *TMK1::TMK1-GFP*, *TMK1::TMK1-FLAG* or *UBQ10::TMK1-3xHA* after gravistimulation or auxin treatments were frozen and grounded to powder in a liquid nitrogen. To analyze the *TMK1*-tagged expression level, proteins were isolated in a mixture of: 50 mM Tris–HCl pH 7.5, 150 mM NaCl, 5 mM dithiothiothreitol (DTT), 1 mM $Na_2MoO_4 \bullet 2H_2O$, 1 mM NaF, 1% TritonX100, Complete EDTA-free Protease Inhibitor cocktail (Roche), PhosSTOP phosphatase inhibitor cocktail (Roche) and clarified by 15 min centrifugation step at 12000 g, 4°C. The analysis was carried out by SDS-PAGE and western blots using Anti-GFP HRP-conjugated (MACS Miltenyi Biotec), anti-FLAG®M2-Peroxidase (HRP) (Sigma), Anti-HA HRP-conjugated, High Affinity (3F10) (Roche) and SuperSignal West Femto Maximum Sensitivity Substrate Detection System (Thermo Scientific). Equal loading was ensured by Bradford protein quantification before loading, and by Ponceau staining of the membrane after protein transfer. Image capture was done using the image analyzer Amersham 600RGB 604 (GE Healthcare), and quantification of the protein signal was done using Fiji software.

Protein microsomal fraction extraction

4-day-old seedling roots were harvested, grounded to powder in a liquid nitrogen, and vortexed vigorously in extraction buffer 1 (50 mM Tris–HCl pH 7.5, 150 mM NaCl, Complete EDTA-free Protease Inhibitor cocktail (Roche), PhosSTOP phosphatase inhibitor cocktail (Roche)) in 1/10 (w/v) ratio. The resulting homogenate was centrifuged at 20000 g for 30 min at 4°C. The pellet was resuspended in extraction buffer 2 (50 mM Tris–HCl pH 7.5, 150 mM NaCl, 0.5% Nonidet P-40, 1% TritonX100, Complete EDTA-free Protease Inhibitor cocktail (Roche), PhosSTOP phosphatase inhibitor cocktail (Roche)), and centrifuged at 12000 g for 20 min at 4°C. The supernatant was used for total protein concentration quantification by Bradford assay. Samples were separated by SDS-PAGE (4-15% Mini-PROTEAN®TGX™ Precast Protein Gels (Bio-RAD)), transferred to a PVDF (polyvinylidene difluoride) membrane and analyzed by immunoblot using the following primary antibodies: affinity-purified TMK1 (1:1000, [58]), AHA2 (1:1000, [81]) and PIN2 (1:1000, [21]) antibodies and anti-ROP6 (C) (1:1000, Abiocode), using anti-Rabbit HRP-conjugated (1:5000, GE Healthcare) as a secondary antibody. Detection was performed using the SuperSignal West Femto Maximum Sensitivity Substrate detection kit (ThermoFisher Scientific). Image capture was done using the image analyzer Amersham 600RGB (GE Healthcare), and quantification of the protein signal was done using Fiji software.

CETSA

For CETSA from protoplasts, 10 µg of plasmid DNA (gGLP9-HA) was used for protoplast transfection, followed by incubation in a sterile 24-well microtiter plate overnight in the dark at room temperature. The incubation buffer was exchanged for protein extraction buffer (50 mM Tris-HCl, pH 7.6, 150 mM NaCl, 10 % glycerol, 5 mM DTT, 1 mM PMSF, 0.5 % NP-40, complete Roche protease inhibitors) and protoplasts were lysed by 10 vigorous ice-vortexing(5s)-ice cycles, 30 min rotation at 4°C, and again 10 vigorous ice-vortexing(5s)-ice cycles. The lysate was centrifuged twice at maximum speed for 10 minutes (4°C) in a table-top centrifuge. The final supernatant represented the protein extract, which was first sampled for Western blotting and then split into two halves supplemented with either 100 µM IAA or mock. IAA/mock-treated extracts were incubated for 1 h on ice with occasional mixing. Next,

the extracts were aliquoted for a 3 min incubation at temperatures between 42 and 47°C in a PCR machine (Bio-Rad) and returned to ice immediately. Finally, the samples were spun down in a tabletop centrifuge (12,000 rpm, 6 min, 4°C) and the supernatants were carefully transferred to new tubes for Western blotting (Anti-HA-HRP as described above).
CETSA from 5-day-old *35S::ABL3-6xHIS-3xFLAG* Arabidopsis seedlings used the same buffer and protocol with the only difference being the protein extraction procedure and the use of a different antibody for Western blotting (Anti-FLAG-HRP as described above). Protein was extracted by adding ice-cold buffer to liquid-nitrogen-ground tissue, followed by centrifugation and supernatant collection as described for protoplast proteins.

Western blot analysis of phosphorylated proteins

To analyze the phosphorylation status of TMK1 *in planta*, after corresponding treatment, 4-day-old *tmk1-1* roots expressing *TMK1::TMK1-FLAG* were grounded to powder in liquid nitrogen and homogenized in ice-cold sucrose buffer (20 mM Tris–HCl pH 8, 0.33 M sucrose, Complete EDTA-free Protease Inhibitor cocktail (Roche), PhosSTOP phosphatase inhibitor cocktail (Roche)), followed by a centrifugation step at 5000 g for 10 min at 4°C. To obtain the membrane protein fraction, the supernatant was centrifuged at 20000 g for 30 min at 4°C and the resulting pellet was solubilized with lysis buffer (20 mM Tris–HCl pH 8, 150 mM NaCl, 1% TritonX100, Complete EDTA-free Protease Inhibitor cocktail (Roche), PhosSTOP phosphatase inhibitor cocktail (Roche)) and centrifuged at 20000 g for 10 min at 4°C. The corresponding supernatant was used for immunoprecipitation assay with anti-FLAG micro beads according to the manufacturer´s instructions (μMACS Epitope Tag Protein Isolation Kit (MACS Miltenyi Biotec)). Samples were separated by SDS-PAGE (4-15% Mini-PROTEAN®TGX™ Precast Protein Gels (Bio-RAD)) and transferred to a PVDF membrane followed by probe with Phos-tag BTL-111 according to the manufacturer's instructions (www.wako-chem.co.jp) to detect protein phosphorylated levels and anti-FLAG®M2-Peroxidase (HRP) (Sigma) antibody to detect the total amount of immunoprecipitated TMK1-FLAG.

Co-immunoprecipitation assays

4-day-old *tmk1-1* seedlings expressing TMK1::TMK1-FLAG were treated with 5, 20 nM IAA or DMSO control for 30 minutes. Roots were harvested, grounded to powder in liquid nitrogen, and subjected to protein microsomal fraction extraction. Solubilized proteins from microsomal fraction were immunoprecipitated using super-paramagnetic micro MACS beads coupled to monoclonal anti-FLAG antibody according to the manufacturer´s instructions (Miltenyi Biotec). WT Col-0 extract was used as a control of the unspecific binding of endogen PIN2. Proteins immunoprecipitated with anti-FLAG antibody were separated by SDS-PAGE (4-15% Mini-PROTEAN®TGX™ Precast Protein Gels (Bio-RAD)), transferred to a PVDF membrane and analyzed by immunoblot with anti-FLAG®M2-Peroxidase (HRP) (Sigma) antibody to detect TMK1-FLAG and with anti-PIN2 antibody to detect co-immunoprecipitated endogenous PIN2.
Tobacco leaves were infiltrated or co-infiltrated with overnight LB suspensions of *Agrobacterium tumefaciens* GV3101 carrying the desired expression plasmids (*35S::ABL3-HA*, *35S::ABL3-mCherry*, *35S::TMK1-HA*, *35S::TMK1-mCherry*). Including an overnight dark incubation, the infiltrated plants were grown for 36 hours, and leaves were subsequently harvested in liquid nitrogen. Frozen leaves were ground on ice in ice-cold extraction buffer (50 mM Tris-HCl, pH 7.6, 150 mM NaCl, 10 % glycerol, 5 mM DTT, 1 mM PMSF, 0.5 % NP-40, complete Roche protease inhibitors). The extracts were centrifuged in a tabletop centrifuge at top speed for 15 min and the supernatant was harvested, followed by a repetition of the same.

The protein extracts were incubated with ChromoTek RFP-Trap Magnetic Agarose (rtma-20, Proteintech) for 1 hour at 4 ºC (rotating), washed 5 times with the extraction buffer, and analyzed by SDS-PAGE. Blotting was an Abcam anti-mCherry antibody (ab167453) and anti-HA-HRP (described above).

Active ROP assay of non-overexpressing plants

5-day-old seedling roots were excised and incubated in ½ MS liquid medium. The roots were treated with 100 nM IAA for 10 minutes and frozen in liquid nitrogen. Total protein was extracted from the treated root tissues using Extraction buffer (25mM HEPES pH 7.4, 100mM KCl, 10mM MgCl2, 1 mM PMSF, 5 mM Na3VO4, 5 mM NaF, 1 mM TCEP, cOmplete Protease Inhibitor Cocktail, Roche) in 2 steps. For every 100 mg of grounded tissue, 400 µl of extraction buffer were added, then incubated with another 400 µl of extraction buffer containing 5% Triton X-100 for one hour. Active ROP proteins were pulled down using His-MBP-CRIB (originally from RIC1 effector, obtained from expressing BL21 E.coli total cell extract) conjugated to HisPurTM Ni-NTA Magnetic Beads (Thermo Fisher) by incubation of 200 µl total protein extract with 25 µl (initial volume) of beads for 2 hours at 4°C. The beads were washed by Washing buffer (25 mM HEPES pH 7.4, 300 mM KCl, 10 mM MgCl2, 12.5 mM imidazole) for 3 times and boiled at 95°C with 30 µl SDS loading dye (BioRad). After removing the beads, the protein samples were separated by 12% SDS-PAGE and analyzed by immunoblot with anti-ROP2 specific antibody (1:10,000, Abiocode). Input samples were isolated from total protein extracts, before addition of Triton X-100 to get an estimate of the present total ROP content.

Quantitative immunoblot analysis

To determine the relative amount of protein in time course experiments, grey values were calculated by ImageJ Gel Analysis tool, where for each band of protein of interest (PI) and normalizing control (NC), membrane background was removed individually. To get relative NC value, all the NC values were divided by the highest one. Subsequently, all the PI values were divided by their respective relative NC values. Final obtained values of PI were normalized dividing by the time point 0 or DMSO control treatment value. Values from three independent experiments were used to determine average and ±SD. For example, for quantitative immunoblot analysis of phosphorylated proteins, it was first determined grey values of TMK1 obtained with Phos-tag BTL-111 probe and anti-Flag antibody at different time points/treatments, tacking into account each membrane background. TMK1-Flag values were used as a protein amount normalizing control (NC). To get NC values of each experiment point, TMK1-Flag values were divided by the highest one. Subsequently, TMK1 Phos-tag values were divided by their respective relative NC values. To compare differences between time points/ treatments, as a final step, the normalized at protein level TMK1 Phos-tag values were divided by the corresponding time point 0 or DMSO control treatment values.

Recombinant protein expression and purification from *E. coli.*

The 6xHis-PIN2 HL recombinant protein was expressed using the 6xHis-PIN2 HL vector [82] in *E. coli* BL21 (DE3) strain upon induction by 0.5 mM IPTG (Isopropyl β-D-1-Thiogalactopyranoside) at 16°C for 12 h. Cells were harvested by centrifugation at 4000 g for 15 min and washed with water. They were then lysed by sonication in lysis buffer (50 mM Tris-HCl pH7.5; 150 mM NaCl; 1 mM EDTA; 1 mM DTT and 1% TritonX100). The lysed solution was centrifuged at 12000 g for 15 min. The supernatant was then purified using Ni-NTA His affinity agarose (Thermo Scientific) according to the manufacturer's instructions. 6xHis- PIN2 HL protein was eluted from the beads in elution buffer (50 mM Tris-HCl pH7.4;

150 mM NaCl and 250 mM imidazole). Eluted protein samples were checked by SDS-PAGE and Coomassie brilliant blue staining (Bio-Safe™ Coomassie Stain, Bio-Rad). The protein concentration was determined with the Bradford method (Quick Start™ Bradford Reagent, Bio-Rad).

TMK1-HA immunoprecipitation

To immunoprecipitate HA-tagged TMK1 protein, roots of 7-day-old *pUBQ10::TMK1-3xHA* and *DEX::TMK1^{K616R}-HA* (previously induced for 48 h with 30 µM dexamethasone) seedlings were frozen and grounded in a liquid nitrogen, and, subsequently, homogenized in protein extraction buffer (PEB: 50 mM Tris-HCl pH7.5, 200 mM NaCl, 1% TritonX100, 10 mM $MgCl_2$, 1 mM $MnCl_2$, Complete (Roche) protease cocktail and PhosSTOP phosphatase inhibitor cocktail (Roche)), followed by the 20 min centrifugation step at 14000 g, 4°C. In a fresh Eppendorf tube, 50 µL anti-HA agarose beads were added (Anti-HA Affinity Matrix, SIGMA; pre-washed with 200 µL PEB) to the supernatant. After 4 h of rotating at 4°C, the samples were spun down again at 2000 g, 4°C, and the supernatant was discarded. The Agarose beads were washed twice with 200 µL PEB, and finally re-suspended into 50 µL PEB to allow further biochemical reactions.

In vitro kinase assay

The *in vitro* kinase assay with [γ-^{32}P]-ATP was conducted as reported[82] with minor modifications. Immunoprecipated TMK1-HA and TMK1^{K616R}-HA (5 µL) from 7-day-old Arabidopsis seedlings, together with the recombinant 6xHis-PIN2 HL (10 µL) from *E.coli*, were added to the kinase reaction buffer (50 mM Tris-HCl pH 7.5, 10 mM $MgCl_2$, 5 mM NaCl, 2.5 mM cold ATP (adenosine 5'-triphosphate), and 1 mM DTT) in the presence of 5 µCi [γ-^{32}P]-ATP (NEG502A001MC; Perkin-Elmer). Reactions were incubated at 25°C for 90 min and afterwards terminated by adding 10 µL 5×SDS loading buffer. 20 µL reaction samples were then separated with 10% SDS-PAGE gel, developed with a phosphor-plate overnight. Eventually, the phosphor-plate was imaged with a Fujifilm FLA 3000 plus DAGE system.

Statistical analysis

Data processing and visualization was done in R version 4.0.4.

Accession Numbers

Gene sequence data from this article can be found in the *Arabidopsis* Genome Initiative databases under the following accession numbers: AT4G02980 (*ABP1*), AT1G66150 (*TMK1*), AT1G24650 (*TMK2*), AT2G01820 (*TMK3*), AT3G23750 (*TMK4)*, AT5G57090 (*PIN2*), AT1G20090 for (*ROP2*), AT4G35020 for (*ROP6*), AT4G30190 (*AHA2*), AT5G46330 (*FLS2*), AT1G72610 (*ABL1*), AT5G20630 (*ABL2*), AT4G14630 (*ABL3*).

2.3.6 Acknowledgments

We thank W. Gray for providing material; N. Gnyliukh and E. Cervenova for help with manuscript preparation; J. Schmid for help with cloning. We thank Dolf Weijers, Mark Roosjen, and Andre Kuhn for discussions and support with phospho-proteomic analyses. We thank the Bioimaging and Life Science facilities at ISTA for their excellent service and assistance. The research leading to these results has received funding from the European Research Council (ERC) under the European Union's Horizon 2020 research and innovation program grant agreement No 742985 and Austrian Science Fund (FWF): I3630-775 B25 to J.F; National Natural Science Foundation of China (Grant 32130010, 31422008), start-up funds

from FAFU to T.X., Y.J. was funded by ERC no. 3363360-APPL under FP/2007-2013. L.R. was supported by FP7-PEOPLE-2011-COFUND ISTFELLOW program (IC1023FELL01) and the European Molecular Biology Organization (EMBO) long-term postdoctoral fellowship (ALTF 985-2016). S.T. was supported by the National Natural Science Foundation of China (32321001).

2.3.7 Contributions

Conceptualization: J.F., L.R.; Methodology: L.R., L.F. I.K.; Investigation: L.R., L.F., M.Z., C.G., A.M., Z.G., I.V., J.H., M.R., S.T., G.M., L.H., L.L.; Resources: L.R., L.F., M.M.M.-B, Y.J., T.X.; Writing: J.F., L.F., L.R.; Review & Editing: all authors; Visualization: L.R., L.F.; Supervision: L.R., L.F., J.F.; Funding Acquisition: J.F.

2.3.8 Figures

Figure 1- Rapid auxin phosphor-response targets PINs in Arabidopsis

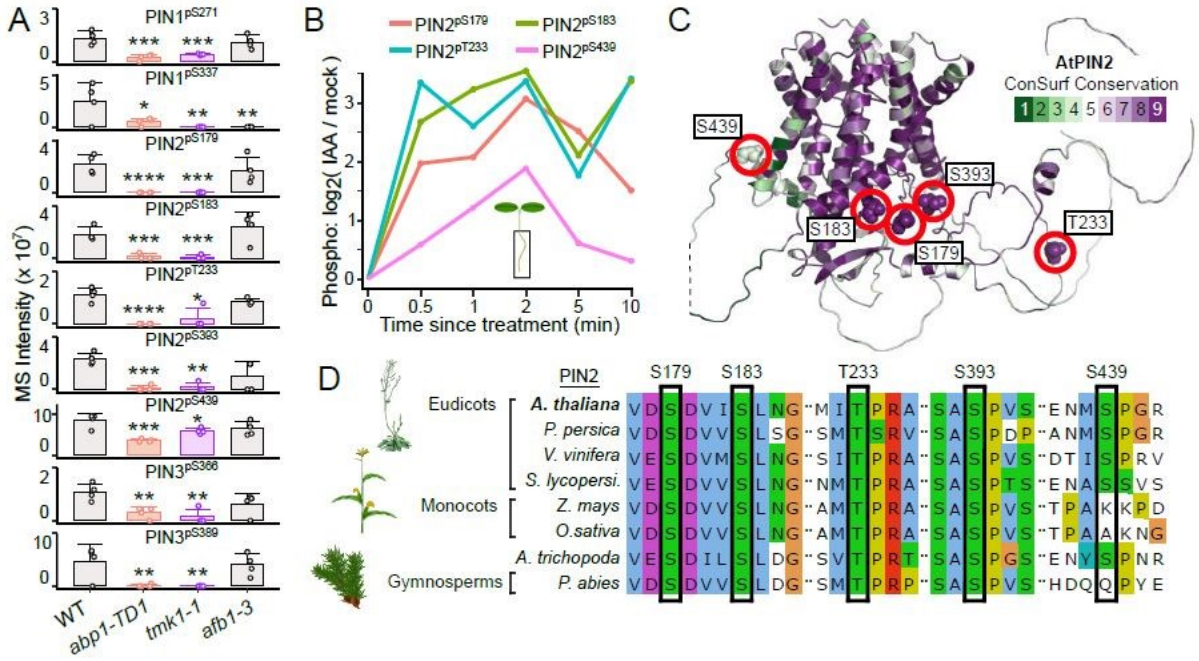

Figure 2.3-1 Rapid auxin phosphor-response targets PINs in Arabidopsis

(A) Overview of PIN phospho-sites downregulated (FDR < 0.05) in *abp1-TD1* and *tmk1-1* auxin-treated (100 nM IAA, 2 min) roots. 4 biological replicates, Mean + SD, permutation-based t-tests with FDR-controlled p-values. *p < 0.05, **p < 0.01, ***p < 0.001, ****p < 0.0001.
(B) Significant PIN2 phospho-site auxin profiles (FDR ≤ 0.01, 100 nM IAA).
(C) Localization of ABP1-TMK1-dependent phospho-sites on a ConSurf conservation-colored AlphaFold2 structure of PIN2.
(D) Multiple sequence alignment of eight PIN2 orthologs with a highlight of Arabidopsis ABP1-TMK1-dependent PIN2 phospho-sites

Figure 2- ABP1-TMK1-dependent PIN2 phospho-sites for gravitropism and PIN2 stability

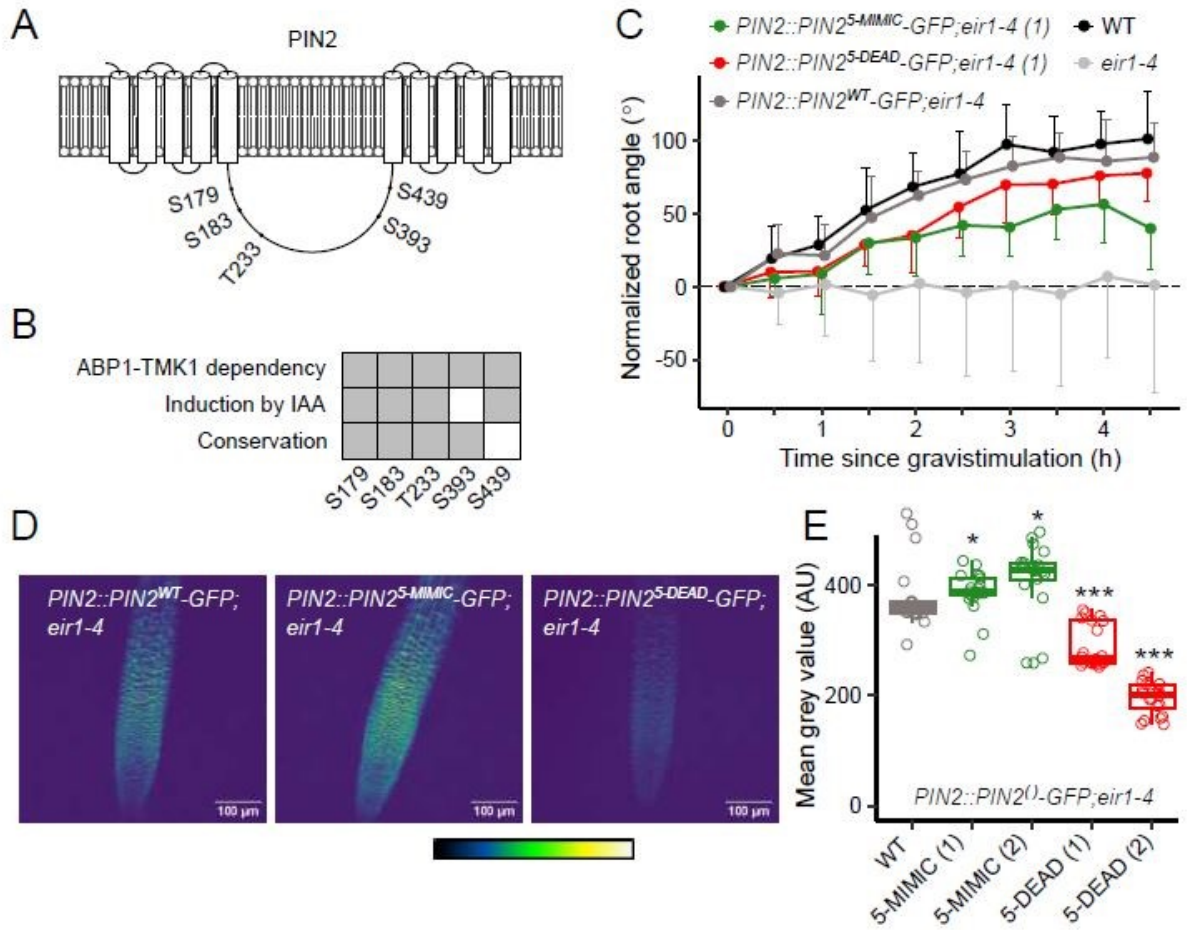

Figure 2.3-2 ABP1-TMK1-dependent PIN2 phospho-sites for gravitropism and PIN2 stability

(A) Schematic of ABP1-TMK1-dependent phospho-sites mapped on the PIN2 hydrophilic loop.
(B) Schematic summarizing properties of the studied PIN2 phospho-sites.
(C) Root gravitropism of PIN2-GFP phospho-lines on medium with sucrose (1 %). Mean + or – SD.
(D) Representative maximum intensity projection images of PIN2-GFP phospho-lines.
(E) Quantification of GFP signal from (D). Kruskal-Wallis analysis followed by Holm-corrected Wilcoxon rank sum tests relative to WT. *p < 0.05, **p < 0.01, ***p < 0.001, ****p < 0.0001.

Figure 3- ABP1/ABL3-TMK1 signaling during early root gravitropism

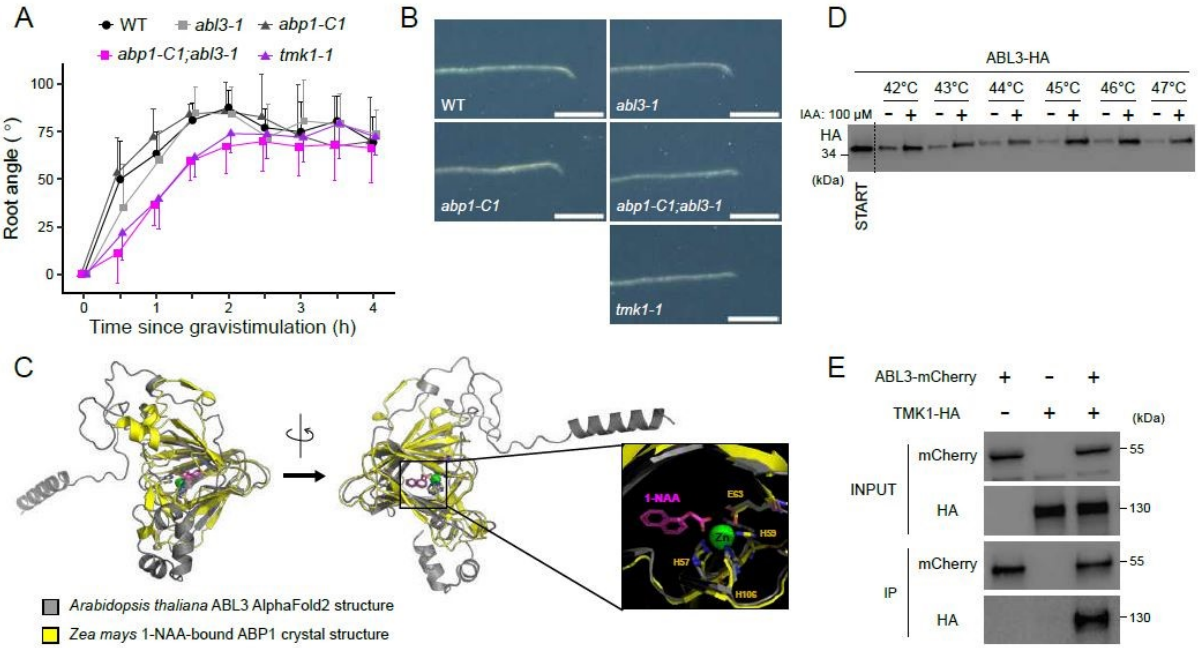

Figure 2.3-3 ABP1/ABL3-TMK1 signaling during early root gravitropism

(A) Mutant root gravitropism profiles on medium without sucrose. Mean + or – SD.
(B) Representative images of mutant roots gravistimulated for 1 hour. The full set of images is shown in Fig. S4E. Scale bar, 100 µm.
(C) Superimposition of Arabidopsis ABL3 AlphaFold2 structure with 1-NAA-bound maize ABP1 crystal structure highlighting a potential auxin-binding cavity of Arabidopsis ABL3.
(D) CETSA assay on *35S::ABL3-HA* Arabidopsis root protoplasts in the presence of 100 µM IAA.
(E) Co-immunoprecipitation from tobacco leaves of TMK1-HA with ABL3-mCherry but not with anti-mCherry beads alone.

Figure 4- Auxin-induced activation of TMK1 and downstream ROP signaling in roots

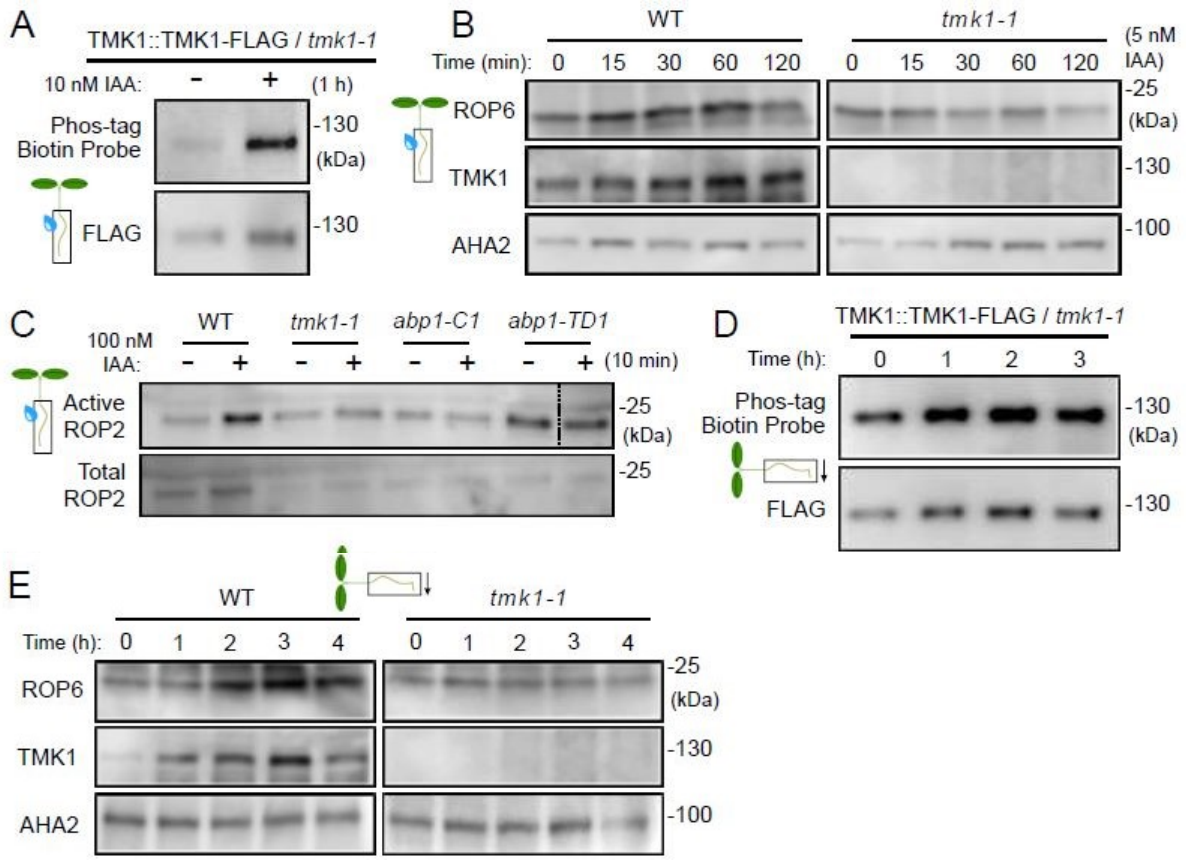

Figure 2.3-4 Auxin-induced activation of TMK1 and downstream ROP signaling in roots

(A) Auxin effect on TMK1 phosphorylation in *TMK1::TMK1-FLAG;tmk1-1* roots assayed through TMK1-FLAG immunoprecipitation and Phos-tag Biotin Probe analysis. Refer to Fig. S5A for quantification of three experimental replicates.
(B) Auxin effect on ROP6 and TMK1 levels in the WT or *tmk1-1* root microsomal protein fractions. Refer to Fig. S5B for quantification of three experimental replicates.
(C) Auxin effect on ROP2 activation assayed by native ROP pulldown from roots of the indicated genotypes. Empty well was edited out from the upper blot for visualization purposes. Refer to Fig. S5D for unedited blot image.
(D) Gravistimulation effect on TMK1 phosphorylation in *TMK1::TMK1-FLAG;tmk1-1* roots assayed through TMK1-FLAG immunoprecipitation and Phos-tag Biotin Probe analysis. Refer to Fig. S5E for quantification of three experimental replicates.
(E) Gravistimulation effect on ROP6 and TMK1 levels in the WT or *tmk1-1* root microsomal protein fractions. Refer to Fig. S5F for quantification of three experimental replicates.

Figure 5- Asymmetric TMK1 activation for PIN2 asymmetry in root gravitropism

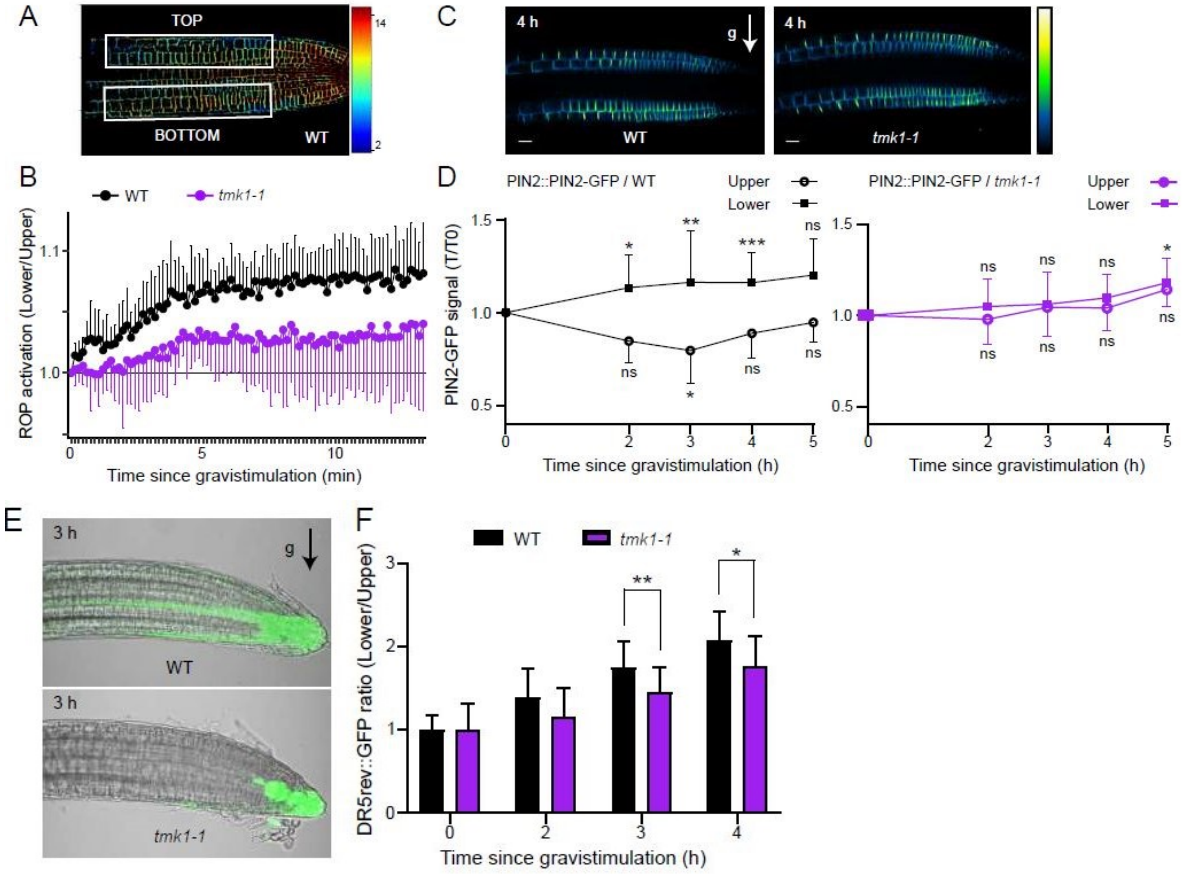

Figure 2.3-5 Asymmetric TMK1 activation for PIN2 asymmetry in root gravitropism

(A) Image of a root with strongly asymmetric ROP activity (reported by the CRAP sensor) in response to 15-minute gravistimulation.
(B) Rapid gravistimulation-induced establishment of asymmetric ROP activity in WT or *tmk1-1* roots.
(C) Representative images of *PIN2::PIN2-GFP* in 4-day-old WT and *tmk1-1* seedlings after 4 hours of gravistimulation. g, gravity vector. Scale bar, 20 µm.
(D) Quantification of gravistimulation-induced PIN2-GFP asymmetry. Normalization to the first timepoint T0 for the upper or lower root side independently. Mean ± SD. Two-way ANOVA with Dunnett's multiple comparisons, **** $p < 0.0001$.
(E) Representative confocal images of asymmetric auxin response (visualized by *DR5rev::GFP*) at the lower side of the root after a 3-hour gravistimulation in WT and *tmk1-1* 4-day-old roots. Refer to Fig. S6H for corresponding images taken before gravistimulation.
(F) Quantification of *DR5rev::GFP* asymmetry as a ratio of fluorescence intensity at the lower side to the upper side of gravistimulated roots at the indicated time points, normalized to the initial fluorescence value. Mean ± SD, n = 10. Two-way ANOVA with Dunnett's multiple comparisons, *$p < 0.05$, **$p < 0.01$. g, gravity vector.

Figure 6- Auxin-mediated TMK1 interaction with and phosphorylation of PIN2

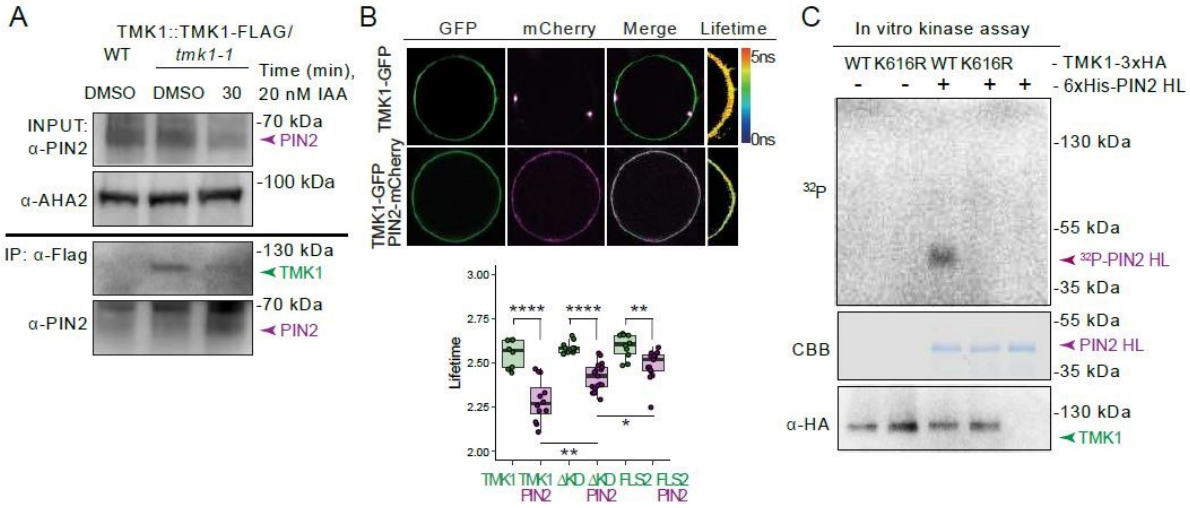

Figure 2.3-6 Auxin-mediated TMK1 interaction with and phosphorylation of PIN2

(A) Auxin promotes the interaction between TMK1 and PIN2 in a co-immunoprecipitation (Co-IP) assay. Microsomal protein fraction from 20 nM IAA- or DMSO-treated roots expressing *TMK1::TMK1-FLAG/tmk1-1* was immunoprecipitated with an anti-FLAG antibody, and endogenous PIN2 was detected by blotting with an anti-PIN2 antibody. See Figure S3A for Co-IP with 5 nM IAA where input PIN2 abundance in the protein microsomal fraction is increased.
(B) FRET-FLIM analysis on transiently expressed *35S::TMK1-GFP, 35S::TMK1$^{\Delta KD}$-GFP, 35S::FLS2-GFP* and *35S::PIN2-mCherry* in root protoplasts. Fluorescence lifetime values are displayed as a heat map (for additional images see Figure S3B). One-way ANOVA with Holm-corrected post hoc tests, *p < 0.05, ****p < 0.0001.
(C) *In vitro* kinase assay showing that TMK1-3xHA directly phosphorylates the 6His-PIN2 hydrophilic loop (HL). Top panel, ^{32}P autoradiography; middle panel, CBB staining; bottom panel, immunoblot with an anti-HA antibody.

Figure S1- Identification of PINs as ABP1-TMK1 phospho-targets by gene ontology analysis

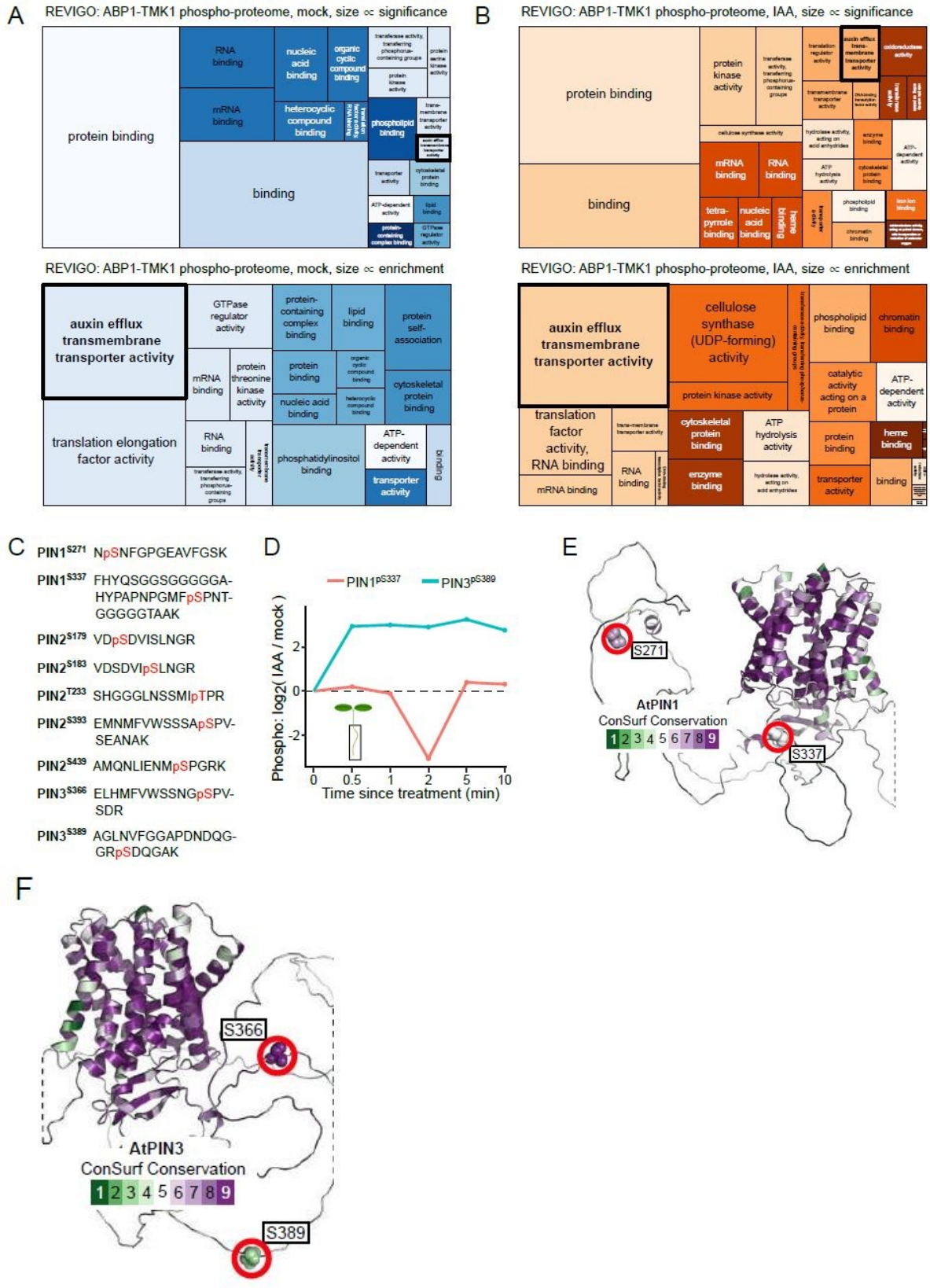

Figure 2.3-7 Identification of PINs as ABP1-TMK1 phospho-targets by gene ontology analysis

(A) Treemap of GO terms enriched for the ABP1-TMK1 phospho-proteome under mock conditions. Box sizes scale with -log10(p-value) (top) or fold enrichment (bottom).
(B) Treemap of GO terms enriched for the ABP1-TMK1 phospho-proteome under auxin treatment (100 nM IAA, 2 min) conditions. Box sizes scale with -log10(p-value) (top) or fold enrichment (bottom).
(C) Overview of phospho-peptides pertaining to PIN phospho-sites from Fig. 1A.
(D) Significant PIN1 and PIN3 phospho-site auxin profiles (FDR ≤ 0.01, 100 nM IAA).
(E) Localization of ABP1-TMK1-dependent phospho-sites on a ConSurf conservation-colored AlphaFold2 structure of PIN1.
(F) Localization of ABP1-TMK1-dependent phospho-sites on a ConSurf conservation-colored AlphaFold2 structure of PIN3.

Figure S2- Supplementary data on PIN2-GFP phospho-lines

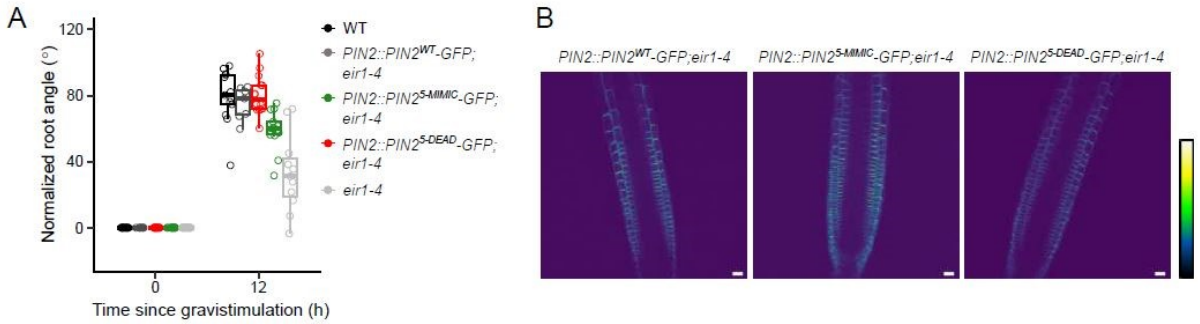

Figure 2.3-8 Supplementary data on PIN2-GFP phospho-lines

(A) Normalized root angles after 12-hour gravistimulation of PIN2-GFP phospho-lines on medium with sucrose (1 %).
(B) Representative median root sections showing PIN2-GFP phospho-line polarity. Scale bar, 20 µm

Figure S3- Expression of TMK genes and analysis of the tmk1-1 mutant

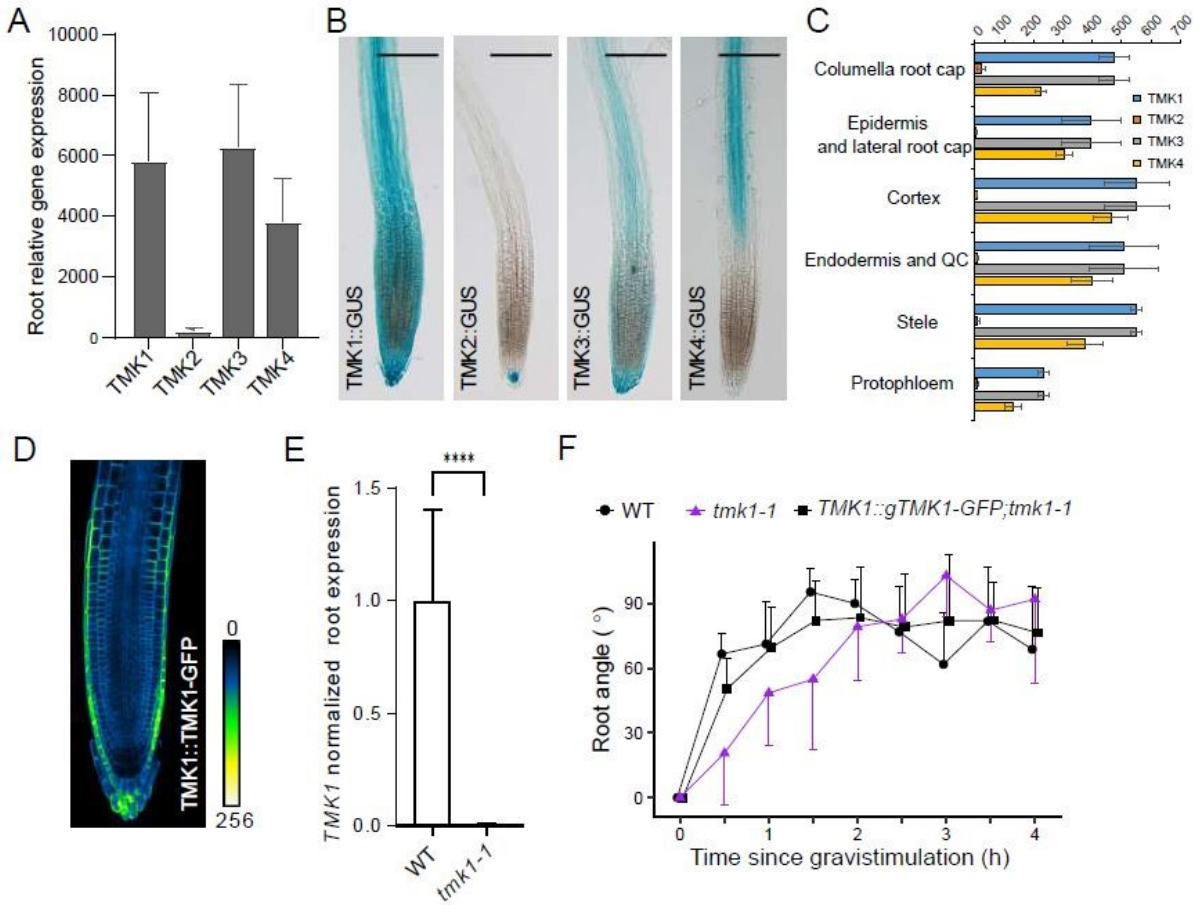

Figure 2.3-9 Expression of TMK genes and analysis of the tmk1-1 mutant

(A) Relative transcription levels of *TMK1, TMK2, TMK3,* and *TMK4* in Arabidopsis roots from 803 samples assayed with the Affymetrix Arabidopsis ATH1 Genome Array. Data was obtained using the Genevestigator databases (https://genevestigator.com). Mean + SD.
(B) Root tip expression pattern of *TMK1*, *TMK2*, *TMK3*, and *TMK4* promoters fused to the GUS transcriptional reporter. Scale bar, 100 µm.
(C) Relative expression levels of *TMK1, TMK2, TMK3* and *TMK4* in different root cell types obtained from high-resolution spatiotemporal microarray analysis of 5-6-day-old roots reported in[56] (ePlant http://bar.utoronto.ca/eplant).
(D) Representative intensity-colored image of a 4-day-old *TMK1::TMK1-GFP;WT* root.
(E) *TMK1* qPCR in *tmk1-1*.
(F) Root gravitropism profiles on medium without sucrose. Mean + or – SD.

Figure S4- Characterization of ABL3 properites

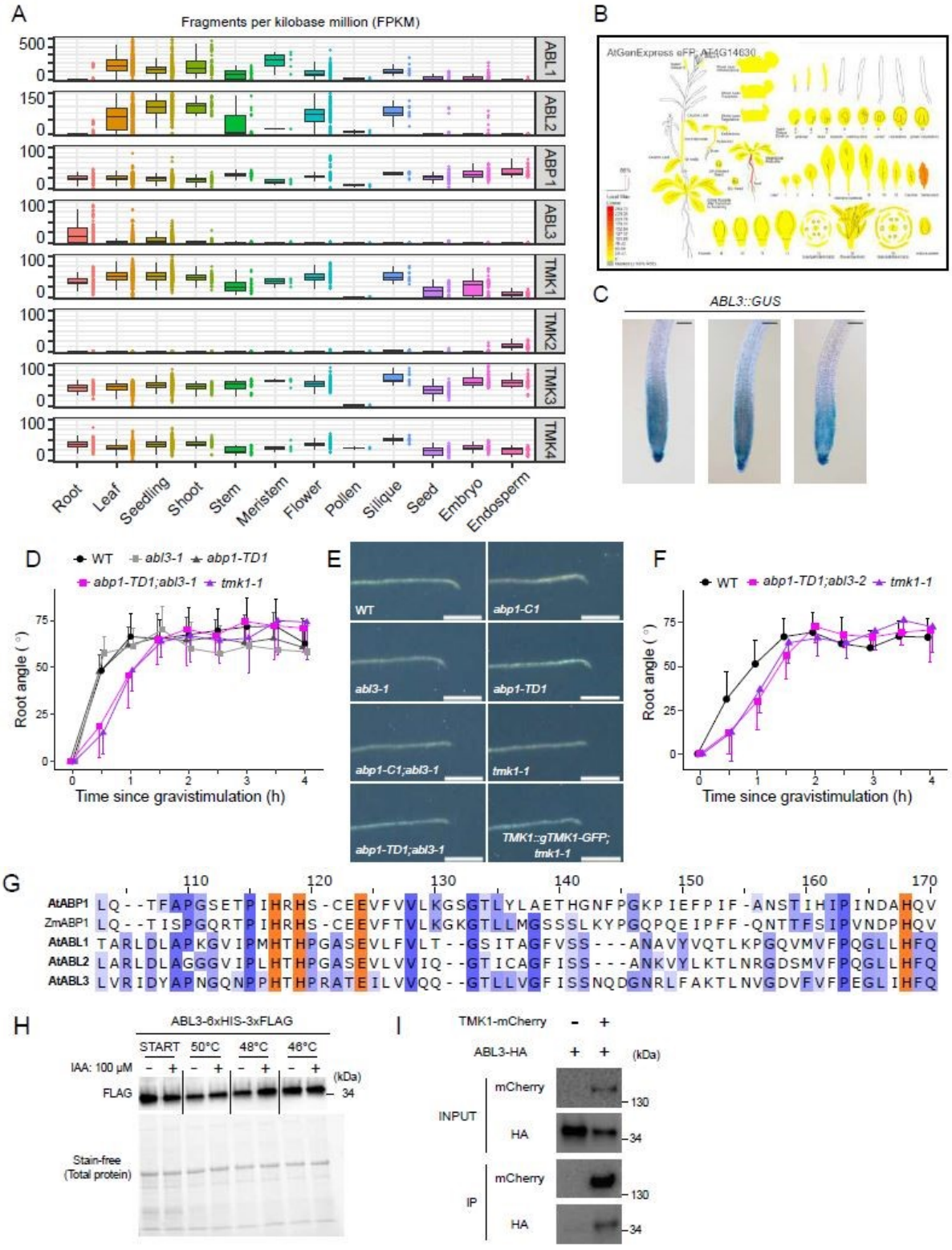

Figure 2.3-10 Characterization of ABL3 properties

(A) Comprehensive expression profiles of *ABL3* and *ABP1/ABL/TMK* genes obtained using[57].
(B) Snapshot of *ABL3* expression pattern obtained using ePlant/TAIR

(C) *ABL3::GUS* staining (2h). Scale bar, 100 µm.

(D) Mutant root gravitropism profiles on medium without sucrose. Mean + or – SD.
(E) Representative images of mutant roots gravistimulated for 1 hour. Scale bar, 100 µm.
(F) Mutant root gravitropism profiles on medium without sucrose. Mean + or – SD.
(G) Multiple sequence alignment of ABP1/ABL protein sequences surrounding the auxin pocket with metal-coordinating residues (orange). Purple coloring highlights conservation.
(H) CETSA assay on *35S::ABL3-6xHIS-3xFLAG* seedlings in the presence of 100 µM IAA.
(I) Co-immunoprecipitation from Arabidopsis root protoplasts of ABL3-HA with TMK1-mCherry but not with anti-mCherry beads alone.

Figure S5-Supplementary data for ROP activation through TMK1

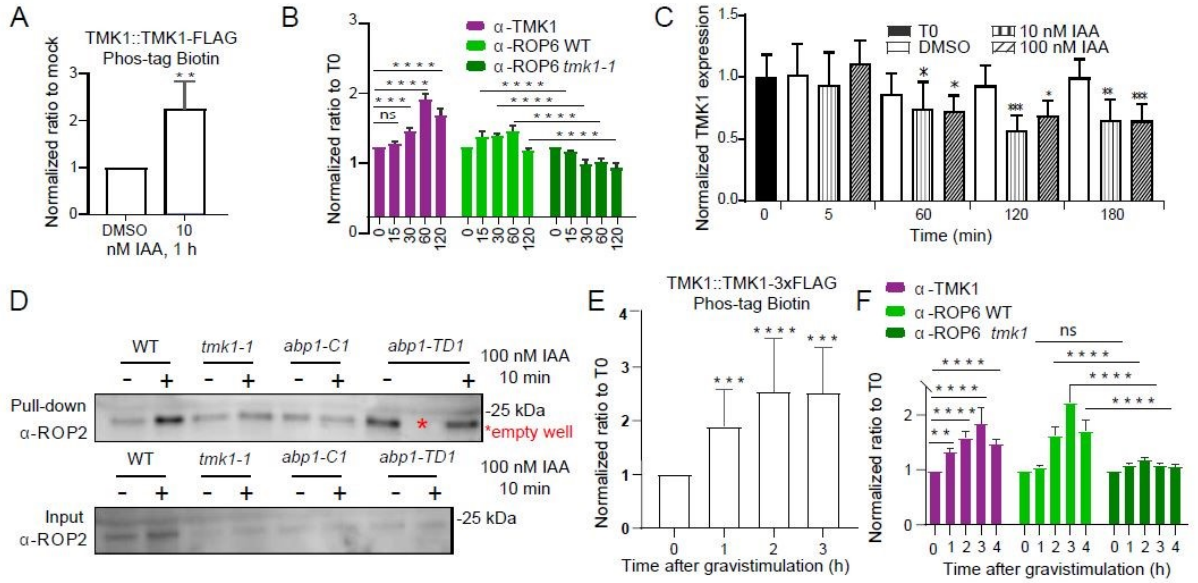

Figure 2.3-11 Supplementary data for ROP activation through TMK1

(A) Quantification of auxin effect on TMK1 phosphorylation in *TMK1::TMK1-FLAG;tmk1-1* roots assayed through TMK1-FLAG immunoprecipitation and Phos-tag Biotin Probe analysis. Phosphorylation levels detected with a Phos-tag Biotin Probe were normalized to signal obtained from anti-FLAG detection, and subsequently to the mock value. Mean ± SD of 3 biological replicates. Unpaired two-tailed t-test, $**p < 0.01$.
(B) Quantification of auxin effect on ROP6 and TMK1 levels in the WT or *tmk1-1* root microsomal protein fractions. Band intensities were normalized to the loading control, and subsequently to the first timepoint T0. Mean ± SD of 3 biological replicates. Two-way ANOVA with Dunnett's multiple comparisons, $****p < 0.0001$.
(C) RT-qPCR of *TMK1* expression after auxin treatment. Normalization was done to *PP2A* as a reference gene. The expression level at the start of the experiment (T0) was set to a relative value of 1.
(D) Auxin effect on ROP2 activation assayed by native ROP pulldown from roots of the indicated genotypes. Full unedited blot relating to Fig. 4C.
(E) Quantification of gravistimulation effect on TMK1 phosphorylation in *TMK1::TMK1-FLAG;tmk1-1* roots assayed through TMK1-FLAG immunoprecipitation and Phos-tag Biotin Probe analysis. Phosphorylation levels detected with a Phos-tag Biotin Probe were normalized to signal obtained from anti-FLAG detection, and subsequently to the first timepoint T0. Mean ± SD of 3 biological replicates. One-way ANOVA with Dunnett's multiple comparisons to timepoint 0 ($****p < 0.0001$).
(F) Quantification of gravistimulation effect on ROP6 and TMK1 levels in the WT or *tmk1-1* root microsomal protein fractions. Band intensities were normalized to the loading control, and subsequently to the first timepoint T0. Mean ± SD of 3 biological replicates. Two-way ANOVA with Dunnett's multiple comparisons, $****p < 0.0001$.

Figure S6- Requirement of TMK1 kinase activity for early root gravitropism

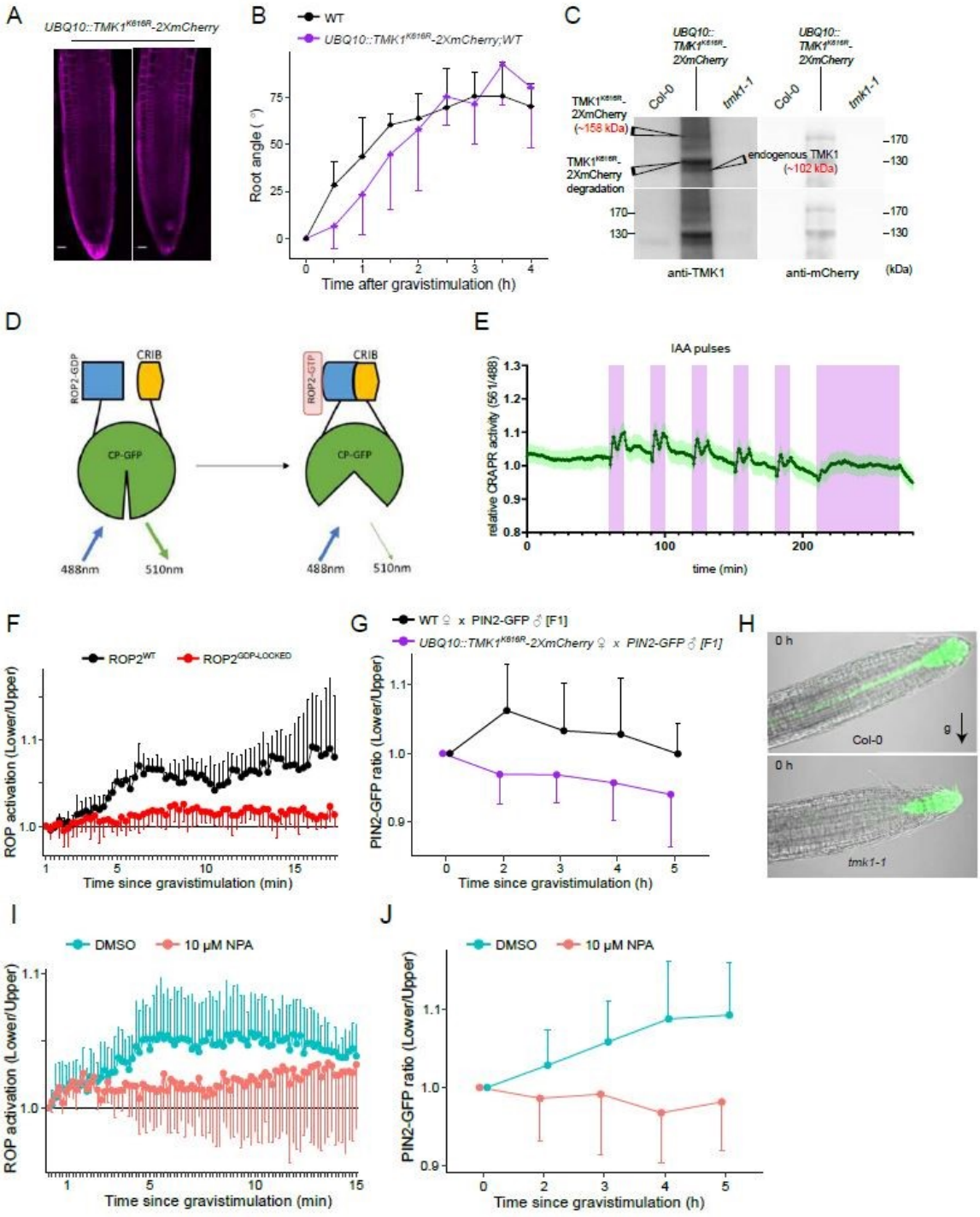

Figure 2.3-12 Requirement of TMK1 kinase activity for early root gravitropism

(A) Representative images of primary roots expressing the *UBQ10::TMK1^{K616R}-mCherry* construct.
(B) Root gravitropism profiles on medium without sucrose. Mean + or – SD.
(C) Native TMK1 protein expression is not silenced in *UBQ10::TMK1^{K616R}-mCherry* roots. Blots are duplicated to depict both the annotated (top) and unannotated (bottom) versions.
(D) Schematic showing the function of the CRAP sensor.
(E) CRAP sensor reports IAA pulses (10nM IAA, highlighted in magenta) in a microfluidic root chip device

(F) Dominant-negative mutation in the CRAP sensor abolishes rapid gravistimulation-induced establishment of CRAP asymmetry in WT roots. Mean + or – SD.
(G) Dominant negative effect of *UBQ10::TMK1^{K616R}-mCherry* on gravistimulation-induced PIN2-GFP asymmetry. Mean + or – SD.
(H) Representative confocal images of *DR5rev::GFP;WT* and *DR5rev::GFP;tmk1-1* roots before gravistimulation.
(I) 10 µM NPA treatment abolishes rapid gravistimulation-induced establishment of CRAP asymmetry in WT roots. Mean + or – SD.
(J) 10 µM NPA treatment abolishes gravistimulation-induced PIN2-GFP asymmetry. Mean + or – SD.

Figure S7- Supplementary data on TMK1-PIN2 interaction

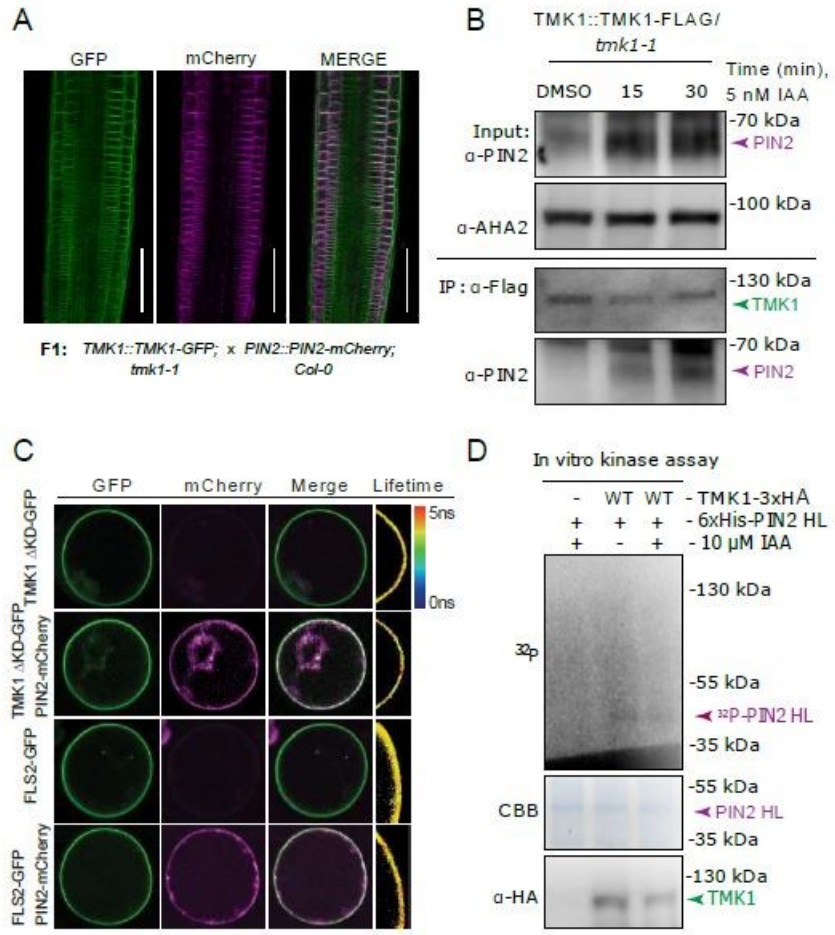

Figure 2.3-13 Supplementary data on TMK1-PIN2 interaction

(A) Co-localization of TMK1-GFP and PIN2-mCherry. (B) Co-IP assay showing the interaction of TMK1 with PIN2 upon low auxin treatment (5 nM IAA). Microsomal protein fraction from WT was used as a control for unspecific binding of endogenous PIN2 (shown in Figure 3A, same experiment)
(C) FRET-FLIM analysis on transiently expressed *35S::TMK1$^{\Delta KD}$-GFP, 35S::TMK1$^{\Delta KD}$-GFP/35S::PIN2-mCherry, 35S::FLS2-GFP* and *35S::FLS2-GFP/35S::PIN2-mCherry* in root protoplasts (the same experiment is shown in Figure 3B). GFP fluorescence lifetime was calculated as described in the Methods section. The heat map depicts fluorescence lifetime values (see Figure 3B for lifetime analysis). (D) *In vitro* kinase assay showing phosphorylation of the 6His-PIN2 HL substrate by TMK1-3xHA in the presence or absence of auxin. Top panel, ^{32}P-autoradiography; middle panel, CBB staining; bottom panel, immunoblot with an anti-HA antibody

2.3.9 References

1. Friml, J. (2021). Fourteen Stations of Auxin. Cold Spring Harb. Perspect. Biol. *14*, a039859. 10.1101/cshperspect.a039859.
2. Han, H., Adamowski, M., Qi, L., Alotaibi, S.S., and Friml, J. (2021). PIN-mediated polar auxin transport regulations in plant tropic responses. New Phytol. *232*. 10.1111/nph.17617.
3. Berleth, T., and Sachs, T. (2001). Plant morphogenesis: Long-distance coordination and local patterning. Curr. Opin. Plant Biol. *4*, 57–62. 10.1016/S1369-5266(00)00136-9.
4. Hajný, J., Tan, S., and Friml, J. (2022). Auxin canalization: From speculative models toward molecular players. Curr. Opin. Plant Biol. *65*, 102174. 10.1016/J.PBI.2022.102174.
5. Adamowski, M., and Friml, J. (2015). PIN-dependent auxin transport: Action, regulation, and evolution. Plant Cell *27*, 20–32. 10.1105/tpc.114.134874.
6. Luschnig, C., and Vert, G. (2014). The dynamics of plant plasma membrane proteins: PINs and beyond. Dev. *141*, 2924–2938. 10.1242/dev.103424.
7. Park, J., Lee, Y., Martinoia, E., and Geisler, M. (2017). Plant hormone transporters: what we know and what we would like to know. BMC Biol. *15*, 1–15. 10.1186/S12915-017-0443-X.
8. Péret, B., Swarup, K., Ferguson, A., Seth, M., Yang, Y., Dhondt, S., James, N., Casimiro, I., Perry, P., Syed, A., et al. (2012). AUX/LAX Genes Encode a Family of Auxin Influx Transporters That Perform Distinct Functions during Arabidopsis Development. Plant Cell *24*, 2874–2885. 10.1105/tpc.112.097766.
9. Zhang, J., Nodzyński, T., Pěnčík, A., Rolčík, J., and Friml, J. (2010). PIN phosphorylation is sufficient to mediate PIN polarity and direct auxin transport. Proc. Natl. Acad. Sci. U. S. A. *107*, 918–922. 10.1073/pnas.0909460107.
10. Wisniewska, J., Xu, J., Seifartová, D., Brewer, P.B., Růžička, K., Blilou, L., Rouquié, D., Benková, E., Scheres, B., and Friml, J. (2006). Polar PIN localization directs auxin flow in plants. Science (80-.). *312*, 883. 10.1126/science.1121356.
11. Prigge, M.J., Platre, M., Kadakia, N., Zhang, Y., Greenham, K., Szutu, W., Pandey, B.K., Bhosale, R.A., Bennett, M.J., Busch, W., et al. (2020). Genetic analysis of the Arabidopsis TIR1/ AFB auxin receptors reveals both overlapping and specialized functions. Elife *9*, e54740.
12. Qi, L., Kwiatkowski, M., Chen, H., Hoermayer, L., Sinclair, S., Zou, M., Del Genio, C.I., Kubeš, M.F., Napier, R., Jaworski, K., et al. (2022). Adenylate cyclase activity of TIR1/AFB auxin receptors in plants. Nature *611*, 133–138. https://doi.org/10.1038/s41586-022-05369-7.
13. Li, L., Verstraeten, I., Roosjen, M., Takahashi, K., Rodriguez, L., Merrin, J., Chen, J., Shabala, L., Smet, W., Ren, H., et al. (2021). Cell surface and intracellular auxin signalling for H+ fluxes in root growth. Nature *599*, 273–277. 10.1038/s41586-021-04037-6.
14. Fiedler, L., and Friml, J. (2023). Rapid auxin signaling: Unknowns old and new. Curr. Opin. Plant Biol. *75*, 102443. 10.1016/j.pbi.2023.102443.
15. Yu, Y., Tang, W., Lin, W., Li, W., Zhou, X., Li, Y., Chen, R., Zheng, R., Qin, G., Cao, W., et al. (2023). ABLs and TMKs are co-receptors for extracellular auxin. Cell *186*, 5457-5471.e17. 10.1016/j.cell.2023.10.017.
16. Sheen, J. (2024). The new horizon of plant auxin signaling via cell-surface co-receptors. Cell Res. *34*, 343–344. 10.1038/s41422-023-00921-0.
17. Friml, J., Gallei, M., Gelová, Z., Johnson, A., Mazur, E., Monzer, A., Rodriquez, L., Roosjen, M., Verstraeten, I., Živanovič, B.D., et al. (2022). ABP1–TMK auxin

perception for global phosphorylation and auxin canalization. Nature *609*, 575–581. 10.1038/s41586-022-05187-x.

18. Kuhn, A., Roosjen, M., Mutte, S., Dubey, S.M., Carrillo Carrasco, V.P., Boeren, S., Monzer, A., Koehorst, J., Kohchi, T., Nishihama, R., et al. (2024). RAF-like protein kinases mediate a deeply conserved, rapid auxin response. Cell *187*, 130-148.e17. 10.1016/j.cell.2023.11.021.
19. Mazur, E., Kulik, I., Hajný, J., and Friml, J. (2020). Auxin canalization and vascular tissue formation by TIR1/AFB-mediated auxin signaling in Arabidopsis. New Phytol. *226*, 1375–1383. 10.1111/NPH.16446.
20. Wabnik, K., Kleine-Vehn, J., Balla, J., Sauer, M., Naramoto, S., Reinö Hl, V., Merks, R.M., Govaerts, W., and Friml, J. (2010). Emergence of tissue polarization from synergy of intracellular and extracellular auxin signaling. Mol. Syst. Biol. *6*, 447. 10.1038/msb.2010.103.
21. Abas, L., Benjamins, R., Malenica, N., Paciorek, T.T., Wiřniewska, J., Moulinier-Anzola, J.C., Sieberer, T., Friml, J., and Luschnig, C. (2006). Intracellular trafficking and proteolysis of the Arabidopsis auxin-efflux facilitator PIN2 are involved in root gravitropism. Nat. Cell Biol. *8*, 249–256. 10.1038/ncb1369.
22. Zhang, Y., Xiao, G., Wang, X., Zhang, X., and Friml, J. (2019). Evolution of fast root gravitropism in seed plants. Nat. Commun. *10*, 1–10. 10.1038/s41467-019-11471-8.
23. Morita, M.T. (2010). Directional Gravity Sensing in Gravitropism. Annu. Rev. Plant Biol. *61*, 705–720. 10.1146/annurev.arplant.043008.092042.
24. Friml, J., Wisniewska, J., Benkova, E., Mendgen, K., and Palme, K. (2002). Lateral relocation of auxin efflux regulator PIN3 mediates tropism in Arabidopsis. Nature *415*, 806–809. 10.1038/415806a.
25. Kleine-Vehn, J., Ding, Z., Jones, A.R., Tasaka, M., Morita, M.T., and Friml, J. (2010). Gravity-induced PIN transcytosis for polarization of auxin fluxes in gravity-sensing root cells. Proc. Natl. Acad. Sci. U. S. A. *107*, 22344–22349. 10.1073/pnas.1013145107.
26. Luschnig, C., Gaxiola, R.A., Grisafi, P., and Fink, G.R. (1998). EIR1, a root-specific protein involved in auxin transport, is required for gravitropism in Arabidopsis thaliana. Genes Dev. *12*, 2175–2187. 10.1101/gad.12.14.2175.
27. Swarup, R., Friml, J., Marchant, A., Ljung, K., Sandberg, G., Palme, K., and Bennett, M. (2001). Localization of the auxin permease AUX1 suggests two functionally distinct hormone transport pathways operate in the Arabidopsis root apex. Genes Dev. *15*, 2648–2653. 10.1101/gad.210501.
28. Fendrych, M., Akhmanova, M., Merrin, J., Glanc, M., Hagihara, S., Takahashi, K., Uchida, N., Torii, K.U., and Friml, J. (2018). Rapid and reversible root growth inhibition by TIR1 auxin signalling. Nat. Plants *4*, 453–459. 10.1038/s41477-018-0190-1.
29. Baster, P., Robert, S., Kleine-Vehn, J., Vanneste, S., Kania, U., Grunewald, W., De Rybel, B., Beeckman, T., and Friml, J. (2013). SCFTIR1/AFB-auxin signalling regulates PIN vacuolar trafficking and auxin fluxes during root gravitropism. EMBO J. *32*, 260–274. 10.1038/emboj.2012.310.
30. Retzer, K., Akhmanova, M., Konstantinova, N., Malínská, K., Leitner, J., Petrášek, J., and Luschnig, C. (2019). Brassinosteroid signaling delimits root gravitropism via sorting of the Arabidopsis PIN2 auxin transporter. Nat. Commun. *10*, 1–15. 10.1038/s41467-019-13543-1.
31. Dubey, S.M., Han, S., Stutzman, N., Prigge, M.J., Medvecká, E., Platre, M.P., Busch, W., Fendrych, M., and Estelle, M. (2023). The AFB1 auxin receptor controls the cytoplasmic auxin response pathway in Arabidopsis thaliana. Mol. Plant *16*, 1120–1130. 10.1016/j.molp.2023.06.008.

32. Tan, S., Luschnig, C., and Friml, J. (2021). Pho-view of Auxin: Reversible Protein Phosphorylation in Auxin Biosynthesis, Transport and Signaling. Mol. Plant *14*, 151–165. 10.1016/J.MOLP.2020.11.004.
33. Zourelidou, M., Absmanner, B., Weller, B., Barbosa, I.C.R., Willige, B.C., Fastner, A., Streit, V., Port, S.A., Colcombet, J., van Bentem, S. de la F., et al. (2014). Auxin efflux by PIN-FORMED proteins is activated by two different protein kinases, D6 PROTEIN KINASE and PINOID. Elife *2014*. 10.7554/ELIFE.02860.
34. Jia, W., Li, B., Li, S., Liang, Y., Wu, X., Ma, M., Wang, J., Gao, J., Cai, Y., Zhang, Y., et al. (2016). Mitogen-Activated Protein Kinase Cascade MKK7-MPK6 Plays Important Roles in Plant Development and Regulates Shoot Branching by Phosphorylating PIN1 in Arabidopsis. PLOS Biol. *14*, e1002550. 10.1371/journal.pbio.1002550.
35. Vega, A., Fredes, I., O'Brien, J., Shen, Z., Ötvös, K., Abualia, R., Benkova, E., Briggs, S.P., and Gutiérrez, R.A. (2021). Nitrate triggered phosphoproteome changes and a PIN2 phosphosite modulating root system architecture. EMBO Rep. *22*, 1–19. 10.15252/embr.202051813.
36. Ötvös, K., Marconi, M., Vega, A., O'Brien, J., Johnson, A., Abualia, R., Antonielli, L., Montesinos, J.C., Zhang, Y., Tan, S., et al. (2021). Modulation of plant root growth by nitrogen source-defined regulation of polar auxin transport. EMBO J. *40*, 1–21. 10.15252/embj.2020106862.
37. Dhonukshe, P., Huang, F., Galvan-Ampudia, C.S., Mähönen, A.P., Kleinevehn, J., Xu, J., Quint, A., Prasad, K., Friml, J., Scheres, B., et al. (2015). Plasma membrane-bound AGC3 kinases phosphorylate PIN auxin carriers at TPRXS(N/S) motifs to direct apical PIN recycling. Dev. *142*, 2386–2387. 10.1242/dev.127415.
38. Jupe, F., Rivkin, A.C., Michael, T.P., Zander, M., Motley, S.T., Sandoval, J.P., Keith Slotkin, R., Chen, H., Castanon, R., Nery, J.R., et al. (2019). The complex architecture and epigenomic impact of plant T-DNA insertions. PLoS Genet. *15*, 1–25. 10.1371/journal.pgen.1007819.
39. Tena, G. (2023). ABP1's new partners. Nat. Plants *9*, 1941. 10.1038/s41477-023-01603-w.
40. Kuhn, A., and Weijers, D. (2024). Distant cousins come to ABP1's rescue. Sci. China Life Sci. *67*, 219–220. 10.1007/s11427-023-2498-0.
41. Dai, N., Wang, W., Patterson, S.E., and Bleecker, A.B. (2013). The TMK Subfamily of Receptor-Like Kinases in Arabidopsis Display an Essential Role in Growth and a Reduced Sensitivity to Auxin. PLoS One *8*, 60990. 10.1371/journal.pone.0060990.
42. Gelová, Z., Gallei, M., Pernisová, M., Brunoud, G., Zhang, X., Glanc, M., Li, L., Michalko, J., Pavlovičová, Z., Verstraeten, I., et al. (2021). Developmental roles of Auxin Binding Protein 1 in Arabidopsis thaliana. Plant Sci. *303*, 110750. 10.1016/j.plantsci.2020.110750.
43. Dunwell, J.M., Purvis, A., and Khuri, S. (2004). Cupins: The most functionally diverse protein superfamily? Phytochemistry *65*, 7–17. 10.1016/j.phytochem.2003.08.016.
44. Chang, C., Eric Schaller, G., Patterson, S.E., Kwok, S.F., and Meyerowitz, E.M. (1992). The TMKl Gene from Arabidopsis Codes for a Protein with Structural and Biochemical Characteristics of a Receptor Protein Kinase. Plant Cell *4*, 1263–1271. 10.1105/tpc.4.10.1263.
45. Oh, M.H., Wang, X., Kota, U., Goshe, M.B., Clouse, S.D., and Huber, S.C. (2009). Tyrosine phosphorylation of the BRI1 receptor kinase emerges as a component of brassinosteroid signaling in Arabidopsis. Proc. Natl. Acad. Sci. U. S. A. *106*, 658–663. 10.1073/PNAS.0810249106.
46. Wang, X., Goshe, M.B., Soderblom, E.J., Phinney, B.S., Kuchar, J.A., Li, J., Asami, T.,

Yoshida, S., Huber, S.C., and Clouse, S.D. (2005). Identification and Functional Analysis of in Vivo Phosphorylation Sites of the Arabidopsis BRASSINOSTEROID-INSENSITIVE1 Receptor Kinase. Plant Cell *17*, 1685–1703. 10.1105/TPC.105.031393.

47. Xu, T., Wen, M., Nagawa, S., Fu, Y., Chen, J.G., Wu, M.J., Perrot-Rechenmann, C., Friml, J., Jones, A.M., and Yang, Z. (2010). Cell surface- and Rho GTPase-based auxin signaling controls cellular interdigitation in Arabidopsis. Cell *143*, 99–110. 10.1016/j.cell.2010.09.003.
48. Xu, T., Dai, N., Chen, J., Nagawa, S., Cao, M., Li, H., Zhou, Z., Chen, X., De Rycke, R., Rakusová, H., et al. (2014). Cell surface ABP1-TMK auxin-sensing complex activates ROP GTPase signaling. Science (80-.). *343*, 1025–1028. 10.1126/science.1245125.
49. Smokvarska, M., Jaillais, Y., and Martinie, A. (2021). Function of membrane domains in rho-of-plant signaling. 663–681. 10.1093/plphys/kiaa082.
50. Pan, X., Fang, L., Liu, J., Senay-Aras, B., Lin, W., Zheng, S., Zhang, T., Guo, J., Manor, U., Van Norman, J., et al. (2020). Auxin-induced signaling protein nanoclustering contributes to cell polarity formation. Nat. Commun. *11*, 1–14. 10.1038/s41467-020-17602-w.
51. Kleine-Vehn, J., Leitner, J., Zwiewka, M., Sauer, M., Abas, L., Luschnig, C., and Friml, J. (2008). Differential degradation of PIN2 auxin efflux carrier by retromer-dependent vacuolar targeting. Proc. Natl. Acad. Sci. U. S. A. *105*, 17812–17817. 10.1073/PNAS.0808073105.
52. Lin, W., Zhou, X., Tang, W., Takahashi, K., Pan, X., Dai, J., Ren, H., Zhu, X., Pan, S., Zheng, H., et al. (2021). TMK-based cell-surface auxin signalling activates cell-wall acidification. Nature *599*, 278–282. 10.1038/s41586-021-03976-4.
53. Dai, N., Wang, W., Patterson, S.E., and Bleecker, A.B. (2013). The TMK Subfamily of Receptor-Like Kinases in Arabidopsis Display an Essential Role in Growth and a Reduced Sensitivity to Auxin. PLoS One *8*, 60990. 10.1371/journal.pone.0060990.
54. Marquès-Bueno, M.M., Armengot, L., Noack, L.C., Bareille, J., Rodriguez, L., Platre, M.P., Bayle, V., Liu, M., Opdenacker, D., Vanneste, S., et al. (2021). Auxin-Regulated Reversible Inhibition of TMK1 Signaling by MAKR2 Modulates the Dynamics of Root Gravitropism. Curr. Biol. *31*, 228–237. 10.1016/J.CUB.2020.10.011.
55. Wang, J., Chang, M., Huang, R., Jiri, F., Yu, Y., Wen, M., Yang, Z., and Xu, T. (2022). Self-regulation of PIN1-driven auxin transport by cell surface-based auxin signaling in Arabidopsis. BioRxiv. https://doi.org/10.1101/2022.11.30.518523.
56. Brady, S.M., Orlando, D.A., Lee, J.Y., Wang, J.Y., Koch, J., Dinneny, J.R., Mace, D., Ohler, U., and Benfey, P.N. (2007). A high-resolution root spatiotemporal map reveals dominant expression patterns. Science (80-.). *318*, 801–806. 10.1126/SCIENCE.1146265.
57. Zhang, H., Zhang, F., Yu, Y., Feng, L., Jia, J., Liu, B., Li, B., Guo, H., and Zhai, J. (2020). A Comprehensive Online Database for Exploring ~20,000 Public Arabidopsis RNA-Seq Libraries. Mol. Plant *13*, 1231–1233. 10.1016/j.molp.2020.08.001.
58. Cao, M., Chen, R., Li, P., Yu, Y., Zheng, R., Ge, D., Zheng, W., Wang, X., Gu, Y., Gelová, Z., et al. (2019). TMK1-mediated auxin signalling regulates differential growth of the apical hook. Nature *568*, 240–243. 10.1038/s41586-019-1069-7.
59. Gao, Y., Zhang, Y., Zhang, D., Dai, X., Estelle, M., and Zhao, Y. (2015). Auxin binding protein 1 (ABP1) is not required for either auxin signaling or Arabidopsis development. Proc. Natl. Acad. Sci. U. S. A. *112*, 2275–2280. 10.1073/PNAS.1500365112.
60. Friml, J.J., Vieten, A., Sauer, M., Weijers, D., Schwarz, H., Hamann, T., Offringa, R., Jurgens, G., Cao, M., Chen, R., et al. (2003). Efflux-dependent auxin gradients establish

the apical-basal axis of Arabidopsis. Nature *426*, 147–153. 10.1038/nature02085.
61. Xu, J., and Scheres, B. (2005). Dissection of arabidopsis ADP-ribosylation factor 1 function in epidermal cell polarity. Plant Cell *17*, 525–536. 10.1105/tpc.104.028449.
62. Asai, S., Cevik, V., Jones, J.D.G., and Shirasu, K. (2023). Cell-specific RNA profiling reveals host genes expressed in Arabidopsis cells haustoriated by downy mildew. Plant Physiol. *193*, 259–270. 10.1093/plphys/kiad326.
63. Jaillais, Y., Hothorn, M., Belkhadir, Y., Dabi, T., Nimchuk, Z.L., Meyerowitz, E.M., and Chory, J. (2011). Tyrosine phosphorylation controls brassinosteroid receptor activation by triggering membrane release of its kinase inhibitor. Genes Dev. *25*, 232–237. 10.1101/gad.2001911.
64. Simon, M.L.A., Platre, M.P., Assil, S., van Wijk, R., Chen, W.Y., Chory, J., Dreux, M., Munnik, T., and Jaillais, Y. (2014). A multi-colour/multi-affinity marker set to visualize phosphoinositide dynamics in Arabidopsis. Plant J. *77*, 322–337. 10.1111/tpj.12358.
65. Karimi, M., Depicker, A., and Hilson, P. (2007). Recombinational cloning with plant gateway vectors. Plant Physiol. *145*, 1144–1154. 10.1104/pp.107.106989.
66. Lampropoulos, A., Sutikovic, Z., Wenzl, C., Maegele, I., Lohmann, J.U., and Forner, J. (2013). GreenGate - A novel, versatile, and efficient cloning system for plant transgenesis. PLoS One *8*. 10.1371/journal.pone.0083043.
67. Huang, R., Zheng, R., He, J., Zhou, Z., Wang, J., Xiong, Y., and Xu, T. (2019). Noncanonical auxin signaling regulates cell division pattern during lateral root development. Proc. Natl. Acad. Sci. U. S. A. *116*, 21285–21290. 10.1073/PNAS.1910916116/SUPPL_FILE/PNAS.1910916116.SAPP.PDF.
68. Ashkenazy, H., Abadi, S., Martz, E., Chay, O., Mayrose, I., Pupko, T., and Ben-Tal, N. (2016). ConSurf 2016: an improved methodology to estimate and visualize evolutionary conservation in macromolecules. Nucleic Acids Res. *44*, W344–W350. 10.1093/NAR/GKW408.
69. Yariv, B., Yariv, E., Kessel, A., Masrati, G., Chorin, A. Ben, Martz, E., Mayrose, I., Pupko, T., and Ben-Tal, N. (2023). Using evolutionary data to make sense of macromolecules with a “face-lifted” ConSurf. Protein Sci. *32*, 1–12. 10.1002/pro.4582.
70. Madeira, F., Pearce, M., Tivey, A.R.N., Basutkar, P., Lee, J., Edbali, O., Madhusoodanan, N., Kolesnikov, A., and Lopez, R. (2022). Search and sequence analysis tools services from EMBL-EBI in 2022. Nucleic Acids Res. 10.1093/NAR/GKAC240.
71. Waterhouse, A.M., Procter, J.B., Martin, D.M.A., Clamp, M., and Barton, G.J. (2009). Jalview Version 2—a multiple sequence alignment editor and analysis workbench. Bioinformatics *25*, 1189–1191. 10.1093/BIOINFORMATICS/BTP033.
72. Reiser, L., Subramaniam, S., Zhang, P., and Berardini, T. (2022). Using the Arabidopsis Information Resource (TAIR) to Find Information About Arabidopsis Genes. Curr. Protoc. *2*, 1–43. 10.1002/cpz1.574.
73. Mi, H., Muruganujan, A., Casagrande, J.T., and Thomas, P.D. (2013). Large-scale gene function analysis with the panther classification system. Nat. Protoc. *8*, 1551–1566. 10.1038/nprot.2013.092.
74. Supek, F., Bošnjak, M., Škunca, N., and Šmuc, T. (2011). REVIGO Summarizes and Visualizes Long Lists of Gene Ontology Terms. PLoS One *6*, e21800. 10.1371/journal.pone.0021800.
75. Czechowski, T., Stitt, M., Altmann, T., Udvardi, M.K., and Scheible, W.R. (2005). Genome-wide identification and testing of superior reference genes for transcript normalization in arabidopsis. Plant Physiol. *139*, 5–17. 10.1104/pp.105.063743.
76. Grones, P., Chen, X., Simon, S., Kaufmann, W.A., De Rycke, R., Nodzyński, T.,

Zažímalová, E., and Friml, J. (2015). Auxin-binding pocket of ABP1 is crucial for its gain-of-function cellular and developmental roles. J. Exp. Bot. *66*, 5055–5065. 10.1093/jxb/erv177.

77. Malamy, J.E., and Benfey, P.N. (1997). Organization and cell differentiation in lateral roots of Arabidopsis thaliana. Development *124*, 33–44. 10.1242/dev.124.1.33.
78. Xu, W., Ding, G., Yokawa, K., Baluška, F., Li, Q.F., Liu, Y., Shi, W., Liang, J., and Zhang, J. (2013). An improved agar-plate method for studying root growth and response of Arabidopsis thaliana. Sci. Rep. *3*, 1–7. 10.1038/srep01273.
79. Thomas, M., Soriano, A., O'Connor, C., Crabos, A., Nacry, P., Thompson, M., Hrabak, E., Divol, F., and Péret, B. (2023). Pin2 Mutant Agravitropic Root Phenotype Is Conditional and Nutrient-Sensitive. Plant Sci. *329*. 10.1016/j.plantsci.2023.111606.
80. von Wangenheim, D., Hauschild, R., Fendrych, M., Barone, V., Benková, E., and Friml, J. (2017). Live tracking of moving samples in confocal microscopy for vertically grown roots. Elife *6*. 10.7554/eLife.26792.
81. Hayashi, Y., Nakamura, S., Takemiya, A., Takahashi, Y., Shimazaki, K., and Kinoshita, T. (2010). Biochemical Characterization of In Vitro Phosphorylation and Dephosphorylation of the Plasma Membrane H+-ATPase. Plant Cell Physiol. *51*, 1186–1196. 10.1093/pcp/pcq078.
82. Tan, S., Abas, M., Verstraeten, I., Glanc, M., Molnár, G., Hajný, J., Lasák, P., Petřík, I., Russinova, E., Petrášek, J., et al. (2020). Salicylic Acid Targets Protein Phosphatase 2A to Attenuate Growth in Plants. Curr. Biol. *30*, 381–395. 10.1016/j.cub.2019.11.058.

2.4 Chapter four: TMK interacting network of receptor like kinases for auxin canalization and beyond

Adapted and modified from:

Monzer A, Mazur E, Rodriguez L, Gallei M, et al. TMK interacting network of receptor like kinases for auxin canalization and beyond. Preprint at https://doi.org/10.1101/2025.02.28.640727 (2025).

TMK1-mediated signaling plays a crucial role in regulating a wide range of developmental processes in plants, making it essential to understand the mechanisms underlying its regulation and the diversity of its signaling pathways. This study investigates the role of novel leucine-rich repeat receptor-like kinases (TINT1–TINT7) as interactors of TMK1 to gain deeper insights into its roles and regulation. By characterizing their evolutionary, structural, and functional properties, we explore their contribution to auxin canalization, a key process in vasculature formation and regeneration. Using molecular and genetic approaches, we demonstrate that most TINTs are involved in canalization. Additionally, we uncover the involvement of TINT-TMK1 interactions in other developmental processes, such as stomatal movement and the gravitropic response of the hypocotyl. Our findings position TINTs as integral components of TMK1-mediated signaling, broadening our understanding of auxin-regulated developmental pathways.

2.4.1 Introduction

The transition of plants to life on land brought numerous challenges, requiring adaptation to constantly changing and often harsh terrestrial conditions. As sessile organisms unable to move to evade unfavorable conditions, plants evolved sophisticated mechanisms to perceive and respond to diverse environmental signals. This adaptive pressure drove the significant expansion of the plasma membrane (PM) receptor-like kinase (RLK) family in land plants, with the model *Arabidopsis thaliana* harboring over 600 RLKs[1]. These receptors enable plants to detect diverse extracellular and environmental signals and activate intracellular signaling pathways crucial for adaptive growth and development[2].

The largest subclass of RLKs is the leucine-rich repeat (LRR) RLKs[3], distinguished by a conserved cytosolic kinase domain (KD) and a variable extracellular domain (ECD) featuring different numbers of LRRs[4]. This structural variability enables them to recognize a wide range of hormonal, peptide-based or other extracellular ligands and regulate diverse biological functions[5]. For instance, BRASSINOSTEROID INSENSITIVE 1 (BRI1) perceives brassinosteroids to regulate plant growth and development[6], while FLAGELLIN SENSING 2 (FLS2) recognizes bacterial flagellin and triggers plant immune responses[7].

Auxin is an essential plant hormone that plays a critical role in growth and development[8]. It regulates a broad spectrum of biological functions through two currently known signaling pathways[9]. The first is the canonical Transport Inhibitor Response 1/Auxin Signaling F-box (TIR1/AFB)-based pathway[10], and the second involves the cell surface complex of the Auxin-Binding Protein 1 (ABP1)/ABP1-likes (ABLs) and Transmembrane Kinase 1 (TMK1)[11,12]. Following auxin perception , the ABP1-TMK1 complex triggers an ultrafast phosphorylation response of thousands of proteins[11,13], potentially regulating diverse cellular processes.

The TMK family in *Arabidopsis thaliana* includes four LRR-RLKs[14]. TMK1 was first identified in 1992[15] and later linked to key processes in auxin-regulated plant development. TMK1 regulates processes, such as root growth [16], lateral root development[17], and the interdigitation of epidermal pavement cells (PCs)[12,18]. Additionally, TMK1 is implicated in apical hook maintenance[19–21] through a unique mechanism where its kinase domain is cleaved and translocated to the nucleus, where it phosphorylates transcriptional regulators. In other processes, such as root bending[22,23] or organogenesis[24], TMK1 interacts with and phosphorylates PIN auxin transporters[25], thereby regulating intercellular auxin fluxes. TMKs, particularly TMK4[26,27], are also involved in the regulation of auxin biosynthesis and mediate crosstalk between auxin and other hormones, such as brassinosteroids[28] and abscisic acid[29].
A particularly fascinating and important auxin-dependent process is auxin canalization[30,31]. Here, the gradual formation of narrow PIN-expressing, auxin transporting channels, involving coordinated tissue polarization and specification, provides positional information for vasculature formation. Auxin canalization relies on a feedback between auxin signaling and directional auxin transport, primarily mediated by PINs[8]. This process ensures that newly formed organs integrate seamlessly with the preexisting vasculature[32,33], mediates formation[34] and regeneration[35] of vasculature, thus maintaining connectivity and functional coherence within the plant. Both TMK1 and ABP1 play critical roles in auxin canalization, specifically in vasculature formation and regeneration[11]. Another complex at the cell surface, involved in auxin canalization by phosphorylating PIN1, consists of two other LRR-RLKs, the Canalization-related Auxin-regulated Malectin-type RLK (CAMEL) and the Canalization-related Receptor-like Kinase (CANAR)[36]. However, auxin canalization is a complex mechanism[31], and many additional players and regulatory mechanisms are yet to be discovered.
To gain novel insights into mechanism of canalization and TMK regulation, we identified, among the PM network of LRR-RLKs, TMK interacting partners (TINTs), which act as potential co-receptors or regulators. Here, we characterize seven of these interactors and explore their roles in auxin signaling and plant development, with a particular focus on auxin canalization.

2.4.2 Results

2.4.2.1 Bioinformatical identification and characterization of TMK interactors

To identify additional players involved in TMK functions, we explored the cell surface interaction network of *Arabidopsis*[37], which encompasses thousands of binary interactions between the extracellular domains of different LRR-RLKs.
Mining this dataset for TMK1-4 revealed an extensive network of TMK interactors (Fig. 1a). From this network, we selected seven most promising potential TMK1 interactors, whose interaction with TMK1 we confirmed *in planta* (Fig. S2). We designated these TMK INTeractors as TINT1 through TINT7 (Fig. S1b). Some of the TINTs have been previously mentioned in different contexts. TINT1 (also known as LRR1) is involved in plant responses to drought[38]. TINT3 (Pollen-specific Receptor-like Kinase 7, PRK7) belongs to the family of pollen-specific receptor-like kinases[39]. TINT6 (Clavata3 Insensitive Receptor Kinase 4, CIK4) functions as a co-receptor for various receptors, prominent among them, the CLAVATA family[40,41].
Phylogenetic analysis revealed that TINTs are not evolutionary close to each other or to TMKs (Fig. S1a). They belong to different subfamilies of the LRR-RLK family based on the number of LRRs in their extracellular domains. TMKs are members of subfamily IX, whereas TINT1, TINT2, TINT3, and TINT4 belong to the subfamily III, TINT5 to subfamily VI, TINT6 to subfamily II, and TINT7 - the largest of the identified interactors - to subfamily XI (Fig. 1c).

Sequence alignment of the kinase domains showed that the ATP-binding lysine (K) is conserved in all TINTs except TINT5 (Fig. 1d). However, subdomain VIb (HRD motif), which forms the catalytic loop, and subdomain VII (DFG motif), which constitutes the activation loop, are conserved only in TINT6 and TINT7 and show alterations in other TINTs (Fig. 1b). This suggests that TINT1 – TINT5 may function as kinase-dead or pseudokinases.
Overall, these analyses identified seven TMK interactors from the LRR-RLKs family, constituting an evolutionary and structurally diverse group; likely including both active and non-active kinases. This diversity is consistent with the role of TMKs as central regulators of many different developmental processes.

2.4.2.2 Confirmation of interaction between TMK1 and TINTs

We employed multiple approaches to confirm *in vivo* the interaction between TMK1 and the selected interactors.
Using a bimolecular fluorescence complementation (BiFC) assay in *Nicotiana benthamiana* leaves, we verified the interaction between the full-length TMK1 with TINT2, TINT3, and TINT4 (Fig. S2a). TMK1 dimerization served as a positive control, whereas TMK2 was used as a negative control for the interaction with TMK1.
We also performed co-immunoprecipitation (co-IP) experiments using different plant tissues. First, we conducted co-IP from *Arabidopsis thaliana* seedlings expressing HA-tagged TINT1, TINT2, TINT3, TINT4, or TINT5 under the ubiquitin (UBQ) promoter. We used an anti-HA antibody for immunoprecipitation, followed by immunoblotting with a specific anti-TMK1 antibody. The results showed that TMK1 can be co-immunoprecipitated with these interactors (Fig. S2b).
To test the interaction of TMK1 with TINT6 and TINT7, we co-expressed FLAG-tagged TMK1 with HA-tagged TINT6 or TINT7 in *Nicotiana benthamiana* leaves. Immunoprecipitation of TINT6 or TINT7 with an anti-HA antibody followed by immunoblotting with an anti-TMK1 antibody demonstrated a co-immunoprecipitation between TMK1 and these two TINTs (Fig. S2c).
Altogether, these results provided *in vivo* confirmation of interactions between TMK1 and TINT1-TINT7.

2.4.2.3 TINT5 localizes to PM, where it interacts with CAMEL LRR-RLK

During further exploration of the LRR-RLK interaction network[37], we noticed that TINT5 is a potential interactor of CANAR, which forms complex with CAMEL and, similarly to TMKs, is involved in canalization[36]. To investigate this interaction, we used Förster resonance energy transfer combined with fluorescence-lifetime imaging microscopy (FRET-FLIM) in *Arabidopsis* protoplasts. We co-expressed GFP-tagged TINT5 with mCherry-tagged CAMEL or CANAR, and quantified the GFP lifetime. The GFP lifetime at the PM showed a significant decrease when TINT5 was co expressed with CAMEL, whereas no significant change was observed with CANAR (Fig. 2a-b). This suggests an interaction between TINT5 and CAMEL at the PM.
To confirm the PM localization, a characteristic presumably shared by all LRR-RLKs[42], we examined TINT5 as an example. We identified a homologous gene to TINT5, sharing 78% nucleotide sequence similarity, which we named TINT5-like. We generated the *pTINT5::TINT5-3HA* and *pTINT5-like::TINT5-like-3HA* transgenic lines to investigate their cellular localization by immunolocalization in *Arabidopsis* seedlings using anti-HA antibodies. This revealed that TINT5 is localized at the PM of the endodermal, epidermal and cortical cells; in the latter two cell files, it co-localizes with TINT5-like (Fig. 2c).

These observations on the example of TINT5 and its homologue show that TINTs are localized at the PM and may link TMKs to other LRR-RLK canalization components such as CAMEL/CANAR.

2.4.2.4 *TINT*s' expression pattern in seedlings

To gain insights into the expression pattern of TINT genes, we first explored publicly available transcriptome data databases[60]. The median Fragments per Kilobase of transcript per Million mapped reads (FPKM) expression values across plant tissues, for *TINT1* to *TINT7* and *TMK1*, revealed distinct expression patterns among these genes (Fig. S3b). *TINT3*, *TINT4*, *TINT6*, and *TINT7* showed low to no expression in specific tissues, while *TMK1*, *TINT1*, *TINT2*, and *TINT5* exhibited moderate to high expression in several tissues.

Next, we examined their spatial expression patterns more closely using transgenic lines harboring a β-glucuronidase (*GUS*) reporter gene driven by the promoter of each *TINT* gene and compared them with *pTMK1::GUS* line in our analysis (Fig. S3a). 5-days-old seedling analysis revealed that *TINT1* is strongly expressed in the elongation zone of the root, with a weaker expression extending towards the root tip and in the vasculature of the cotyledons. *TINT2* showed more focused expression in the root tip, particularly in the root cap and meristematic zone, with some extension into the elongation zone and also in the root-hypocotyl junction. *TINT3* was primarily expressed in the root-hypocotyl junction and in lateral root primordia. *TINT4* expression was restricted to the root-hypocotyl junction. *TINT5* showed expression in both the root tip and the root-hypocotyl junction, while *TINT6* was localized to the root cap and meristematic zone in the root tip. Finally, *TINT7* was exclusively expressed in the cotyledons, showing a strong and distinct pattern along its vasculature and also in the stomata. The *pTINT1-7::GUS* expression patterns largely overlaps with that of *pTMK1::GUS*, in particular in the root tip.

As expected, the *TINT* genes show overlapping but distinct expression patterns in *Arabidopsis* seedlings. Most *TINT* genes are expressed in root regions, while *TINT7* is uniquely expressed in the cotyledon vasculature and stomata.

2.4.2.5 *TINTs'* expression during vasculature regeneration in inflorescence stems

As the main developmental role of the ABP1-TMK auxin perception complex is in auxin canalization-mediated vasculature regeneration[11], we focused on the role of *TINTs* in this process. First, we analyzed their spatial and temporal expression patterns in inflorescence stems following at 2, 4 and 6 days after wounding (DAW), which interrupted the stem vasculature. Using the *TINT::GUS* lines, we inferred TINT promotor activity associated with vasculature regeneration (Fig. 3).

As shown previously[11], *TMK1::GUS* showed elevated GUS activity at 2 DAW in the outer tissues of the wounded area, with a further increase at 4 and 6 DAW, particularly around the wound (Fig. 3a). The expression was notably stronger in the differentiating cells. Similarly, *TINT1::GUS* exhibited a gradual increase in signal around the wound, with the highest levels observed at 6 DAW. *TINT2* displayed elevated expression above the wound at 2 DAW, extending around the wound at 4 and 6 DAW (Fig. S4). In contrast, *TINT3* had no expression at 2 DAW, confined to the outer tissues, with a slight extension to the area around the wound at 4 and 6 DAW. *TINT4* was expressed around and below the wound at 2 DAW, as well as in a narrow area around the wound. At 4 and 6 DAW, GUS activity was very high and extended throughout the area surrounding the wound. *TINT5* showed increased expression in the outer tissues above the wound at 2 DAW, followed by a stronger response around the wound at 4 DAW. However, by 6 DAW, *TINT5* expression decreased, remaining only in cells around the

wound. *TINT6* demonstrated extended expression in cells around the wound but no activity was detected in the regenerated vasculature. *TINT7* was expressed only in the preexisting vasculature, particularly in the vascular bundles and below the wound, with no expression observed around the wound (Fig. S4).
Taken together, most of the *TINT* genes are expressed during vasculature regeneration, displaying partially overlapping temporal and spatial expression patterns with strong expression around the wound (such as *TINT1*, *TINT2* and *TINT4*), while *TINT7* remains confined to the preexisting vasculature.

2.4.2.6 **Vasculature regeneration defects in *tint* mutant stems**

To test the functional requirement of TINTs in vasculature regeneration, we isolated and confirmed *tint* loss-of-function mutants. (Fig. S1c).
We assessed the ability of these mutants to regenerate vasculature in the inflorescence stems following wounding. A precise cut was made in the stems, and after 6 days, Toluidine Blue O (TBO) staining was used to visualize the differentiated vasculature (Fig.4a). In the wild type (WT) plants, fully developed vasculature successfully circumvented the wound site with visible connections between the preexisting and newly formed vasculature (Fig. 4b). Similarly, *tint1*, *tint2*, and *tint4* showed complete regeneration of vasculature around the wound (Fig. 4c, Fig. S5). In contrast, regeneration in *tint3*, *tin5*, *tint6*, and *tint7* was either partial or completely absent, with respective percentages (90%, 60%, 100% and 100%) indicating the combined frequency of partial or no regeneration observed (Fig. 4c). These vasculature regeneration defects closely resembled those observed in the *tmk* mutants (Fig. 4b). Notably, when we examined the venation patterns in the cotyledons of *tint* loss-of-function mutants, all of them showed normal development, forming the typical 4-loop vein pattern as in WT (Fig. S5c). This is consistent with largely normal venation in *tmk* mutants. Thus, *tint3*, *tint5*, *tint6* and *tint7*, similar to *tmk* mutants, show specific defects in vasculature regeneration (Fig. 4b-c).
To further test the common action of TINTs and TMKs in vasculature regeneration, we generated and tested some *tint tmk1* double mutants. The *tint5 tmk1-1* double mutant showed a more pronounced defect than the single mutants (Fig. S7 a-b). A similar trend was observed in *tint6 tmk1-1* (Fig. S5 a-b) and *tint7 tmk1-1* double mutants (Fig. S5 a-b). These observations suggest that the combined loss of TMK1 with TINT5, TINT6, or TINT7 leads to a more significant disruption in vasculature regeneration.
Altogether, these results collectively show the common function of TMK1 with TINT3, TINT5, TINT6, and TINT7 in vasculature regeneration processes, providing additional genetic support for their interaction with TMK1.

2.4.2.7 **Roles of TINT5 and TINT7 in vasculature regeneration and auxin canalization**

Due to strong defects in vascular regeneration observed in the *tint5*, *tint6* and *tint7* mutants, we selected these genes for an in-depth analysis of their role in auxin canalization.
The key feature of auxin canalization is auxin's ability to promote and form its own transport channels, which in turn establish new vasculature paths[31]. To examine this, we applied a droplet of exogenous auxin (Indole-3-Acetic Acid, IAA) as a localized auxin source to the side of the stem below the wound, to induce *de novo* vasculature formation[43] (Fig. 5a). The forming vasculature was visualized using TBO staining 4 days after application (Fig. 5b). Ninety percent of WT stems formed continuous vasculature from the local auxin source; however, *tint5* and *tint6* exhibited, similarly to the *tmk1-1* mutant, reduced *de novo* vasculature formation, with this effect being more pronounced in the double mutants of *tint5 tmk1-1* and *tint6 tmk1-1* (Fig. 5c). The *tint7* and *tint7 tmk1-1* mutants showed even stronger defects; being

unable to form any vasculature from the auxin source (Fig. 5c, Fig. S6a.). These results demonstrate that TINT5, TINT6 and TINT7 share a common function with TMK1 not only in vasculature regeneration but also in its *de novo* formation from the localized auxin source.
Auxin canalization relies on the feedback loop between auxin perception and its directional transport mediated by PIN auxin transporters, leading to a formation of PIN1-expressing auxin channels [31]. To gain insights into TINT5 and TINT7 involvement in these processes, we visualized auxin-transporting channels using the auxin response marker *DR5rev::GFP*[44] and the *pPIN1::PIN1-GFP*[32]. The gradually narrowing channel-like patterns can be observed both during regeneration after wounding and during *de novo* vasculature formation from the localized auxin source[31,43]. Indeed, as reported in the WT, we observed the formation of DR5- and PIN1-positive channels circumventing the wound and reconnecting the preexisting vasculature (Fig. S6b). Similar DR5- and PIN1-positive channels formed from the places of local auxin application, predicting the formation of new vasculature (Fig. 5e-f). The *tint5* and *tint7* mutants exhibited defective formation of DR5- and PIN1-marked channels in both cases as compared to WT patterns (Fig. 5d, Fig. S6c)). Notably, in the mutants, the GFP-positive cells were positioned at the outer edge of the stem without forming the characteristic channel-like pattern (Fig. S6b).
Altogether, these results collectively establish the involvement of TINT5 and TINT7 in auxin channel formation in a similar way to what has been shown for TMK proteins[11].

2.4.2.8 **TINT5 and TINT5-like are redundantly involved in auxin canalization**

Given that TINT5 has a close homologue, TINT5-like, we tested a potential functional redundancy between these two proteins. We crossed the *tint5* and *tint5-like* single mutants to generate *tint5 tint5-like* double mutant.
We assessed the phenotype of the *tint5 tint5-like* double mutant in vasculature regeneration after wounding and in *de novo* regeneration. Indeed, the *tint5 tint5-like* double mutant exhibited a more severe phenotype than the single mutants in both processes (Fig. S7). This supports the involvement of TINT5 and its homologue in auxin canalization.
These results confirm redundant action of TINT5 and TINT5-like in auxin canalization.

2.4.2.9 **TINT6 in auxin canalization and hypocotyl bending termination processes**

Auxin-induced repolarization of PIN auxin transporters is a key component of the canalization mechanism[31]. Nonetheless, a similar phenomenon has been observed during other processes as well. For example, during shoot gravitropism, auxin-induced repolarization of PIN3 is essential for the termination of gravitropic bending[45]. Thus, these two processes share a common feature of the auxin effect on PIN polarity.
While analyzing gravitropic response of etiolated hypocotyls in different *tint* mutants, we observed impaired responses in the *tint6* and *tint6 tmk1-1* mutants (Fig. 6a). The *tint6* hypocotyls exhibited hyperbending with an average bending angle of 56˚, as compared to WT hypocotyls (angle of about 40 ˚), while the double mutant *tint6 tmk1-1* showed reduced bending with an angle of 34˚ (Fig. 6b).
These results on the *tint6* hypocotyl bending phenotype suggest a genetic link between auxin-induced PIN repolarization during canalization and the termination of gravitropic bending.

2.4.2.10 **Roles of TINT7 and TMK1 in stomata movement**

Given that *TINT7* is unique among *TINTs* for being highly expressed in stomatal cells (Fig. 7a), we investigated its potential function in this context. *TMK1* is also expressed in stomata and plays a significant role in abscisic acid (ABA) signaling[29], a key hormone regulating

stomatal movement and water loss[46]. Nonetheless, the role of TMKs in stomatal movement have never been systematically studied.
To explore a role of TINT7 in stomatal development or function, we first assessed the stomatal density in the *tint7* mutant and the *tint7 tmk1-1* double mutant. No significant differences in stomatal density were observed as compared to WT plants (Fig. S8a). Next, we evaluated the kinetics of stomatal movement (opening and closure) under different conditions. Following exposure to ABA, which promotes stomatal closure[46], the *tint7* mutant exhibited reduced closure compared to WT (Fig. S8b). Conversely, in response to light, the *tint7* mutant, similar to the *tmk1-1* single mutant, displayed greater stomatal opening compared to WT (Fig. 7b-c). This effect was more pronounced in the *tint7 tmk1-1* double mutant, which showed the highest rate and extent of stomatal opening (Fig. 7b-c).
Thus, the impaired stomatal movement phenotype in the *tint7* and *tint7 tmk1-1* mutants reveals a not yet well-characterized role of TMK signaling in this process.

2.4.3 Discussion and conclusion

2.4.3.1 TMK1 is part of large LRR-RLK interaction network

TMK1 is a notable receptor-like kinase involved in a broad range of essential plant functions. Its auxin sensing complex with ABP1 mediates the phosphorylation of about a thousand downstream targets[11,13]. However, the precise mechanisms behind these phosphorylation events remain largely unknown and it is unclear whether this global phosphorylation response underlies all TMKs' functions.
To gain deeper insights into TMKs' roles and regulation, we investigated seven LRR-RLKs as potential TMK1 interactors (TINT), selected from the binary interaction network of LRR-RLKs[37], and confirmed their association with TMK1 *in planta*. Here, we provide the initial characterization of this LRR-RLK TMK interacting network.
TINTs are evolutionary divergent within LRR-RLK family and classified into diverse subfamilies. For instance, TINT6 belongs to subfamily II, which consists mainly of co-receptors[47], some of which regulate meristem maintenance, anther development, and other functions. It is possible that TINT6 also acts as a co-receptor for TMK1 in various biological functions. In contrast, TINT7, being a larger receptor, likely has its own specific ligand, whose signaling converges with TMK-mediated auxin signaling. Notably, the alignment and analysis of the kinase domains revealed that all TINTs, except for TINT6 and TINT7, are likely pseudokinases. Due to their structural flexibility, pseudokinases can bring together multiple components of signaling networks or regulate active kinases allosterically, either enhancing or inhibiting their function[48,49]. This predominance of pseudokinases among TINT interactors raises intriguing questions about whether this pattern is coincidental or indicative of an evolutionary adaptation.
Regardless, the evolutionary, structural, and functional diversity of TINTs suggests that they were co-opted into the TMK pathway at several independent occasions during evolution and likely contribute to the diversity of functions and extensive regulation of TMK-based signaling.

2.4.3.2 TINTs are part of TMK and CAMEL/CANAR regulatory network for auxin canalization

Auxin canalization is fundamental to plant development and survival in response to environmental challenges[31]. This unique property of auxin depends on the feedback regulation between its perception and transport, with ABP1/TMK auxin perception and PIN-mediated auxin transport serving as the respective principal components[11,22,24]. Nonetheless, the further mechanistic details remain poorly understood.

Vasculature regeneration around the wound and *de novo* vasculature formation from the local auxin source are preceded by formation of PIN1- and DR5-positive auxin channels; thus being classical manifestations of auxin canalization[31]. Among the TMK1 interactors, TINT3, TINT5, TINT6, and TINT7, based on the corresponding loss-of-function mutants, are required for these processes, similar to TMKs.
Two other LRR-RLKs, CAMEL and CANAR have been also identified as key components of auxin canalization[36]. Our findings revealed that TINT5 interacts not only with TMK1 but also with CAMEL, which, when considered alongside the very similar auxin canalization and vasculature regeneration defects observed in the *tmks*, *camel* and *tint5* mutants, highlight the potential importance of this interaction network in auxin canalization. Notably, the more pronounced canalization defetcs seen in the *tint5 tmk1-1* double mutant further emphasizes the need to investigate the functional implications of the TINT5 interaction with CAMEL and TMK1 in regulating auxin canalization.
Overall, the involvement of majority of TINTs along with TMKs in auxin canalization processes provides further genetic support for the interaction between TMKs and TINTs. Using TINT5 as an example, it also shows that the TINTs can link TMKs with other canalization components such as CAMEL and CANAR.

2.4.3.3 TMK1 interactors suggest additional roles of TMK-based signaling

TMKs have been implicated in other processes beyond canalization, including apical hook opening, lateral root formation, leaf epidermal cell interdigitation, and others[12,14,16–19,22–24].
Furthermore, other processes besides canalization involve auxin's effect on PIN polarity. One of the best-characterized cases is the termination of shoot gravitropic bending, where, at later stages of the response, auxin accumulating at the lower side of the shoot leads to PIN3 repolarization, which is required for bending termination[45,50]. We found that TINT6 and TMK1 are involved in the gravitropic response of hypocotyls. The hyperbending observed in the *tint6* mutant suggests a disruption in the termination of bending. The rescue of this effect, or even reduced bending in the *tint6 tmk1-1* double mutant, implies a functional interaction between TINT6 and TMK1 in regulating the hypocotyl's gravitropic response. These initial insights link auxin canalization and shoot bending termination genetically; however, the underlying mechanism and whether it involves PIN repolarization remain a topic for future investigation.
Characterization of *TINT7* revealed a connection to stomatal movement. Stomata and their regulated movement are key to regulating gas exchange and water balance, thus playing a vital role in photosynthesis and transpiration[51]. We observed *TINT7* expression in stomata, and the *tint7* mutant showed reduced stomatal closure in response to ABA and enhanced opening in response to light, revealing TINT7's role in stomatal movement. Additionally, the stomatal movement phenotype of *tmk1* and the more pronounced phenotype in the *tint7 tmk1-1* double mutant revealed a common function of TINT7 and TMK1 in this process. Further analysis will establish whether these mutants are more susceptible to water loss due to excessive stomatal opening and reduced responsiveness to ABA, a key hormone induced by osmotic stress during drought[52]. Thus, the TINT7 functional analysis provides the first insight into the role of TMK-mediated signaling in stomatal movement.
In summary, the functional analysis of various TINT proteins confirmed known and revealed new roles of TMKs in different developmental processes.

2.4.4 Material and methods

Plant material, and growth conditions

The *Columbia-0* (*Col-0*) ecotype was the background of all the used lines of *Arabidopsis thaliana* (*A. thaliana*). Seeds were sterilized using chlorine gas overnight, followed by stratification for 48h in the dark at 4°C. Seedlings were grown on ½ MS medium plates (0.44% Murashige and Skoog basal salts, 1% sucrose, and 0.8% phyto-agar, pH 5.7) under long-day conditions (16 h light/ 8 h dark cycles, 22 ± 2°C) for 4 to 10 days, depending on specific assays, or in the soil under similar conditions. The T-DNA insertion line *tmk1-1* (SALK_016360) were previously reported[19]. The other T-DNA insertion lines were obtained from NASC: *tint1* (SALKseq_053366), *tint2* (SALKseq_033657), *tint3* (SALKseq_086592), *tint4* (SALK_094070), *tint5* (SALKseq_131589), *tint5like* (SALK_078409C), *tint6* (SALK_123502C), *tint7* (SALK_101617C).
The GUS lines of *pTINT1* through *TINT5* were obtained and previously reported[53]. The line *pTMK1::GUS* was also previously reported[11].

Plasmid construction and plant transformation
To generate the transgenic GUS lines of *TINT6* and *TINT7,* genomic fragments covering respectively 1000 bp and 1500 bp upstream from the start codon of *TINT6* and *TINT7* were amplified from the genomic DNA (gDNA) of *Col-0* and then inserted into the vector pGWB533. The resulting constructs were transformed into *Arabidopsis* plants by floral dipping in *Agrobacterium tumefaciens* cultures.
To generate the transgenic lines expressing HA-tagged TINT under ubiquitin promoter, the coding sequence (CDS) of each gene, without a stop codon, was amplified from *Col-0* complementary DNA (cDNA) through PCR with the corresponding primers attB1TINTCDS-Fw and attB2TINTnCDS-Rv (Supplementary table 1). This applies for *TINT1* through *TINT5*. By a BP reaction, the resulting sequences were inserted into pDONR221, which were then recombined with *pDONR P4-P1r pUBQ10*[54] and *pDONR P2R-P3 3xHA* into pB7m34GW vector by a MultiSite Gateway LR reaction. The resulting constructs were transformed into *Arabidopsis* plants by floral dipping in *Agrobacterium tumefaciens* cultures.
BiFC constructs were obtained by performing Gateway LR recombination of the gene entry clones with either pDEST–^{GW}SCYNE for SCFP3A^{N} or pDEST–^{GW}SCYCE for SCFP3A^{C} [55].
TINT6 and *TINT7* were amplified using primers with > 15bp overlapping sequences from *Col-0* cDNA, named TINT6/TINT7CDS-Fw and TINT6/TINT7CDS-Rv, designed for the Gibson Assembly method. The amplified sequences were assembled into the linearized *pDONR221* vector to generate the entry clone using the NEBuilder 409 HiFi DNA Assembly kit (E2621L); and then recombined with *pUBQ10*[54] and *pDONR P2R-P3 3xHA* into *pB7m34GW* vector by a MultiSite Gateway LR reaction.
To generate *pTINT5::TINT5-3HA*, *pTINT5-like::TINT5-like-3HA* constructs, we first amplified the promoter regions (1027 bp for *pTINT5* and 1292 bp for *pTINT5-like*) from *Col-0* gDNA with overlapping sequences. The amplified promoters were inserted into the linearized *pDONR P4-P1r* vector to generate the entry clone using the NEBuilder 409 HiFi DNA Assembly kit (E2621L). Similarly, *TINT5* and *TINT5-like* were amplified from *Col-0* cDNA with overlapping sequences, and then assembled into the linearized *pDONR221* vector. The entry clones of the promoter and the CDS regions were recombined by a Multisite Gateway LR reaction with *pDONR P2R-P3 3xHA* into *pB7m34GW* vector.
For FRET-FLIM: *p35S::CANAR-mCherry* and *p35S::CAMEL-mCherry* are previously reported[36]. To generate the construct p*35S::TINT5-GFP,* we used Gateway Cloning to recombine the entry vector of *TINT5* into *pB7FWG2.*
The lines *PIN2::PIN2-GFP*, *DR5rev::GFP* were described before[32,44]. We generated *PIN2::PIN2-GFP* tint5/tin7 and *DR5rev::GFP tint5/tint7* by genetic crosses with *tint5/tint7.*

The mutants *tint5* and *tint5-like* were crossed to generate the double mutant *tint5 tint5-like.* Equally, the double mutants of *tint5/tint6/tint6* were obtained by crosses with *tmk1-1.*

Bioinformatics

The interaction network was built using Cytoscape (version 3.10.3)[56], based on the provided interaction data[37]. The data was imported into Cytoscape, where the network was visualized, analyzed, and further refined to depict potential interactions between the proteins of interest.
The protein sequence alignment was performed using ClustalW, a multiple sequence alignment tool[57]. Sequences were aligned according to the default settings of ClustalW.
The phylogenetic tree was constructed using a multiple sequence alignment, they were performed with the "build" function of ETE3 version 3.1.3[58], as implemented on GenomeNet (https://www.genome.jp/tools/ete/). The tree was generated using FastTree with the slow nearest-neighbor interchange (NNI) method and MLACC=3 to make the maximum-likelihood NNIs more exhaustive[59]. The values at the nodes represent Shimodaira-Hasegawa (SH)-like local support.
The RNA-seq data was retrieved from the available online database on (https://plantrnadb.com/athrdb/)[60]. The expression data was processed and visualized in a heat map to display the median FPKM (fragments per kilobase of transcript per million mapped reads) expression of the genes of interest across different tissues. The heat map was generated using R.

GUS staining

5-day-old seedlings were stained in 0.1 M sodium phosphate buffer (pH 7.0) containing 0.5 mM $K_3[Fe(CN)_6]$, 0.5 mM K4[Fe(CN)6], and X-Gluc at 37°C for 1 h (*TMK1::GUS*), 1.5 h (*TINT2::GUS*, *TINT5::GUS*, *TINT6::GUS*), 2.5 h (*TINT1::GUS*, *TINT3::GUS*, *TINT4::GUS*) or 6 h (*TINT7::GUS*). Further, samples were incubated overnight in 80% (v/v) ethanol at room temperature. Tissue clearing was conducted as previously described[61]. DIC microscopy for analysis of the GUS staining assay was performed using an Olympus BX53 microscope equipped with 10x and 20x air objectives and a DP26 CCD camera.

Vasculature regeneration after wounding in inflorescence stems

The regeneration experiments were performed as described previously[35,43,62]. Immature inflorescence stems (9–10 cm tall) of *Arabidopsis* were decapitated using a sharp razor blade. The apical floral parts (1–2 cm) were removed, and an artificial weight (a 2.5 g lead ball attached to a plastic tube) was applied to the stems. To prevent bending, decapitated stems were supported with a wooden stick. This setup allowed secondary tissue development in the basal parts of the immature stems (5-mm segments above the rosette) within six days of weight application.
For regeneration analysis, the inflorescence stems were precisely wounded with a razor blade about 5 mm from the rosette, in the transversal plane of the basal sectors with vascular cambium and secondary tissues. The plants remained covered with artificial weights throughout the experiment. Axillary buds above the rosette were not removed, serving as the source of endogenous auxin. Stem segments were cut at 0, 4, and 6 days after wounding using an automated vibratome (Leica VT1200 S), then sectioned at 70-µm-thick. Thee native sections were stained with 0.025% TBO aqueous solution, and regeneration was assessed in stems with fully developed, closed cambial rings and secondary tissues in the basal parts. The sections were observed under a bright-field microscope (Zeiss Axioscope.A1), and images of the vasculature were captured at 10× magnification using an Axiocam 506 camera.

The analysis of GFP reporter lines (*DR5rev::GFP* and *PIN1::PIN1-GFP*) was conducted 4 days after wounding using the Olympus FLUOVIEW FV1000 confocal laser-scanning microscope.

GUS staining after wounding in inflorescence stems

For the observation of GUS activity after wounding, the same technique as used for regeneration analysis was applied. After 2, 4, and 6 days of wounding, stem segments were incubated in X-Gluc solution at 37°C. Afterward, they were fixed in 70% ethanol at room temperature. Samples with positive GUS reactions were sectioned at 70 µm using an automated vibratome. The native sections were then cleared in a solution containing 4% HCl and 20% methanol for 15 min at 65°C, followed by incubation in 7% NaOH and 70% ethanol for 15 min at room temperature. To rehydrate the samples, they were incubated in successive ethanol solutions (70%, 50%, 25%, and 10%) for 10 min each at room temperature, followed by a 10-min incubation in a solution of 25% glycerol and 5% ethanol. Finally, the seedlings were mounted in 50% glycerol and observed under a bright-field microscope. GUS activity images were captured at 10× magnification using a camera.

Auxin-induced canalization in inflorescence stems (*de novo* vasculature formation)

The auxin canalization experiments were performed as described before[43], using *Arabidopsis* plants with young, 10-cm-tall inflorescence stems. Stems were wounded by making a transversal incision 3–4 mm above the rosette to disrupt the vascular cambium and secondary tissues, thereby interrupting the polar basipetal auxin transport. Then an exogenous auxin application of 10 µM IAA (Sigma-Aldrich, 15148-2G) in a droplet of lanolin paste was applied below the cut, which was replaced every two days to maintain a consistent auxin presence. Samples were collected, and longitudinal stem sections were manually prepared using a NIKON SMZ1500 stereomicroscope. The sections were stained with 0.05% TBO and mounted in 50% glycerol aqueous solution. Images were captured using an Olympus BX43 microscope with an Olympus SC30 Camera.

The analysis of GFP reporter lines (*DR5rev::GFP* and *PIN1::PIN1-GFP*) was conducted 4 days after local applications using the Olympus FLUOVIEW FV1000 confocal laser-scanning microscope.

Cotyledon vasculature analysis

To observe vein patterns in cotyledons, shoot tissues, including cotyledons from 10-day-old seedlings of each genotype, were harvested and cleared in 70% ethanol for 3 days, with the solution being changed intermittently. The samples were then incubated cleared in a solution containing 4% HCl and 20% methanol for 15 min at 65°C, followed by incubation in 7% NaOH and 70% ethanol for 15 min at room temperature. To rehydrate the samples, they were incubated in successive ethanol solutions (70%, 50%, 25%, and 10%) for 10 min each at room temperature, followed by a 10-min incubation in a solution of 25% glycerol and 5% ethanol. Finally, the seedlings were mounted in 50% glycerol and observed under a stereomicroscope (Olympus SZX16 Stereo).

Vein patterns in the cotyledons were evaluated and categorized as either defective or non-defective. Cotyledons with exactly four closed loops were considered non-defective. Additionally, cotyledons were deemed non-defective if any of the two lower loops were open from the bottom. Conversely, cotyledons exhibiting more or fewer than four loops, any extra branches, or open loops, were classified as defective. The number of analyzed cotyledons was between 80 and 100 per genotype.

Tobacco (*Nicotiana bethamiana)* infiltration

Constructs were transformed into *Agrobacterium tumefaciens* GV3101 and grown on LB plates at 28˚C for 48 hours. Subsequently, liquid LB suspensions carrying the desired plasmids were grown overnight at 28-30 ˚C, after which young tobacco leaves were infiltrated or co-infiltrated. Additionally to an overnight in the dark, the plants were grown under normal conditions for 36 hours. The infiltatred leaves were then either harvested for co-immunoprecipitation assay or used for bimolecular fluorescence complementation (BiFC) imaging.

Bimolecular fluorescence complementation (BiFC) assay in *Nicotiana benthamiana*

BiFC assays in *Nicotiana benthamiana* were performed by co-infiltrating the leaves with *p35s::TMK1-SCFP3A*^{N} and *p35S::TINT-SCFP3A*^{C}, *p35S::TMK1-SCFP3A*^{C}, *or p35S::TMK2-SCFP3A*^{C}. Imaging was then performed two days after using Zeiss LSM800 microscope.

Co-immunoprecipitation (Co-IP) assay

To immunoprecipitate HA-tagged TINT proteins, either 5-day old *Arabidopsis* seedlings from the corresponding transgenic line (expressing HA-tagged TINT under ubiquitin promoter) or leaves from infiltrated or co-infiltrated *Nicotiana benthamiana* (see above) were harvested, ground into powder using liquid nitrogen, and homogenized in the lysis buffer (150 mM NaCl, 1% Triton X-100, 50 mM Tris HCl pH 8, Complete protease cocktail and PhosStop phosphatase inhibitor cocktail (Roche)). The total protein extract is obtained after 30 minutes centrifugation at 14000 g, 4°C. Imunoprecipitation was then performed following the manufacturer's instructions (Miltenyi Biotec) using microMACS beads coupled to a monoclonal anti-HA antibody. The immunoprecipitated proteins antibody were separated by SDS-PAGE using 10% Mini-PROTEAN®TGX™ Precast Protein Gels (Bio-RAD), transferred to a PVDF membrane, and analyzed by immunoblotting. TINT-HA was detected using anti-HA HRP-conjugated, High Affinity (3F10) antibody (Roche), while co-immunoprecipitated TMK1-FLAG from *Nicotiana benthamiana* was detected with anti-FLAG® M2-Peroxidase (HRP) antibody (Sigma). For *Arabidopsis* samples, endogenous TMK1 was detected using anti-TMK1 antibody (Nordic Biosite), which was incubated overnight at 4°C, followed by incubation with anti-rabbit HRP antibody at room temperature for 2 hours. Signal detection was performed using the SuperSignal West Femto Maximum Sensitivity Substrate Detection System (Thermo Scientific), and images were captured with an Amersham 600RGB 604 image analyzer (GE Healthcare).

FRET-FLIM in *Arabidopsis* root suspension culture protoplasts

Protoplasts from *Arabidopsis* root cell suspension cultures were isolated using a PEG-mediated transformation method. Three-day-old cells were collected by centrifugation into a 50 ml Falcon tube and incubated for 3-4 hours in dark in a petri dish containing an enzyme solution. This solution included 1% of Cellulase RS, 0.2% macroenzyme dissolved in the B5-0.34M glucose-mannitol (GM) solution. Following a 5-minute centrifugation and two washes with the GM solution, the cells were transferred to a 0.28M sucrose solution in a 15ml Falcon tube and floated by spinning at 800 rpm for 7 minutes. The floating cells were then collected into a microcentrifuge tube and diluted to a final concentration of $4\times10^{\wedge6}$ cells/mL using the GM solution.

For transfection, 50 µL of protoplasts were mixed with 10 µg of high-purity plasmid DNA corresponding to the appropriate vectors and 150 µL of PEG buffer. The mixture was incubated in the dark at room temperature for 60 minutes, followed by a single wash with $Ca(NO3)_2$

solution. The transfected cells were then resuspended in 500 µL of GM solution, transferred to a 24-well plate, and incubated overnight at room temperature in the dark before imaging.
Imaging of FRET-FLIM experiments was performed the next day using a Leica SP8 equipped with a FALCON FLIM detector. Fluorescence lifetime measurements were acquired using LAS X software (FLIM).

Immunolocalization

Whole-mount *in situ* immunolocalization was performed on 4d old seedlings of *Arabidopsis* following the published protocol[63].The anti-HA antibody (Thermo Fisher, Monoclonal Antibody (2-2.2.14)) was applied at a 1:500 dilution, and the secondary Cy3 Anti-Mouse IgG (Sigma-Aldrich, Sheep Anti-Mouse IgG) was used at a 1:600 dilution. Imaging of the immuno-stained roots was performed using Zeiss LSM800 microscope (Cy3: excitation at 548 nm and emission at 561 nm).

Hypocotyl gravitropism assays

Plates containing *Arabidopsis* seeds were placed vertically in the growth room under light for 6 hours to induce germination. The plates were then covered with aluminum foil and placed in a box to maintain darkness for an additional 4 days. Following this, the seedlings were subjected to a 90-degree rotation to provide gravity stimulation. After 24 hours, the plates were scanned using an EPSON V700 scanner, and the bending angle of the seedlings was measured using ImageJ.

Stomata patterning

Stomatal patterning was analyzed using cotyledons from 10-day-old seedlings. The cotyledons were placed on a slide with water and covered with a cover slip, then imaged using an Olympus BX53 microscope equipped with 10x and 20x air objectives and a DP26 CCD camera. The number of stomata was quantified within a defined area of consistent size across all samples using ImageJ software.

Stomatal movement assays

To prepare samples for stomatal movement assays, healthy 7^{th} or 8^{th} rosette leaves were selected from 4-week-old *Arabidopsis* plants. Leaves were carefully excised to prevent tissue damage, cut into small pieces, and the lower epidermal peel was prepared. The isolated epidermal peels were placed in a 24-well plate, with double-sided tape in each well and a bottom cover slip. Buffer solutions were added to the wells depending on the assay. For the light-induced opening assay, the buffer contained 10 mM MES-KOH (pH 6.15) and 10 mM KCl to induce stomatal closure overnight. For the ABA treatment assay, the buffer included10 mM MES-KOH (pH 6.15), 30 mM KCL and 50 µM $CaCl_2$. The plate was incubated overnight at 22°C under plant growth conditions (150 µmol/m²/s light intensity, 16-hour light/8-hour dark cycle) to stabilize the samples.
The following morning, 3 hours into the circadian light cycle, the epidermal peels were transferred to fresh buffer solutions corresponding to their respective treatments. For the ABA assay, 10 µM ABA was added to induce stomatal closure. For the light-induced opening assay, the peels were exposed to direct light to trigger stomatal opening. Stomatal movements were observed using a Nikon Ti2E inverted microscope with a 40× objective, capturing images every 5 minutes over a 4-hour period. Stomatal widths were measured throughout the experiment using ImageJ image analysis software.

2.4.5 Acknowledgments

We deeply appreciate M. Wrzaczek's constructive input and insightful discussions, which significantly enriched this work. We thank L. Fiedler for helping with the heat map and for the discussions. We also thank the facilities at ISTA, the imaging and optics (IOF) and Lab Support (LSF) facilities for their service and assistance.

2.4.6 Contributions

A.M. took over the project, designed and executed the experiments, analyzed the data, and wrote the manuscript. L.R. contributed to the initial conceptualization and early stages of the project. E.M., M.Z., M.G., M.S., and E.Č. assisted with specific aspects of the methodology and data collection. J.F. conceptualized and supervised the study and contributed to the manuscript writing.

2.4.7 Figures

Figure 1- Overview of TINTs

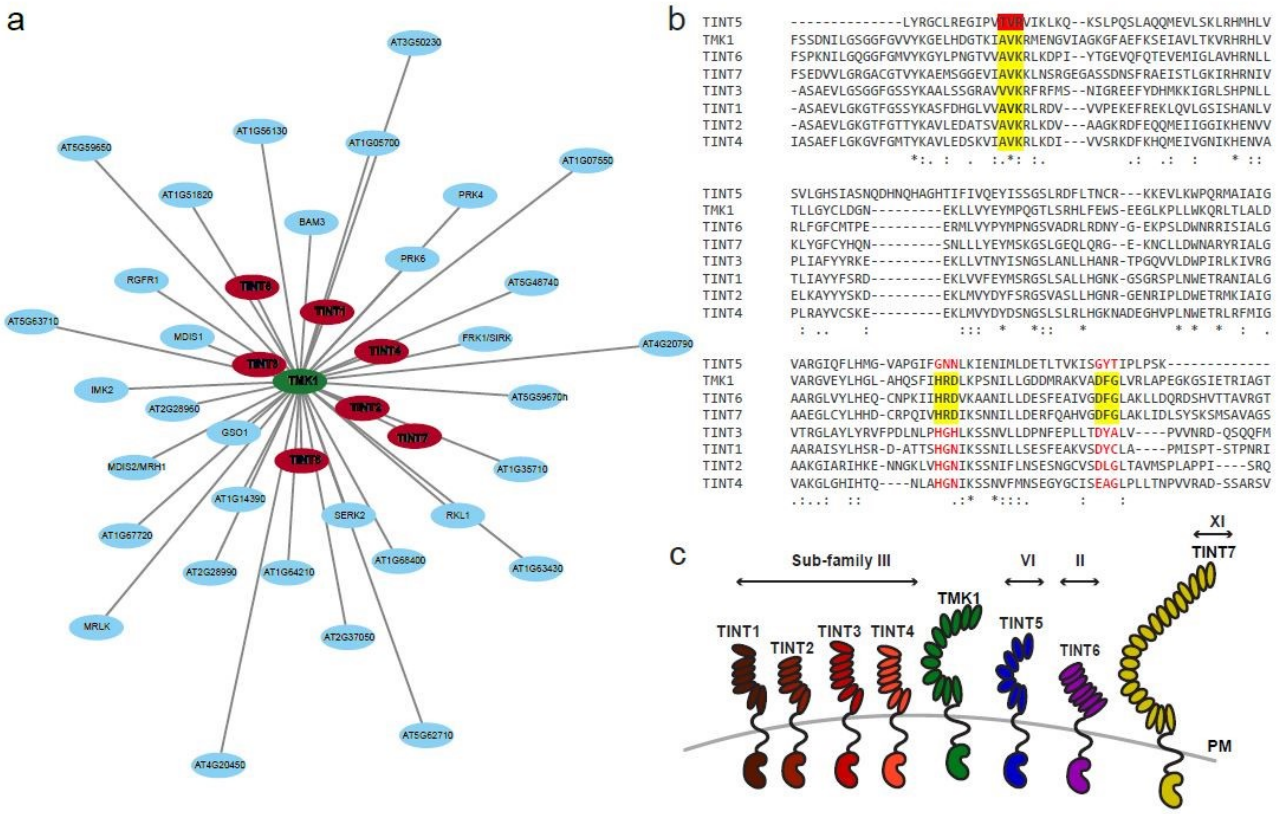

Figure 2.4-1 Overview of TINTs

(a) Interaction network of TMK1 (in green). Nodes represent individual proteins, and edges indicate predicted or known interactions. Key candidates, TINT1 through TINT7, are displayed in red.

(b) Sequence alignment of the kinase domains (KD) of TINT1 through TINT7 and TMK1. Conserved residues are marked with asterisks (*), colons (:), and periods (.) representing different degrees of conservation across sequences. Key functional motifs, including ATP-binding lysine (K), catalytic loop (HRD motif), and activation loop (DFG motif) are highlighted. TMK1 and TINT sequences illustrate variability in conserved motifs important for kinase activity.

(c) Schematic representation of TINTs with TMK1 at the plasma membrane, illustrating their classification into sub-families and relative extracellular domain (ECD) sizes.

Figure 2- Localization of TINT5 and its interaction with CAMEL

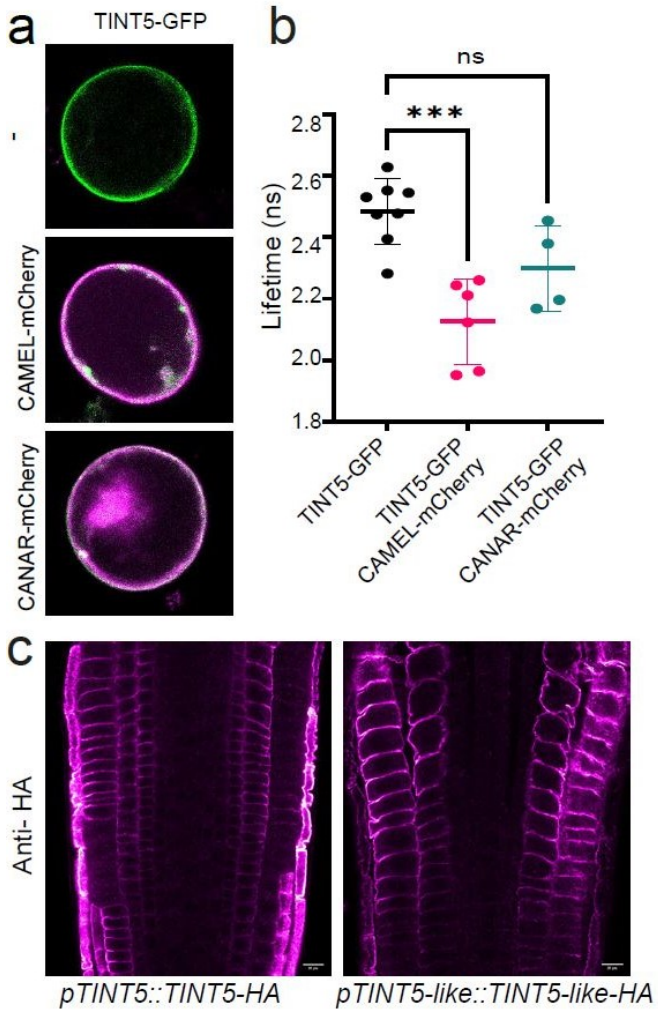

Figure 2.4-2 Localization of TINT5 and its interaction with CAMEL

(a) Representative images of *Arabidopsis* root protoplasts transformed with constructs encoding *p35S::TINT5-GFP* and *p35S::CAMEL/CANAR-mCherry* in FRET/FLIM assay.

(b) Quantitative measurement of the GFP lifetime (FRET/FLIM) as indicated in the graph with the mean ± SD. Statistical significance is indicated by asterisks *(*** $p < 0.001$) and "ns" for non-significant ($p > 0.05$),* as determined by Dunnett's multiple comparisons test.

(c) Representative confocal images of *pTINT5::TINT5-3HA* and *pTINT5-like::TINT5-like-3HA* primary root tips after immunostaining with an HA antibody, showing the localization of TINT5 and TINT5-like. TINT5 is localized at the plasma membrane of the endodermal, epidermal and cortical cells, while TINT5-like is localized in the epidermal and cortical cells.

Figure 3- *TINT* expression during vasculature regeneration

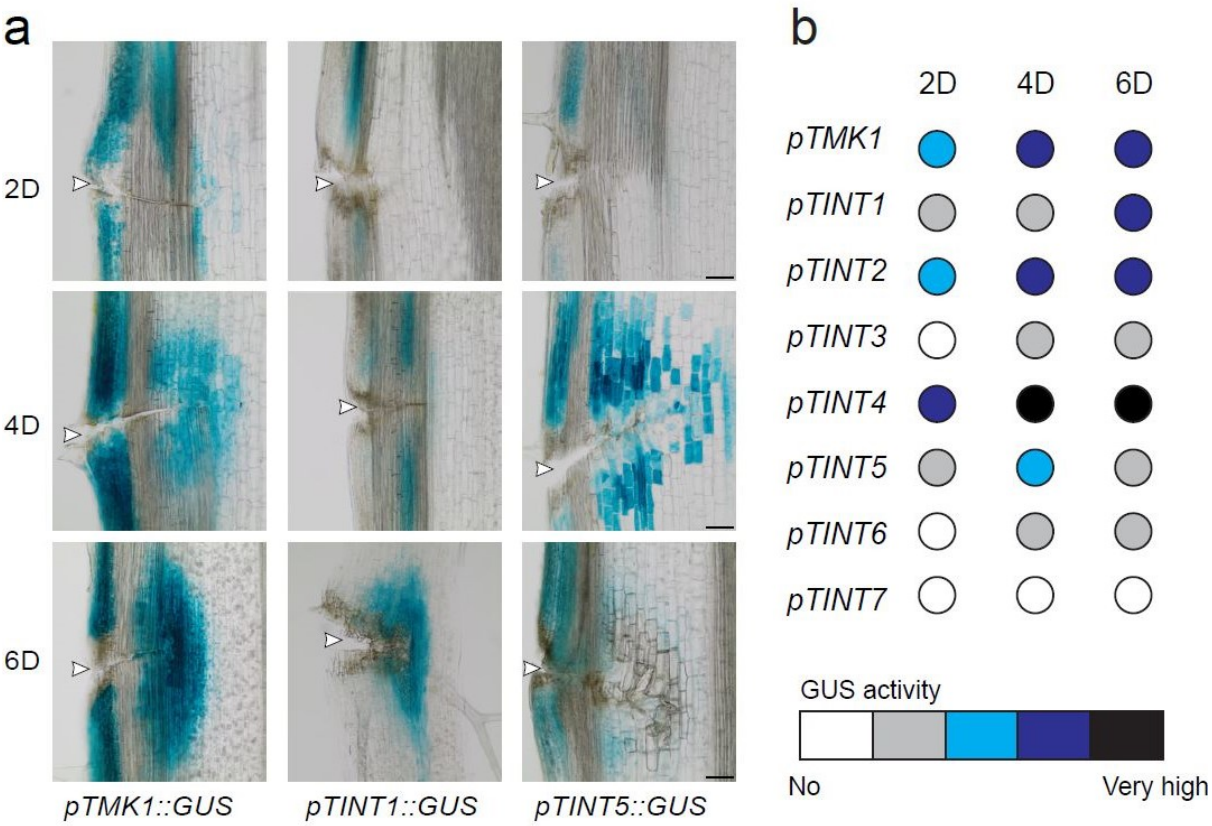

Figure 2.4-3 TINT expression during vasculature regeneration

(a) Representative images of the GUS staining of inflorescence stems during vasculature regeneration at 2, 4 and 6 days after wounding (DAW). *TMK1*, *TINT1*, and *TINT5* showed different expression patterns. White arrowheads indicate the wounding site. Scale bar, 100 µm.

(b) Visual quantification of GUS staining intensity in cells surrounding the wound for each genotype at 2, 4, and 6 DAW. Color gradients represent expression levels, from white indicating the lack of expression to black indicating very high expression. The highest GUS reaction was observed in *pTINT4::GUS*. A high and extended GUS activity was also found in *pTMK1::GUS* and *pTINT2::GUS.* No *TINT7* expression was observed in the regenerated vasculature.

Figure 4- TINT and TMK1 in vasculature regeneration after wounding

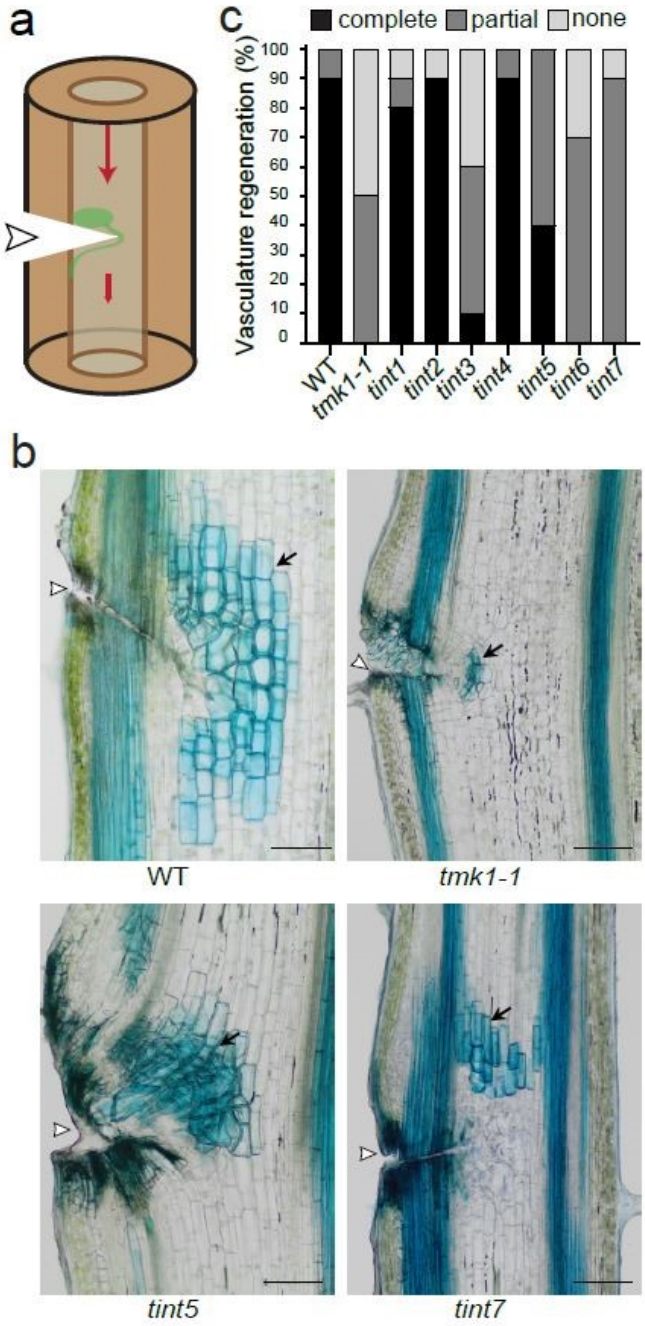

Figure 2.4-4 TINT and TMK1 in vasculature regeneration after wounding

(a) Schematic representation of vasculature regeneration in an inflorescence stem after wounding. White arrowhead indicates the wounding site. Red arrows indicate auxin flow. Green indicates the accumulation of auxin above the wound and the formed auxin channel guiding regenerated vasculature circumventing the wound.

(b) Representative images of the TBO staining at 6 DAW showing vasculature regeneration in the inflorescence stems. WT vasculature regenerated completely around the wound, however *tmk1-1*, *tint5* and *tint7* mutants regenerated only partially. White arrowheads indicate the wounding site. Black arrows indicate the regenerated vasculature. Scale bar, 100 µm.

(c) Quantification of the vasculature regeneration across genotypes, categorized as complete (fully formed vasculature), partial (limited and partially developed vasculature), or none (no vessel formed around the wound), at 6 DAW. n=10 plants per genotype.

Figure 5- TINT and TMK1 in auxin channel formation

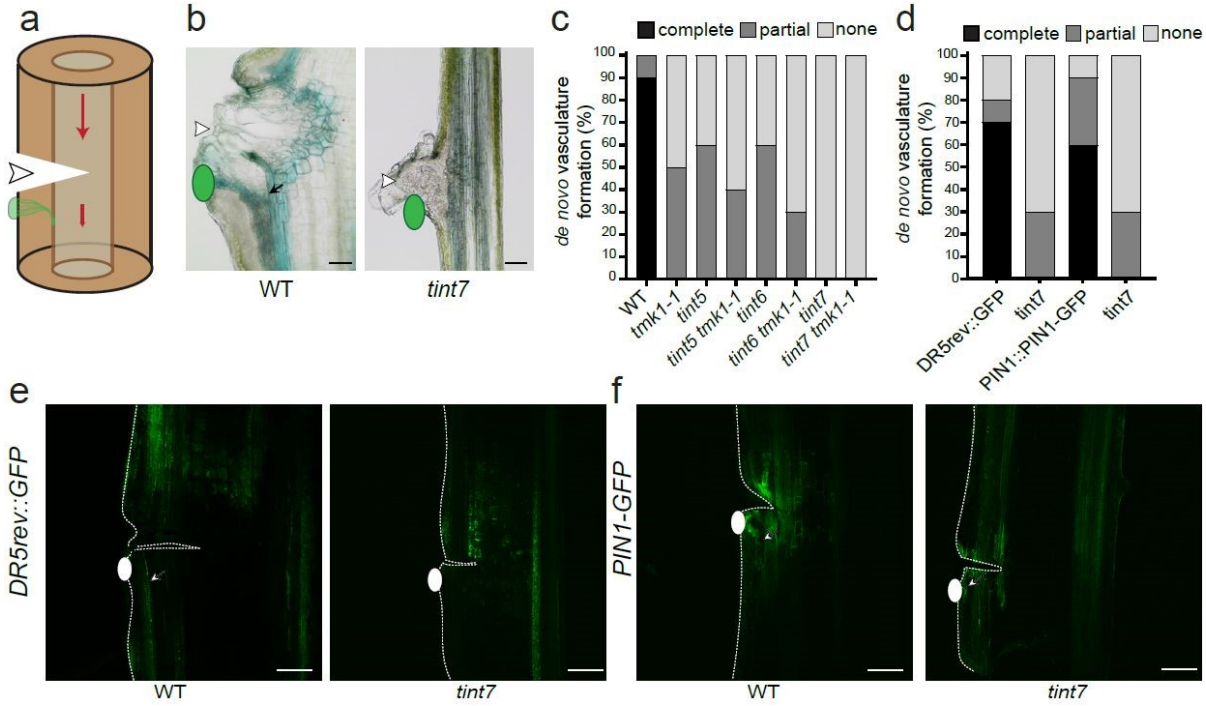

Figure 2.4-5 TINT and TMK1 in auxin channel formation

(a) Schematic representation of canalization and *de novo* vasculature formation from local application of auxin to wounded stems. White arrowhead indicates the wounding site. Red arrows indicate auxin flow. Green indicates the local application of auxin (IAA) and *de novo* formed auxin channel guidig formation of vasculature.

(b) Representative images of the TBO staining of *de novo* vasculature formation and canalization at 6 days after IAA application (DAA) (green ovals) following wounding. WT vasculature regenerated fully from auxin application, while *tint7* showed no regeneration. White arrowheads indicate the wounding site. Black arrow indicate the regenerated vasculature from the applied source of auxin. Scale bar, 100 µm.

(c) Quantification of *de novo* vasculature formation from a local source of auxin in WT, *tmk1-1*, *tint* and double mutants, categorized as complete (fully formed vasculature), partial (limited and partially developed vasculature), or none (no vessel formed) at 6 DAA. n=10 plants per genotype.

(d) Quantification of *de novo* vasculature formation from a local source of auxin in *DR5rev::GFP* and *PIN1::PIN1-GFP* lines, categorized as complete (fully formed channels), partial (limited or partially developed channels), and none (no channels formed) at 4 DAA. n=10 plants per genotype.

(e-f) Exogenous application of IAA (white ovals) below the wounding site to the stem of *DR5rev::GFP* (e) and *PIN1::PIN1-GFP* (f) triggered the complete development of auxin and PIN1 channels respectively (indicated by white arrows), but not in the *tint7* mutant. 4 DAA. Scale bar, 100 µm.

Figure 6- TINT6 function in regulating hypocotyl bending

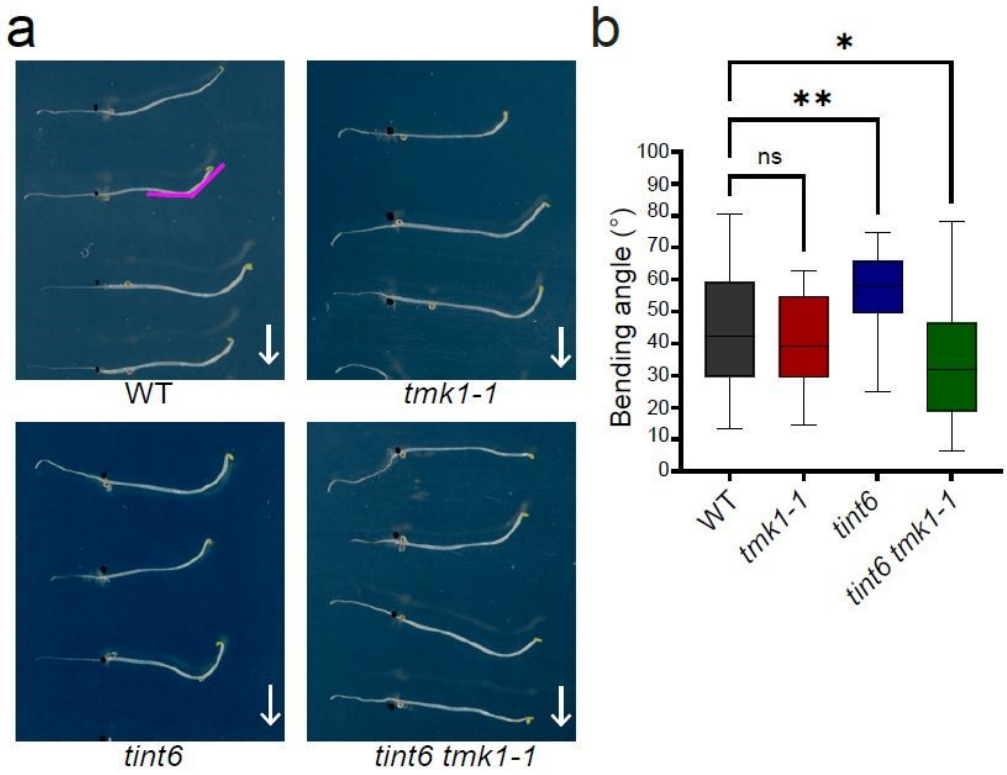

Figure 2.4-6 TINT6 function in regulating hypootyl bending

(a) Representative images of the hypocotyl gravitropic response in WT, *tmk1-1*, *tint6* and the double mutant *tint6 tmk1-1* after 24 hours of gravistimulation. The white arrow indicates the direction of gravity, and the pink angle marks the curvature measured after 24 hours of gravistimulation.

(b) Quantification of hypocotyl bending angles after 24 hours. Values represent the average curvature with minimum and maximum ranges. WT hypocotyls showed an average bending of 44°, *tint6* exhibited hyperbending, while *tint6 tmk1-1* showed hypobending. Statistical significance is indicated by asterisks *(* $p < 0.05$, ** $p < 0.01$) and "ns" for non-significant ($p > 0.05$),* as determined by Dunnett's multiple comparisons test.

Figure 7- TINT7 function in regulating stomatal movement

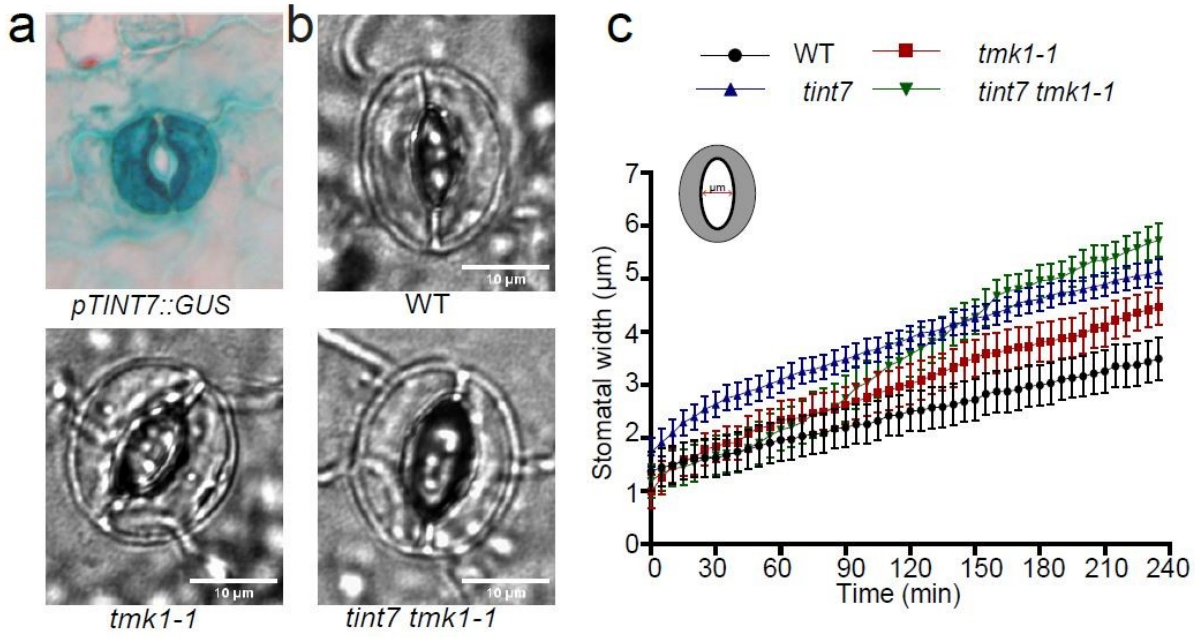

Figure 2.4-7 TINT function in regulating stomatal movement

(a) Representative image of *pTINT7::GUS* expression in stomata of the cotyledon of 5-day-old *A. thaliana* seedlings.

(b) Representative images of stomatal opening after 4 hours of light in WT, *tmk1-1*, and *tint7 tmk1-1*. Scale bar, 10 µm.

(c) Quantification of stomatal opening kinetics during light exposure. Stomatal width was measured every 5 minutes, as indicated in the scheme, and the average width with SEM is displayed in the graph. Stomatal opening in *tmk1-1* is greater than in WT, with *tint7* showing more opening than *tmk1-1*, *and tint7 tmk1-1* exhibiting the most pronounced opening. n >13 per genotype.

Figure S1- Phylogenetic analysis and characterization of TINT in *Arabidopsis*

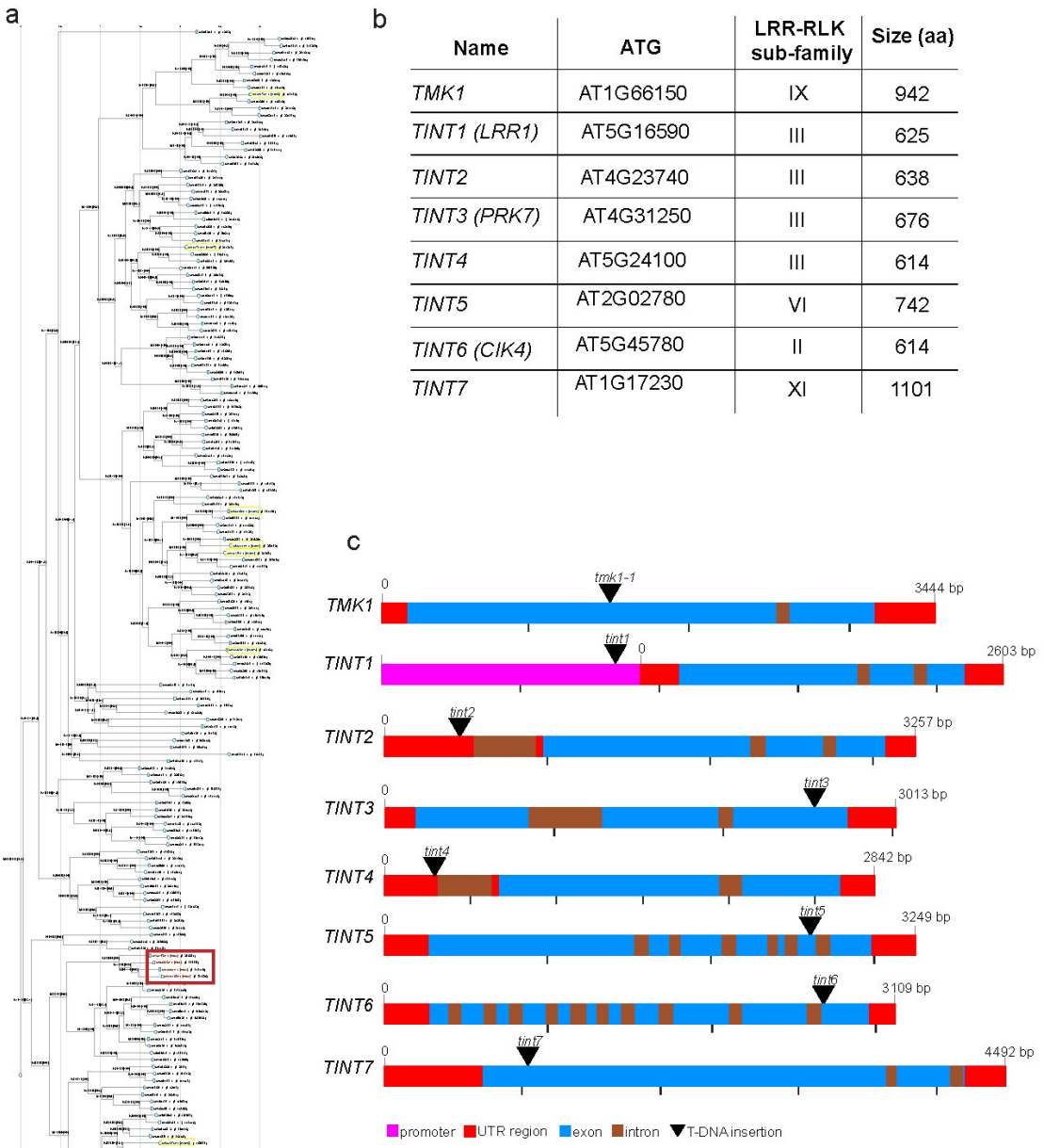

Name	ATG	LRR-RLK sub-family	Size (aa)
TMK1	AT1G66150	IX	942
TINT1 (LRR1)	AT5G16590	III	625
TINT2	AT4G23740	III	638
TINT3 (PRK7)	AT4G31250	III	676
TINT4	AT5G24100	III	614
TINT5	AT2G02780	VI	742
TINT6 (CIK4)	AT5G45780	II	614
TINT7	AT1G17230	XI	1101

Figure 2.4-8 Phylogenetic analysis and characterization of TINT in Arabidopsis

(a) Phylogenetic tree of LRR-RLKs in *Arabidopsis*, with the TMK family highlighted in red boxes and the TINT family highlighted in yellow boxes. The tree was constructed using FastTree with maximum-likelihood analysis. Node values represent Shimodaira-Hasegawa (SH)-like local support, with higher values reflecting stronger confidence in the tree structure.

(b) Table summarizing the TINT proteins, including their gene identifiers (ATG), retrieved from the *Arabidopsis* Information Resource (TAIR), their LRR-RLK subfamily, and protein size (in amino acids).

(c) Schematic representation of the genomic DNA (gDNA) regions of *TMK1* and *TINT,* with the transcriptional start site marked as zero. The black triangle indicates the site of the T-DNA insertion in the mutants.

Figure S2- Confirmation for the interaction of TINTs with TMK1

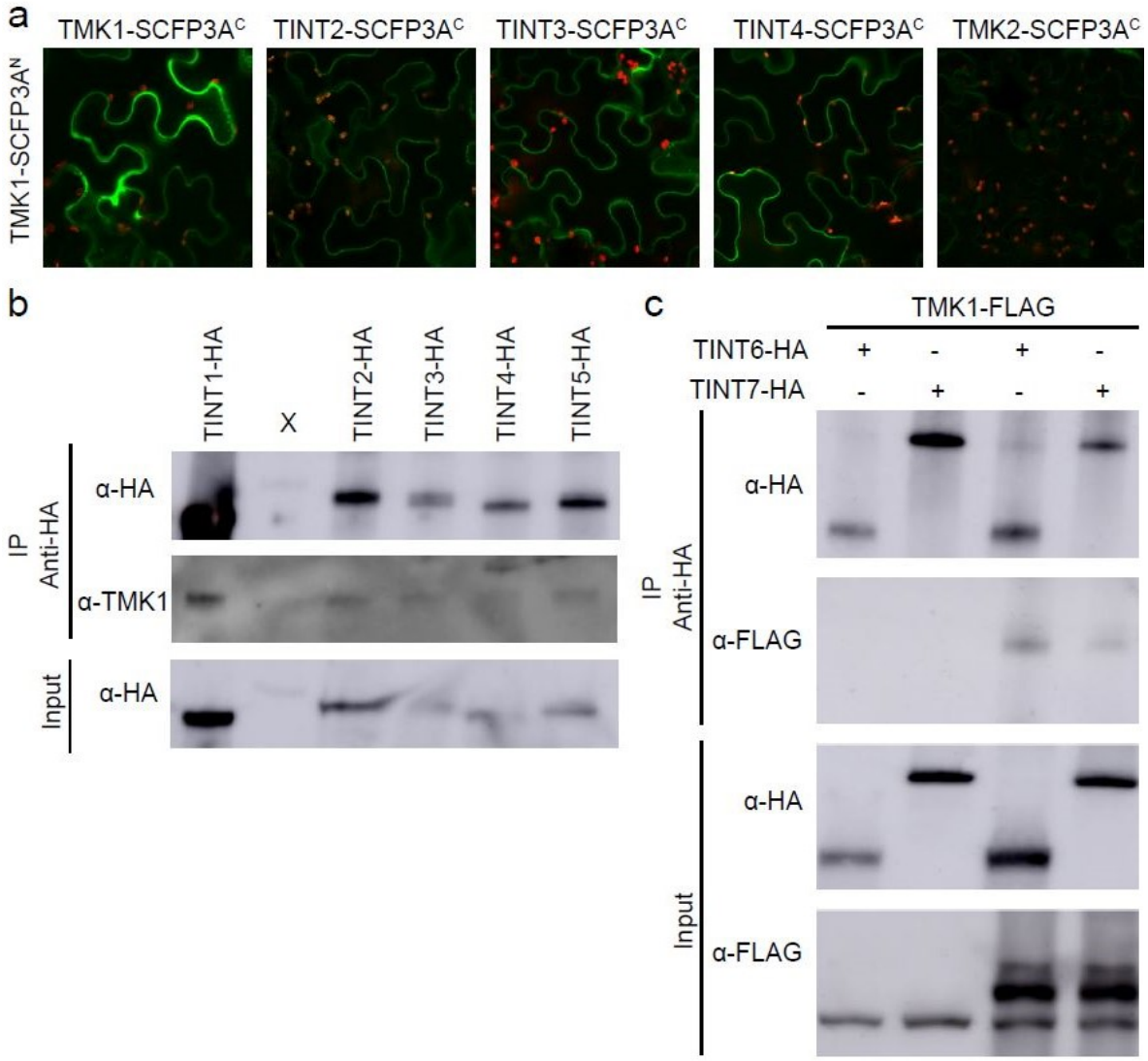

Figure 2.4-9 Confirmation for the interaction of TINTs with TMK1

(a) BiFC assay performed in *Nicotiana benthamiana* leaves co-expressing constructs for split the super cyan fluorescent protein (SCFP3A) by fusing the N-terminus of SCFP3A to TMK1 and the C-terminus to the protein of interest. Protein-protein interaction was assessed by fluorescence complementation. The complementation signal was observed with TINT2, TINT3, and TINT4. TMK1-SCFP3A^N served as a positive control, while TMK2-SCFP3A^N was used as a negative control.

(b) Co-immunoprecipitation assay from *Arabidopsi*s seedlings expressing the corresponding TINT with HA tag under the ubiquitin promoter (*pUBQ10::TINTn-3HA*). TINT proteins were immunoprecipitated using HA antibody beads, and an antibody against TMK1 was used to assess co-immunoprecipitation. While the interaction is observed, the bands are weak due to the use of an endogenous antibody.

(c) Co-immunoprecipitation assay from *Nicotiana benthamiana* leaves co-expressing *p35S::TMK1-FLAG* with *pUBQ10::TINT6/TINT7-3HA*. TINT proteins were immunoprecipitated using HA antibody beads, and an antibody against FLAG was used to assess co-immunoprecipitation. The interaction between TINT6/TINT7 and TMK1 was observed.

Figure S3- Expression pattern of *TINT*s

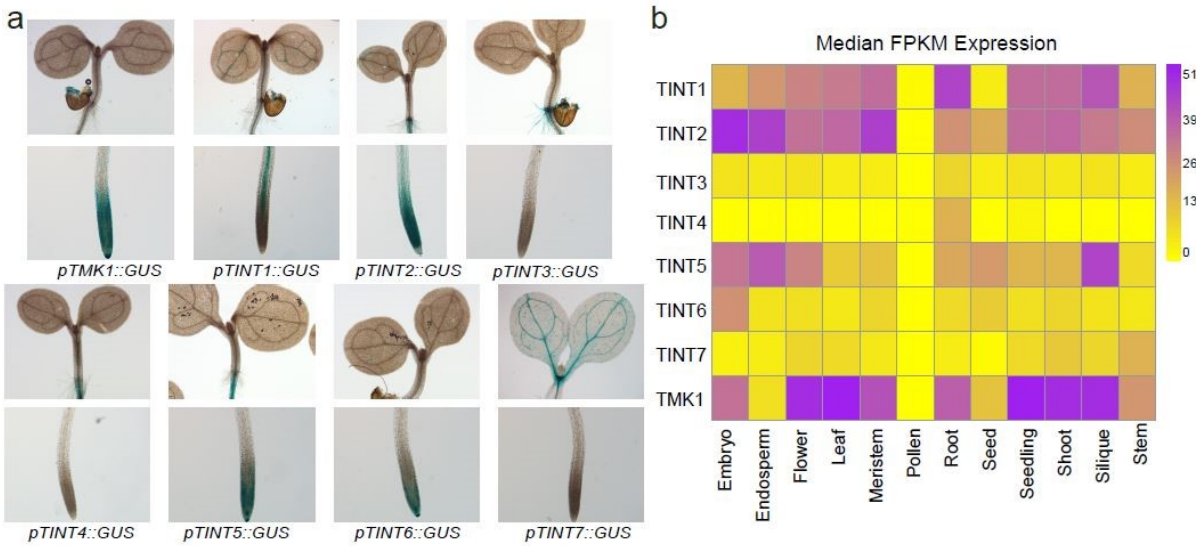

Figure 2.4-10 Expression pattern of TINTs

(a) Representative images of the GUS staining of 5-day-old *Arabidopsis* seedlings showing different expression of TINTs across the root, shoot, and cotyledons.
(b) Heat map of the expression profiles of *TMK1* and *TINT* genes, showing the median FPKM expression values across different plant tissues. Expression levels range from 0 (no detectable expression) to 51 (high expression).

Figure S4- *TINT* expression during vasculature regeneration

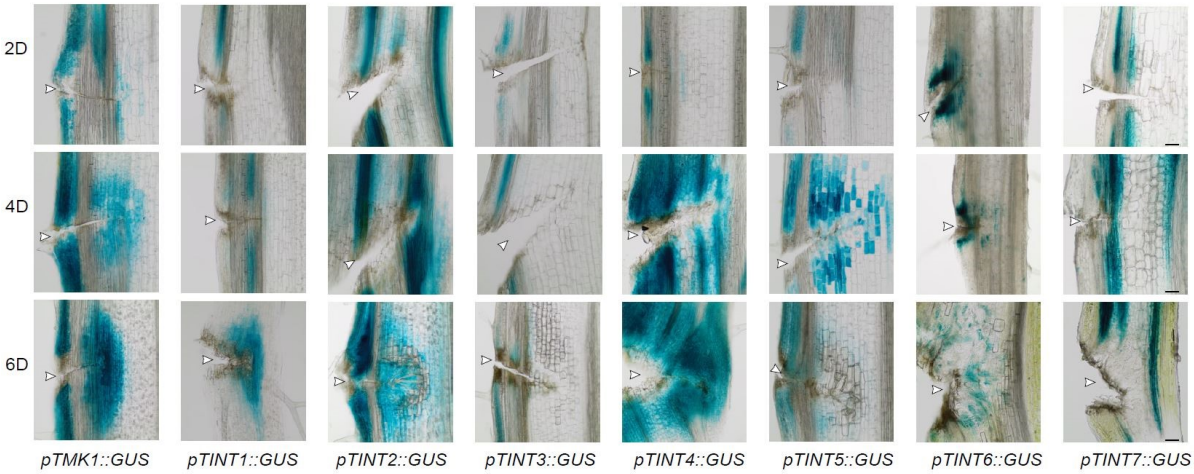

Figure 2.4-11 TINT expression during vasculature regeneration

Representative images of the GUS staining of inflorescence stems during vasculature regeneration at 2, 4 and 6 days after wounding (DAW) in GUS lines. White arrowheads indicate the wounding site. Scale bar, 100 µm.

Figure S5- TINT and TMK1 in vasculature regeneration after wounding

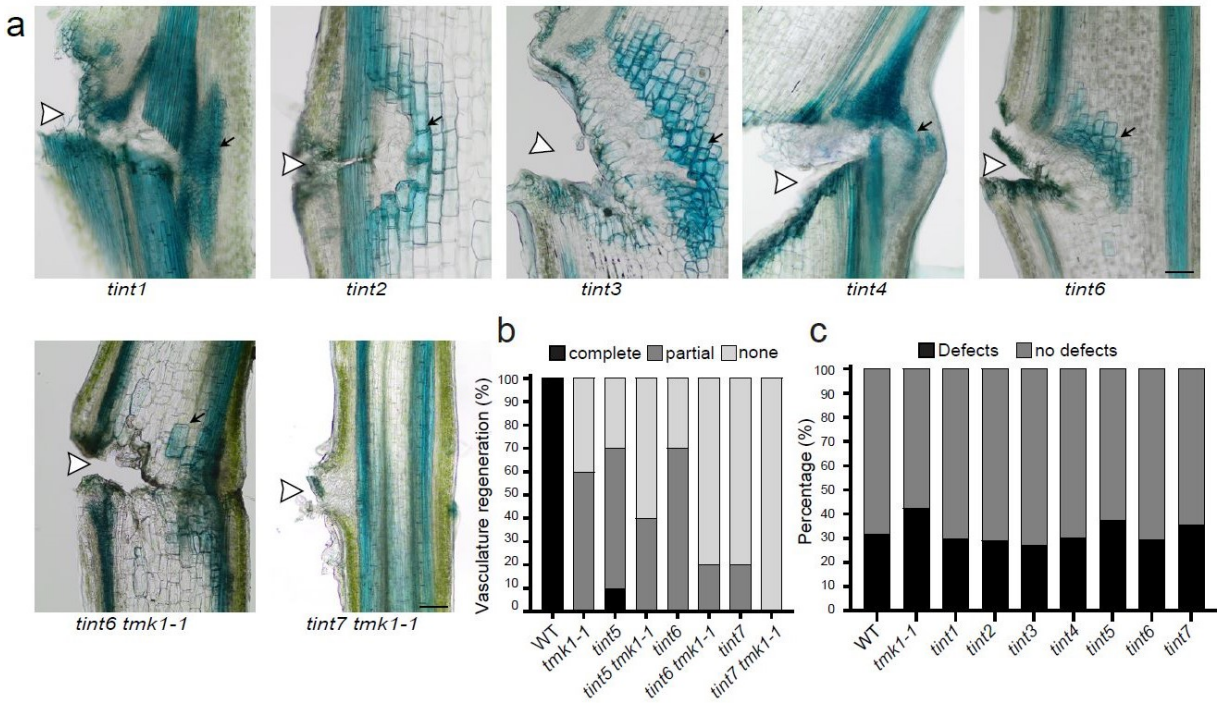

Figure 2.4-12 TINT and TMK1 in vasculature regeneration after wounding

(a) Representative images of the TBO staining at 6 DAW showing vasculature regeneration in the inflorescence stems. Stems of *tint1*, *tint2*, and *tint4* regenerated fully around the wound, while *tint3* and *tint6* showed partial regeneration. The *tint6 tmk1-1* double mutant developed single vessels, and the *tint7 tmk1-1* mutant showed no vasculature regeneration. White arrowheads indicate the wounding site. Black arrows indicate the regenerated vasculature. Scale bar, 100 µm.

(b) Quantification of the vasculature regeneration in the single and double mutants, categorized as complete (fully formed vasculature), partial (limited and partially developed vasculature), or none (no vessel formed around the wound) at 6 DAW. n=10 plants per genotype.

(c) Quantification of the cotyledon vasculature phenotype, categorized as no defects (4 loops, all closed), or defects (fewer or more than 4 loops, or open loops except for the bottom loops open at the bottom). All mutants exhibited normal cotyledon vasculature development, similar to WT. n >100 per genotype.

Figure S6- TINT and TMK1 in auxin channel formation

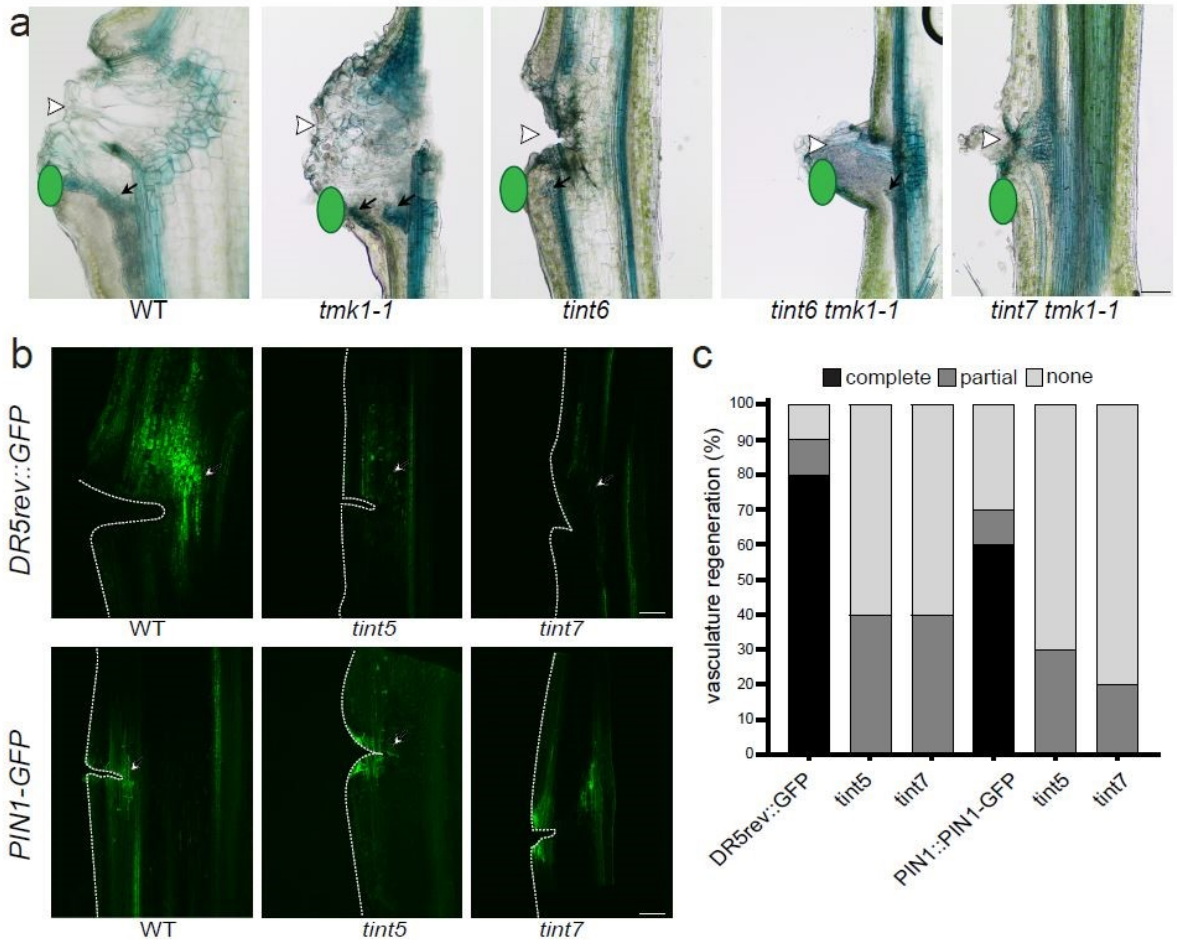

Figure 2.4-13 TINT and TMK1 in auxin channel formation

(a) Representative images of the TBO staining of *de novo* vasculature formation and canalization at 6 days after IAA application (DAA) (green ovals) following wounding. WT vasculature regenerated fully from auxin application, while *tmk1-1*, *tint6*, and *tint6 tmk1-1* mutants regenerated partially. The mutants *tint7* and *tint7 tmk1-1* showed no regeneration. White arrowheads indicate the wounding site. Black arrows indicate the regenerated vasculature from the applied source of auxin. Scale bar, 100 µm.

(b) Wounding of the stem of *DR5rev::GFP* and *PIN1::PIN1-GFP* triggered the complete development of auxin and PIN1 channels respectively (indicated by white arrows), but not in *tint5*, or *tint7* mutant. 4 DAW. Scale bar, 100 µm.

(c) Quantification of vasculature formation after wounding in *DR5rev::GFP* and *PIN1::PIN1-GFP* lines, categorized as complete (fully formed channels), partial (limited or partially developed channels), and none (no channels formed) at 4 DAW. n=10 plants per genotype.

Figure S7- TINT5 and TINT5-like in canalization and vasculature regeneration after wounding

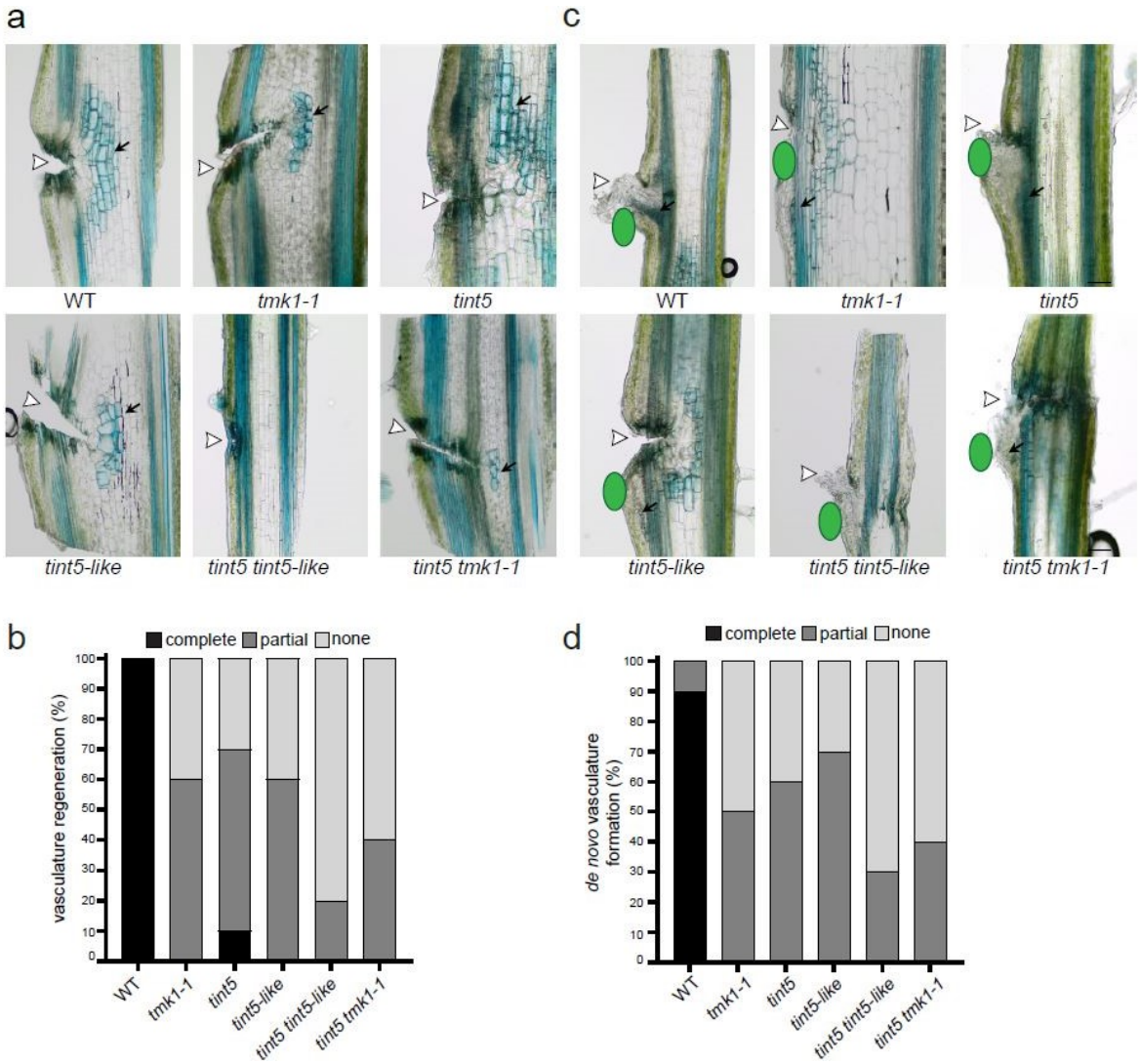

Figure 2.4-14 TINT5 and TINT5-like in canalization and vasculature regeneration after wounding

(a) Representative images of the TBO staining at 6 DAW showing the vasculature regeneration in the inflorescence stems. WT vasculature regenerated completely around the wound, while *tmk1-1*, *tint5*, *tint5-like*, and *tint5 tint5-like* showed defects in regeneration. The double mutant *tint5 tmk1-1* developed only single vessels. White arrowheads indicate the wounding site. Black arrows indicate the regenerated vasculature. Scale bar, 100 µm.

(b) Quantification of the vasculature regeneration in *tmk1-1*, *tint5*, *tint5-like* single and double mutants, categorized as complete (fully formed vasculature), partial (limited and partially developed vasculature), or none (no vessel formed around the wound) at 6 DAW. n=10 plants per genotype.

(c) Representative images of the TBO staining at 6 DAA of *de novo* vasculature formation and canalization from exogenous application of auxin (green ovals) following wounding. WT vasculature regenerated fully from auxin application, while all the shown mutants showed defects in regeneration. White arrowheads indicate the wounding site. Black arrows indicate the regenerated vasculature from the applied source of auxin.

(d) Quantification of *de novo* vasculature formation from a local source of auxin in *tmk1-1*, *tint5*, *tint5-like* single and double mutants, categorized as complete (fully formed vasculature), partial, and none (no channels formed) at 6 DAA. n=10 plants per genotype.

Figure S8- TINT7 function in regulating stomatal movement

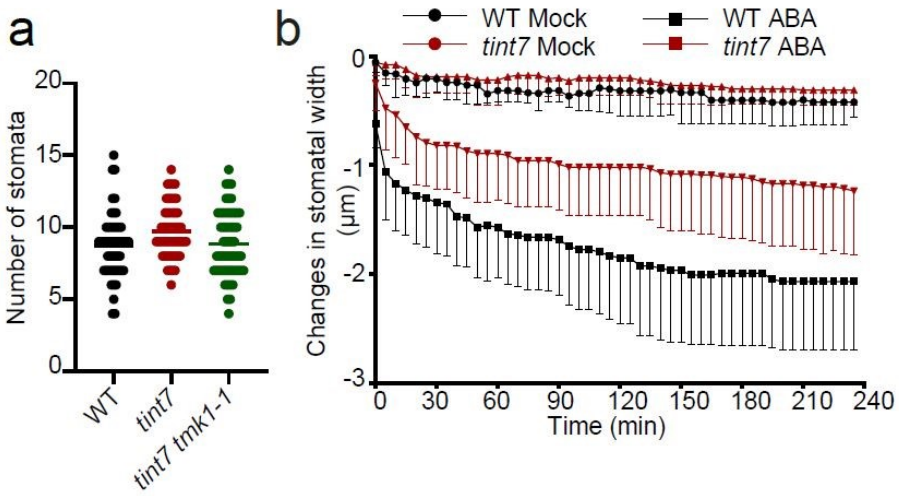

Figure 2.4-15 TINT7 function in regulationg stomatal movement

(a) Graph showing the number of stomata in a given area of cotyledons from WT, *tint7*, and *tint7 tmk1-1*. The mutants exhibited a similar number of stomata compared to WT. n ≥ 50 per genotype.

(b) Quantification of stomatal closure kinetics after ABA treatment. The changes in stomatal width were measured every 5 minutes, and the average change with SD is displayed in the graph. In mock conditions, stomatal width in WT and *tint7* remained largely unchanged. However, when treated with ABA, *tint7* stomata closed less than WT. n ≥ 9 per genotype.

2.4.8 References

1. Liu, J., Li, W., Wu, G. & Ali, K. An update on evolutionary, structural, and functional studies of receptor-like kinases in plants. *Front. Plant Sci.* **15**, 1305599 (2024).
2. Zhu, Q. *et al.* Advances in Receptor-like Protein Kinases in Balancing Plant Growth and Stress Responses. *Plants* **12**, 427 (2023).
3. Shiu, S.-H. & Bleecker, A. B. Plant Receptor-Like Kinase Gene Family: Diversity, Function, and Signaling. *Sci. STKE* **2001**, (2001).
4. Liu, P.-L., Du, L., Huang, Y., Gao, S.-M. & Yu, M. Origin and diversification of leucine-rich repeat receptor-like protein kinase (LRR-RLK) genes in plants. *BMC Evol Biol* **17**, 47 (2017).
5. Hohmann, U., Lau, K. & Hothorn, M. The Structural Basis of Ligand Perception and Signal Activation by Receptor Kinases. *Annu. Rev. Plant Biol.* **68**, 109–137 (2017).
6. Jiang, J., Zhang, C. & Wang, X. Ligand Perception, Activation, and Early Signaling of Plant Steroid Receptor Brassinosteroid Insensitive 1. *JIPB* **55**, 1198–1211 (2013).
7. Chinchilla, D. *et al.* A flagellin-induced complex of the receptor FLS2 and BAK1 initiates plant defence. *Nature* **448**, 497–500 (2007).
8. Friml, J. Fourteen Stations of Auxin. *Cold Spring Harb. Perspect. Biol.* **14**, (2022).
9. Gallei, M., Luschnig, C. & Friml, J. Auxin signalling in growth: Schrödinger's cat out of the bag. *Curr. Opin. Plant. Biol.* **53**, 43–49 (2020).
10. Salehin, M., Bagchi, R. & Estelle, M. $SCF^{TIR1/AFB}$ -Based Auxin Perception: Mechanism and Role in Plant Growth and Development. *Plant Cell* **27**, 9–19 (2015).
11. Friml, J. *et al.* ABP1–TMK auxin perception for global phosphorylation and auxin canalization. *Nature* **609**, 575–581 (2022).
12. Yu, Y. *et al.* ABLs and TMKs are co-receptors for extracellular auxin. *Cell* **186**, 5457-5471.e17 (2023).
13. Kuhn, A. *et al.* RAF-like protein kinases mediate a deeply conserved, rapid auxin response. *Cell* **187**, 130–148 (2024).
14. Dai, N., Wang, W., Patterson, S. E. & Bleecker, A. B. The TMK Subfamily of Receptor-Like Kinases in Arabidopsis Display an Essential Role in Growth and a Reduced Sensitivity to Auxin. *PLoS ONE* **8**, (2013).
15. Chang, C. *et al.* The TMK1 gene from Arabidopsis codes for a protein with structural and biochemical characteristics of a receptor protein kinase. *Plant Cell* **4**, 1263–1271 (1992).
16. Li, L. *et al.* Cell surface and intracellular auxin signalling for H+ fluxes in root growth. *Nature* **599**, 273–277 (2021).
17. Huang, R. *et al.* Noncanonical auxin signaling regulates cell division pattern during lateral root development. *Proc. Natl. Acad. Sci. U.S.A.* **116**, 21285–21290 (2019).
18. Xu, T. *et al.* Cell Surface ABP1-TMK Auxin-Sensing Complex Activates ROP GTPase Signaling. *Science* **343**, 1025–1028 (2014).
19. Cao, M. *et al.* TMK1-mediated auxin signalling regulates differential growth of the apical hook. *Nature* **568**, 240–243 (2019).
20. Gu, B. *et al.* Modulation of receptor-like transmembrane kinase 1 nuclear localization by DA1 peptidases in Arabidopsis. *Proc. Natl. Acad. Sci. U.S.A.* **119**, (2022).
21. Wang, J. L. *et al.* WAV E3 ubiquitin ligases mediate degradation of IAA32/34 in the TMK1-mediated auxin signaling pathway during apical hook development. *Proc. Natl. Acad. Sci. U.S.A.* **121**, (2024).
22. Rodriguez, L. *et al.* Cell surface auxin signalling directly targets PIN-mediated auxin fluxes for adaptive plant development. Preprint at https://doi.org/10.1101/2022.11.30.518503 (2022).

23. Marquès-Bueno, M. M. *et al.* Auxin-Regulated Reversible Inhibition of TMK1 Signaling by MAKR2 Modulates the Dynamics of Root Gravitropism. *Curr. Biol.* **31**, 228-237.e10 (2021).
24. Wang, J. *et al.* Self-regulation of PIN1-driven auxin transport by cell surface-based auxin signaling in Arabidopsis. Preprint at https://doi.org/10.1101/2022.11.30.518523 (2022).
25. Luschnig, C. & Friml, J. Over 25 years of decrypting PIN-mediated plant development. *Nat. Commun.* **15**, 9904 (2024).
26. Wang, Q. *et al.* A phosphorylation-based switch controls TAA1-mediated auxin biosynthesis in plants. *Nat. Commun.* **11**, (2020).
27. Li, B. *et al.* TMK4-mediated FIP37 phosphorylation regulates auxin-triggered N-methyladenosine modification of auxin biosynthetic genes in Arabidopsis. *Cell Reports* **43**, 114597 (2024).
28. Yu, Z. *et al.* Auxin promotes hypocotyl elongation by enhancing BZR1 nuclear accumulation in *Arabidopsis*. *Sci. Adv.* **9**, eade2493 (2023).
29. Yang, J. *et al.* TMK1-based auxin signaling regulates abscisic acid responses via phosphorylating ABI1/2 in Arabidopsis. *Proc. Natl. Acad. Sci. U.S.A.* **118**, (2021).
30. Sachs, T. The Control of the Patterned Differentiation of Vascular Tissues. in *Advances in Botanical Research* vol. 9 151–262 (Elsevier, 1981).
31. Hajný, J., Tan, S. & Friml, J. Auxin canalization: From speculative models toward molecular players. *Curr. Opin. Plant. Biol.* **65**, (2022).
32. Benková, E. *et al.* Local, Efflux-Dependent Auxin Gradients as a Common Module for Plant Organ Formation. *Cell* **115**, 591–602 (2003).
33. Balla, J., Kalousek, P., Reinöhl, V., Friml, J. & Procházka, S. Competitive canalization of PIN-dependent auxin flow from axillary buds controls pea bud outgrowth. *Plant J.* **65**, 571–577 (2011).
34. Scarpella, E., Marcos, D., Friml, J. & Berleth, T. Control of leaf vascular patterning by polar auxin transport. *Genes Dev.* **20**, 1015–1027 (2006).
35. Mazur, E., Benková, E. & Friml, J. Vascular cambium regeneration and vessel formation in wounded inflorescence stems of Arabidopsis. *Sci. Rep.* **6**, (2016).
36. Hajný, J. *et al.* Receptor kinase module targets PIN-dependent auxin transport during canalization. *Science* **370**, 550–557 (2020).
37. Smakowska-Luzan, E. *et al.* An extracellular network of Arabidopsis leucine-rich repeat receptor kinases. *Nature* **553**, 342–346 (2018).
38. Chen, X. *et al.* Arabidopsis U-box E3 ubiquitin ligase PUB11 negatively regulates drought tolerance by degrading the receptor-like protein kinases LRR1 and KIN7. *JIPB* **63**, 494–509 (2021).
39. Takeuchi, H. & Higashiyama, T. Tip-localized receptors control pollen tube growth and LURE sensing in Arabidopsis. *Nature* **531**, 245–248 (2016).
40. Hu, C. *et al.* A group of receptor kinases are essential for CLAVATA signalling to maintain stem cell homeostasis. *Nature Plants* **4**, 205–211 (2018).
41. Escocard De Azevedo Manhães, A. M., Ortiz-Morea, F. A., He, P. & Shan, L. Plant plasma membrane-resident receptors: Surveillance for infections and coordination for growth and development. *JIPB* **63**, 79–101 (2021).
42. Jose, J., Ghantasala, S. & Roy Choudhury, S. Arabidopsis Transmembrane Receptor-Like Kinases (RLKs): A Bridge between Extracellular Signal and Intracellular Regulatory Machinery. *IJMS* **21**, 4000 (2020).
43. Mazur, E., Kulik, I., Hajný, J. & Friml, J. Auxin canalization and vascular tissue formation by TIR1/AFB-mediated auxin signaling in Arabidopsis. *New Phytologist* **226**, 1375–1383 (2020).

44. Friml, J. *et al.* Efflux-dependent auxin gradients establish the apical–basal axis of Arabidopsis. *Nature* **426**, 147–153 (2003).
45. Rakusová, H. *et al.* Termination of Shoot Gravitropic Responses by Auxin Feedback on PIN3 Polarity. *Current Biology* **26**, 3026–3032 (2016).
46. Lim, C., Baek, W., Jung, J., Kim, J.-H. & Lee, S. Function of ABA in Stomatal Defense against Biotic and Drought Stresses. *IJMS* **16**, 15251–15270 (2015).
47. Xi, L., Wu, X. N., Gilbert, M. & Schulze, W. X. Classification and Interactions of LRR Receptors and Co-receptors Within the Arabidopsis Plasma Membrane – An Overview. *Front. Plant Sci.* **10**, 472 (2019).
48. Zeqiraj, E. & Van Aalten, D. M. Pseudokinases-remnants of evolution or key allosteric regulators? *Current Opinion in Structural Biology* **20**, 772–781 (2010).
49. Sheetz, J. B. & Lemmon, M. A. Looking lively: emerging principles of pseudokinase signaling. *Trends in Biochemical Sciences* **47**, 875–891 (2022).
50. Han, H., Rakusová, H., Verstraeten, I., Zhang, Y. & Friml, J. $SCF^{TIR1/AFB}$ Auxin Signaling for Bending Termination during Shoot Gravitropism. *Plant Physiol.* **183**, 37–40 (2020).
51. Pillitteri, L. J. & Dong, J. Stomatal Development in Arabidopsis. *The Arabidopsis Book* **11**, e0162 (2013).
52. Chua, L. C. & Lau, O. S. Stomatal development in the changing climate. *Development* **151**, dev202681 (2024).
53. Wu, Y. *et al.* Genome-Wide Expression Pattern Analyses of the Arabidopsis Leucine-Rich Repeat Receptor-Like Kinases. *Molecular Plant* **9**, 289–300 (2016).
54. Jaillais, Y. *et al.* Tyrosine phosphorylation controls brassinosteroid receptor activation by triggering membrane release of its kinase inhibitor. *Genes Dev.* **25**, 232–237 (2011).
55. Gehl, C., Waadt, R., Kudla, J., Mendel, R.-R. & Hänsch, R. New GATEWAY vectors for High Throughput Analyses of Protein–Protein Interactions by Bimolecular Fluorescence Complementation. *Molecular Plant* **2**, 1051–1058 (2009).
56. Shannon, P. *et al.* Cytoscape: A Software Environment for Integrated Models of Biomolecular Interaction Networks. *Genome Res.* **13**, 2498–2504 (2003).
57. Madeira, F. *et al.* The EMBL-EBI Job Dispatcher sequence analysis tools framework in 2024. *Nucleic Acids Research* **52**, W521–W525 (2024).
58. Huerta-Cepas, J., Serra, F. & Bork, P. ETE 3: Reconstruction, Analysis, and Visualization of Phylogenomic Data. *Mol Biol Evol* **33**, 1635–1638 (2016).
59. Price, M. N., Dehal, P. S. & Arkin, A. P. FastTree 2 – Approximately Maximum-Likelihood Trees for Large Alignments. *PLoS ONE* **5**, e9490 (2010).
60. Zhang, H. *et al.* A Comprehensive Online Database for Exploring ∼20,000 Public Arabidopsis RNA-Seq Libraries. *Molecular Plant* **13**, 1231–1233 (2020).
61. Malamy, J. E. & Benfey, P. N. Organization and cell differentiation in lateral roots of *Arabidopsis thaliana*. *Development* **124**, 33–44 (1997).
62. Mazur, E. *et al.* Clathrin-mediated trafficking and PIN trafficking are required for auxin canalization and vascular tissue formation in Arabidopsis. *Plant Science* **293**, 110414 (2020).
63. Sauer, M. & Friml, J. Immunolocalization of Proteins in Plants. in *Plant Developmental Biology* (eds. Hennig, L. & Köhler, C.) vol. 655 253–263 (Humana Press, Totowa, NJ, 2010).

3 Conclusions

Auxin plays a pivotal role in plant development, orchestrating growth through both, transcriptional and non-transcriptional signaling pathways. While the canonical TIR1/AFB-mediated auxin signaling has been extensively studied, the mechanisms of non-canonical pathways remain less understood. This thesis investigates the cell-surface ABP1-TMK1-dependent pathway, shedding light on its activation, downstream phosphorylation events, and its role in regulating key developmental processes.

The history of ABP1 in auxin signaling has been difficult, often controversial, with long-standing debates about its functional significance. In chapter one, our findings reaffirmed ABP1's auxin-binding ability and its dual localization in the endoplasmic reticulum (ER) and extracellular space, solidifying its significance in auxin perception. Building on this, we established ABP1-TMK1 as a central auxin perception and signaling module, mediating ultrafast phosphorylation events. Notably, we identified its essential role in auxin canalization and vascular tissue regeneration, emphasizing its broader impact on plant development.

In chapter two, we extended our investigation to the evolutionary conservation of auxin-mediated phosphorylation across the green lineage. Our findings highlighted the role of B4 RAF-like kinases in this ancient and widespread phosphorylation-based auxin response, linking rapid auxin signaling to cytoplasmic streaming, a fundamental cellular response to auxin.

A key focus of Chapter Three was identifying targets of TMK1-mediated phosphorylation, particularly the PIN auxin transporters, given their crucial role in auxin function. Among them, PIN2 was found to interact with TMK1, leading to its phosphorylation. This modification plays a critical role in root gravitropism, as it stabilizes PIN2 asymmetrically, reinforcing auxin transport dynamics required for root bending. Additionally, we identified ABP1 and ABL3 as functionally redundant upstream regulators of this mechanism, further establishing a positive feedback loop between cell-surface auxin signaling and auxin transport.

To further dissect the TMK1 signaling pathway, in Chapter Four, we identified and characterized seven TMK1 interactors (TINTs), a structurally and evolutionarily diverse group of receptor-like kinases (RLKs). Many of these TINTs play crucial roles in auxin canalization, particularly in vascular tissue regeneration, while others contribute to hypocotyl gravitropism and stomatal movement. By uncovering this network of interactors, our study provides key insights into the complexity of the auxin canalization network and helps bridge TMK1-mediated auxin signaling with other essential developmental processes.

Together, these findings significantly advance our understanding of the ABP1-TMK1 auxin signaling pathway and its diverse functions in plant growth and development. By identifying the ultrafast phosphorylation as a key downstream event, its evolutionary conservation, and its molecular targets, this work lays the foundation for a more integrated model of auxin signaling and transport, thus uncovering new regulatory mechanisms underlying plant development.

4 Future Directions

Unresolved questions in the cell-surface auxin signaling
Understanding auxin signaling at the cell surface has been essential in uncovering the mechanisms behind its rapid responses. The identification of ABP1-TMK1 as a key complex of this pathway provided crucial insights, yet several intriguing questions remain. One particularly puzzling observation is that while auxin-induced phosphorylation events are abolished in the mutants *tmk1* and *abp1*, these mutants do not exhibit strong phenotypes under normal conditions. This raises fundamental questions about potential compensatory mechanisms or alternative pathways that overcome the loss of phosphorylation-based signaling. Investigating these mechanisms could reveal novel layers of auxin regulation.

TMK1 interactors
One of the key findings of this study is the identification of TMK1 interactors (TINTs), many of which are potential pseudokinases. An important next step would be to clone and express their kinase domains (KDs) *in vitro* to assess their activity and confirm whether they function as active kinases. For those that are active, it would be interesting to test their activity in response to auxin. Additionally, exploring whether TINTs can influence TMK1 activity, and vice versa, could provide key insights into their functional interplay.
Moreover, since TMK1 belongs to a family of four other closely related receptors, it would be insightful to investigate the interactions between TINTs and these other TMK family members.

TINTs and the complexity of auxin canalization
Canalization, a crucial process for vascular regeneration and formation from a localized auxin source, involves multiple TINTs working together with TMK1. While their collective role in this process is evident, the mechanisms by which they function remain unknown. Do all TINTs act through a common pathway, or do they have specialized roles? The connection between TINT5 and CAMEL/CANAR further complicates this network, raising the question of whether a broader receptor complex governs canalization. Higher-order tint mutants could help clarify whether their roles are additive or if certain TINTs have unique, non-redundant functions. However, the *tint7* single mutant already fails to form vasculature from a localized auxin source, making it challenging to include in a higher-order mutant analysis. Given that TINT7 is a large receptor, the possibility of it having its own ligand and signaling pathway is high. This raises the question of whether TINT7-mediated signaling works in parallel with TMK1 or through cross-talk with the TMK1 pathway to regulate auxin canalization. Additionally, testing the ability of the active kinases to phosphorylate key targets, such as PIN1, would provide insights into their functional mechanisms.

TMK1 and TINT6 in hypocotyl gravitropism
The involvement of TINT6 and TMK1 in hypocotyl gravitropism presents another direction worth exploring. The finding that the *tint6* mutant exhibits enhanced bending while *tmk1-1* alone does not, yet the *tmk1-1 tint6* double mutant shows hypobending, suggests a complex regulatory interaction. This could mean that while TINT6 has independent roles, its interaction with TMK1 is crucial for maintaining the proper balance of the response. One key question is whether TINT6 plays a role in the second PIN3 repolarization event triggered by auxin, which could be tested using PIN3-GFP reporter lines in *tint6* and double mutant backgrounds. Another open question is whether TINT6 functions as a co-receptor for TMK1, given its established role as a co-receptor for other receptors. Further experiments could include kinase and phosphorylation assays, additional phenotypic analyses; overexpression of TINT6 in the

tmk1-1 background, and rescue experiments by complementing TINT6 into the double mutant background to see if the normal phenotype is restored. Additionally, although the hypocotyl bending angle was determined after 24 hours of gravitropism, it would be interesting to examine the bending angle kinetics in the single and double mutants to reveal any differences in response timing.

TMK1 and TINT7 in stomatal movement

While TMK1 and TINT7 are implicated in regulating stomatal movement, the underlying mechanisms remain poorly understood. It would be interesting to determine whether this regulation of stomatal dynamics requires auxin or occurs independently through the TMK1 and TINT7 pathways. Given that TINT7 is a large receptor, there is also the possibility of other ligands being involved in the process.

5 Additional references

References used in the Introduction.

1. Darwin, C. The 'Power of movement in plants.'--1880. in *The life and letters of Charles Darwin, including an autobiographical chapter, Vol. 3, 7th thousand rev.* (ed. Darwin, F.) 329–338 (John Murray, London, England, 1888). doi:10.1037/13004-011.
2. Went, F. W. *On Growth-Accelerating Substances in the Coleoptile of Avena Sativa*. (1926).
3. Kögl, F., Erxleben, H. & Haagen-Smit, A. J. Über die Isolierung der Auxine a und b aus pflanzlichen Materialien. 9. Mitteilung über pflanzliche Wachstumsstoffe. *Hoppe-Seyler´s Zeitschrift für physiologische Chemie* **225**, 215–229 (1934).
4. Perrot-Rechenmann, C. Cellular Responses to Auxin: Division versus Expansion. *Cold Spring Harbor Perspectives in Biology* **2**, a001446–a001446 (2010).
5. Rayle, D. L. & Cleland, R. E. The Acid Growth Theory of auxin-induced cell elongation is alive and well. *Plant Physiology* **99**, 1271–1274 (1992).
6. Liu, Cm., Xu, Zh. & Chua, N. H. Auxin Polar Transport Is Essential for the Establishment of Bilateral Symmetry during Early Plant Embryogenesis. *Plant Cell* 621–630 (1993) doi:10.1105/tpc.5.6.621.
7. Bohn-Courseau, I. Auxin: A major regulator of organogenesis. *Comptes Rendus. Biologies* **333**, 290–296 (2010).
8. Evans, MichaelL., Ishikawa, H. & Estelle, MarkA. Responses of Arabidopsis roots to auxin studied with high temporal resolution: Comparison of wild type and auxin-response mutants. *Planta* **194**, (1994).
9. Balla, J. *et al.* Auxin flow-mediated competition between axillary buds to restore apical dominance. *Sci Rep* **6**, 35955 (2016).
10. Aloni, R. The Induction of Vascular Tissues by Auxin. in *Plant Hormones: Biosynthesis, Signal Transduction, Action!* (ed. Davies, P. J.) 485–518 (Springer Netherlands, Dordrecht, 2010). doi:10.1007/978-1-4020-2686-7_22.
11. Ellis, C. M. *et al. AUXIN RESPONSE FACTOR1* and *AUXIN RESPONSE FACTOR2* regulate senescence and floral organ abscission in *Arabidopsis thaliana*. *Development* **132**, 4563–4574 (2005).
12. Lee, H., Kim, H., Park, J. M., Cho, H. S. & Jeon, J. H. PIN -mediated polar auxin transport facilitates root−obstacle avoidance. *New Phytologist* **225**, 1285–1296 (2020).
13. Fu, J. & Wang, S. Insights into Auxin Signaling in Plant-Pathogen Interactions. *Front. Plant Sci.* **2**, (2011).
14. Jing, H., Wilkinson, E. G., Sageman-Furnas, K. & Strader, L. C. Auxin and abiotic stress responses. *Journal of Experimental Botany* **74**, 7000–7014 (2023).
15. Salehin, M., Bagchi, R. & Estelle, M. $SCF^{TIR1/AFB}$ -Based Auxin Perception: Mechanism and Role in Plant Growth and Development. *Plant Cell* **27**, 9–19 (2015).